



HAL
open science

Simulation par dynamique moléculaire de la dissolution de la cellulose dans les fluides supercritiques et les mélanges cosolvants/fluides supercritiques

Ivan Vyalov

► **To cite this version:**

Ivan Vyalov. Simulation par dynamique moléculaire de la dissolution de la cellulose dans les fluides supercritiques et les mélanges cosolvants/fluides supercritiques. Chimie théorique et/ou physique. Université Lille1 - Sciences et Technologies, 2011. Français. NNT: . tel-01581898

HAL Id: tel-01581898

<https://hal.science/tel-01581898>

Submitted on 5 Sep 2017

HAL is a multi-disciplinary open access archive for the deposit and dissemination of scientific research documents, whether they are published or not. The documents may come from teaching and research institutions in France or abroad, or from public or private research centers.

L'archive ouverte pluridisciplinaire **HAL**, est destinée au dépôt et à la diffusion de documents scientifiques de niveau recherche, publiés ou non, émanant des établissements d'enseignement et de recherche français ou étrangers, des laboratoires publics ou privés.

Copyright

UNIVERSITÉ LILLE 1
LABORATOIRE DE SPECTROCHIMIE INFRAROUGE ET RAMAN

École doctorale : Optique et Lasers, Physico-Chimie, Atmosphère

Unité de recherche : Laboratoire de Spectrochimie Infrarouge et Raman

Thèse présentée par : VYALOV Ivan

Soutenue le 9 décembre 2011

Pour obtenir le grade de docteur de l'Université Lille 1

Discipline/Spécialité : Physique

Titre de la thèse :

**Simulation par Dynamique Moléculaire de
la Dissolution de la Cellulose dans les
Fluides Supercritiques et les Mélanges
Cosolvants/Fluides Supercritiques**

Thèse dirigée par :

IDRISSI Abdenacer Directeur de Thèse, HDR

KISELEV Michael Co-Directeur de Thèse, Professeur

Rapporteurs :

FEDOROV Maxim V. Professeur

SOETENS Jean Christophe Professeur

Jury :

BUNTINX Guy DR CNRS

JEDLOVSZKY Pal Professeur

AFFOUARD Frédéric Professeur

UNIVERSITÉ LILLE 1
LABORATOIRE DE SPECTROCHIMIE INFRAROUGE ET RAMAN

Doctoral school: Optique et Lasers, Physico-Chimie, Atmosphère

University department: Laboratoire de Spectrochimie Infrarouge et Raman

Thesis defended by: VYALOV Ivan

Defended on Friday 9th December, 2011

In order to become Doctor from Université Lille 1

Subject/Speciality: Physics

Thesis title:

**Molecular Dynamics Simulation of
Dissolution of Cellulose in Supercritical
Fluids and Mixtures of
Cosolvents/Supercritical Fluids**

Ph. D. thesis supervised by:

IDRISSI Abdenacer supervisor, HDR
KISELEV Michael co-supervisor, Professor

Recorders:

FEDOROV Maxim V. Professor
SOETENS Jean Christophe Professor

Dissertation committee:

BUNTINX Guy DR CNRS
JEDLOVSZKY Pal Professor
AFFOUARD Frédéric Professor

Mots clés: Cellulose – Dissolution – Simulation par ordinateur, Cellobiose – Solvation, Solvants non aqueux, Dynamique moléculaire, Fluides supercritiques, Monte-Carlo, Thermodynamique statistique

Keywords: cellulose dissolution, cellobiose solvation, computer simulations, molecular dynamics, monte carlo, supercritical fluids, nonaqueous solutions, statistical thermodynamics

Cette thèse a été préparée au



Laboratoire de Spectrochimie Infrarouge et Raman
Laboratoire de Spectrochimie Infrarouge et Raman – UMR 8516
Université Lille 1 Sciences et Technologies
Bâtiment C5
59655 Villeneuve d'Ascq Cedex – France

☎ 03 20 43 49 89
FAX 03 20 43 67 55
✉ secretariat-lasir@univ-lille1.fr
Site lasir.univ-lille1.fr

*To my Mom and Dad,
to my Grandma and Grandpa,
and to Maria,
your love and wisdom
always help me.*

Acknowledgements

This work was done under the direction of my dear chiefs Abdenacer IDRISSE, Michael KISELEV, to whom I would like to express my gratitude. I appreciate their great job in guiding me (what is already a difficult job), helping me with a good advice in scientific questions and also sharing their life experience.

I feel sincere gratitude to my opponents: Maxim Fedorov, professor at University of Strathclyde, Glasgow and Jean-Christophe Soetens, professor at University of Bordeaux who have found the time and read this work and expressed their remarks and critics to it. I appreciate the work of the dissertation committee: Guy Buntinx, the director of LASIR; Pál Jedlovszky, professor at Eszterházy Károly College, Eger and Frédéric Affouard, CNRS Researcher at University of Lille 1.

I would like to say the words of gratitude to the lab and everybody here whose kindness and warm attitude helped me a lot during my staying in LASIR.

This work would never be possible without help and facilities of Centre de Ressources Informatiques of University of Lille 1. I would like to thank sincerely Yvon Tinel for his help with software and hardware issues always happening when dealing with big computers.

I would like to kindly thank the CRIHAN centre as well. Their computational facilities allowed me to perform such large scale calculations.

Abstract

Cellulose is insoluble in neat supercritical CO₂ and the main objective of this work was to investigate mixtures of scCO₂ with polar cosolvents for the development of new processing technologies for the cellulose dissolution. The objective is achieved by studying the dissolution process of monomer of cellulose and its various polymorphs. The effect of the t/d parameters on the dissolution process was analyzed by molecular dynamics simulation. We begin with analyzing structure of pure supercritical fluids and mixtures of supercritical fluids/cosolvents using unconventional tools: Voronoi tessellations and nearest neighbours approach.

Thermodynamics of the mixtures of scCO₂/cosolvents is analysed in order to check the validity of the potential models used in our simulations for what the method of thermodynamic integration to calculate the energy, entropy and free energy of mixing was applied. To analyze the dissolution of cellulose we started from studying the solvation free energy of cellobiose (cellulose monomer) which was calculated from molecular dynamics simulations using free energy perturbation method. The influence of conformational degrees of freedom on solvation free energy of cellobiose was also considered.

Finally, the direct dissolution of cellulose crystals models in well-known good cellulose solvent (1-ethyl-3-methylimidazolium chloride) and then considered supercritical solvents. It was found that various mixtures of CO₂ with cosolvents do not dissolve cellulose but they can considerably affect its crystalline structure whereas ammonia fluid can dissolve cellulose and this process is significantly influenced by temperature, pressure and density.

Contents

List of Tables	xiii
List of Figures	xv
I Introduction and Methodology	1
1 INTRODUCTION	3
1.1 Supercritical fluids	8
1.2 Cellulose and cellulose solvents	13
1.3 Cellulose polymorphism.	18
2 METHODOLOGY	23
2.1 Statistical Thermodynamics	24
2.2 Monte Carlo Simulations	29
2.3 Molecular Dynamics Simulations	32
2.4 Analysis of molecular simulations data	34
2.5 Free energy methods	40
II Development of the problem	45
3 STRUCTURE OF SUPERCRITICAL SOLVENTS	49
3.1 Structure of pure supercritical fluids: carbon dioxide and ammonia . .	50
3.2 Properties of mixtures of carbon dioxide with cosolvents	123
4 CELLOBIOSE SOLVATION	143
4.1 Cellobiose solvation	144

5	CELLULOSE NANOCRYSTALS DISSOLUTION	159
5.1	Introduction	160
5.2	Cellulose nanocrystals in ionic liquid.	163
5.3	Cellulose nanocrystals in supercritical mixtures of scCO ₂ /acetone and scCO ₂ /ethanol	166
5.4	Cellulose nanocrystals in liquid and supercritical ammonia.	178
6	CONCLUSIONS AND PERSPECTIVES	187
6.1	Conclusions.	188
6.2	Perspectives.	192
	Bibliography	193

List of Tables

1.1	Amineoxides family cellulose solvents	16
3.1	Values of the Temperatures, T, Molar Volumes, V_m , Pressures, P, and Box Lengths Used in the Molecular Dynamic Simulations	53
3.2	Parameters of the Intermolecular Interaction Potential of CO ₂	54
3.3	Mean values and standard deviations of the properties of the Voronoi polyhedra of the CO ₂ system along the liquid–gas coexistence curve . .	73
3.4	Geometrical and Energetical Parameters of the Six Potential Models of Ammonia	83
3.5	Comparison between the Calculated Critical Temperature, T_C and Critical Density, ρ_C and the Corresponding Experimental Values	84
3.6	Parameters of the molecular potential model of ammonia	112
3.7	Characteristics of the simulated systems	126
3.8	Geometry parameters of the potential models used	128
3.9	Interaction parameters of the potential models used	129
4.1	Systems for cellobiose solvation simulations	146
5.1	Nonbonded interaction energy of cellulose polymorphs in CHARMM carbohydrates force field, normalized by one unit cell.	160

List of Figures

1.1	Argon liquid–gas coexistence curve.	8
1.2	Effect of different cosolvents concentration on solubility of naproxen at 333.1K and 179.3 bar (from (Ting et al. 1993))	12
1.3	Intra- and intermolecular hydrogen bonds in cellulose.	13
1.4	Viscose process	14
1.5	Formation of chemical bond between cellulose and imidazolium cation in presence of acetate anion.	17
1.6	Intrasheet hydrogen bonds in polymorphs I(left) and II(right).	19
1.7	Arrangements of chains of cellulose I _β (left) and II(right).	20
1.8	Complete cellulose polymorphs conversion scheme.	20
1.9	NMR and diffraction spectra of different cellulose polymorphs	21
2.1	Periodic boundary conditions in two dimensions. Color central image represents a system interacting with its (gray) images.	27
2.2	Definition of the nearest neighbors distribution functions.	35
2.3	Nearest neighbors distance distributions and their sum as the total $g(r)$	35
2.4	2-d demonstration of Voronoi tessalation.	37
3.1	Pictorial representation of the nearest neighbor approach	52
3.2	Average distance between a probe CO ₂ molecule and its nearest neighbors	55
3.3	Distributions of the Lennard-Jones interaction energy	57
3.4	Distribution of the Lennard-Jones interaction between a probe CO ₂ molecule and its nearest neighbors	58
3.5	Orientation distributions between a probe CO ₂ molecule and its first and second nearest neighbors	60
3.6	Effect of the temperature on the average distance between a probe CO ₂ molecule and its first nearest neighbors	61

3.7	Effect of the temperature on the distribution of the Lennard-Jones interactions between a probe CO ₂ molecule and its first, third, and fifth nearest neighbor	62
3.8	Effect of the temperature on the distribution of the electrostatic interactions between a probe CO ₂ molecule and its first, third, and fifth nearest neighbor	63
3.9	Effect of the temperature on the average values of the electrostatic, the Lennard-Jones, and the total interaction energies between a probe CO ₂ molecule and its nearest neighbors, n	64
3.10	Effect of the temperature on the orientation distributions between a probe CO ₂ molecule and its first, second, third, and fourth nearest neighbors	65
3.11	Effect of the temperature on the orientation distributions between a probe CO ₂ molecule and its first and third nearest neighbors	66
3.12	VP volume distribution of the CO ₂ molecules along the liquid–gas coexistence curve	74
3.13	VP reciprocal volume (local density) distribution of the CO ₂ molecules along the liquid–gas coexistence curve ($250 \text{ K} \leq T \leq 303 \text{ K}$) and along the critical isochore ($306 \text{ K} \leq T \leq 313 \text{ K}$). The legend is the same as in Figure 3.12	75
3.14	Illustration of the fitting of the obtained VP reciprocal volume distributions by Gaussians	76
3.15	Distribution of the radius of the elemental spherical vacancies among the CO ₂ molecules along the liquid–gas coexistence curve	77
3.16	Correlation between the mean VP volume of the CO ₂ molecules $\langle V \rangle$ and the cube of the mean radius of the elemental spherical vacancies among the molecules	77
3.17	VP asphericity parameter distribution of the CO ₂ molecules along the liquid–gas coexistence curve	78
3.18	Pictorial representation of the orientation between a reference ammonia molecule and its first nearest neighbor. The angles θ_A is that between the molecular axis and that joining the nitrogen atoms of the two molecules. The angles θ_B is that between the neighbor molecular axis and that joining the nitrogen atoms of the two molecules.	82
3.19	Comparison between the calculated radial distribution functions . . .	85
3.20	Comparison between the experimental and the calculated liquid–gas coexistence curves for the six potential models used in our simulations.	86
3.21	Nearest neighbor radial distributions for $n = 1-54$	87

3.22	First nearest neighbor radial distributions $p_{NH}(n = 1, r, T)$ calculated along the isobar 50 bar and at various temperatures in the range between 259 and 500 K	88
3.23	Average values of the interaction energy between a reference ammonia molecule and its first nearest neighbor, as a function of temperature.	89
3.24	Radial distribution functions $g_{NN}(r)$ and coordination number (right axis) at various temperatures along the isobar 135 bar.	90
3.25	Radial distribution function $g_{NN}(r)$ and the fluctuations of distance of the nearest neighbors $\Delta r_{N-N}(n, T = 250 \text{ K})$	91
3.26	Average distance, $r_{N-N}(n, T)$, between a reference ammonia molecule and its nearest neighbors	92
3.27	Fluctuation of the average distance $\Delta r_{\alpha-\beta}(n, T)$ along the isobar 50 bar and in the range of temperature between 250 and 500 K.	93
3.28	Nearest neighbor relative orientational distribution	94
3.29	Experimental and simulated liquid–vapor coexistence curves of ammonia along the 135 bar isobar	98
3.30	Density distribution of the VP of the ammonia molecules, as obtained along the 135 bar isobar at various temperatures in the range between 250 and 500 K	100
3.31	Mean value of the reciprocal VP volume, characterizing the local density ρ (left) and the corresponding standard deviation σ_ρ (right) of the $P(\rho)$ distribution as a function of the temperature.	101
3.32	Volume distribution of the VP of ammonia molecules, as obtained along the 135 bar isobar at various temperatures in the range between 250 and 500 K. The arrow indicates the increase of the temperature.	102
3.33	Standard deviation σ_V of the volume of the VP distribution as a function of the temperature.	103
3.34	Number of faces distribution of the VP of ammonia molecules, as obtained along the 135 bar isobar at various temperatures in the range between 250 and 500 K	104
3.35	Correlation between average VP volume, V , and average number of VP faces, NE	105
3.36	Face area distribution of the VP, as obtained along the 135 bar isobar at various temperatures in the range between 250 and 500 K	106
3.37	Distribution of the radius of the spherical voids present in ammonia, as obtained along the 135 bar isobar at various temperatures in the range between 250 and 500 K	107
3.38	Behavior of (a) the void radius average distance and (b) the corresponding fluctuation as a function of temperature. figure	107

3.39	Equilibrium snapshots of ammonia, as taken from the simulations performed at (a) $T = 250$ K and (b) $T = 420$ K.	108
3.40	Distribution of the total surface area of the VP distributions, as obtained along the 135 bar isobar at various temperatures in the range between 250 and 500 K	109
3.41	Distribution of the asphericity parameter of the VP, as obtained along the 135 bar isobar at various temperatures in the range between 250 and 500 K.	110
3.42	Diffusion coefficient of ammonia as function of temperature.	111
3.43	Comparison between the calculated and experimental densities along the isobar 135 bar (Lemmon, Mclinden, and Friend 2005).	113
3.44	Comparison between the calculated and experimental thermal expansion (Lemmon, Mclinden, and Friend 2005).	113
3.45	Comparison between the calculated and experimental diffusion coefficient (O'Reilly, Peterson, and Scheie 1973; Grob et al. 1997).	113
3.46	Definition of the principal axes of ammonia.	114
3.47	Reorientation correlation functions of ammonia	115
3.48	Temperature behavior of the reorientation and rotation correlation times	116
3.49	Angular velocity correlation functions	117
3.50	Angular velocity correlation functions about the principal molecular axis z	118
3.51	Radial distribution functions g_{N-N}	121
3.52	2D correlation signal of the g_{N-N} radial distribution function	122
3.53	Behavior of the microscopic density.	122
3.54	Integrand of the thermodynamic integration	130
3.55	Composition dependence of the molar volume of the ethanol/ CO_2 and acetone/ CO_2 systems simulated.	133
3.56	Voronoi polyhedra volume distribution	135
3.57	Composition dependence of the change of the molar volume accompanying the mixing of ethanol and acetone	137
3.58	Composition dependence of the molar energy, free energy and entropy of the ethanol/ CO_2 and acetone/ CO_2	138
3.59	Composition dependence of the change of the molar energy (top panel), free energy (middle panel) and entropy (bottom panel) accompanying the mixing of ethanol with CO_2	139
3.60	Composition dependence of the change of the molar energy, free energy and entropy accompanying the mixing of acetone with CO_2	140
3.61	Equilibrium snapshots of the ethanol/ CO_2 mixed systems	141
3.62	Size distribution of the ethanol clusters	141

4.1	The macroscopic changes of cellulose models after treatment by supercritical mixture of solvents	144
4.2	Illustration of switching off of the interactions between cellobiose and solvent media.	148
4.3	Definition of conformational degrees of freedom of cellobiose: Dihedral angles φ (O5-C1-O4-C4) and ψ (C1-O4-C4-C5)	149
4.4	Free energy map of cellobiose in vacuum along φ and ψ coordinates.	150
4.5	Free energy maps of cellobiose in ammonia for: a) 243 K, b) 390 K, c) 420 K, d) 450 K.	151
4.6	Free energy maps of cellobiose for: a) CO ₂ , b) CO ₂ -acetone c) CO ₂ -ethanol, d) EMIMCl.	151
4.7	Cut of free energy surface of cellobiose in water along φ and ψ coordinates	152
4.8	Cut of free energy surfaces along φ and ψ coordinates(left-hand column) and probabilities to observe φ and ψ from MD-trajectories(right-hand column)	153
4.9	FEP graphs with and without conformational sampling for cellobiose in water	154
4.10	FEP graphs with and without conformational sampling for cellobiose in EMIMCl	155
4.11	FEP graphs for cellobiose in scCO ₂ and its mixtures with acetone and ethanol	156
4.12	FEP graphs with conformational sampling for cellobiose in scCO ₂ and its mixtures with acetone and ethanol	157
4.13	FEP graphs of cellobiose solvation in ammonia for thermodynamical parameters corresponding to those in Table 4.1	157
5.1	Side-view of cellulose polymorphs nanocrystals	162
5.2	Snapshots of the first timesteps of cellulose simulation of polymorphs I _{β} and III _I in EMIMCl ionic liquid.	164
5.3	Radii of gyration of cellulose polymorphs in emim.	165
5.4	RMSDs of cellulose polymorphs.	167
5.5	Final snapshots of simulations of cellulose polymorphs in EMIMCl. Polymorph types are subscribed directly on the figure.	168
5.6	Snapshots of the first timestep of cellulose simulation of polymorphs I _{α} and IV _{II} in scCO ₂ /acetone mixture.	170
5.7	Cellulose snapshot in the moment of internal rearrangement in CO ₂ /acetone mixture	171
5.8	Radii of gyration (a) and RMSDs (b) of cellulose polymorphs in scCO ₂ /acetone mixture.	172

5.9	Radii of gyration (a) and RMSDs (b) of cellulose polymorphs in scCO ₂ /ethanol mixture.	174
5.10	Structural rearrangement in cellulose crystal in scCO ₂ /ethanol mixture	175
5.11	Final snapshots of cellulose I _β (solvent molecules were removed for better perception)	175
5.12	Radii of gyration (a) and RMSDs (b) of cellulose polymorph IV _{II} in scCO ₂ /ethanol/[urea]TM	
5.13	Changes of ROG during the 200ns-long run in scCO ₂ /ethanol/urea tertiary mixture.	178
5.14	Thermodynamic points for cellulose in ammonia simulations	180
5.15	Radii of gyration of cellulose IV _{II} polymorph in ammonia along the isobar 135 bar.	181
5.16	RMSDs of cellulose IV _{II} polymorph in ammonia along the isobar 135 bar.	182
5.17	Radii of gyration of cellulose I _β polymorph in ammonia along the isobar 135 bar.	183
5.18	Initial snapshots of cellulose in liquid and supercritical ammonia. Temperatures are subscribed below the figures.	184
5.18	Figure 5.18–Continuation. Initial(left-hand side) and final(right-hand side) snapshots of configurations of cellulose nanocrystals in ammonia. Temperatures are subscribed under the figures.	185

Part I

Introduction and Methodology

Chapter **1**

INTRODUCTION

THERE is a growing awareness of the ecological impact of chemical production and it is now widely recognized that the development of clean synthetic methodologies can offer a new avenues to benign and cost-effective processes. This quest for green chemistry engenders a tremendous challenge for fundamental research in chemistry. One aspect of research toward more sustainable processes for chemical synthesis is the scientific evaluation of potential replacements for toxic solvents. In particular, in chemical production, synthesis is mainly carried out in solution phase, and organic solvents are usually the first choice. These solvents are often problematic owing to their toxicity, flammability, or environmental hazards. Isolation of the pure product, recycling of reagents and solvent makeup or disposal are important cost factors for downstream processing in solution- phases synthesis. On the other hand, the solvent can play a crucial role in the stabilisation of reactive intermediates and often has a decisive influence on the rate of selectivity of a particular reaction. These constraints apply in processing cellulose into variety chemicals with large added value.

Cellulose is the most abundant natural polymer that constitutes the cell wall of plants. Chemically, it is a poly[β -(1-4)-D-glucopyranose], a linear polysaccharide which shows a high degree of hydrogen bonding and crystallinity. The biggest cellulose source for commercial product is wood, which contains about 40% cellulose from dry weight. Cellulose is more or less separated from other wood components in the chemical pulping process, resulting in a pulp with cellulose content of 70-94%. The chemical pulps are divided into paper grade and dissolving grade depending on their composition and use. Paper grade contains less cellulose than dissolving grade pulp and is ready for applications as such, whereas the dissolving pulp must be further processed prior to its end-use. The world production of chemical pulp is 118 million tons, from which only 2.5% is dissolving grade pulp despite its higher degree of upgrading. One reason for this unbalance is more complex use of dissolving pulp compared to paper grade pulp. The production of cellulosic fiber films, casings, and other high-value special products requires the dissolution of cellulose which is the key for a successful use of cellulose in a chemical process. The difficulty comes from the strong febrile structure of cellulose, which restricts its dissolution into cheap and common solvents without chemical changes. Many approaches were proposed to achieve the dissolution of cellulose All the current chemical processes to dissolve cellulose have the drawback associated with the toxicity of the used solvents and environmental hazard, with limited solvency, with the problem arising in developing closed processes, and high power consumption in solvent regeneration. Consequently, there is considerable incentive to find alternative chemical process (new solvent) to dissolve cellulose which should have a low impact to the environment. The supercritical fluid technology has been considered for processing different forms of cellulose. The high level of interest in Supercritical Fluid (SCF) Technology first appeared as a result of the environmental benefits associated with their re-

placement of organic solvents. Supercritical Fluids have since demonstrated a number of unique properties that enhance many types of chemical process operations and have consequently found numerous applications throughout industry. By far the most widely used SCF within industry is Supercritical Carbon Dioxide (scCO_2), due to its low toxicity, natural abundance, chemical inertness, non-flammability and relative low cost. Importantly CO_2 is also a gas in ambient conditions, allowing easy removal from materials without the need for costly drying processes. Aside from the many environmental and economic benefits, scCO_2 also exhibits a number of very important chemical processing properties. Investigate of binary mixture of carbon dioxide with organic solvents for the development of new supercritical fluid processing technologies. One of the practical objectives is the replacement or reduction of environmentally objectionable organic solvents in physicochemical processing. By employing mixtures, one can also use the fluid composition as an additional parameter to fine-tune the properties of processing fluids for a specific application, such as those involved in polymer processing. Mixture composition along with pressure and temperature is used as a key parameter to optimize the dissolution process. The motivation of this research is the potential benefits that could result from successful utilization of supercritical fluids for effective dissolution of cellulose.

My thesis research was carried out in the frame of a collaborative project between the LASIR laboratory at the university of Lille and the Institute of solution chemistry-the Russian Academy of Sciences on the optimization of the dissolution process of cellulose using supercritical fluids. The strategy of this project is to combine experimental (vibration spectroscopy, NMR, neutrons scattering, and time resolved spectroscopy) and theoretical approach (mainly classical molecular dynamics) in order to understand at fundamental level the intermolecular interactions involved in the dissolution process of cellulose, in pure supercritical fluids as well as in a mixture of these fluids with co-solvents. The work carried during my thesis concentrate on using molecular dynamics simulation in order to provide molecular-scale analysis of the structural and dynamical properties of pure supercritical fluids and the mixture of these fluids with co-solvents as well as of the dissolution of different model of cellulose and its nanocrystal polymorphs forms in various solvents and supercritical fluids.

The manuscript of thesis will be organized as follows: In the chapter 1, general introduction on the supercritical fluids as well as on cellulose properties is given. The aim was to summarize the state of art on the various processes used to dissolve cellulose. In the chapter 2 information on the methodology used in this thesis is explained, particularly, on the various statistical functions which help to characterize the local structure and on the free energy methods which allows to address the thermodynamic aspect of the dissolution process. As we are dealing with large size molecules with many possible conformations, we explain in the same chapter, the

metadynamics method which aim is to accelerate rare events and then to reduce the time duration to sample the phase space of the studied system. In the chapter 3, we summarize, our already published papers on the analysis of the local structure in pure supercritical fluids as well as in a mixture supercritical CO₂ and co-solvents. In the chapter 4 we deal with the cellulose monomer—cellobiose we started by its free energy of solvation and the influence of conformational substates on it. Finally, in the chapter 5 the dissolution of five polymorph forms of cellulose was analyzed in various solvents and in supercritical fluids.

The main results of the thesis are summarized in the chapter 6. Based on the knowledge gathered during this thesis, the ideas on how to complete and to progress in the analysis of the dissolution of cellulose are given in the perspective of this thesis.

The materials of this thesis were partly presented in following papers:

1. A. Idrissi et al. (Dec. 2009a). “Assessment of the Spatial Distribution in Sub- and Supercritical CO₂ Using the Nearest Neighbor Approach: A Molecular Dynamics Analysis”. In: *The Journal of Physical Chemistry B* 113.48, pp. 15820–15830. ISSN: 1520-6106. URL: <http://dx.doi.org/10.1021/jp9042107>
2. A. Idrissi et al. (2010). “Local structure in sub- and supercritical CO₂: A Voronoi polyhedra analysis study”. In: *J. Mol. Liq.* 153.1, pp. 20–24
3. T. Tassaing et al. (2010). “Supercritical ammonia: A molecular dynamics simulation and vibrational spectroscopic investigation The structure of liquid carbon dioxide and carbon disulfide Analysis of the transverse and the longitudinal pseudodiffusion of CO₂ in sub- and supercritical states: A molecular-dynamics analysis”. In: *The Journal of Chemical Physics* 133.21, pp. 214505–8
4. I. Vyalov et al. (2010). “Investigation of the Local Structure in Sub and Supercritical Ammonia Using the Nearest Neighbor Approach: A Molecular Dynamics Analysis”. In: *J. Phys. Chem. B* 114.46. doi: 10.1021/jp108701t, pp. 15003–15010
5. I. Vyalov et al. (2011b). “Reorientation relaxation in supercritical ammonia”. In: *Journal of Molecular Liquids* 159.1. Intermolecular Interactions and Liquid Structure, Selected Papers on Molecular Liquids presented at the EMLG/JMLG 2009 Annual Meeting 6 - 10 September 2009, pp. 31–37. ISSN: 0167-7322. DOI: 10.1016/j.molliq.2010.09.012. URL: <http://www.sciencedirect.com/science/article/pii/S016773221000303X>
6. A. Idrissi et al. (2011b). “Heterogeneity of the Local Structure in Sub- and Supercritical Ammonia: A Voronoi Polyhedra Analysis”. In: *The Journal of Physical Chemistry B* 115.31, pp. 9646–9652. DOI: 10.1021/jp204078u. eprint: <http://pubs.acs.org/doi/pdf/10.1021/jp204078u>. URL: <http://pubs.acs.org/doi/abs/10.1021/jp204078u>
7. Abdenacer Idrissi et al. (2011c). “Assessment of the potential models of acetone/CO₂ and ethanol/CO₂ mixtures by computer simulation and thermody-

amic integration in liquid and supercritical states”. In: *Phys. Chem. Chem. Phys.* 13 (36), pp. 16272–16281. DOI: 10.1039/C1CP21042D. URL: <http://dx.doi.org/10.1039/C1CP21042D>

The principal conferences where these results were reported are:

1. A. Idrissi et al. (2009b). “Local structure in sub and supercritical ammonia: a molecular dynamics analysis”. In: *EMLG/JMLG Annual Meeting: Intermolecular Interactions and Liquid Structure*
2. I. Vyalov, A. Idrissi, and M. Kiselev (2010a). “Cellobiose solvation free energy in scCO₂ with cosolvent”. In: *Germany: Trilateral Seminar (Russia, Germany, France) : Solvation in Complex Liquids by Theory and Experiment, 23-25 June*
3. I. Vyalov, A. Idrissi, and M. Kiselev (2010b). “Clustering and structure of sub- and supercritical fluids.” In: *Journées Nord-Ouest Européennes des Jeunes Chercheurs, Villeneuve d’Ascq, 18-19 Mars*
4. I. Vyalov, A. Idrissi, and M. Kiselev (2011). “Modelling solvation cellobiose in supercritical CO₂ and its mixtures with ethanol and acetone.” In: *29th EMLG/JMLG Annual Meeting: New outlook on molecular liquids from short scale to long scale dynamics*
5. I. Vyalov et al. (2011a). “Modelling solvation of nanocrystal polymorph of cellulose in supercritical CO₂ and its mixtures with ethanol and acetone.” In: *Supercritical fluids (SCF): fundamentals, technologies, innovations”, 4–7 July, Listvyanka, lake Baykal.*
6. A. Idrissi et al. (2011a). “Assessment of the potential models of acetone/CO₂ and ethanol mixtures by computer simulation and thermodynamic integration.” In: *Supercritical fluids (SCF): fundamentals, technologies, innovations”, 4–7 July, Listvyanka, lake Baykal.*

1.1 Supercritical fluids

1.1.1 Introduction.

Phase diagram of any substance in pressure-temperature coordinates is divided into several regions corresponding to states of matter by coexistence lines (Figure 1.1). In line separating liquid and gas phase necessarily ends at temperature and pressure called critical and denoted by T_C and P_C . At parameters above these values one cannot distinguish liquid and gas phase and transition between them can be carried out continuously via state that is called supercritical.

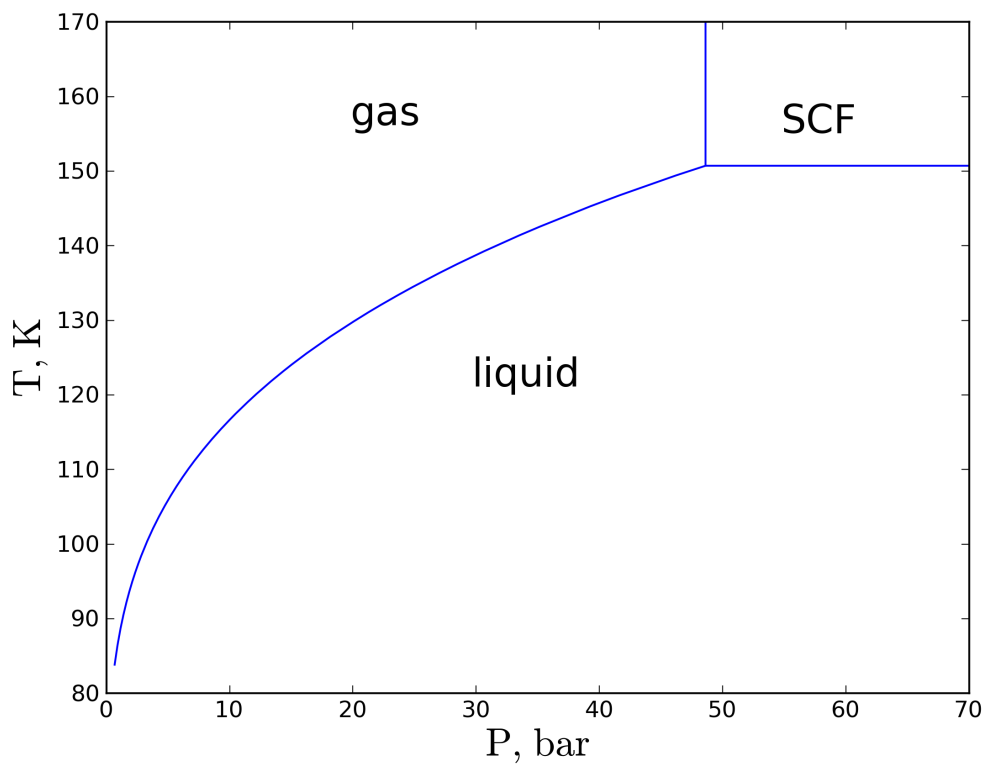


Figure 1.1: Argon liquid–gas coexistence curve.

The history of this discover(Ivanov 2008) comes to 1822 when Charles Cagniard de la Tour conducted his experiments and a bit later Faraday. The problem of describing of phase transitions in fluids goes through XIX and XX to our century. Then there were studies of T. Andrews with CO_2 after which the concept of critical temperature and pressure were introduced. Andrews also assumed universality of these concepts and their applicability to every substance. The real breakthrough was the dissertation

of van der Waals supplemented by Maxwell construction of equal areas. From now on it became possible to describe qualitatively continuity of liquid and gaseous phases with critical point and metastable states. Another success of van der Waals was an introduction of the law of corresponding states where he showed that taking critical point as a reference and expressing parameters in units of critical ones (T^* , P^* , ρ^*) equation of state becomes universal. The phenomena of critical opalescence and its connection to density fluctuations was first pointed out by Smoluchowski. In light of this fact the increase of compressibility can be explained by the increase of fluctuations. And the Ornstein-Zernike theory was first able to explain critical opalescence.

However, although the most of the physics necessary for industrial applications was established already in XIXth—very beginning of the XXth century the history of application of SCFs in chemical technology begins only in 1978 from the first plant for decaffeination of coffee beans. However, on the tide of growing interest to green chemistry supercritical fluids are making up for a lost century and now this field is growing tremendously.

While every substance that can reach its critical point without decomposition could potentially be an SCF it is more advantageous to use those of them whose critical parameters are close to normal conditions. If we compare for example scCO₂ and scH₂O it becomes obvious that even thermostating of water at critical point could be a problem. Another problem is in degradation of many organic solutes at temperatures of supercritical water. From the other hand, critical point close to normal conditions is characteristic for non-polar molecules that cannot dissolve sufficiently polar solutes.

The most popular SCFs are scCO₂ and other supercritical solvents is used at present moment: Water, ethane, ethene, fluorofom, xenon.

1.1.2 General properties of SCFs

The properties of supercritical fluids are known to be between those of a liquid and gas phase taking benefits from both. Having liquid-like density means high dissolving power and enhancement of other density-dependent properties like, for example, dielectric constant. Solubility grows exponentially with pressure and one can adjust solubility of solute by changing pressure what is used in order to achieve high selectivity in extraction by means of SCFs.

Speaking of another side of supercritical solvents one should discuss gas-like properties, a namely: Viscosity, diffusivity and surface tension. The dynamic viscosity η of SCF is of the same value as in the gaseous state. Together with high density ρ this leads to low kinematic viscosity $\nu = \eta/\rho$ what leads to efficient mass transfer. Diffusivity of SCF is also high what makes this media advantageous for those processes where diffusion is the limiting stage.

1.1.3 Properties of SCFs near the critical point

From the other hand thermodynamic response functions such as heat capacity, isothermal compressibility and isobaric expansion coefficient are not intermediate between those of vapour and liquid. They have either maximum or diverge near the critical point. The coefficient of self-diffusion does not have an anomaly near the critical point, however the phenomenon called “critical slowing-down” is observed near the critical point and binary diffusion coefficient becomes zero.

Proximity of the critical point makes SCFs even more interesting for chemical processes. Thus, a number of properties becomes zero (ΔH_{vap}), others diverge (isothermal compressibility). Sometimes such behaviour can be predicted already from a phase diagram. For instance, an isotherm T_c in the P, V -plane has an inflection point with first derivative equal to zero and some properties follow already from these fact: For instance the maximum of the thermal expansion coefficient, α_p . But the most important feature of fluid near its critical point consists in large density fluctuations characteristic to this point in PVT-diagram. A supercritical fluid is called to be in compressible regime and the extent of phase diagram where one can observe this behaviour goes till $\approx 1.3T^*$. This question was intensively studied by experimental: Small angle neutron and x-ray scattering, dynamic light scattering (Saitow, Kajiya, and Nishikawa 2005); theoretical and simulation techniques: Molecular dynamics and Monte Carlo simulations.

One of the most emphasized properties of supercritical fluids not far from the critical point compared to liquid state is the increase of the thermodynamic response functions such as molar heat capacity C_p , the isobaric thermal expansivity α_p , and the isothermal compressibility β . As a consequence, density-dependent properties of supercritical fluids can be varied continuously and markedly from gas-like to liquid-like values with a small change in pressure or/and temperature (Tucker 1999). This feature makes SCFs attractive alternatives to liquid solvents for use in the developments of new chemical processes. From the microscopic point of view such behaviour of response functions is associated with the formation of inhomogeneities in fluid near the critical point at supercritical conditions (Stanley 1987; Tucker and Maddox 1998; Tucker 1999).

The application of common means of equilibrium statistical mechanics such as radial distribution functions is unreasonable for studying the spatially inhomogeneous systems as was pointed out long time ago (Balesku 1975). Problems arise due to the averaging of $g(r)$ over the regions of both low and high local density (Goodyear, Maddox, and Tucker 2000b). As it was realized number of works devoted to studying of the inhomogeneity in supercritical fluids by means of clustering analysis has appeared (Yoshii and Okazaki 1998; Mountain 1999; Rovere, Heermann, and Binder 1990; Goodyear, Maddox, and Tucker 2000a; Martinez, Ravi, and Tucker 1996).

There is another point one should emphasize. All the works mentioned above had

one sufficient drawback, namely, it was necessary to introduce arbitrary threshold parameter to decide whether the particle belongs to cluster or not. This limits applications of clustering analysis and makes them subjective as it is every time necessary to fit the threshold parameter to observed picture. Moreover parameter chosen for one thermodynamic state is not be suitable under other conditions what makes impossible studying the evolution of inhomogeneity with the change of temperature and/or pressure.

Thus, we can see that even though counting clusters in molecular dynamics looks like not very difficult task problems can be faced on this path starting from the very definition of what cluster is and continuing ambiguity of their recognition. Moreover, in fluid one cannot speak about inhomogeneity itself, but only that fluid is more homogeneous in one state than in the other.

1.1.4 Using cosolvents to increase solubility

The most frequently used supercritical fluid is carbon dioxide which itself, of course, is not a good solvent for polar molecules. One example of such an intrainer effect is the solubility of urea (Catchpole et al. 2005) in neat scCO_2 at pressure 150 bar and temperature 313 K is $3.6 \cdot 10^{-6}$ mole fraction and mixture containing 0.1 mole fractions of ethanol dissolves already $1.31 \cdot 10^{-3}$.

Another famous example of cosolvent effect on dissolution of naproxen (Ting et al. 1993) is shown on Fig 1.2. Solubility of naproxen increases in more than 11 times when the mole fraction of 1-propanol in scCO_2 increases from 1.75 to 5.25 mole fraction.

Thus, it was early become recognized that even a small addition of cosolvent can increase solubility dramatically in nonpolar supercritical fluids which represent majority of used sc-solvents. This effect is explained by different factors but for those solutes that can form hydrogen bonds it is usually advantageously to add cosolvents that form hydrogen bonds with it.

Example of urea illustrates clearly the point that dissolution of substance capable to form hydrogen bonds is more efficient at elevated fraction of cosolvent able to form hydrogen bonds. Therefore, we have already binary mixture of solvents and need phase diagrams to be sure that we operate in one phase and under supercritical conditions of the mixture. Phase diagrams for most used supercritical binary mixtures are well-known by this moment. Let us mention few works:

- CO_2 -ethanol (Pöhler and Kiran 1997b)
- CO_2 -methanol (Reighard, Lee, and Olesik 1996)
- CO_2 -acetone (Pöhler and Kiran 1997a)
- CO_2 -propanol (Yeo et al. 2000)

From the point of view of simulations we also need to have molecular models of solvents that adequately describe experimental data. This problem of is being solved

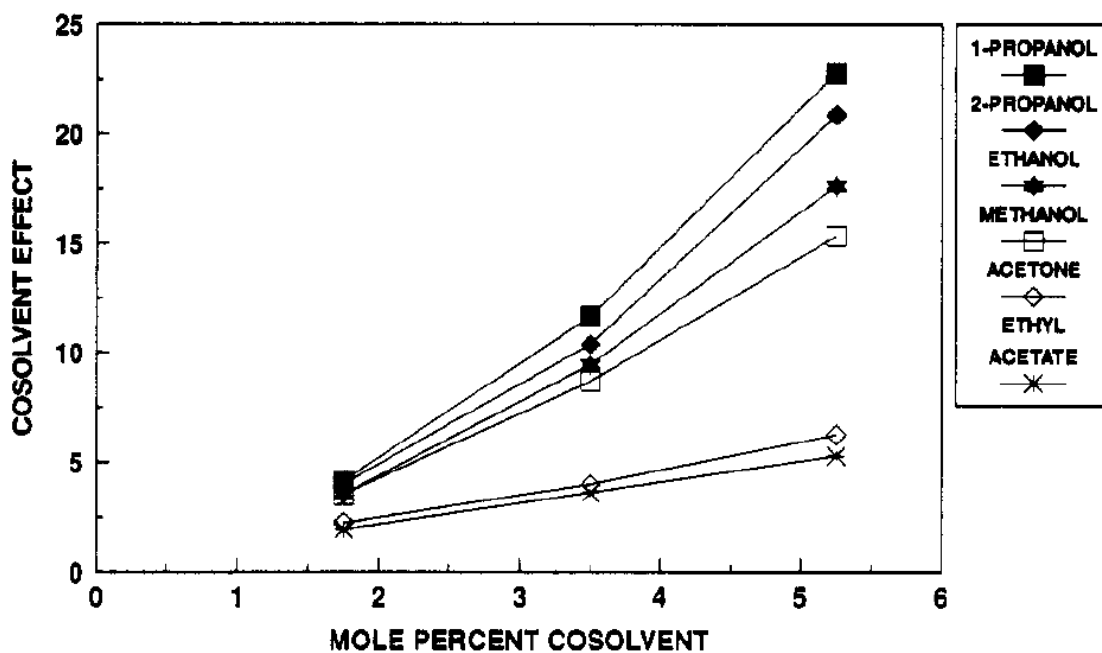
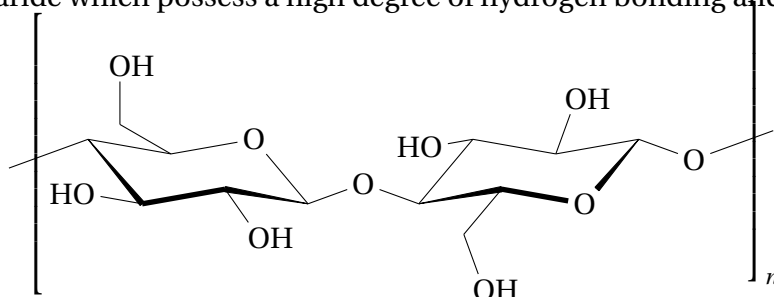


Figure 1.2: Effect of different cosolvents concentration on solubility of naproxen at 333.1K and 179.3 bar (from (Ting et al. 1993))

by applying Gibbs ensemble Monte Carlo technique which is described in section 2.2. There is a whole family of potentials called “Transferable Potentials for Phase Equilibria Force Field” (TraPPE) that were parametrized to predict vapour-liquid co-existence curve of neat liquids. However, they have proved to be successful in predicting mixtures’ properties as well (Potoff and Siepmann 2001; Stubbs, Potoff, and Siepmann 2004).

1.2 Cellulose and cellulose solvents

From the chemist's point of view cellulose is a poly[cellobiose], a linear polysaccharide which possess a high degree of hydrogen bonding and crystallinity:



At a bigger scale cellulose forms sheet structure sewn by intra- and intersheet hydrogen bonds, these patterns are discussed in section 1.3.

Cellulose remains insoluble in common solvents due to high crystallinity and huge number of intra- and intermolecular hydrogen bonds sewing the crystal. Another difficulty comes from the strong fibrillar structure of cellulose as depicted of Fig. 1.3, which restricts its dissolution into cheap and common solvents without chemical changes.

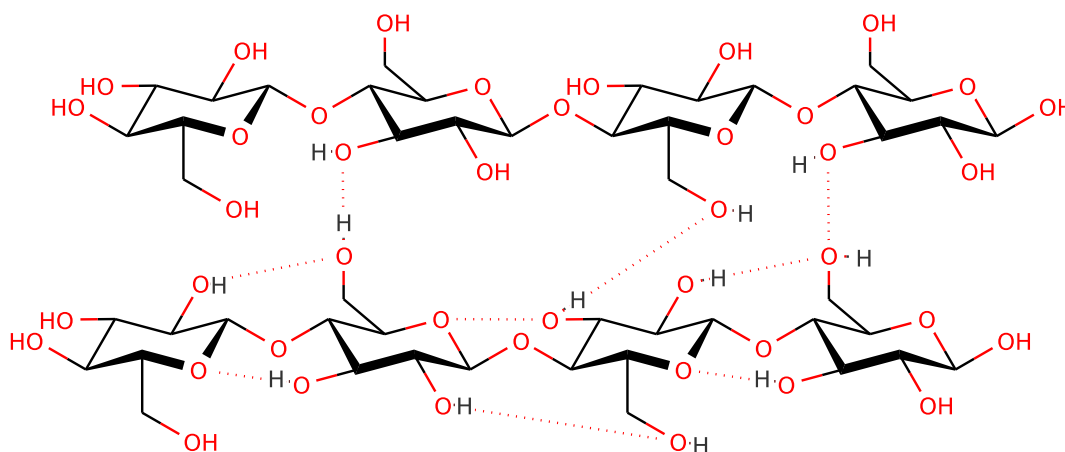


Figure 1.3: Intra- and intermolecular hydrogen bonds in cellulose.

In spite of difficulties, industry demanded to invent cellulose solvents as it was very tempting to use such a cheap raw material as wood and cotton for production new materials. By the present time nomenclature of cellulose solvents counts a lot that can be subdivided into two broad groups: Derivatizing and non-derivatizing. First group includes those solvent that form covalent bonds with cellulose and second relies only on intermolecular interactions. Below we briefly discuss main representatives of both groups.

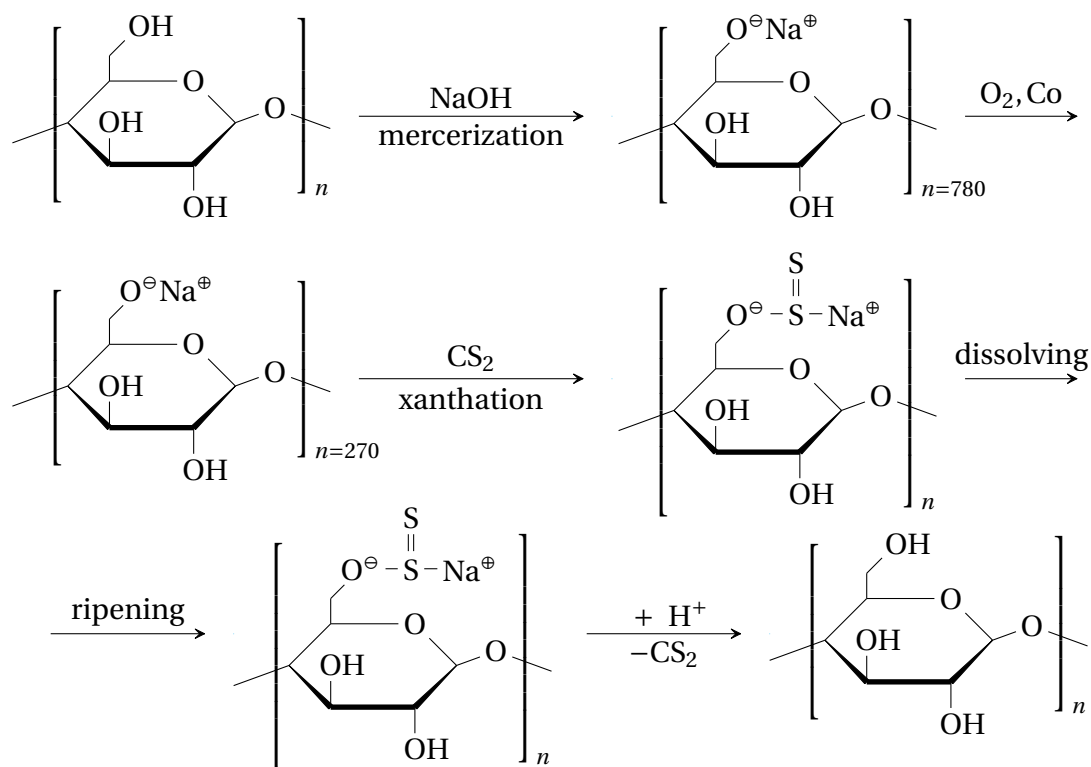


Figure 1.4: Viscose process

1.2.1 Viscose process

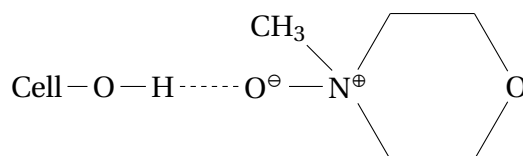
Most of the regenerated cellulose items are manufactured by the viscose process. Indeed, in this process, (see Figure 1.4) the fiber is produced by the following manner: First, wood pulp is mercerized in 18-19% aqueous sodium hydroxide (NaOH) at room temperature ($18\text{-}25^\circ\text{C}$) for 24h. In this process, strong chemical interactions take place, resulting in a cleavage of intra- and inter- molecular bond linkages to form the sodium cellulose I intermediate. This intermediate reacts with carbon disulfide (CS_2) at $20\text{-}30^\circ\text{C}$ for 1-2h to form hydrophilic cellulose xanthogenate (viscose). This derivative is then decomposed to cellulose II, sulfate and carbon disulfide by neutralization of sodium hydroxide. The process is represented by the following scheme:

The cellulose II may be also obtained from cotton linter (cellulose I) by the cuprammonium process, dissolution of cotton linter (cellulose I) in cuprammonium solution and subsequent solidification and regeneration of the dissolved intermediate.

1.2.2 N-methylmorpholin-N-oxide and Lyocell process

In order to treat the toxic gas emissions during the viscose process and to reduce the use of toxic solvents, new solvent systems(1) for cellulose were intensively studied as alternatives to viscose and cuprammonium processes. One of the most important alternatives is the NMMO process (Rosenau et al. 2001)(2-5) which is a direct process, and it provides solutions of cellulose with concentrations between 10 and 15% in N-methylmorpholin-N-oxide and is used in the production of fibers. As the result of problems in handling the NMMO, particularly with the fiber quality, however NMMO processes becomes more and more widespread during last years.

The proceses of dissolution of cellulose in NMMO and in NMMO·H₂O comes to formation of strong hydrogen bonded complexes between cellulose and solvent (being highly-polar compound) according to the following scheme:



This idea is supported by results of molecular dynamics simulations of cellulose models in NMMO and trimethylamine-N-oxide media (Kast et al.; Marhoefer et al.). Among the questions authors addressed there was one that can be posed as follows: Why in spite of structural similarity NMMO dissolves cellulose and trimethylamine-N-oxide (TMAO) does not? It was found that judging by partial radial distribution functions TMAO possess lower affinity to cellohexaose.

Other trimethylamine N-oxides. There is a broad range of tertiary amine N-oxides that dissolve cellulose (Bochek 2003; Varga 1980). Interestingly, in spite of structural similarities there exists striking difference in their dissolving power. The most noticeable example are triethylamine N-oxide and trimethylamine N-oxide. The former well dissolves cellulose while the latter does not, even though having higher dipole moment. Somehow reversed situation is observed in systems with already described NMMO and N-ethylmorpholine N-oxide where ethyl derivative does not dissolve cellulose and methyl- does. The situation can be summarized in the Table 1.1 (Bochek 2003):

1.2.3 Dissolution of cellulose in ionic liquids

Room-temperature ionic liquids are exactly what follows from their name. Their main feature is that they are salts molten under moderate conditions (<100 °C). The most common representatives of this class of substances are cations of alkylimidazolium (R₁R₂IM⁺), tetrabutylammonium (NR₄⁺), alkylpyridinium (RPy⁺, etc. Counter

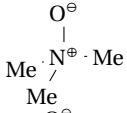
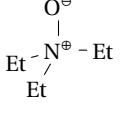
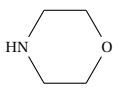
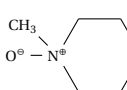
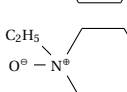
Amine N-oxide	Formula	μ, D	Dissolves cellulose?
TMAO		5.14	No
TEAO		4.52	Yes
MO		4.05	No
NMMO		4.25	Yes
NEMO		4.12	No

Table 1.1: Amineoxides family cellulose solvents

ions are hexafluorophosphate (PF_6^-), tetrafluoroborate (BF_4^-), nitrate (NO_3^-), acetate AcO^- as well as inorganic anions F^- , Cl^- , Br^- .

Ionic structure of this reagents allows to break hydrogen bonds in cellulose. However, there is no simple means to predict whether given ionic liquid will dissolve cellulose or not. Consider, for example, two cations: $[\text{EMIM}]^+$ and $[\text{TBAM}]^+$ and take three complementary anions: Cl^- , F^- , AcO^- . Now, cellulose dissolution power of $[\text{EMIM}]^+$ will be greater for AcO^- then for Cl^- (Pinkert et al. 2009). And the solution of $[\text{TBAM}]^+\text{F}^-$ in dimethylsulfoxide will dissolve cellulose immediately, while the same system but with chloride anion will not dissolve cellulose at all (Heinze et al. 2000). These examples reveal the complexity of phenomena of interactions between ionic liquids and cellulose.

For the first case it was shown that $[\text{EMIM}]^+\text{AcO}^-$ forms covalent bond with cellulose, Fig. 1.5, what leads to increase of dissolution power: For the case of tetrabutylammonium salts in DMSO it is not yet understood why there is such a significant difference in ability to dissolve cellulose. So, we can conclude that there is a broad field of studying of processes of dissolution of cellulose in ionic liquids and optimization of these processes.

Non-derivatizing solvents are quite sensitive to amount of water in system. For $[\text{TBAM}]^+\text{F}^-$ maximum salt/water ratio is advised to be 1/2. This could be considered as a drawback but from the other hand it facilitates the cellulose recovering processes — one needs just to add water.

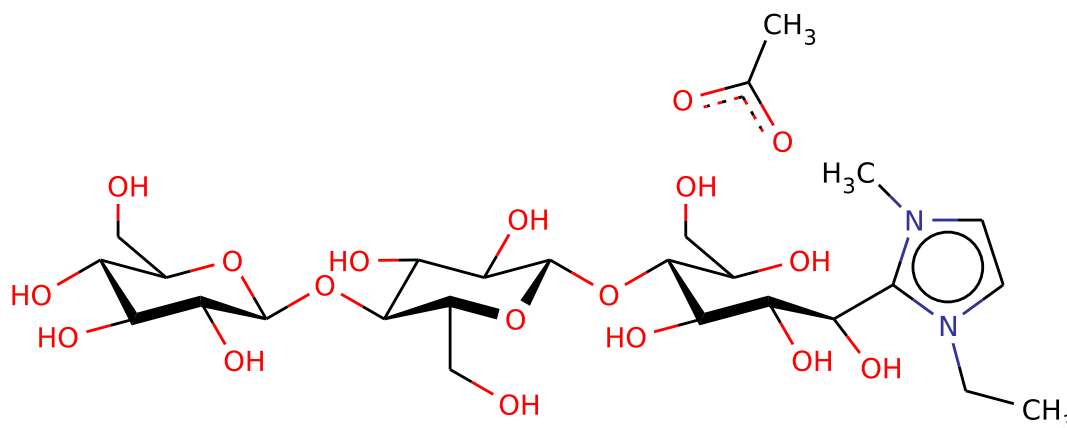


Figure 1.5: Formation of chemical bond between cellulose and imidazolium cation in presence of acetate anion.

1.2.4 Other solvent systems

Other alternatives use aprotic solvents with addition of LiCl, C_3H_7NO with N_2O_4 , $C_4H_4F_3O_2$, (6) and aqueous solvents like aqueous $ZnCl_2$, NaOH, and H_3PO_4 . (7-13) Most of these solvents have not found practical use because of such reasons as toxicity and environmental hazard, limited solvency, problem arising in developing closed processes, and high power consumption in solvent regeneration. For such reasons, the discovery of a new solvent that has low impact to the environment became urgent for developing a process to manufacture cellulose II.

1.2.5 Supercritical fluids as cellulose solvents

As a consequence, the supercritical fluid technology has been considered for processing different forms of cellulose (14-21). DiNoia et al. (15) reported that cellulose acetate/butyrate remains insoluble in neat $scCO_2$ and in CO_2 with ethanol or chlorodifluoromethane co-solvent. However, the authors of this work limited the operating conditions to a maximum of $85^\circ C$ and 1245 bar. Kiran and Pohler (16) showed that ethanol is a better co-solvent than acetone, Indeed a single phase can be obtained at pressures as low as 70 bar, however, 70 wt.% co-solvent is needed to obtain very low operating pressures. Boumghar et al. (22) conducted the dissolution of cellulose in the range $160-170^\circ C$ and pressures comprised between 40.0 and 50.0 MPa. The dissolution was 80% and the recovery of cellulose accounted for 70%. (Sasaki et al. 2000) showed that cellulose dissolves in high temperature water ($400^\circ C$) because of the cleavage of hydrogen linkages in cellulose crystal. in order to produce cellulose II in a rapid and selective manner, Sasaki et al. (24) explored the conditions for dissolving microcrystalline cellulose in high temperature and high pressure wa-

ter without catalyst and from their finding it was suggested that this method had a high potential as an alternative technique for the conventional cellulose II production methods (viscose, cupramonium, NMMO processes). (Ogihara et al. 2005) succeeded to show that microcrystalline cellulose (230 DP) were found to be dissoluble in water over temperatures ranging from 315 to 355°C at high pressures. The dissolution temperatures change systematically with density and show a minimum temperature of dissolution at densities around 800 kg/m³.

However, the main problem of treatment of cellulose at high temperatures is that it starts to degrade under already 160°C. Thus, under conditions of supercritical water $T_{\text{crit}} = 374^\circ\text{C}$ cellulose degrades readily (Sasaki et al. 2000; Ogihara et al. 2005). Though this process can be utilized for wastes decomposition it is not applicable for industrial production of new materials. Acetone ($T_{\text{crit}} = 235^\circ\text{C}$), ethanol ($T_{\text{crit}} = 241^\circ\text{C}$), methanol ($T_{\text{crit}} = 239^\circ\text{C}$) — all polar substances that could struggle against hydrogen bonds of cellulose have too high critical temperature (Ishikawa and Saka 2001).

Among substances that have critical point below 160°C and capable to form hydrogen bonds there is ammonia. Liquid ammonia and amines are used as swelling agents and are known as the best cellulose activators. Liquid ammonia does not dissolve cellulose itself but it was used as a solvent with inorganic salts modifiers (NaI, NaNO₃, NaCNS, NH₄CNS, etc.) (Scherer 1931). Supercritical ammonia was never considered as a cellulose solvent even though it is used for obtaining of one of cellulose polymorphs (see below).

1.3 Cellulose polymorphism.

The problem of dissolution of cellulose arises partly due to its crystalline structure. Similar to many crystals, cellulose fibers can be packed into unit cell in different ways with different geometries and energies. Such an ability is called polymorphism and for cellulose there are 7 known polymorphs. Here we will briefly discuss their properties, interconversion paths and influence on solubility of polymer according to (Zugenmaier 2007; Klemm and Heinze 1998; Klemm 1998).

Natural cellulose is known to form two crystal packing simultaneously: One-chain triclinic I_α and two-chain monoclinic modification I_β . These are representatives of an ordinary native cellulose and are the most important from the point of view of industry. Their intrasheet hydrogen bonds pattern is very similar but I_α and I_β differ in intersheet hydrogen bonds arrangement.

Besides native cellulose cellulose II is the most important from industrial point of view. Mercerization of cellulose in sodium hydroxide leads to polymorph II formation with two antiparallel chains in unit cell. The same structure can be obtained after regeneration of cellulose from solution. The difference in intrasheet hydrogen

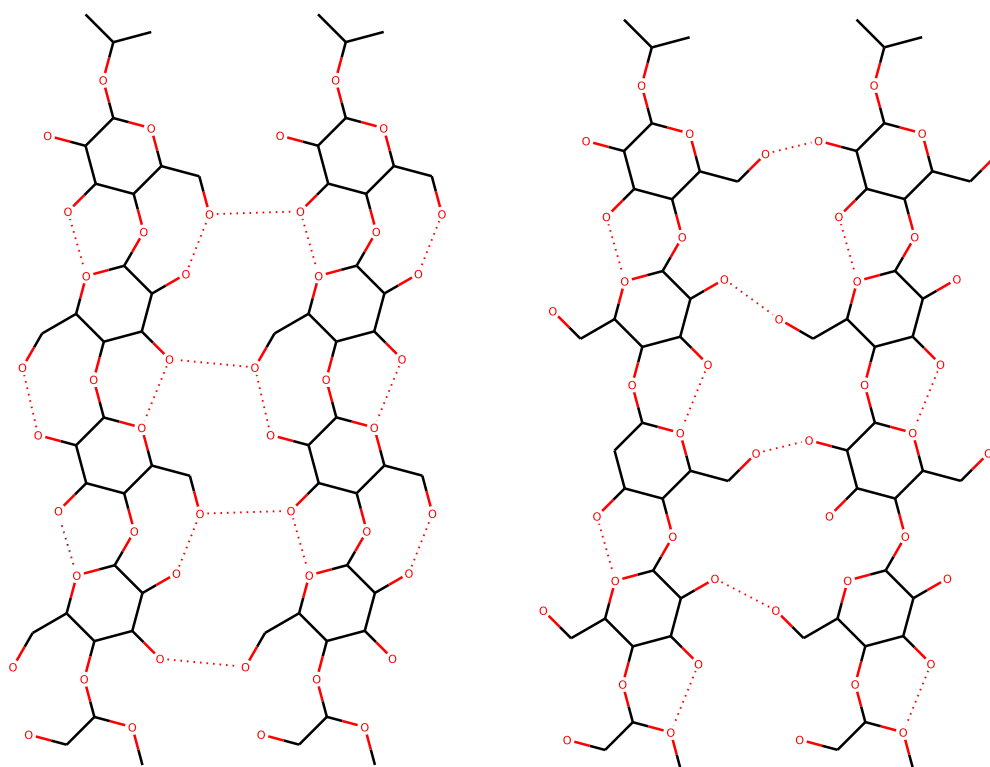


Figure 1.6: Intrashheet hydrogen bonds in polymorphs I(left) and II(right).

bonds is shown on Fig. 1.6 and arrangement of sheets themselves is depicted on the Fig. 1.7 (picture taken from Zugenmaier 2007). What is not shown, however, on both of these pictures is that direction of cellulose fibers of neighboring sheets of cellulose I is parallel and that of cellulose II is antiparallel.

Cellulose forms modification III when treated by waterless liquid ammonia at 30°C , however, this modification is different depending on whether it was obtained from I_{β} or from II forming polymorphs III_I and III_{II} respectively.

From them one can get polymorphs IV_I and IV_{II} respectively by heating with glycerol. Such a description can give an idea of cellulose polymorphs notion but in fact their interconversion scheme is a little bit richer (Figure 1.8)

Obviously difference in structure of cellulose, arrangement of hydrogen bonds leads to different lattice energies as well as reactivity of cellulose. This can be seen at first place on NMR-spectra and on X-ray diffractograms. One can see that in series of polymorphs $I \rightarrow II \rightarrow III_I \rightarrow III_{II} \rightarrow IV_I \rightarrow IV_{II}$ their spectra approach those of amorphous cellulose. What it means on practice is that cellulose with weaker crystal lattice will more readily undergo any reaction than native or mercerized cellulose what can be easily seen in experiment, for instance it was shown (Igarashi, Wada, and Samejima 2007) that enzymatic hydrolysis of cellulose $III_I \rightarrow$ ten times faster than

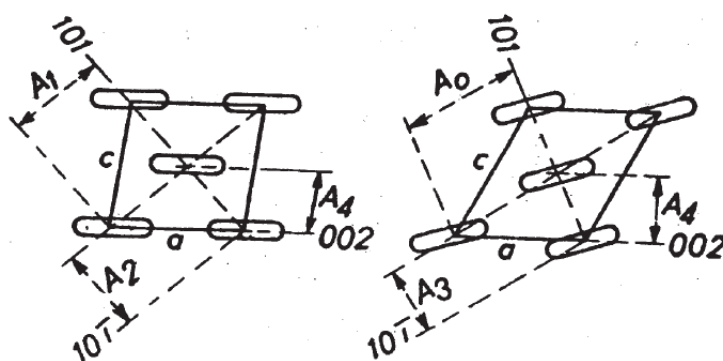


Figure 1.7: Arrangements of chains of cellulose I_{β} (left) and II (right).

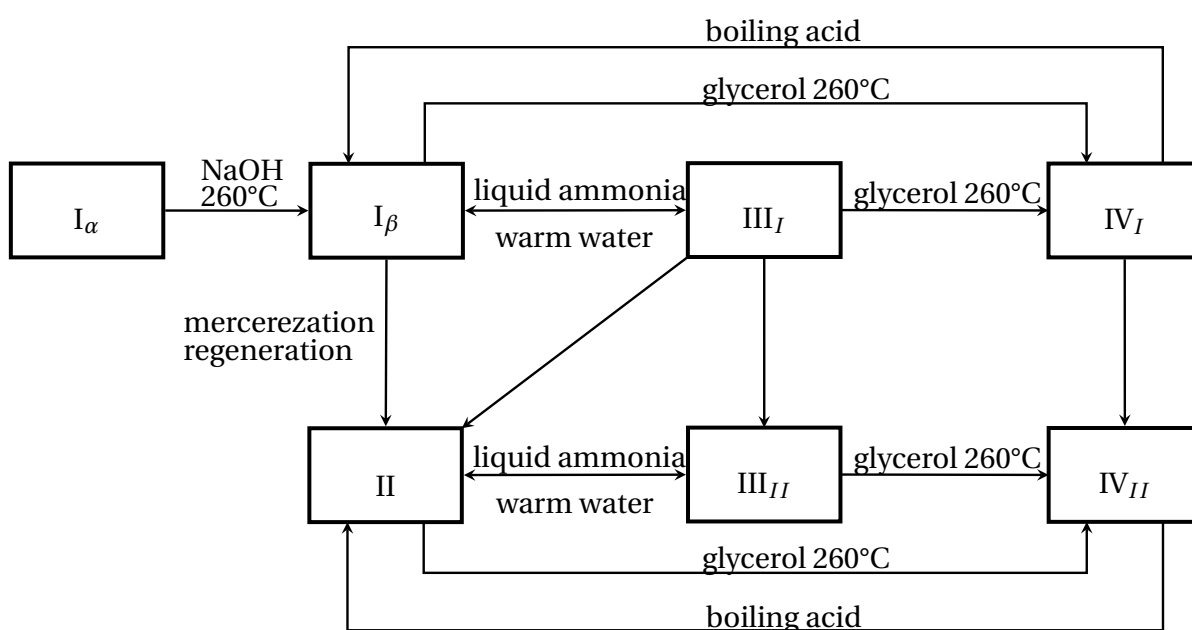


Figure 1.8: Complete cellulose polymorphs conversion scheme.

hydrolysis of II \rightarrow . For computational studies it is more advantageously to take those polymorphs whose lattice energy is higher. These polymorphs are less stable and consequently it is possible to study their dissolution spending less computational efforts. That is why among cellulose polymorphs we first studied cellulose IV_{II} and in case of success checked others.

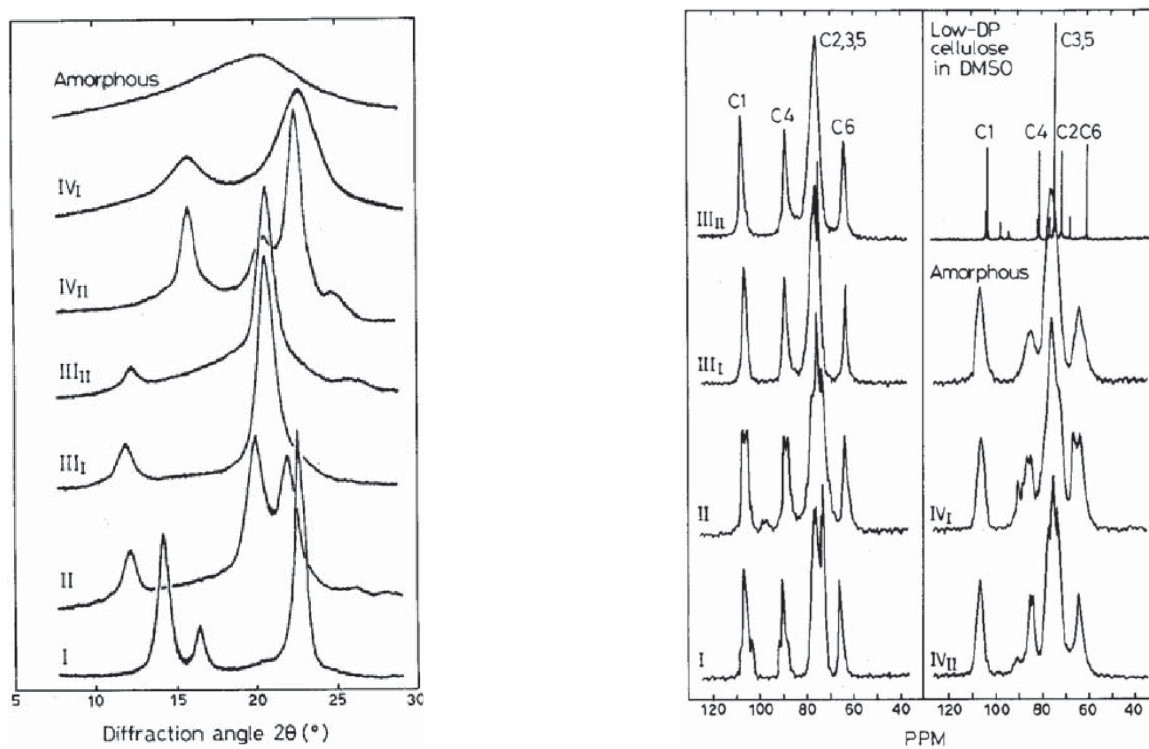


Figure 1.9: NMR and diffraction spectra of different cellulose polymorphs

Chapter **2**

METHODOLOGY

2.1 Statistical Thermodynamics

One of the goals of classical statistical thermodynamics is to put a background behind thermodynamics supplementing it with mechanistic approach to macroscopic phenomena. Moreover, in principle, statistical mechanics is able to predict behaviour of the matter without appealing to experiment. In practice, however, we need some sort of experiment to supplement theory.

There are two main reasons why purely atomistic approach is not enough and we need statistical mechanics to describe physico-chemical problems and solve them. First of all, there is an enormous number of degrees of freedom in usual systems of interest (10^{23} of atoms). But this is not the main problem as even for moderately large systems which are accessible to our computers at present time (10^3 — 10^6) we need somehow compress data because raw molecular trajectories are almost useless. Such a machinery is provided by statistical thermodynamics which establishes laws of averaging of mechanical quantities to obtain macroscopic observables. The most fundamental concepts for statistical mechanics are, thus, an ensemble and an ensemble average.

Statistical ensemble is the set of copies of the system with different microscopical states (points in phase space of coordinates(x) and momenta(p)) corresponding to one particular macroscopical state. There exist equilibrium and non-equilibrium ensembles. Among equilibrium ensembles most often used are:

- Microcanonical (NVE)
- Canonical (NVT)
- Isobaric (NPT)
- Grand canonical (μ PT),

where symbols in parentheses denote macroscopical state parameters. Other ensembles in addition to the simplest microcanonical allow to represent systems under different experimental conditions, for example: Constant temperature in autoclave, constant temperature and pressure of solution in open bowl, open systems with adsorption on zeolite, etc.

The macroscopic quantity of interest will be the average over the ensemble. However, microstates are distributed in some way in phase space and to take it into account we introduce the ensemble distribution function $f(x)$, which is normalized and non-negative. Our macroscopic observable will be, thus:

$$A = \int f(x)a(x)dx \tag{2.1}$$

For particular microcanonical ensemble:

$$A = \langle a(x) \rangle \equiv \frac{1}{\mathcal{Z}} \int a(x) \mathcal{F}(\mathcal{H}(x)) dx \quad (2.2)$$

$$\mathcal{Z} = \int \mathcal{F}(\mathcal{H}(x)) dx, \quad (2.3)$$

where \mathcal{Z} is a partition function which is a measure of the number of microscopic states in the phase space accessible to given macroscopic parameters. Partition function is not only necessary to satisfy the normalization condition $\int f(x) a(x) dx = 1$ but is valuable by itself since many thermodynamic quantities can be expressed via it. $\mathcal{F}(\mathcal{H}(x))$ is an equilibrium distribution function. For microcanonical ensemble partition function is written as follows:

$$\mathcal{F}(\mathcal{H}(x)) = \frac{\delta(\mathcal{H}(x) - E)}{\Omega(N, V, E)} \quad (2.4)$$

$$\Omega(N, V, E) = \frac{E_0}{N! h^{3N}} \int \delta(\mathcal{H}(x) - E) dx, \quad (2.5)$$

where h — Planck's constant and N — number of molecules, $N!$ appears in order to take into account indistinguishability of particles.

Our discussion will be mostly related to canonical ensemble for which the distribution and partition functions are:

$$\mathcal{F}(\mathcal{H}(x)) = \frac{e^{-\beta \mathcal{H}(x)}}{Q(N, V, T)} \quad (2.6)$$

$$Q(N, V, T) = \frac{1}{N! h^{3N}} \int e^{-\beta \mathcal{H}(x)} dx \quad (2.7)$$

Finally, for NPT-ensemble the distribution and partition functions are:

$$\mathcal{F}(\mathcal{H}(x)) = \frac{e^{-\beta \mathcal{H}(x) - \beta PV}}{\Delta(N, P, T)} \quad (2.8)$$

$$\Delta(N, P, T) = \frac{1}{V_0 N! h^{3N}} \int e^{-\beta \mathcal{H}(x) - \beta PV} dx \quad (2.9)$$

Another class of quantities are so-called thermal quantities that are not ensemble averages but proportional to the whole partition function. These are, for example, entropy S and Helmholtz A and Gibbs G free energies:

$$S = k \ln \Omega(N, V, E) \quad (2.10)$$

$$A = -k \ln Q(N, V, T) \quad (2.11)$$

$$G = -k \ln \Delta(N, P, T) \quad (2.12)$$

It is impossible to measure or calculate these quantities as they are proportional to the whole partition function. Nevertheless, one can measure difference between two states of, for instance, $\Delta A = A_1 - A_2$.

To accomplish this brief overview of statistical mechanics we should make bridge between ensemble averages that are used in theory and time averages that are observed in laboratory and (below) in molecular dynamics simulations. This is done by accepting the ergodic hypothesis, saying that an ensemble average equals to the limit of the time-average:

$$\langle a(x) \rangle \equiv \frac{\int a(x) \delta(\mathcal{H}(x) - E) dx}{\int \delta(\mathcal{H}(x) - E) dx} = \lim_{\mathcal{T} \rightarrow \infty} \frac{1}{\mathcal{T}} \int_0^{\mathcal{T}} a(x_t) dt \quad (2.13)$$

2.1.1 Numerical experiments in statistical mechanics.

Periodic boundary conditions. Let us describe here how one avoids dealing with finite size of molecular systems that can be treated on modern computers. In order to obtain bulk properties of liquids we should somehow get rid of interfaces and this is achieved by applying periodic boundary conditions(PBC). This means that simulation box is represented by three - dimensional torus. From the point of view of molecules it means that when a given molecule leaves a simulation box crossing one face it enters the box from the opposite face. For two-dimensional periodic boundary conditions this will look like on Fig. 2.1. There is a lot of various types of periodic boundary conditions(Allen and Tildesley 1999), in this work, however, we use only cubic PBC.

Molecular mechanics force fields. Unfortunately, analytical evaluation of partition functions and thermodynamic properties is impossible for real-life systems. In order to calculate properties from theory one has to appeal to numerical experiments. There are two main techniques that allow generating ensembles and obtaining statistical properties of atomistic systems: Monte Carlo and molecular dynamics. They are based on quite different ideology but share input information and some rules of distributions generating. Here we will discuss these common properties and basics of methods will be discussed in separate sections.

First of all, we must specify rules according to which particles interact with each other in the system. This is done by choosing intermolecular(non-bonded) potential and for large fluid systems pair potential are often a reasonable choice. In this work we use combination of Lennard-Jones and electrostatic potentials:

$$U_{nb} = \sum_{i < j} \left\{ 4\epsilon \left[\left(\frac{\sigma}{r} \right)^{12} - \left(\frac{\sigma}{r} \right)^6 \right] + \frac{q_i q_j}{r} \right\}, \quad (2.14)$$

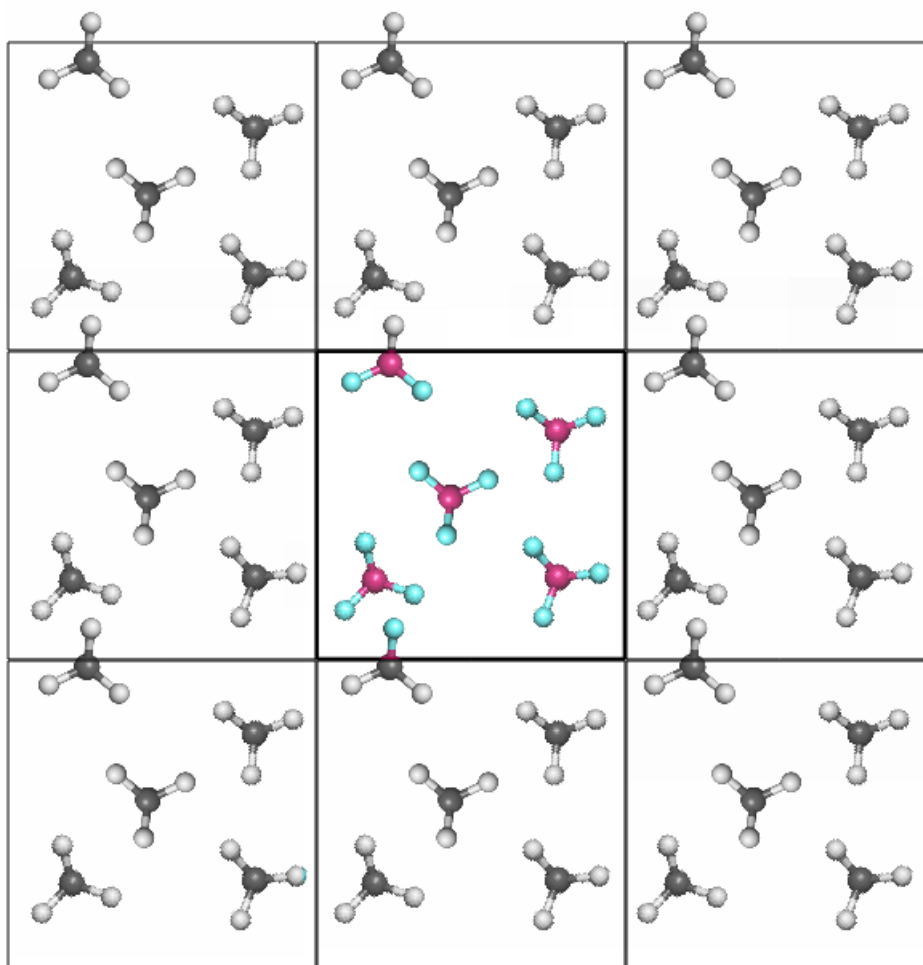


Figure 2.1: Periodic boundary conditions in two dimensions. Color central image represents a system interacting with its (gray) images.

where r is interparticle distance, q atomic charges, σ is the zero-point of Lennard-Jones potential and ϵ — its well-depth.

It is convenient to divide intermolecular forces into two classes: Short-range and long-range interactions. Short-range interactions are those that decay faster than r^{-3} and can be safely truncated. In this case we can consider only interactions of molecules with their neighbors in the main box not taking into account further images. For fast molecular simulations truncation of Lennard-Jones interactions occurs at distance $\approx 2.5 - 3\sigma$ at such difference the truncation error cannot be considered as negligible and one has to apply additional technique to allow for it. The first method is called “tail correction” and consists simply in cutting off the interactions at r_c and

introducing the term

$$U^{tc} = \frac{8}{3} \pi \rho \epsilon \sigma \left[\frac{1}{3} \left(\frac{\sigma}{r_c} \right)^9 - \left(\frac{\sigma}{r_c} \right)^3 \right] \quad (2.15)$$

The problem with this method is that the interaction function contains discontinuity and is not appropriate for most popular molecular dynamics integrators. In order to avoid this drawback one uses shift of the potential function by constant making potential zero at r_c and accounting the same correction to potential energy.

Another, more difficult, story happens with electrostatic term which decays slowly than r^{-3} . One has to account for the interactions of every molecule with all periodic images of the system what cannot be used in efficient way directly. Here, we will only mention several methods for dealing with this problem, they are: Ewald summation method, reaction field method, particle mesh Ewald, etc.

While small solvent molecules can be treated as rigid using constraints algorithms, for large molecules intramolecular potentials are of great importance. Internal potentials are usually separated into bonds stretching, angle bending and changing of dihedral angles and is given by this formula(CHARMM conventions):

$$U_b = U_{bond} + U_{angle} + U_{tors} \\ = k(r_{ij} - r_0)^2 k_\theta(\theta - \theta_0) + k_{ub}(r_{ik} - r_{ub})^2 + \begin{cases} k(1 + \cos(n\psi + \varphi)) & \text{if } n > 0 \\ k(\psi - \varphi)^2 & \text{if } n = 0 \end{cases}, \quad (2.16)$$

where

- U_{bond} — energy of bond stretching, k is force constant and r_0 is the equilibrium distance
- U_{angle} — energy of angular vibrational motion, k_θ is force constant associated with this motion and k_{ub} — Urey-Bradley constant, θ_0 is an equilibrium angle
- U_{tors} — torsional energy of changing dihedral angle between two planes defined by four atoms i, j, k, l , a namely, between planes formed by i, j, k and j, k, l . n represents periodicity, for $n > 0$, φ is the phase shift angle and k is the multiplicative constant, for $n = 0$ φ is an equilibrium angle and k is the force constant.

2.2 Monte Carlo Simulations

The Monte Carlo (Binder and Heermann 2010; Berg 2004; Newman and Barkema 1999; Frenkel and Smit 2002) method was the first molecular simulations technique. Its main idea is to generate stochastic trajectory in configuration space according to distribution function in target ensemble. Metropolis et al. proposed importance sampling to approach it.

First, consider observable in canonical ensemble:

$$\langle \mathcal{A} \rangle = \int \mathcal{A}(x) f_{NVT} dx \quad (2.17)$$

Choosing random quantity with distribution ρ we can estimate the integral as

$$\langle \mathcal{A} \rangle = \langle \mathcal{A}(x) f_{NVT} / \rho \rangle \quad (2.18)$$

If we now take $\rho = f_{NVT}$ we should obtain a good estimate of the integral and:

$$\langle \mathcal{A} \rangle_{NVT} = \langle \mathcal{A} \rangle_{\text{trials}} \quad (2.19)$$

Now we have to find such a method of generation random states that allows us to get canonical distribution after large number of steps. We could take random vectors x but better convergence is achieved by employing Markov chains obeying two conditions:

1. The result of trial move is in a state space $x_1, x_2, \dots, x_m, x_n$.
2. The result of each trial depends only on preceding trial result.

Let $P(x \leftarrow y)$ be a probability for a system to move from microstate y to microstate x then it means that $P(x \leftarrow y)$ is a rule for generating a Markov Chain. However, we have to introduce detailed balance condition in order this rule to be valid:

$$P(x \leftarrow y) f(y) = P(y \leftarrow x) f(x), \quad (2.20)$$

where $f(x)$ and $f(y)$ are probabilities to be in states x and y correspondingly. Metropolis introduces the rule for generating trial moves $x \leftarrow y$ denoted $T(x \leftarrow y)$. The normalization condition for rules is:

$$\int T(x \leftarrow y) dx = 1 \quad (2.21)$$

After generating the trial move we either accept or reject it (in the latter case we roll back setting $x = y$). Let $A(x \leftarrow y)$ be the probability that the move is accepted. Then the transition probability will be given by:

$$P(x \leftarrow y) = A(x \leftarrow y) T(x \leftarrow y), \quad (2.22)$$

and detailed balance condition (2.20) becomes:

$$A(x \leftarrow y)T(x \leftarrow y)f(y) = A(y \leftarrow x)T(y \leftarrow x)f(x) \quad (2.23)$$

Acceptance probabilities are related by:

$$A(x \leftarrow y) = \frac{T(y \leftarrow x)f(x)}{T(x \leftarrow y)f(y)}A(y \leftarrow x) = r(x \leftarrow y)A(y \leftarrow x) \quad (2.24)$$

And the final acceptance probability will be:

$$A(x \leftarrow y) = \min [1, r(x \leftarrow y)] \quad (2.25)$$

In canonical ensemble with partition function (2.7) the acceptance probability will be given by:

$$A(r' \leftarrow r) = \min [1, e^{-\beta[U(r')-U(r)]}]. \quad (2.26)$$

This equation, however, cannot be applied directly, as it is impossible to move all the particles at once. That is why Monte Carlo moves are performed for molecules one by one. During the main Monte Carlo loop computer takes one of N molecules and performs translational and rotational moves evaluating energy and accepting or rejecting these moves. For more complicated ensembles one performs other moves such as changing volume, particle insertion/deletion, etc.

Gibbs ensemble Monte Carlo Simulation method that allows determination of phase coexistence without direct simulations of interface is Gibbs ensemble Monte Carlo (Panagiotopoulos 1987; Frenkel and Smit 2002).

The condition for phase coexistence is equality of their pressures (P_1, P_2, \dots, P_N), temperatures (T_1, T_2, \dots, T_N) and chemical potentials ($\mu_1, \mu_2, \dots, \mu_N$). One could not set up an ensemble whose only macroscopic parameters were intensive variables and has to choose at least one extensive. In Gibbs ensemble Monte Carlo there are N boxes representing N phases such that total number of particles M in boxes are constant and their total volume V is constant. Special Monte Carlo moves representing the equilibration of chemical potentials and pressures are, correspondingly:

- Deletion of particle from one box and insertion it into another
- Box volume change

Performing these moves allows us to equilibrate μ , P and T formally staying in extended version of NVT ensemble. In this work we employ Gibbs ensemble Monte Carlo in order to get coexistence curves of different supercritical fluids.

However, if we approach the critical point it becomes impossible to distinguish liquid and gas phase and large fluctuations occur in the box. And to calculate the

critical density, ρ_C , and the critical temperature, T_C , one has to fit obtained T- ρ co-existence curves to the law of rectilinear diameters (see (2.27)) and to the scaling law (see (2.28)) In these equations, A and B are constants, β is the critical exponent, and is equal to 0.32, ρ_l and ρ_g are the liquid and gas densities, respectively.

$$\frac{\rho_l + \rho_g}{2} = \rho_C + A(T - T_C) \quad (2.27)$$

$$\rho_l - \rho_g = B(T - T_C)^\beta \quad (2.28)$$

2.3 Molecular Dynamics Simulations

Molecular dynamics (Allen and Tildesley 1999; Frenkel and Smit 2002; Rapaport 2004; Tuckerman 2009) is the method of generating phase space distribution by solving equations of motion of system. In simplest case of molecular dynamics in NVE ensemble these are the Newtonian equations of motion:

$$\frac{d\mathbf{r}_i}{dt} = \frac{\mathbf{p}_i}{m_i} \quad (2.29)$$

$$\frac{d\mathbf{p}_i}{dt} = \mathbf{F}_i \quad (2.30)$$

Solving these one obtains trajectory $\mathbf{r}(t)$ of system. According to ergodic hypothesis (2.13) we can get ensemble averages from such trajectories though the problem of ergodicity is more sufficient here than in Monte Carlo simulations what is partly due to deterministic nature of molecular dynamics. For a complex system when a of conformations are observed it could be very difficult to get relevant statistics on phase space accessible to system and, thus, to get reliable estimate of an observable A .

Things become more complicated when dealt with other than NVE ensembles. Consider the case of NVT ensemble. Instead of ordinary phase space bigotten by Hamiltonian equations:

$$\dot{q}_i = \frac{\partial \mathcal{H}}{\partial p_i}, \quad \dot{p}_i = -\frac{\partial \mathcal{H}}{\partial q_i} \quad (2.31)$$

one frequently takes an extended phase space where artificial degrees of freedom represent energy fluctuations. For instance, according to Nosé Hamiltonian takes the form:

$$\mathcal{H}_N = \sum_{i=1}^N \frac{p_i^2}{2m_i s^2} + U(\mathbf{r}_1, \dots, \mathbf{r}_N) + \frac{p_s^2}{2Q} + gkT \ln s, \quad (2.32)$$

here Q is a parameter determining the time scale on which velocities are rescaled in order to maintain desired kinetic energy corresponding to target temperature. Parameter s scales velocity of particles and g is responsible for proper canonical physical phase space distribution. This is an example of deterministic canonical molecular dynamics.

There is a lot of other methods to generate the canonical distribution. One of the most utilized is the Langevin thermostat. Here the stochastic Langevin equations of motions are used which are non-deterministic and time-irreversible:

$$\ddot{\mathbf{r}}_i(t) = \frac{\mathbf{F}_i(t)}{m_i} - \gamma(t) \dot{\mathbf{r}}_i(t) + \frac{\mathbf{R}_i(t)}{m_i}, \quad (2.33)$$

where $R_i(t)$ is a stochastic force and $\gamma(t)$ a positive atomic friction coefficient. Many thermostats use a single friction coefficient for all atoms what leads to the simplified form of equation:

$$\ddot{r}_i(t) = \frac{F_i(t)}{m_i} - \gamma(t) - \dot{r}_i(t), \quad (2.34)$$

where $\gamma(t)$ is no more a positive constant whose positive value means now the heat flow from the system to the bath and negative — an opposite direction of the flow.

Consider now integration of equations of motion in simplest case of microcanonical molecular dynamics. Simplest way is to expand the position into Taylor series up to second order term:

$$\begin{aligned} r_i(t + \Delta t) &\approx r_i(t) + \Delta t \dot{r}_i(t) + \frac{1}{2} \Delta t^2 \ddot{r}_i(t) \\ &\approx r_i(t) + \Delta t v_i(t) + \frac{\Delta t^2}{2m_i} F_i(t) \end{aligned} \quad (2.35)$$

. Writing the same expansion back into time:

$$r_i(t - \Delta t) \approx r_i(t) - \Delta t v_i(t) + \frac{\Delta t^2}{2m_i} F_i(t), \quad (2.36)$$

and summing these equations we get:

$$r_i(t + \Delta t) + r_i(t - \Delta t) = 2r_i(t) + \frac{\Delta t^2}{m_i} F_i(t). \quad (2.37)$$

And final equation that corresponds to Verlet algorithm(Verlet 1967) looks like this:

$$r_i(t + \Delta t) = 2r_i(t) - r_i(t - \Delta t) + \frac{\Delta t^2}{m_i} F_i(t). \quad (2.38)$$

This algorithm does not evaluate velocities but if needed they can be constructed at any point of the trajectory using following equation:

$$v_i(t) = \frac{r_i(t + \Delta t) - r_i(t - \Delta t)}{2\Delta t} \quad (2.39)$$

In order to start simulation one has to choose initial conditions: Positions and velocities. For atomic and simple molecular systems it can be a reasonable choice to take particles distributed on the crystal lattice and thermalizing this solid obtain distribution of particles characteristic to liquid. Another option is to put molecules randomly avoiding their overlap. The most interesting approach is to use combinatorial optimization techniques to systematically pack molecules maximizing distance between their atoms(Martínez and Martínez 2003; Martínez et al. 2009).

Initial velocities are usually taken from Maxwell-Boltzmann distributions:

$$f(v) = \sqrt{\frac{m}{2\pi kT}} e^{-\frac{mv^2}{2kT}} \quad (2.40)$$

2.4 Analysis of molecular simulations data

2.4.1 Radial distribution function.

During the molecular dynamics simulations one can get statical and dynamical properties of a system. Here we will discuss dynamical and structural properties and methods of studying of thermodynamics will be covered in the next section.

The pair distribution function is of particular importance in molecular simulations and in canonical ensemble is obtained according to such formula:

$$g^2(r_1, r_2) = \frac{1}{QN! \lambda^{3N}} \frac{N(N-1)}{\rho^2} \int_{D(V)} e^{-\beta U(r_1, r_2, r_3, \dots, r_N)} dr_3 \dots dr_N, \quad (2.41)$$

this function depends both on r_1 and r_2 , however if we study homogeneous liquid we can bring it to the function of the interatomic distance r only. Noticing that a liquid system is spatially isotropic and correlation function should only depend on the distance between two particles we can write:

$$\begin{aligned} g(r) &= \frac{N-1}{4\pi\rho} \int_0^{2\pi} d\varphi \int_0^\pi \sin\theta d\theta \int_{D(V)} e^{-\beta U(r)} dR dr_3 \dots dr_N \\ &= \frac{N-1}{4\pi\rho} \langle \delta(r - r') \rangle_{r', \theta', \varphi', R, r'_3, \dots, r'_N} \end{aligned} \quad (2.42)$$

Radial distribution function gives, thus, local density around the given particle and is a measure of the probability of finding two particles a distance r apart in canonical ensemble.

Properly normalizing and integrating $g(r)$ from 0 to R one obtains number of particles in sphere with thickness R . Coordination number is obtained by integration from 0 to first minimum of $g(r)$:

$$N_1 = 4\pi\rho \int_0^{r_{\min}} r^2 g(r) dr. \quad (2.43)$$

Radial distribution function is not only a structural measure but also can be used to express many thermodynamic quantities such as internal energy (assuming pair additivity of potential), pressure and even chemical potential in such a way:

$$\langle \mathcal{A} \rangle = \frac{1}{V^2} \int_0^\infty dr_i dr_j g(r_i, r_j) a(r_i, r_j) 4\pi r^2 dr \quad (2.44)$$

2.4.2 Nearest neighbors radial distribution functions.

In the frame of molecular simulations, the radial distribution function is a major means by which structure is usually described in fluid systems. However, this statistical property does not provide sufficient details on the nature of the local environment due to its intrinsic averaging process. As a consequence, several approaches

were developed to get a deeper insight into the local structure of molecular systems (the spatial extent of the local structure is defined by the position of the first minimum in the center of mass—center of mass radial distribution function).

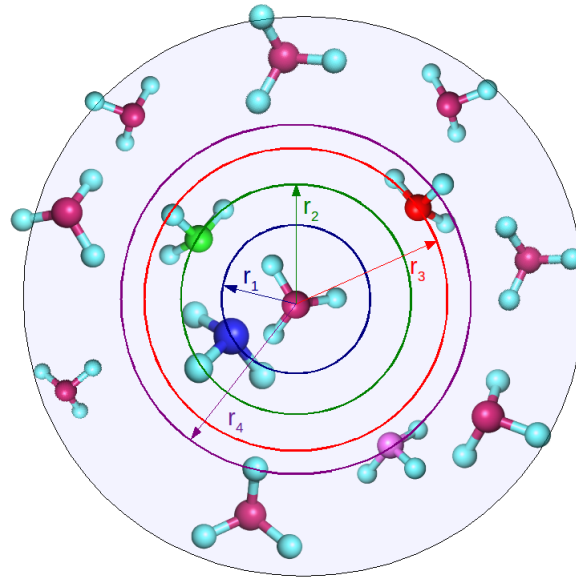


Figure 2.2: Definition of the nearest neighbors distribution functions.

Corresponding nearest neighbor distribution functions can be seen on Fig. 2.3.

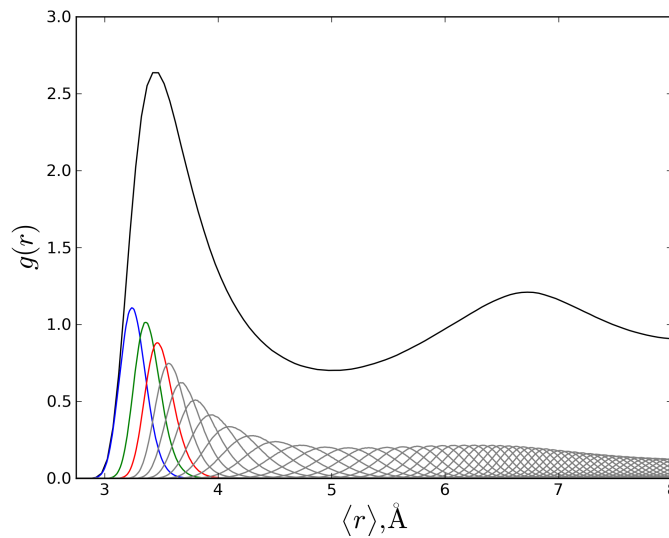


Figure 2.3: Nearest neighbors distance distributions and their sum as the total $g(r)$.

Another approach allowing us deeper insight into local structure of system is the nearest neighbor approach. It allows us to calculate the density probability of nearest neighbors distribution. Here the neighbors of a central atom are sorted by distance into the first neighbors, second neighbors, etc.(2.2). Their sum will be the total $g(r)$:

$$\sum_{i=1}^{\infty} p_i(r) = g(r) \quad (2.45)$$

2.4.3 Voronoi tessellations.

Another technique of studying of local structure is the Voronoi polyhedra analysis being a very efficient tool. In a given three-dimensional configuration of seeds the VP of a given seed is the locus of the spatial points that are closer to this seed than to any other one. In studying the local structure of disordered fluids the seeds represent the centers of the molecules. (It should be noted that in crystalline phases the VPs of the atoms are equivalent with their well known Wigner–Seitz cells.) Due to this definition, the Voronoi tessellation divides the space between the seeds without gaps and overlaps. Therefore, the volume of a VP provides direct information on the space that is available for its central particle, which is related to the free volume available for it. Conversely, the reciprocal volume of the VP is a measure of the local density around this particle. Further, the area of a VP face (relative to that of the other faces) provides information on the vicinity of the corresponding neighbor—closer neighbors share, in general, larger faces. The vertices of the VP are the locus of the points that are equally far from four seeds and are farther from the other seeds than from these four ones. Therefore, the VP vertices are the points at which the distance of the closest seed (molecule) is of local maxima. Due to this property, the VP vertices are the centers of the largest empty spherical cavities that are located between the molecules. The radius of such an elemental cavity is simply the distance R of the VP vertex from the central particle. It should be finally noted that the relation between the various properties of the VP in disordered systems with the fundamental distribution functions of statistical mechanics, such as the pair correlation functions, is not at all obvious and certainly not unique first of all because VP can only describe the local environment of the molecules, and hence the short range structure of the system, whereas statistical mechanical distribution functions are related to properties in the full distance range. Discussion of the relation between the VP properties and the first peak of the corresponding pair correlation function can be found elsewhere in the literature.

The local structure of various disordered systems, such as hard sphere and Lennard-Jones liquids, molten and hydrated salts, liquid metals, water under different thermodynamic conditions, including supercritical, supercooled, and negative pressure states, other hydrogen bonding liquids, grafted and soft polymers as well as hydrated

phospholipid membranes have been successfully characterized by means of Voronoi analysis. It should also be noted that the use of Voronoi analysis is not limited to the investigation of disordered materials; from biophysics to astrophysics and from neurosciences to bioinformatics it has numerous applications.

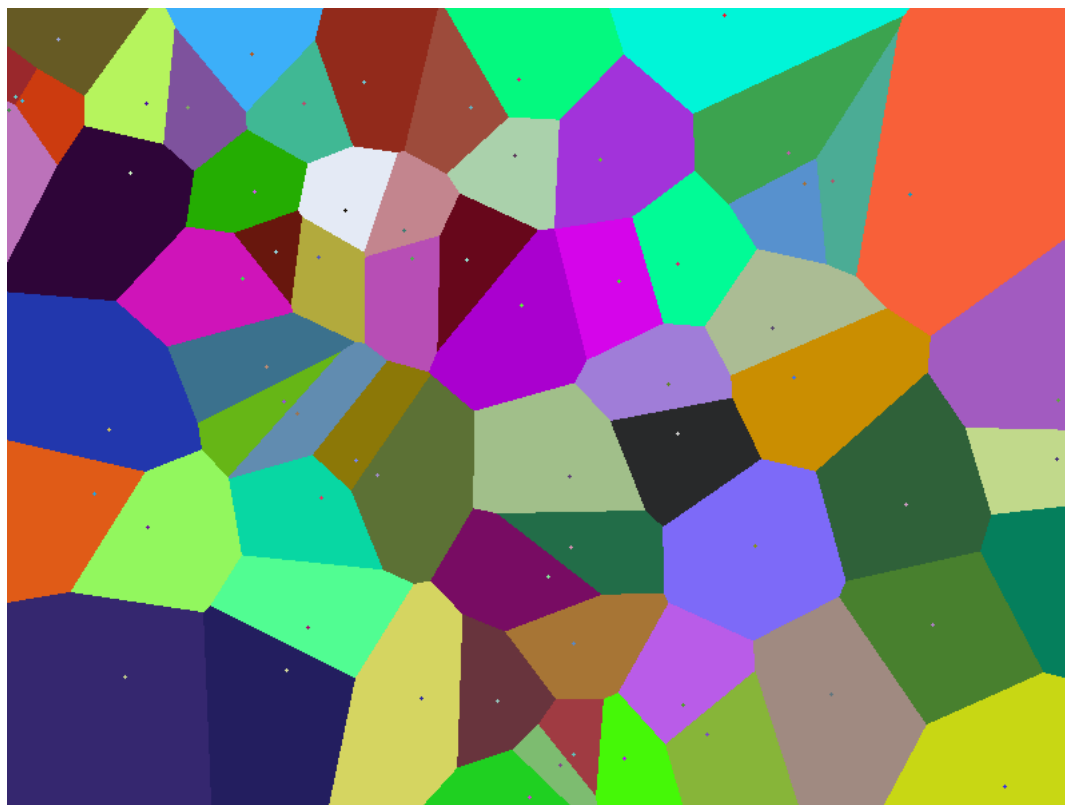


Figure 2.4: 2-d demonstration of Voronoi tessalation.

Two-dimensional case of Voronoi diagram can be seen on Fig. 2.4. Of course, three-dimensional case is much more complicated but the problem is solved long time ago and there is a lot of computational geometry packages that allow efficient construction of Voronoi tessalation and its duality — Delaunay triangulation (Preparata and Shamos 1985; Okabe 2000).

In our analysis we will consider following measure and topological characteristics of Voronoi polyhedra (N. 2000). The VP of the molecules can be characterized by the number of its edges (N_E), vertices (N_V), and faces (N_F), the area of its individual faces (A), its total surface area (S), volume (V), and reciprocal volume, characterizing the local density around the molecules, ρ . The first three of these properties are typical topological characteristics, while the last four are the most widely used metric properties. Further, the VP vertices are the locations of the largest empty spheres

(spherical vacancies) present between the molecules. These vacancies can be characterized by their radius R , which is the distance of the given vertex from the central molecule of the VP. These properties are characterized here by their full statistical distributions as well as by the mean values and standard deviations of these distributions. The distribution, mean value, and standard deviation of the quantity X are denoted here as $P(X)$, X , and σ_X , respectively.

2.4.4 Root-mean-square deviation.

As it was already mentioned molecular dynamics simulations, and what follows from the very name of the method, provide information about dynamics of the system. And the field of study is not limited to equilibrium properties such as structure and thermodynamic functions of the system. One can try investigate evolution of non-equilibrium system in time. However, we would need measure of similarity in order to compare system with itself in different moments in time. The most popular such measure is the root-mean-square deviation which is given by following formula:

$$RMSD(n\Delta t) = \sqrt{\frac{\sum_{\alpha=1}^{N_{\alpha}} (r_{\alpha}(t) - r_{\alpha}(t_{\text{ref}}))^2}{N_{\alpha}}}. \quad (2.46)$$

This is the variant of formula with discretized time which is used in MD simulations. N_{α} is the number of particles in system, $r_{\alpha}(t)$ and $r_{\alpha}(t_{\text{ref}})$ are the positions of α^{th} atom in moment of time t and reference time respectively. Reference position can be chosen as r in the first time step of simulation, and this is used most frequently, or as an r averaged over the trajectory.

2.4.5 Radius of gyration.

It is the measure of the size of an object given by ensemble of points. It is calculated as the root mean square distance between these points and reference points which is most frequently a center of mass of a molecule. In biomolecular simulations it is used to track folding-unfolding processes and is a good measure of molecule compactness. We used discretized equation for radius of gyration which is similar to that of RMSD (2.46):

$$ROG(t) = \sqrt{\frac{\sum_{\alpha=1}^{N_{\alpha}} (r_{\alpha}(t) - r_{cm}(t))^2}{N_{\alpha}}}, n = 0, \dots, N_t - 1 \quad (2.47)$$

During the molecular dynamics or Monte Carlo simulations one can face with such a problem when RMSD and ROG measures are applied. If a system consists of

a large molecule (or a complex of molecules bonded by intermolecular interactions) in a bath of solvent molecules and this central molecule possess translational movement then it can go out from the box from the one side and return from the opposite site. In RMSD and ROG it will be seen as large jumps of the function. Thus, translational and rotational motions should be separated from internal motions in such a way:

- For the first timestep, one finds the linear transformation such that the coordinate origin becomes the center of mass of the system and its principal axes of inertia are parallel to the three coordinates axes.
- This provides a reference configuration \mathcal{C}_{ref} .
- For any other frames f , finds and applies the linear transformation that minimizes the RMS distance between timestep f and \mathcal{C}_{ref} .

2.5 Free energy methods

The unquestionable benefit of MD and MC simulations is their ability to provide insight into structure and dynamics of atomistic systems. However, from the macroscopic point of view chemical systems are governed by the laws of thermodynamics and we would like to extract this information from microscopical trajectories of molecules. Consider, for example, system in canonical ensemble for which the criterion of stability is the negativity of Helmholtz free energy (2.11) of formation. But in order to calculate it we would have to evaluate canonical partition function (2.7) which is prohibitively large multidimensional integral. However, what we can do is to calculate the difference in free energy between two states predicting which state is thermodynamically more stable, and thus, the direction of the chemical process.

2.5.1 Free energy perturbation

Let us continue considering our example of two states of a system which we will call \mathcal{A} and \mathcal{B} . These two systems possess different potential energy $U_{\mathcal{A}}(\mathbf{r})$ and $U_{\mathcal{B}}(\mathbf{r})$. Helmholtz free energy difference between these two states will be $\Delta A_{\mathcal{A}\mathcal{B}} = A_{\mathcal{A}} - A_{\mathcal{B}}$. And in terms of their partition functions:

$$Q_{\mathcal{A}}(N, V, T) = \frac{1}{N!h^{3N}} \int e^{-\beta\mathcal{H}_{\mathcal{A}}(\mathbf{r})} d\mathbf{r} \quad (2.48)$$

$$Q_{\mathcal{B}}(N, V, T) = \frac{1}{N!h^{3N}} \int e^{-\beta\mathcal{H}_{\mathcal{B}}(\mathbf{r})} d\mathbf{r} \quad (2.49)$$

and the free energy difference is therefore:

$$\Delta A_{\mathcal{A}\mathcal{B}} = A_{\mathcal{A}} - A_{\mathcal{B}} = -kT \ln \left(\frac{Q_{\mathcal{B}}}{Q_{\mathcal{A}}} \right) = -kT \ln \left(\frac{Z_{\mathcal{B}}}{Z_{\mathcal{A}}} \right), \quad (2.50)$$

where $Z_{\mathcal{A}}$ and $Z_{\mathcal{B}}$ are the configurational integrals for states \mathcal{A} and \mathcal{B} respectively. We can replace ratio of partition functions by ratio of configurational integrals due to integrating out momentum contributions. After simple manipulations we get (after Zwanzig):

$$\begin{aligned} \frac{Z_{\mathcal{B}}}{Z_{\mathcal{A}}} &= \frac{1}{Z_{\mathcal{A}}} \int e^{-\beta U_{\mathcal{A}}(\mathbf{r})} e^{-\beta(U_{\mathcal{B}}(\mathbf{r}) - U_{\mathcal{A}}(\mathbf{r}))} d\mathbf{r} \\ &= \left\langle e^{-\beta(U_{\mathcal{B}}(\mathbf{r}) - U_{\mathcal{A}}(\mathbf{r}))} \right\rangle_{\mathcal{A}} \end{aligned} \quad (2.51)$$

And final equation will be, thus, as follows:

$$\Delta A_{\mathcal{A}\mathcal{B}} = -kT \ln \left\langle e^{-\beta(U_{\mathcal{B}} - U_{\mathcal{A}})} \right\rangle_{\mathcal{A}} \quad (2.52)$$

This equation, however, is quite difficult to apply when systems differ significantly. As it implies that important regions in configurational space of \mathcal{B} coincides with important regions of configurational space of \mathcal{B} which is not the fact quite often. This limitation can be overcome if we employ a little modification of free energy perturbation method known as staging technique. We can consider Hamiltonian of the system as a function of $\lambda \in [0, 1]$ such that $\lambda = 0$ corresponds to reference state and $\lambda = 1$ — to target state. The most obvious choice is to make Hamiltonian a linear function of λ :

$$\mathcal{H}(\lambda_i) = \lambda_i \mathcal{H}_{\mathcal{B}} + (1 - \lambda_i) \mathcal{H}_{\mathcal{A}} = \mathcal{H}_{\mathcal{A}} + \lambda_i \Delta \mathcal{H}, \quad (2.53)$$

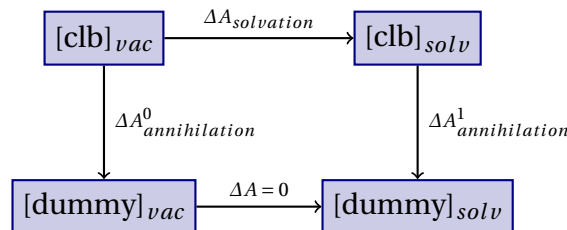
substituting this into the formula for the total free energy difference gives:

$$\Delta A = -\frac{1}{\beta} \sum_{i=1}^{N-1} \ln \left\langle e^{-\beta \Delta \lambda_i \Delta U} \right\rangle_{\lambda_i} \quad (2.54)$$

Then staging is applied another problem arises. Numerical instabilities are observed when λ approaches boundary values. Here interactions are weak but not equal to zero and surroundings of the molecule clash into it causing poorly estimated $\langle \Delta U \rangle$. Among methods to get rid of this effect the modification of Lennard-Jones parameters are the most effective:

$$U_{ij}^{vdW}(r_{ij}, \lambda) = 4\epsilon_{ij} \lambda^n \left\{ \frac{1}{\left[\alpha_{vdW}(1-\lambda)^2 + \left(\frac{r_{ij}}{\sigma_{ij}} \right)^6 \right]^2} - \frac{1}{\alpha_{vdW}(1-\lambda)^2 + \left(\frac{r_{ij}}{\sigma_{ij}} \right)^6} \right\} \quad (2.55)$$

To apply free energy perturbation method one has to choose the reaction coordinate that represents the physical chemistry of the problem. For instance, to study the solvation free energy one can use following thermodynamic cycle:



This thermodynamic cycle is called double annihilation and to obtain the solvation free energy one has to perform switching off the intermolecular parameters of solute molecule surrounded by solvent molecules and in vacuum. The last contribution is zero (there is no interaction between solute and solvent) and mutating

from dummy atoms in solvent to dummy atoms in vacuum produce zero free energy change. Thus, solvation free energy will be just:

$$\Delta A_{\text{solvation}} = -\Delta A_{\text{annihilation}} \quad (2.56)$$

2.5.2 Thermodynamic integration

Another way to obtain free energy change as an ensemble average is to calculate free energy derivative. Let us see how it works.

First, like in free energy perturbation with large perturbation we will consider free energy as a linear function of coupling parameter λ .

$$U(\lambda) = (1 - \lambda)U_{\mathcal{A}} + \lambda U_{\mathcal{B}}. \quad (2.57)$$

Here, again we have \mathcal{A} a reference system and \mathcal{B} — target system. We assume that free energy of \mathcal{A} is known and the partition function for a system with a potential energy function that corresponds to a value of λ between 0 and 1 is

$$Q(N, V, T, \lambda) = \frac{1}{\Lambda^{3N}} \int e^{-\beta U(\lambda)} d\mathbf{r}. \quad (2.58)$$

The derivative of canonical free energy $A(\lambda)$ with respect to λ is an ensemble average:

$$\begin{aligned} \left(\frac{\partial A(\lambda)}{\partial \lambda} \right)_{N, V, T} &= -\frac{1}{\beta} \frac{\partial}{\partial \lambda} \ln Q(N, V, T, \lambda) = -\frac{1}{\beta Q(N, V, T, \lambda)} \frac{\partial Q(N, V, T, \lambda)}{\partial \lambda} \\ &= \frac{\int \frac{\partial U(\lambda)}{\partial \lambda} e^{-\beta U(\lambda)} d\mathbf{r}}{\int e^{-\beta U(\lambda)} d\mathbf{r}} = \left\langle \frac{\partial U(\lambda)}{\partial \lambda} \right\rangle_{\lambda} \end{aligned} \quad (2.59)$$

And the free energy difference between systems \mathcal{A} and \mathcal{B} is given by integrating (2.59):

$$A(\lambda = 1) - A(\lambda = 0) = \int_{\lambda=0}^{\lambda=1} d\lambda \left\langle \frac{\partial U(\lambda)}{\partial \lambda} \right\rangle_{\lambda} \quad (2.60)$$

Numerical instabilities similar to those in free energy perturbation method can arise in thermodynamic integration as well. In order to circumvent them one can choose non-linear coupling of two states:

$$U(\lambda) = \lambda^4 U_{\mathcal{B}} + (1 - \lambda)^4 U_{\mathcal{A}} = \lambda^4 U_{\mathcal{B}} \quad (2.61)$$

We would prefer those reference states for which analytical evaluation of free energy is possible. For instance, if we would like to calculate free energy of mixing of two components we would take an ideal gas as a reference state.

$$\Delta A = A_{\mathcal{B}} - A_{\text{id.gas}} = \int_0^1 4\lambda^3 \langle U_{\mathcal{B}} \rangle_{\lambda} d\lambda \quad (2.62)$$

2.5.3 Rare events and metadynamics.

Different conformations of large molecules are usually separated by pronounced maxima in free energy landscape. When these maxima rise values of few kT it takes quite a while for molecule to switch from one conformation to another. Time scales available to molecular dynamics simulations are limited to tens or at best hundreds of nanoseconds while such switches happen very seldom (rare events) though very quickly. One could ask the question on possibility of acceleration of these rare events. In fact, there are several classes of methods aimed on this and we will consider one representative of one class that tackle the problem by flattening a free energy landscape of a system. Our method of choice is metadynamics.

In this method the free energy basins are flattened by inserting time-dependent potential that depends on the history of the system's trajectory. Once the free energy minimum is filled the free energy barrier is lowered and system can overcome it to "fall down" into neighboring minimum. When all minimum are filled in we can reconstruct the free energy profile from the final potential.

In canonical ensemble the probability distribution to observe a given state of the system is given by an ensemble average:

$$P(s_1, \dots, s_n) = \left\langle \prod_{\alpha=1}^n \delta(f_{\alpha}(r_1, \dots, r_N) - s_{\alpha}) \right\rangle, \quad (2.63)$$

exploiting the ergodic hypothesis we replace phase space average with a time average over the dynamical trajectory:

$$P(s_1, \dots, s_n) = \lim_{\mathcal{T} \rightarrow \infty} \frac{1}{\mathcal{T}} \int \prod_{\alpha=1}^n \delta(f_{\alpha}(r_1, \dots, r_N)) dt. \quad (2.64)$$

If we now represent δ -function as the limit of a Gaussian function

$$\delta(x - a) = \lim_{\sigma \rightarrow \infty} \frac{1}{\sqrt{2\pi\sigma^2}} e^{-(x-a)^2/2\sigma^2} \quad (2.65)$$

we obtain:

$$P(s_1, \dots, s_n) = \lim_{\mathcal{T} \rightarrow \infty} \lim_{\Delta s \rightarrow \infty} \frac{1}{\sqrt{2\pi\Delta s^2} \mathcal{T}} \int_0^{\mathcal{T}} \prod_{\alpha=1}^n \exp \left[-\frac{(s_{\alpha} - f_{\alpha}(r_1(t), \dots, r_N(t)))^2}{2\Delta s^2} \right] dt \quad (2.66)$$

Representing $P(s_1, \dots, s_n)$ in discretized appropriate to molecular dynamics simulations way we get the sampling technique to recover the free energy surface cut along the s_1, \dots, s_N coordinates. Moreover, taking biasing potential of form:

$$U_G(r_1, \dots, r_N, t) = W \sum_{t=\tau_G, 2\tau_G, \dots} \exp \left[-\sum_{\alpha=1}^n \frac{f_{\alpha}(r) - f_{\alpha}(r_G(t))^2}{2\Delta s^2} \right] \quad (2.67)$$

we can escape free energy minima and recover the whole free energy surface.

Part II

Development of the problem

MODELING the dissolution of polymers is not an easy task especially when this polymer is, like cellulose, sewn with numerous hydrogen bonds. We see three ways to approach cellulose dissolution:

1. use of solvation free energy—naive approach implying that the system well dissolving monomer (in thermodynamics sense) will be able to dissolve the polymer as well;
2. conformational mobility of cellulose chains which means that solvent causing internal rotation of sugar rings around glycosidic bond will be preferable for destroying hydrogen bonds network
3. direct studies of hydrogen bonds breaking in cellulose microcrystals.

To begin with, we started examining the thermodynamics of cellobiose conformational mobility and free energy of solvation studies in different solvent systems. Chapter 4 is devoted to solvation of cellobiose .

In chapter 5 we study the behaviour of cellulose nanocrystals in different solvent system on different time scales. Brute force technique of almost direct observations allows us to predict cellulose dissolution in different solvents.

And in the following chapter we address the question of noticeable properties of supercritical fluids that can sufficiently affect their dissolving abilities.

Chapter **3**

**STRUCTURE OF SUPERCRITICAL
SOLVENTS**

3.1 Structure of pure supercritical fluids: carbon dioxide and ammonia

3.1.1 Local structure in carbon dioxide

Assessment of the Spatial Distribution in Sub- and Supercritical CO₂ Using the Nearest Neighbor Approach: A Molecular Dynamics Analysis

Many spectroscopic investigations have focused on the local structural information that may be extracted from the behavior of both the shift of the vibration modes and the associated width. These two observables exhibit remarkably similar behaviors in various systems when approaching the critical isochore (CI) along the liquid–gas coexistence curve (CC). These results are indicative of common underlying local structural features when approaching the CI. Indeed, spectroscopic studies show that the peak position of the vibration modes such as the two dyads of CO₂ (Nakayama et al. 2000; Longelin 2003), the CH stretching mode in ethane (D et al. 1992), and the CO stretching mode in methanol (Saitow, Kajiya, and Nishikawa 2005) is dependent on density (from gas-like to liquid-like density). In general, the peak positions of these vibration modes were fitted using one Lorentzian function. The nonlinear dependence of the shift was associated with the enhancement of the local density, and a linear dependence suggests its absence. Moreover, the width of the studied vibration modes increases along the liquid–gas CC and decreases along the CI. In a recent work by Cabaço et al. (Cabaço et al. 2007), a band shape analysis of the two vibration dyad modes of CO₂ (1285 and 1388 cm⁻¹) shows that each one may be decomposed into two well-defined Lorentzian profiles. In each vibration mode, the higher frequency contribution was associated with a probe CO₂ molecule interacting through usual van der Waals interaction with each neighbor; the lower frequency contribution was related to the transition of CO₂ involved in a transient (CO₂)₂ dimer. Moreover, Musso et al. (Musso et al. 2002; Musso et al. 2004) measured the Raman spectra of the vibration mode of N₂ at 2327 cm⁻¹ and provided the behavior of the position and the width of this mode as the CI is approached from above along the gas–liquid CC. The results show that the asymmetry (see Figure 8 of (Musso et al. 2002)) increases along the CC and decreases along the CI and that the asymmetry is the pertinent parameter (compared to the behavior of the width) to trace back the closeness to the CI. These results suggest that the vibration profile (in particular that of the two dyads of CO₂) may be resultant of two contributions associated with a particular spatial distribution of molecules at a level of the local environment. If we make the hypothesis that the nearest neighbors are prized to exert a stronger influence on each other than on any of the other molecules, one expects that the changes in the position of a vibration mode as obtained by vibration spectroscopy (Raman or infrared) are mainly

determined by the nature of the local structure. The characterization of the changes in the nature of the local structure is then essential to analyze the different contributions to the studied vibration profile. In the investigation of this problem, computer simulation methods can provide a particularly useful tool. In a computer simulation, the appropriately chosen model of the system is seen in atomistic resolution, and hence, a detailed insight that cannot be obtained by any experiment is provided in the system. In the frame of these simulations, the radial distribution function is a major means by which structure is usually described in fluid systems. However, this statistical property does not provide sufficient details on the nature of the local environment due to its intrinsic averaging process. As a consequence, several approaches were developed to get a deeper insight into the local structure of molecular systems (the spatial extent of the local structure is defined by the position of the first minimum in the center of mass–center of mass radial distribution function). In this section, the nearest neighbor approach (Idrissi, Damay, and Kiselev 2007) was used to characterize the local structure of the CO₂ system along its liquid gas CC and along the CI. The distributions of the radial, orientation, and energy interaction between a reference CO₂ molecule and its subsequent nearest neighbors were calculated. In this approach, the neighbors of a central atom are sorted by distance into the first neighbor, second neighbor, etc. (see Figure 3.1). We then calculated separate nearest neighbor radial distribution functions, $p_{\alpha-\beta}(n,r,T)$, where α is a probe molecule, β is the n^{th} nearest neighbor at distance r from molecule α , and T is the temperature. In the same manner, we can characterize the orientation distribution $q_{\alpha-\beta}I(n,T,\cos(\theta))$ between α and β molecules as follows: for a distance r between the probe molecule α and the n^{th} nearest neighbor molecule β , we calculate $\cos(\theta)$, where θ is the angle between the unit vectors along the molecular axes of the two molecules and we average over all choices of a reference molecule (see Figure 3.1). The total interaction energy distribution $E_{TOT}(n,T)$ between α and β molecules was also calculated. In order to get more insight into the contribution of the different components of the intermolecular interaction to the resultant local structure, the electrostatic (EL), $E_{EL}(n,T)$, and the Lennard-Jones (LJ), $E_{LJ}(n,T)$, interaction energies were also calculated.

This section is organized as follows: in the first part, details on the molecular dynamics simulations are given as well as the statistical quantities used to characterize the local structure. In the second part, the behavior of the previously defined observables is used to show what we can learn about the local structure of CO₂ at liquid-like density ($T = 250$ K). In the third part, the effect of the temperature along the liquid–gas CC and along CI on the behavior of these statistical quantities is analyzed. In the last part, a conclusion is given.

Simulation Details.

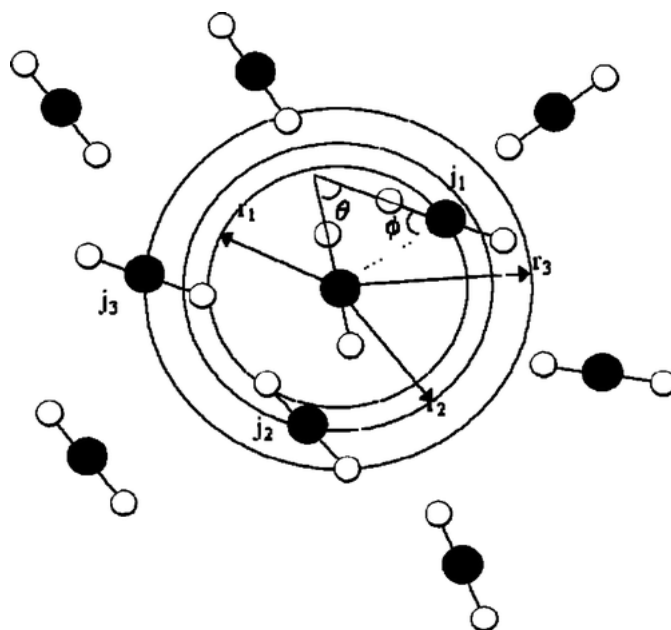


Figure 3.1: Pictorial representation of the nearest neighbor approach: r_i ($i = 1-3$) is the distance between a probe CO_2 molecule and its nearest neighbors j_1 , j_2 , and j_3 . The orientation is defined by two angles θ (between the molecular axes) and (between a molecular axis and an axis joining the center of masses of the two molecules).

Molecular Dynamics Simulations. Molecular dynamics simulations of the CO_2 fluid have been performed at eight different temperatures, i.e., at 250, 270, 285, 298, and 303 K (along the liquid–gas CC) and at 306, 313, and 320 K (along the CI) in the isothermal–isobaric (N,p,T) ensemble. As pointed out in our previous works (Idrissi et al. 2005; Idrissi et al. 2006), the disadvantages of using the molecular dynamics simulation to study supercritical fluids (particularly near the critical point) is related to the box size (which limits the correlation length explored) and to the knowledge of the critical point associated with the intermolecular potential model used in the simulation (the determination of which is not trivial). We examined then the dependence of the statistical quantities used in the analysis of the local structure for $N = 864$ and $N = 2048$ CO_2 molecules, and the results show no dependence on N . Furthermore, the correlation length ξ associated with the density fluctuation was evaluated by neutron scattering to be equal to 8.34 Å at $T = 305.8$ K and $P = 7.43$ MPa, to 10.49 Å at $T = 306$ K and $P = 10.49$ MPa (Nishikawa and Tanaka 1995), and to 10.49 Å at $T = 310$ K and $P = 10.1$ MPa (Ishii et al. 1995a). Molecular dynamics simulation must then adopt the basic cell with each side longer than 40 Å in order to reproduce roughly 75% of the total density fluctuation in CO_2 (Ishii et al. 1995a). Thus, here we have chosen to perform molecular dynamics simulations with $N = 864$ CO_2 molecules, which corresponds to

T (K)	V_m (cm ³ /mol)	P (MPa)	L (Å)	
250	41.90	0.2 ± 10	29.60	CC
270	47.00	0.5 ± 9	40.70	CC
285	52.28	1.0 ± 7	42.19	CC
298	60.00	5.0 ± 5	44.16	CC
303	72.83	6.0 ± 4	47.32	CC
306	94.42	8.0 ± 4	51.36	CI
313	94.42	9.0 ± 4	51.36	CI
320	94.42	11.0 ± 4	51.36	CI

Table 3.1: Values of the Temperatures, T, Molar Volumes, V_m , Pressures, P, and Box Lengths Used in the Molecular Dynamic Simulations

edge lengths of the cubic basic box between 29.6 Å (at T = 250 K) and 51.36 Å (at T = 306 K). Standard periodic boundary conditions have been applied. Details on the thermodynamic conditions are summarized in Table 3.1

CC indicates the liquid gas coexistence curve, and CI indicates the critical isochore. The Zhang potential has been used for CO₂ (Zhang and Duang 2005). This force field contains Lennard-Jones and charge-charge electrostatic interactions. The total potential is written as where $r_{i\alpha j\beta}$ is a radial distance between site α on molecule i and site β on molecule j , $q_{i\alpha}$ is the charge on site α on molecule i , and $q_{j\beta}$ is the charge on site β on molecule j . σ and ϵ are the LJ parameters. The values of the charge on these sites were calculated from the quadrupole moment of CO₂. The parameters of the potential model are given in Table 3.2. The simulations have been performed using the DL_POLY program (Smith and Forester 1996). The temperature and pressure of the system have been kept constant by means of the weak coupling algorithms of Berendsen (Berendsen et al. 1984), using the coupling parameter values of 0.1 ps (temperature) and 0.5 ps (pressure). All site-site interactions have been truncated to zero beyond the center-center cutoff distance of 15 Å. The long-range part of the electrostatic interactions has been accounted for using the Ewald summation method. The equations of motion have been integrated using the leapfrog algorithm, employing an integration time step of 2 fs. The systems have been equilibrated by generating 5 ns long trajectories, for each temperature. Then, in the 1600 ps long production stage, 800 000 sample configurations per system, separated by 160 fs long trajectories each, have been dumped for further analysis.

Calculated Properties. The parameters chosen for the analysis of these nearest radial distributions are the average distance $r_{\alpha-\beta}(n,T)$ between a reference molecule α and a molecule β belonging to the n^{th} neighbor class $p_{\alpha-\beta}(n,r,T)$; the corresponding root-mean-square average distance and the corresponding root $\Delta r_{\alpha-\beta}(n,T)$. These

site	$(\epsilon_\alpha/k_B)/K$	$\sigma_\alpha/\text{\AA}$	$D_\alpha/\text{\AA}$	q_α/e
O	82.656	3.0000	1.163	-0.2944
C	28.854	2.7918	0.000	0.5888

Table 3.2: Parameters of the Intermolecular Interaction Potential of CO₂

parameters are defined by using the following equations: and The root-mean-square average distance $\Delta r_{\alpha-\beta}(n,T)$ characterizes the width of the distribution; a large value of $\Delta r_{\alpha-\beta}(n,T)$ reflects flexible structure (large fluctuation) of the corresponding class of neighboring $p_{\alpha-\beta}(n,r,T)$.

Results and Discussion.

Local Structure at Liquid-Like Density (T = 250 K). We have calculated $p_{\alpha-\beta}(n,r,T = 250K)$ for $\alpha-\beta = (C-C)$, $n \leq 120$, and $r \leq 11 \text{ \AA}$. The corresponding average distance, $r_{C-C}(n,T = 250K)$, as well as the mean average fluctuation $\Delta r_{C-C}(n,T = 250K)$ are given in Figure 3.2. The average distance $r_{C-C}(n,T = 250K)$ increases nonlinearly with n , which is revealed by calculating the first and second derivatives of $r_{C-C}(n,T = 250K)$ with respect to n (see the inset of Figure 3.2a). A minimum occurs at $n = 3$, while a maximum occurs at $n = 10$. Furthermore, the minimum in $\Delta r_{C-C}(n,T = 250K)$ around $n = 3$ indicates that the molecules occupying this position undergo a small fluctuation in their radial distance. This position defines some kind of border along which the motion of molecules is reduced. The high fluctuation of $\Delta r_{C-C}(n,T = 250K)$ around $n = 10$ suggests that these molecules have a large probability to occupy the nearest class of neighbors below and beyond $n = 10$. The behavior of both $r_{C-C}(n,T = 250K)$ and $\Delta r_{C-C}(n,T = 250K)$ reveals that the first shell determined by the position of the first minimum in the C-C radial distribution function (and which coincides with the position of $n = 10$ at $r = 5.5 \text{ \AA}$) is structured in two subshells: the first one encompasses the nearest neighbors below $n = 3$, and the second one lies between $n = 3$ and $n = 10$. The second shell lies between the position of the first minimum (at $n = 10$ and $r = 5.5 \text{ \AA}$) in the C-C radial distribution function and the position of its second minimum (at $n = 40$ and $r = 9 \text{ \AA}$). The behavior of both $r_{C-C}(10 < n < 40, T = 250K)$ and $\Delta r_{C-C}(10 < n < 40, T = 250K)$ suggests that, for the second shell, the same picture (the existence of two subshells) may apply, even if in this region the maxima in the behavior of both the rates of increase of $r_{C-C}(n = 40, T = 250K)$ and of $\Delta r_{C-C}(n = 40, T = 250K)$ occur with less intensity as compared to that in the first shell. Finally, as we recede further and further, the behavior of both $r_{C-C}(n > 50, T = 250K)$ and $\Delta r_{C-C}(n > 50, T = 250K)$ indicates that the neighbors are equidistantly positioned relative to a probe CO₂ molecule. The behavior of $r_{C-C}(n,T = 250K)$ and $\Delta r_{C-C}(n,T = 250K)$ may be correlated with the behavior of the EL and LJ intermolec-

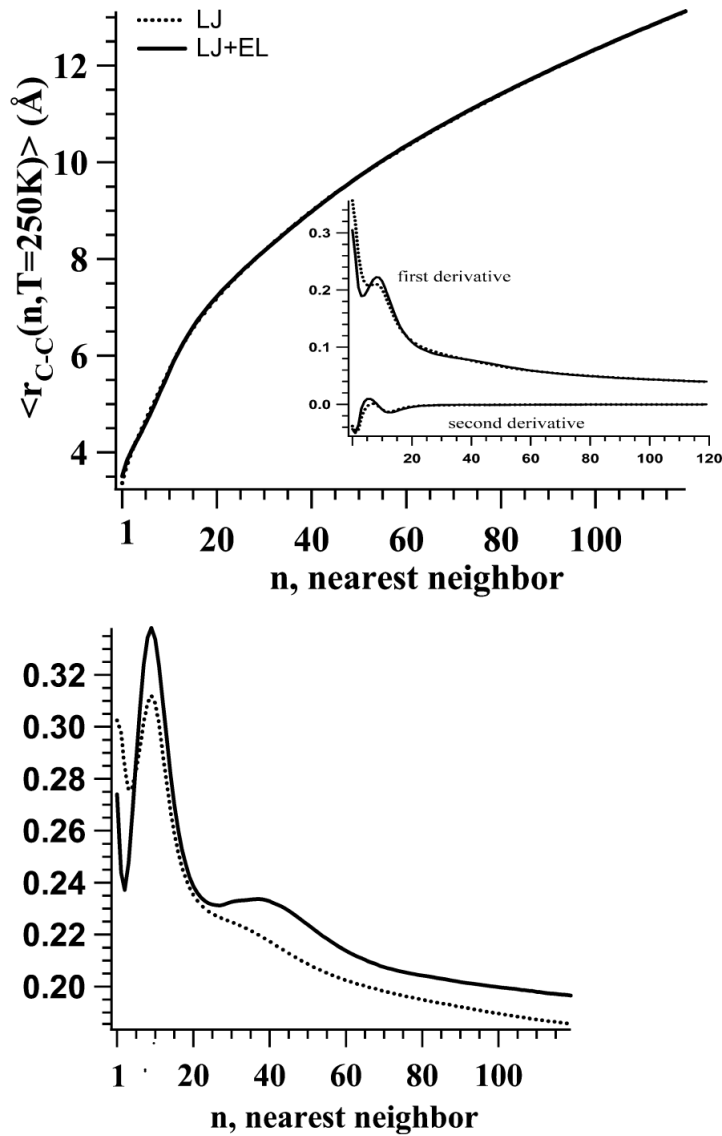


Figure 3.2: Average distance between a probe CO_2 molecule and its nearest neighbors, n . The inset shows the behavior of the first and second derivatives of the average distance with respect to n . (b) The fluctuations of the average distance between a probe CO_2 molecule and its nearest neighbors, n . The same as in part a.

ular interactions between a probe CO_2 molecule and its nearest neighbors. In order to corroborate this idea, the EL interaction energy, $E_{EL}(n, T = 250\text{K})$, the LJ interaction energy, $E_{LJ}(n, T = 250\text{K})$, and the total interaction energy, $E_{TOT}(n, T = 250\text{K})$, distributions as well as the corresponding average values were calculated. An illustration of

the behavior of these distributions (for $n = 1-8$) as well as the corresponding average value are given in Figure 3.3 a, b, c, and d, respectively. For the first nearest neighbor, $E_{EL}(n, T = 250\text{K})$ is expansive and it has a slight asymmetric character with respect to the attractive (negative values) and repulsive (positive values) contributions. As n increases, the contribution of the negative energy values increases, indicating the increase of the attractive character of $E_{EL}(n, T = 250\text{K})$. The maximum of this increase is observed for the third nearest neighbor. For the subsequent nearest neighbor ($n \geq 4$), the negative side of these distributions is reduced in favor of a gradual increase of the small negative values and a development of an intense contribution around zero energy. The occurrence of a minimum in the average EL interaction energy values clearly illustrates this behavior (see Figure 3.3d). The $E_{LJ}(n, T = 250\text{K})$ distribution has negative values. With increasing n , these distributions shift to small energy values with a noticeable slowing down of this shift for the third nearest neighbor and, concomitantly, an increase of the contribution of the low energy side is observed. This is quantified by the occurrence of an inflection point in the behavior of the LJ interaction energy average values (see Figure 3.3).

The motion of molecules occupying the third nearest neighbor position is largely restricted along an edge defined by the average distance $r(n=3, T = 250\text{K})$. Indeed, a minimum occurs at this distance for the rate of increase of $r(n=3, T = 250\text{K})$, $\Delta r_{C-C}(n=3, T = 250\text{K})$ and $E_{EL}(n=3, T = 250\text{K})$ and an inflection point is observed at this position for $E_{EL}(n=3, T = 250\text{K})$. This indicates that strong attractive intermolecular interactions prevent the molecules occupying this position from moving out into farther positions. Furthermore, in order to rationalize the effect of the EL and LJ interaction energy contributions to the resultant behavior of these parameters, we made the same calculations at the same density; however, the EL interaction energy was set to zero. The behavior of the average distance, the corresponding fluctuation, as well as the LJ interaction energy (the only contribution) and the corresponding average values are depicted in Figure 3.2a, b, Figure 3.4, and Figure 3.3d, respectively. They show that the rate of increase of $r(n, T = 250\text{K})$ and the behavior of $\Delta r_{C-C}(n, T = 250\text{K})$ is the same as that obtained when the EL interaction energy was considered. However, the minima occur at furthest nearest neighbors (around 5–6), although with less intensity. This clearly demonstrates that both a balance between the repulsive and attractive sides in the case of the EL interaction energy distributions and a balance between the strong (large negative values) and weak (small negative values) attractive character of the LJ interactions energy distributions affect the rate of increase of $r(n, T = 250\text{K})$ and the behavior of $\Delta r_{C-C}(n, T = 250\text{K})$. Indeed, the decrease in the rate of increase of $r(1 \leq n \leq 3, T = 250\text{K})$ is due to the concomitant increase of the attractive character of both the LJ and EL interaction energy distributions.

The radial arrangement as well as the nature of the intermolecular interactions involved in the previously discussed local structure may result in a strong orientation

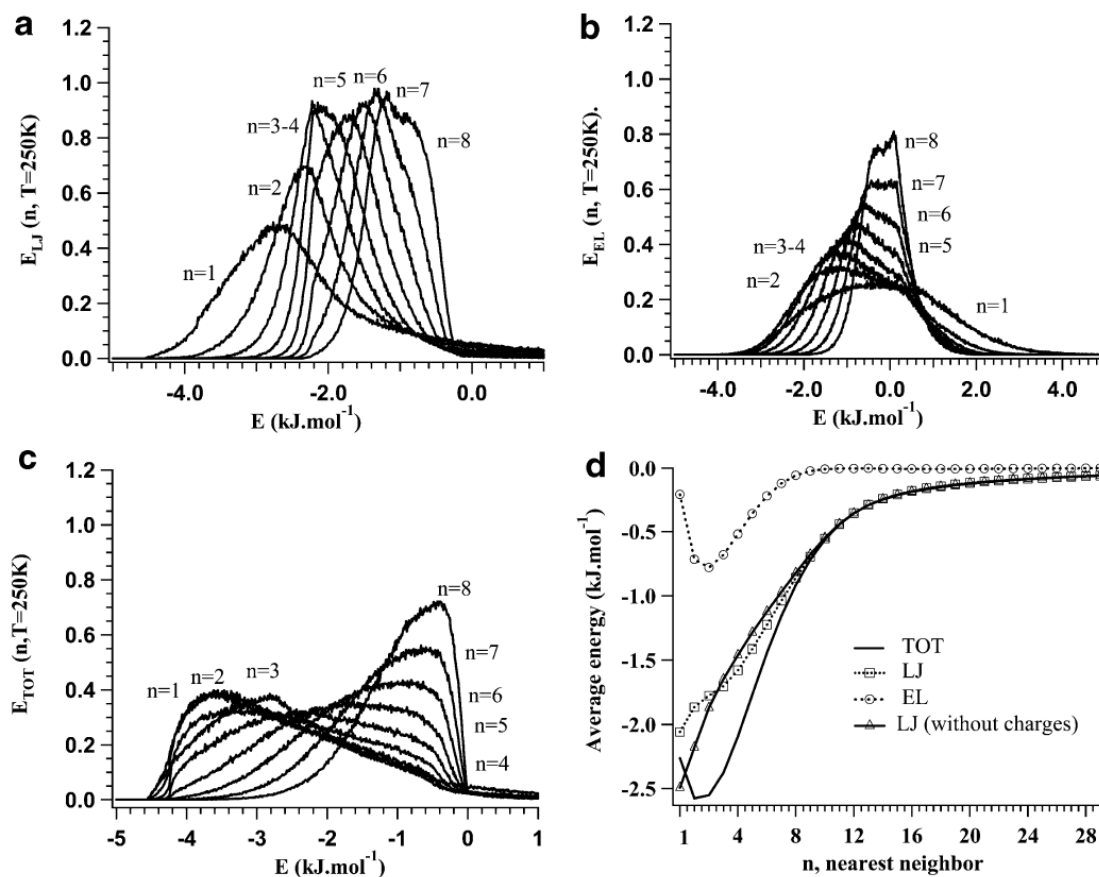


Figure 3.3: (a) Distributions of the Lennard-Jones interaction energy between a probe CO₂ molecule and its nearest neighbors (n = 1–8). These distributions were obtained in the case where both the electrostatic and Lennard-Jones interactions are considered in the molecular dynamics simulations. (b) Distributions of the electrostatic interaction energy between a probe CO₂ molecule and its nearest neighbors (n = 1–8). These distributions were obtained in the case where both the electrostatic and Lennard-Jones interactions are considered in the molecular dynamics simulations. (c) Distribution of the total interaction energy between a probe CO₂ molecule and its nearest neighbors (n = 1–8). These distributions were obtained in the case where both the electrostatic and Lennard-Jones interactions are considered in the molecular dynamics simulations. (d) Average values of the electrostatic, the Lennard-Jones, and the total interaction energy between a probe CO₂ molecule and its nearest neighbors, n. The average values of the interaction energy where only Lennard-Jones interactions are considered in the molecular dynamics simulations are also given (triangles).

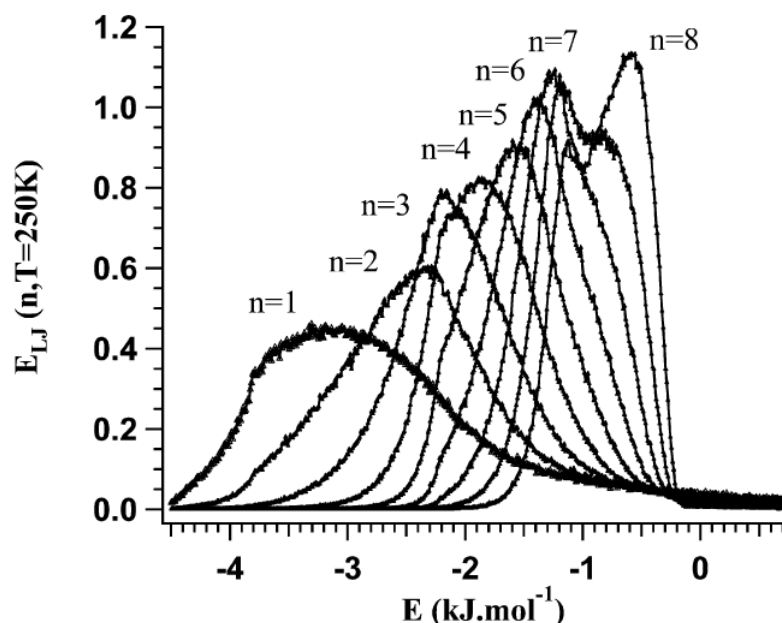


Figure 3.4: Distribution of the Lennard-Jones interaction between a probe CO_2 molecule and its nearest neighbors ($n = 1-8$). These distributions were obtained in the case where only the Lennard-Jones interactions are considered in the molecular dynamics simulations.

between CO_2 molecules. We therefore calculated $q_{\alpha-\beta I}(n, T = 250\text{K}, \cos(\theta))$ for every nearest neighbor n . These orientation distributions are given in Figure 3.5 as a function of the nearest neighbor number, n (< 5). They show that the closest neighbor has a higher probability to have a parallel orientation. The second one also has a higher probability to have a parallel configuration. However, the distribution $q_{\alpha-\beta I}(n = 3, T = 250\text{K}, \cos(\theta))$ is characterized by the fact that almost all of the orientations are equally probable to occur. For $q_{\alpha-\beta I}(n = 4, T = 250\text{K}, \cos(\theta))$, the perpendicular orientation (T-shape) dominates. The behavior of the farthest nearest neighbor orientation distribution $q_{\alpha-\beta I}(n \geq 6, T = 250\text{K}, \cos(\theta))$ witnesses the loss of the perpendicular orientation in favor of a random one (figure not shown). However, the one-dimension definition used here to characterize the orientation is certainly incomplete and there is still an ambiguity about the description of the orientation between two CO_2 molecules. It is possible to clear up the picture (although not completely) using the double cosine distribution, $q_{\alpha-\beta II}(n, T = 250\text{K}, \cos(\theta), \cos(\phi))$, where a second angle is introduced. It characterizes the orientation between a reference CO_2 molecular axis and the vector joining the carbon atoms of two CO_2 molecules (see Figure 3.1). The double cosine distributions are shown in Figure 3.5 for $n = 1-4$. They reveal that the first nearest

neighbor has a parallel configuration with a angle of about 60° . The second nearest one has almost the same configuration as the first. For the third nearest neighbor, the orientation is a mixture of three configurations occurring with slightly higher probabilities: the parallel configuration ($\theta 0^\circ, 60^\circ$), the perpendicular configuration ($\theta 90^\circ, 0^\circ$), and, finally, the X perpendicular configuration ($\theta 90^\circ, 90^\circ$). These orientations are a result of constraints associated with the large attractive character of the interactions involving this nearest neighbor and its restricted motion along an edge defined by the average distance $r(n, T = 250K)$. The double cosine distribution of the fourth nearest neighbor shows that the configuration ($\theta 90^\circ, 0^\circ$) is the dominant contribution and it coexists with remnant configurations of ($\theta 0^\circ, 60^\circ$) and ($\theta 90^\circ, 90^\circ$).

Effect of Temperature. The effect of temperature on $r_{C-C}(n, T)$ and $\Delta r_{C-C}(n, T)$ ($n \leq 120$) is given in Figure 3.6. The behavior of $E_{LJ}(n = 1, 3, 5, T)$ and $E_{EL}(n = 1, 3, 5, T)$ is illustrated in Figure 3.7 and Figure 3.8, respectively. The corresponding average values are given in Figure 3.9. Finally, the effect of temperature on the orientation between a reference CO_2 molecule and its nearest neighbors is given in Figure 3.10 for the one-dimension definition (for $n = 1-6$) and in Figure 3.11 for the two-dimension definition (for $n = 1$ and 3). With increasing temperature along the liquid-gas CC, $r_{C-C}(n, T)$ increases which expresses the obvious expansion of the system. Furthermore, the minimum in the rate of increase of $r_{C-C}(n, T)$ (see the inset of Figure 3.6a) as well as the minimum occurring in $\Delta r_{C-C}(n, T)$ tend to disappear. This may result from the disordering effect of thermal motion which becomes more and more effective. Along the CI, $r_{C-C}(n, T)$ and $\Delta r_{C-C}(n, T)$ are not affected by increasing the temperature. This suggests that, along the CI, the local structure depends more on density than on temperature. When increasing the temperature along the liquid-gas CC, the weight of the negative side in $E_{EL}(n, T)$ is gradually reduced, and this tendency is accentuated when increasing n . As a consequence, the minimum in the average value associated with $E_{EL}(n, T)$ decreases (less negative) and shifts to occur for a lower position of the nearest neighbor. The $E_{LJ}(n, T)$ distribution has a predominantly attractive character (negative values). The distributions shift to lower negative values, and this distribution becomes bimodal near the CI with a contribution near 0 kJ/mol and the second contribution around -1 kJ/mol. The average values associated with $E_{LJ}(n, T)$ distributions decrease, and the inflection point around $n = 3$ disappears as the temperature increases along the liquid-gas CC (see Figure 3.9). When approaching the CI, the contribution of the LJ interaction energy tends to overcome that of the EL interaction energy contribution, and it results in the disappearance of the minimum in the behavior of the total energy average value.

When increasing the temperature along the liquid-gas CC and along the CI, the orientation distributions $q_{\alpha-\beta}^I(n, T, \cos(\theta))$ and the double cosine distributions $q_{\alpha-\beta}^{II}(n, T, \cos(\theta), \cos(\phi))$ reveal that the parallel orientation between a probe CO_2 molecule and its first nearest

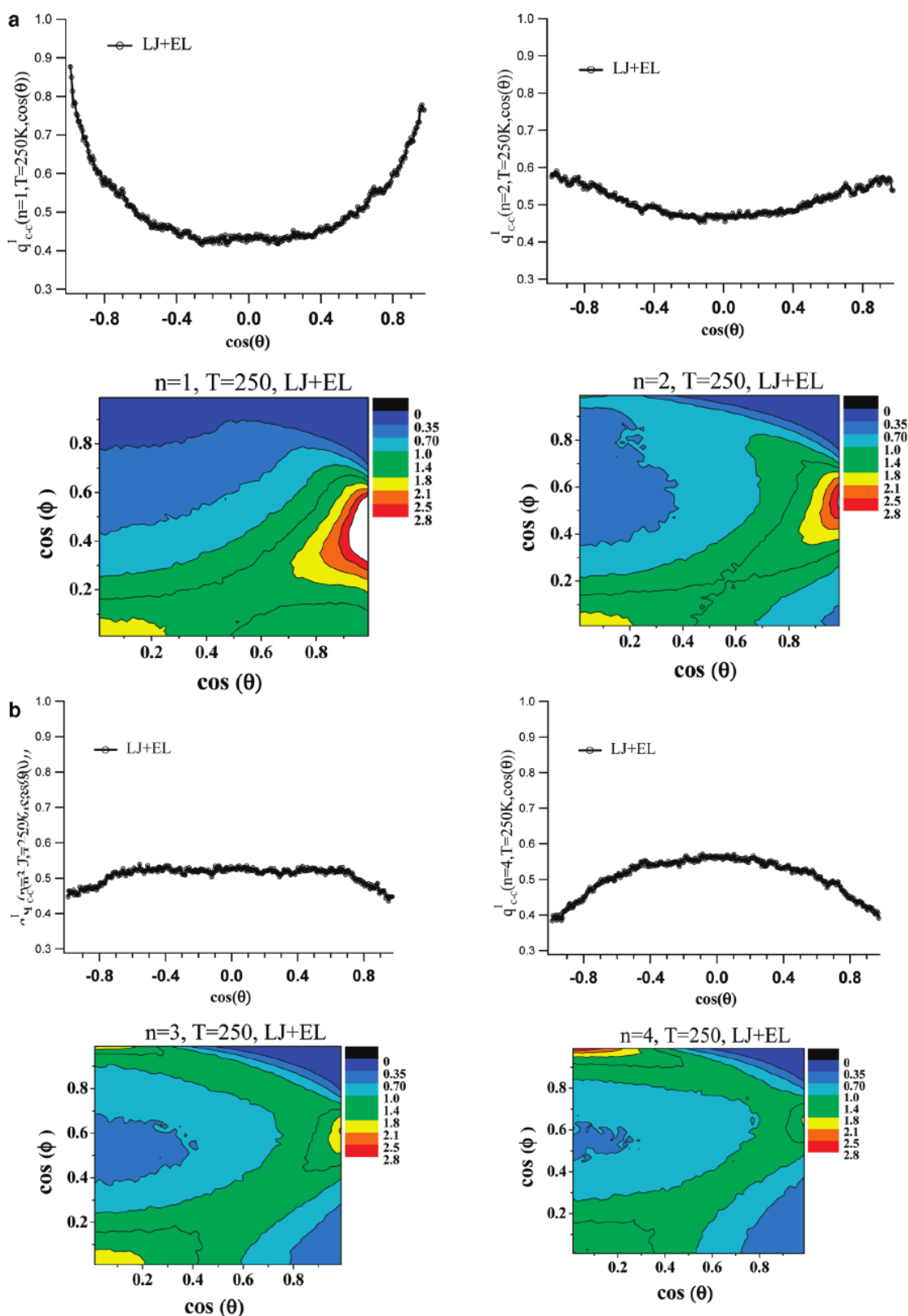


Figure 3.5: (a) Orientation distributions between a probe CO_2 molecule and its first and second nearest neighbors. The angle θ is the one between their molecular axes, and is that between a molecular axis and the axis joining the center of masses of the two molecules. (b) Orientation distributions between a probe CO_2 molecule and its third and fourth nearest neighbors. The same legend as in part a.

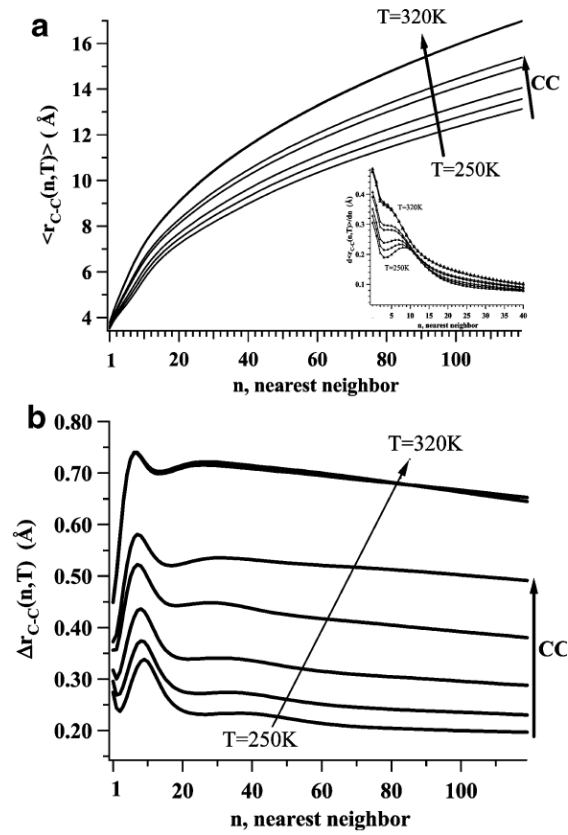


Figure 3.6: (a) Effect of the temperature on the average distance between a probe CO₂ molecule and its first nearest neighbors, $n < 120$ ($n = 0$ is the first nearest neighbor). Molecular dynamics simulations have been performed at eight different temperatures, i.e., at 250, 270, 285, 298, and 303 K (along the liquid–gas coexistence curve (CC)) and at 306, 313, and 320 K (along the critical isochore). The first derivative of the average distance with respect to n is given in the inset. (b) Effect of the temperature on the fluctuation of the average distance between a probe CO₂ molecule and its first nearest neighbors, $n < 120$ ($n = 0$ is the first nearest neighbor). The same legend as in part a.

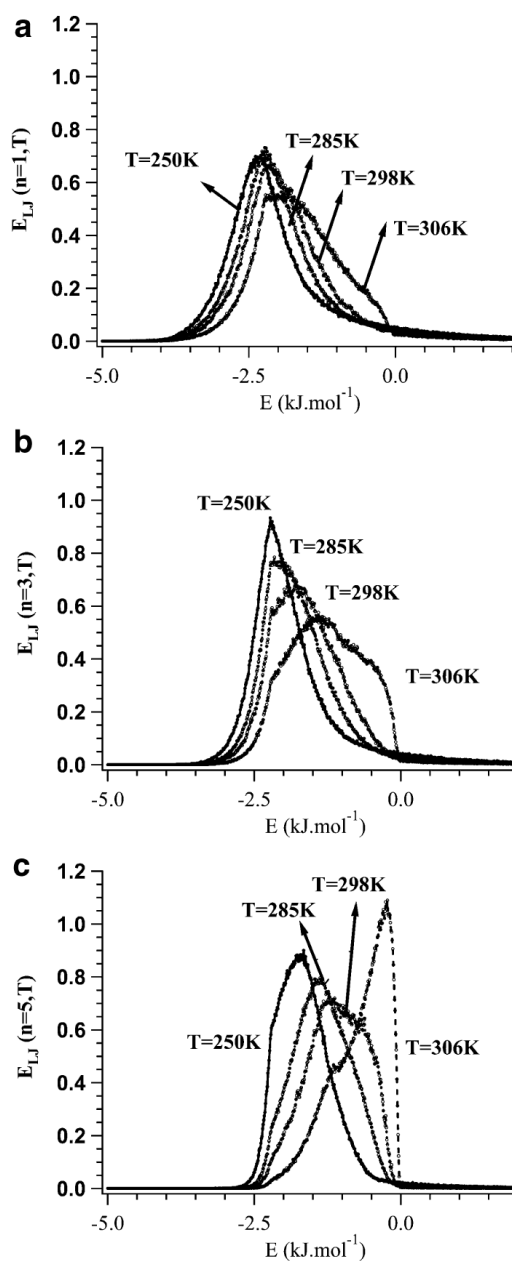


Figure 3.7: Effect of the temperature on the distribution of the Lennard-Jones interactions between a probe CO_2 molecule and its first, third, and fifth nearest neighbor. These distributions were obtained in the case where both the electrostatic and Lennard-Jones interactions are considered in the molecular dynamics simulations.

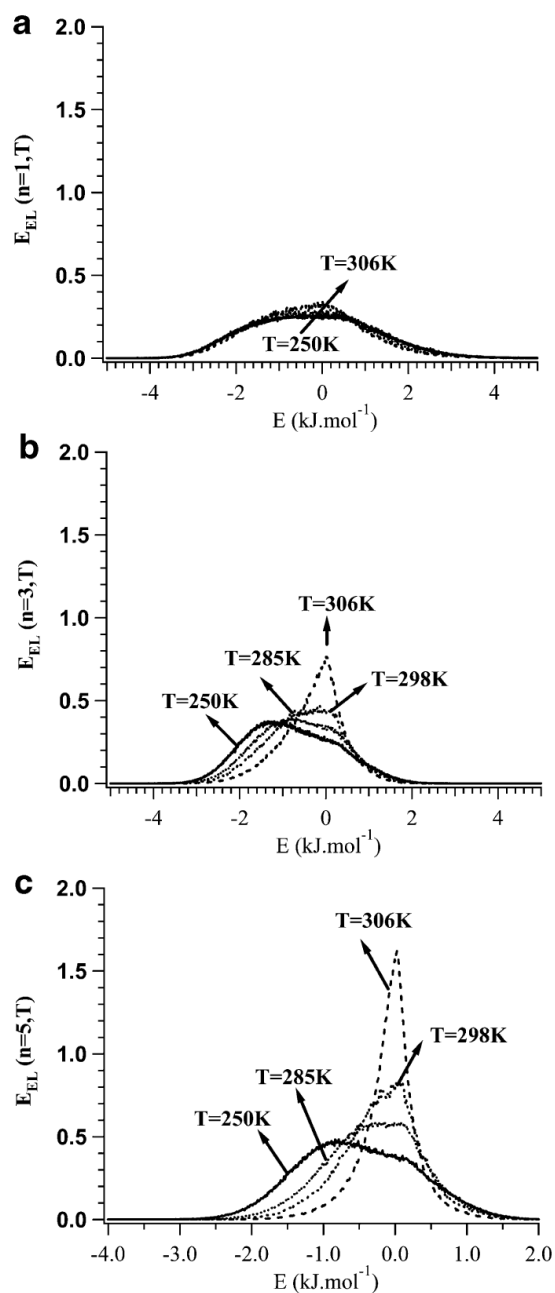


Figure 3.8: Effect of the temperature on the distribution of the electrostatic interactions between a probe CO_2 molecule and its first, third, and fifth nearest neighbor. These distributions were obtained in the case where both the electrostatic and Lennard-Jones interactions are considered in the molecular dynamics simulations.

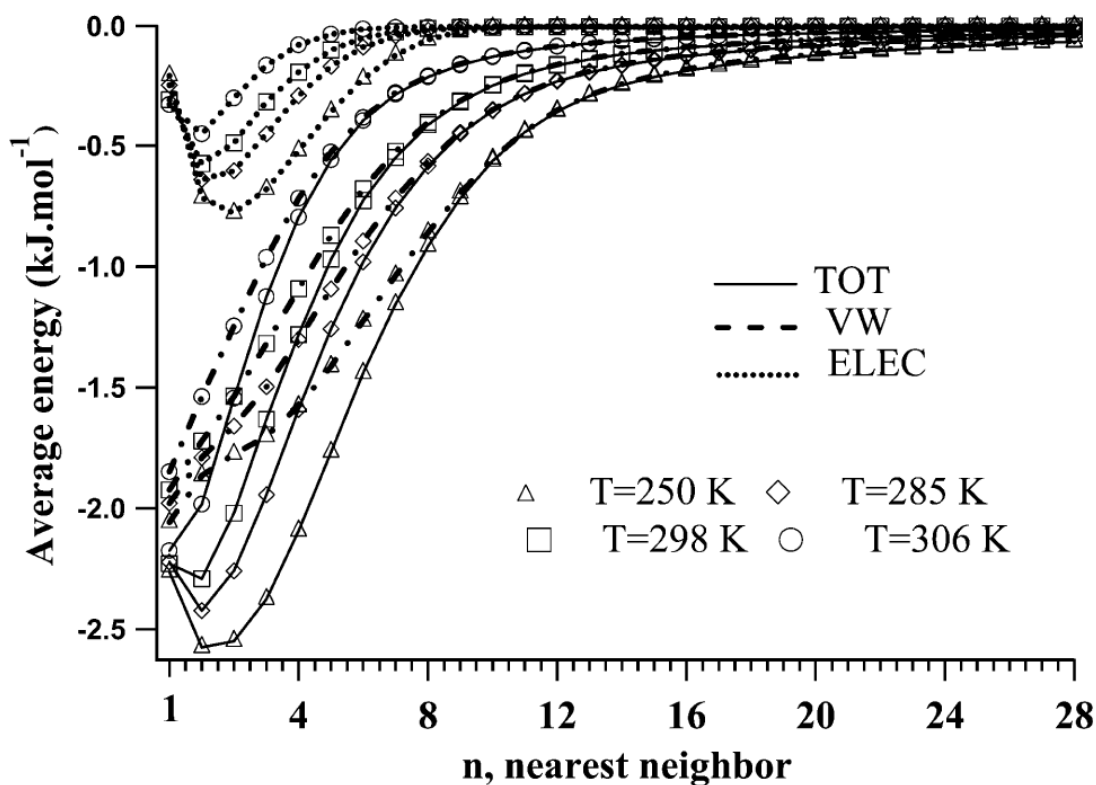


Figure 3.9: Effect of the temperature on the average values of the electrostatic, the Lennard-Jones, and the total interaction energies between a probe CO_2 molecule and its nearest neighbors, n . These average values were obtained in the case where both the electrostatic and Lennard-Jones interactions are considered in the molecular dynamics simulations.

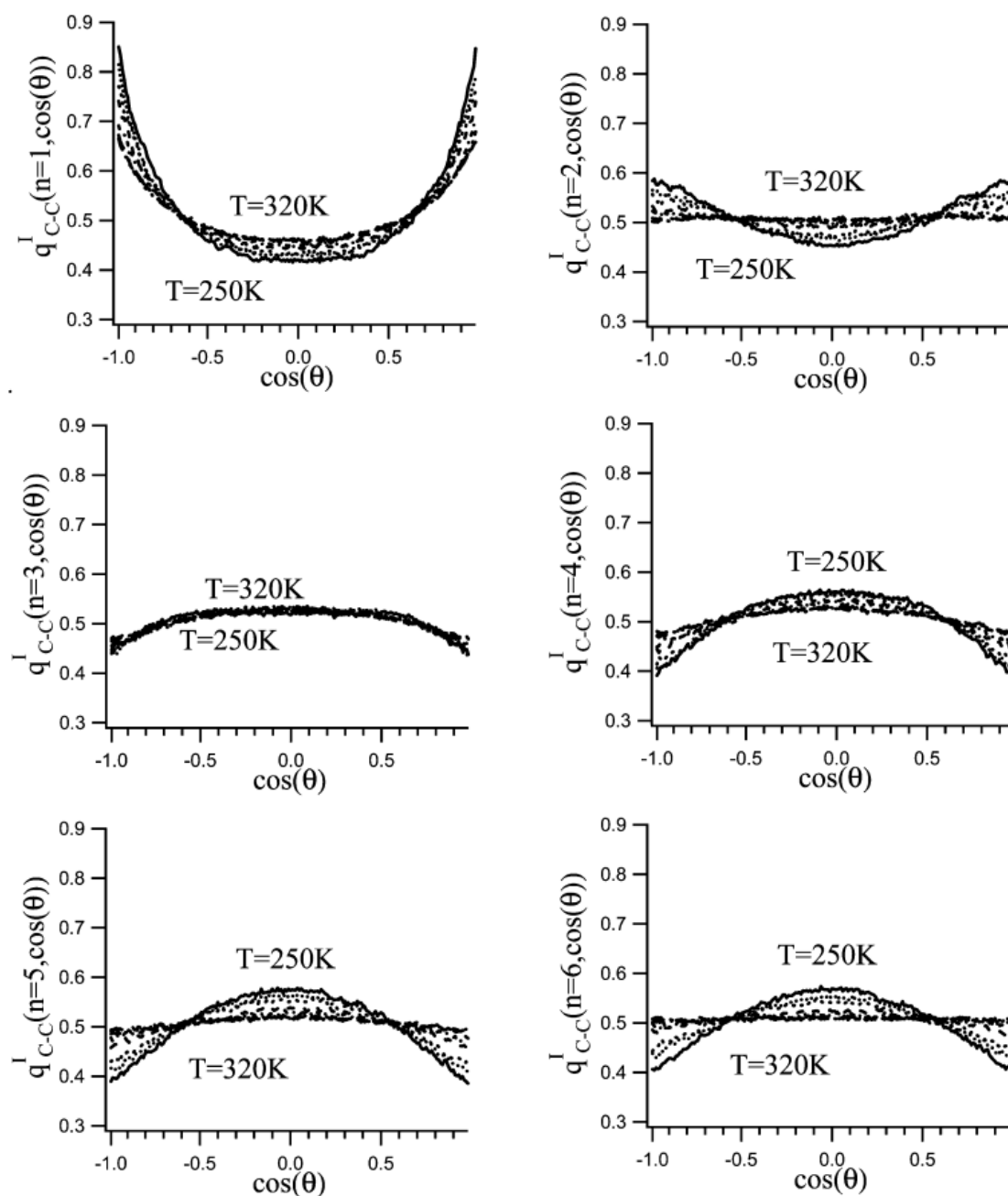


Figure 3.10: Effect of the temperature on the orientation distributions between a probe CO₂ molecule and its first, second, third, and fourth nearest neighbors. The angle θ is the one between their molecular axes. These distributions were obtained in the case where both the electrostatic and Lennard-Jones interactions are considered in the molecular dynamics simulations.

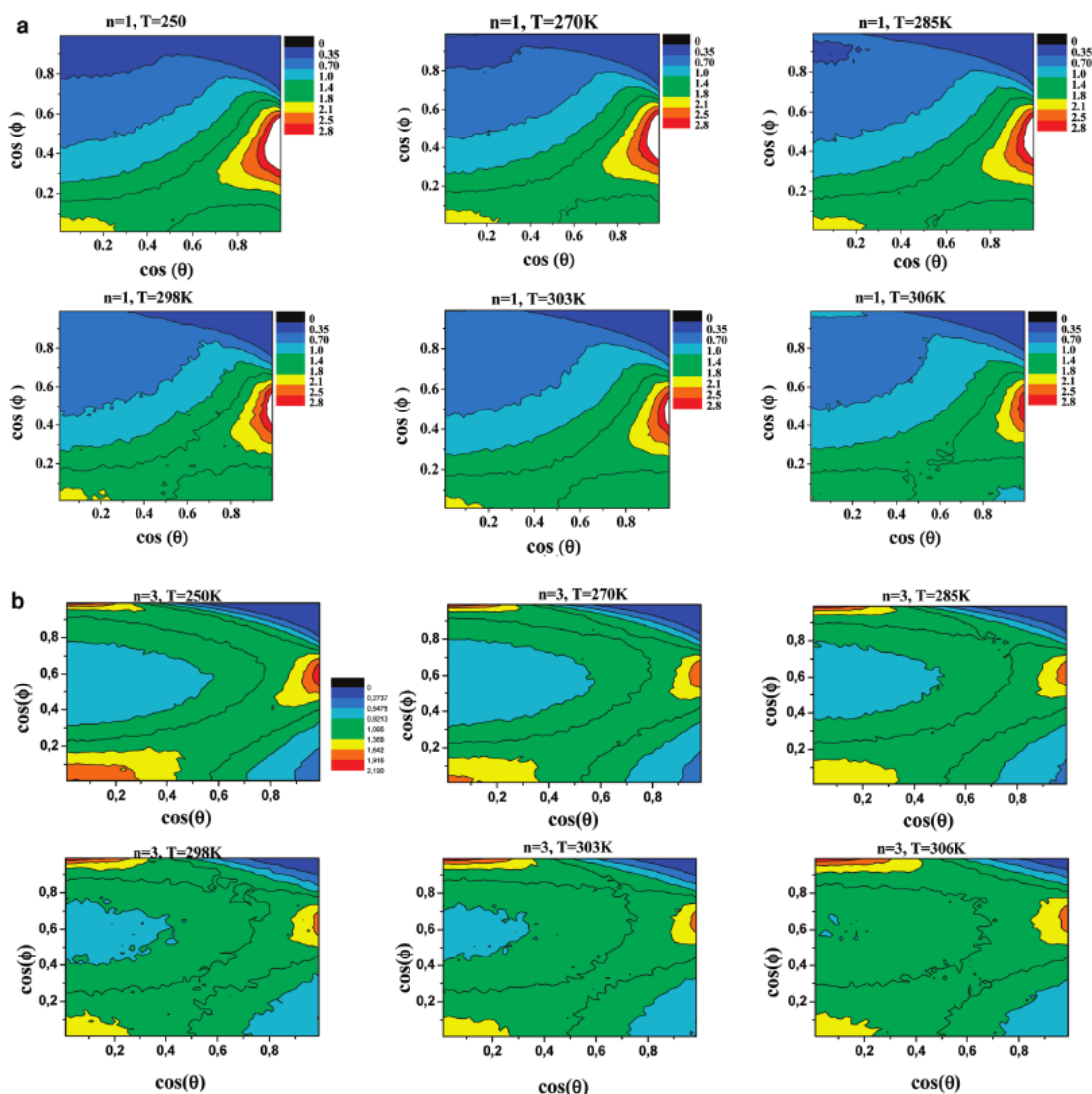


Figure 3.11: Effect of the temperature on the orientation distributions between a probe CO_2 molecule and its first and third nearest neighbors. The angle is the one between the molecular axis and an axis joining the center of masses of the two molecules. Both the electrostatic and Lennard-Jones interactions are considered in the molecular dynamics simulations.

neighbor does not change drastically. The orientation distribution involving farther nearest neighbors tends to be random. The results show that $q_{\alpha-\beta}I(n=3, T, \cos(\theta))$ is not affected, whereas the double cosine distribution $q_{\alpha-\beta}II(n=3, T, \cos(\theta), \cos(\theta))$ reveals that the probability of the parallel, X, and perpendicular configurations is sensibly reduced.

Local Structure and the Profile of the Vibration Modes. How will the local structure, as revealed by the radial, orientation, and interaction energy distributions of the nearest neighbors discussed previously, shape the vibration profile as obtained by Raman spectroscopy (see (Nakayama et al. 2000; Cabaco et al. 2008; Idrissi et al. 2010))? This may be answered qualitatively by starting from the fact that the vibration frequencies of a molecule in fluid are sensitive to the molecule's instantaneous local environment (Musso et al. 2002; Cabaco et al. 2008). As this environment changes due to molecular dynamics, these frequencies fluctuate in time; the behavior of the position of the vibration mode provides information about the average local structure of the liquid. The line width, on the other hand, is in general sensitive to both the distribution of the local structure around a probe and its fluctuations. In particular, we can expect that the effect of the temperature on the frequency positions of the vibration modes of a probe CO₂ molecule is mainly determined by the local structure. A general definition for the spatial extent of the local structure or first shell around a probe CO₂ molecule is associated with the position of the first minimum in the center of mass–center of mass radial distribution. In this work, we obtain the information about the local structure around a probe CO₂ molecule by using accessible structural parameters from MD simulations which are the radial, orientation, and energy interaction distributions involving its nearest neighbors. One can expect a difference in how the nearest neighbors are distributed around a probe CO₂ molecule, between low (along the liquid–gas CC) and high temperature (along the CI). The aforementioned results show that the CO₂ molecules belonging to this local structure around a probe molecule have different behaviors with respect to the average distance, the associated fluctuation, the orientation, and the energy interaction. These results suggest that the Raman vibration modes of CO₂ may be deconvoluted into two contributions: the first one is associated with the CO₂ molecule in the environment of its nearest neighbors, characterized by a small radial fluctuation of the average distance, strong attractive character of the interaction, and strong orientation (parallel configuration); the second contribution is associated with the CO₂ molecule in an environment of its nearest neighbors characterized by large fluctuation of the average distance, weak attractive character of the interaction, and an almost random orientation configuration. These results are consistent with our previous Voronoi analysis (Idrissi et al. 2010). Indeed, the local structure of CO₂ along the liquid–gas CC and along the CI was analyzed through the metric properties of the Voronoi polyhedra (VP) of the

molecules, such as the volume, reciprocal volume, and asphericity of the VP as well as the radius of the vacancies between the molecules. The behavior of these properties (i.e., their distributions as well as the associated average and fluctuation values) provides clear evidence of the inhomogeneous character of the distribution of the CO₂ molecules in the system, when the temperature becomes close to the critical point. Particularly, it was shown that the behavior of the reciprocal volume of the VP (i.e., a measure of the local density around the molecules) becomes clearly bimodal. The first of these peaks was associated with the molecules that are in a high local density environment (small fluctuation of CO₂ molecules forming the Voronoi polyhedron), whereas the other peak reflects the low local density with respect to a reference CO₂ molecule. Our results are in line with the recent Raman analysis by Cabaço et al. (Cabaço et al. 2007), where the two vibration modes of CO₂ were decomposed into two well-defined Lorentzian contributions. Our results confirm that these two contributions are associated with the local structure around a probe CO₂ molecule involving the first shell neighboring molecules; however, our results are at variance with their interpretation of the physical meaning of the two contributions. Furthermore, a close analysis of the vibration profiles of CO₂ (see Figure 2 in (Arakcheev et al. 2003) and Figure 3 in (Nakayama et al. 2000)) or of the C–F mode in CHF₃ (Saitow et al. 2003; Saitow et al. 2001), C–O mode in methanol (Saitow, Kajiya, and Nishikawa 2005), shows that a second contribution is indicated by the noticeable gap between the experimental spectral profile and the one Lorentzian function used to adjust this profile. Finally, the aforementioned analysis of the local structure in the CO₂ system will serve as a basis for analysis of the ongoing experiment where the Raman spectra of the vibration modes of CO₂ are recorded at the same thermodynamic conditions of this work.

Conclusion. In this section, we have presented a detailed investigation of the local structure of CO₂ along the coexistence curve and along the critical isochore by analyzing the radial average distance between a probe CO₂ molecule and its nearest neighbors, as well as their orientation and interaction energy distributions. The main idea behind this study is to connect qualitatively the change in the local structure to the change in the profile of CO₂ vibration modes, along the same thermodynamic points. Furthermore, the analysis presented in this section leads to a vivid picture of the changes occurring at a level of the local structure of CO₂, showing the main implied radial, orientation, and energy interaction distributions, and informing about the dependence of these distributions on the thermodynamic points considered in this study. We have found that at low temperature, far from the critical point, the behavior of the fluctuation of the average distance with respect to a probe CO₂ molecule and its nearest neighbors, their orientation, and the energy interaction distribution suggests that its first shell is divided into two subshells. The first subshell

is characterized by a low fluctuation in the average distance, by a strong attractive character of the electrostatic and Lennard-Jones interactions, as well as a strong orientation (parallel configuration). Conversely, the second subshell is characterized by a high fluctuation of the average distance, and a decrease of the attractive character of the electrostatic and Lennard-Jones interactions. The closest nearest neighbor belonging to this second subshell has a perpendicular configuration with respect to the probe molecule, while the farthest have a random orientation. With increasing the temperature along the liquid–gas CC, there is an obvious increase of the fluctuation in the average distance, a decrease of the attractive character of the electrostatic and LJ interactions, and an increase of the random character of the orientations. As a consequence, the difference between the two subshells becomes blurred. These results suggest that the vibration modes of CO₂ may be deconvoluted into two contributions: the first one is associated with the CO₂ molecule in the environment of its nearest neighbors characterized by a small radial fluctuation of the average distance, strong attractive character of the interaction, and a strong orientation (parallel configuration); the second contribution is associated with the CO₂ molecule in an environment of its nearest neighbors characterized by a large fluctuation of the average distance, weak attractive character of the interaction, and almost a random orientation configuration.

A Voronoi polyhedra analysis of local structure in sub- and supercritical CO₂.

Introduction. The estimation of the change of the nature of the local structure along the liquid–gas coexistence curve and along the critical isochore is essential in analyzing the behaviour of the shift and the width of a Raman active vibrational mode. In particular, the behaviour of the width associated with CO₂ vibrational modes was traced back to the change of the homogeneous/inhomogeneous character of the CO₂ molecules distribution (Idrissi et al. 2009a). In order to check the validity of this interpretation, computer simulation methods can provide a particularly useful tool. In a computer simulation the appropriately chosen model of the system is seen in atomistic resolution, and hence such a detailed insight is provided into the system that cannot be obtained by any experiment. There are many parameters that can be used to characterize the local structure in a condensed phase. Among these properties, the radial distribution function is a major means, by which the structure is usually described in fluid systems. However, this statistical property does not provide sufficient details on the nature of the local environment in fluid systems, because of the averaging process, taken over the whole volume of the studied system. In fact, even in such cases when the dynamical properties of the molecules differ by several orders of magnitude, the radial distribution function may only reveal minor differences. As a consequence, several additional approaches have been developed to get more insight into the local structure of molecular systems. Among these approaches, the method of the Voronoi polyhedra (Voronoi 1908; N. 2000; Okabe 2000) proved to be particularly useful in characterizing the local environment of the molecules in disordered phases (Finney 1970; Ruocco, Sampoli, and Vallauri 1992; Ruocco et al. 1993; Montoro et al. 1994; Voloshin et al. 1995; Jedlovszky and Mezei 1999; Jedlovszky and Mezei 2000; Voloshin, Beaufile, and Medvedev 2002; Tokita et al. 2004; Idrissi et al. 2008). The purpose of the present section is to investigate the local structure of CO₂ upon approaching the critical point using the method of the Voronoi polyhedra, and also to point out the inhomogeneous nature of the spatial distribution of the CO₂ molecules in such thermodynamic states.

The section is organised as follows. The next section presents the methods applied and details of the calculations carried out, concerning both the molecular dynamics simulations performed and the VP analyses done. Then, in the third section the results are presented and discussed in detail. Finally, in the last section the main conclusions of this study are summarised.

Calculation details.

Molecular dynamics simulations. As pointed by Drozdov and Tucker (Drozdov and Tucker 2001), the difficulties occurring when using computer simulation methods in studying supercritical fluids (in particular, at the vicinity of the critical point)

are related to the size of the basic simulation box, which limits the correlation length of the system to be explored, and to the exact knowledge of the critical point associated with the intermolecular potential model used in the simulation (the determination of which is far from being trivial). The correlation length ξ in CO₂ was evaluated by neutron scattering, and was found to be in the range between 5.0 and 19.0 Å along the T = 310 K isotherm for densities ρ ranging from 0.159 to 0.695 g/cm³ (Ishii et al. 1996; Ishii et al. 1995a; Ishii et al. 1995b). (The critical point of CO₂ is at T = 304.1 K and $\rho = 0.467$ g/cm³ (Zhang and Duang 2005).) As it was suggested by these authors, molecular dynamics simulation of CO₂ in these thermodynamic states must adopt a basic cell with each side longer than 40 Å, in order to reproduce roughly 75 % of the total density fluctuations in the system [16], [17] and [18]. Thus, here we have chosen to perform molecular dynamics simulations with N = 864 CO₂ molecules, which correspond to edge lengths of the cubic basic box between 40.703 Å (at T = 250 K) and 51.358 Å (at T = 306 K). An integration time step of 2.5 fs has been used in integrating the equations of motion. The system has been equilibrated for 2 ns, followed by a 0.5 ns long run of data collection at each thermodynamic state point considered.

Among the numerous potential models of CO₂ that can be found in the literature, we have chosen the model of Zhang (Zhang and Duang 2005), which is known to reproduce well a number of experimental data, such as the total radial distribution function, density, diffusion coefficient, etc., in a broad range of thermodynamic states. The critical point of this potential model is also close to the experimental one (Zhang and Duang 2005).

Simulations have been performed along the liquid–gas coexistence curve (Zhang and Duang 2005) at temperatures of 250 K, 270 K, 285 K, 298 K, and 303 K, and along the 94.4 cm³/mol isochore (corresponding to the experimental critical isochore (Zhang and Duang 2005)) at 306 K and 313 K. It should finally be mentioned that, due to large fluctuations occurring at the immediate vicinity (i.e., within 0.5 K) of the critical point, the temperature range between 303 K and 306 K is excluded from our analysis.

Voronoi polyhedra analysis. In a three dimensional system of seeds the Voronoi polyhedra (VP) (Voronoi 1908; N. 2000; Okabe 2000) of a given seed is the locus of the spatial points that are closer to this seed than to any other one. Thus, by calculating the Voronoi tessellation the space can be unambiguously divided between the seeds; the VP of each seed represents the volume element that belongs to this particular seed. In applying the Voronoi analysis for molecular systems the seeds are evidently the individual molecules; and the volume V of a VP represents the space that is available for its central molecule. Conversely the reciprocal volume of a VP $\rho = 1/V$ can be a measure of the local density around its central particle. The local environment of the molecules can be characterized by the shape of the corresponding VP. To quantify this property Ruocco et al., proposed to use the asphericity parameter η of the VP

(Ruocco, Sampoli, and Vallauri 1992), defined as $\ell\%C$ where S is the total surface area of the VP. The value of η is unity for a perfect sphere, and it becomes larger for less spherical objects.

The VP vertices are generally shared by four polyhedra, and hence they are the points that are equally far from four seeds (molecules), and are closer to these four seeds than to any other one. Thus, making an infinitesimally small step from such a vertex to any direction gets closer at least to some of the nearest seeds. In other words, the VP vertices are the spatial points where the distance of the nearest seed is of local maximum. Consequently, these vertices are the centres of the largest possible elemental spherical cavities (vacancies) that are located between the seeds (molecules), and the radius R of such a vacancy is simply the distance of the corresponding VP vertex from the central seed.

In calculating the Voronoi tessellation in the systems studied the position of each CO_2 molecule has been represented by that of its C atom. Similarly to our previous studies (Jedlovsky and Mezei 2000) and (Idrissi et al. 2008), the VP of the molecules have been determined using the algorithm of Ruocco et al. (Ruocco, Sampoli, and Vallauri 1992). The volume and total surface area of the VP have been calculated as described in the following papers (Jedlovsky and Mezei 1999; Jedlovsky and Mezei 2000; Okabe 2000).

In order to characterize the local structure of the CO_2 molecules along the liquid–gas coexistence curve and along the critical isochore we have calculated the volume, density, and asphericity parameter of the VP of the molecules as well as the radius of the spherical vacancies located among the molecules. Although we have also calculated several topological properties of the VP, such as the number of their vertices and faces, these properties are not included in the following discussion, because they have been found to be insensitive to the details of the local structure (see Table 3.1), in accordance with the results of our previous work (Jedlovsky and Mezei 1999) on sub- and supercritical water.

V is the VP volume, ρ is the reciprocal volume of the VP (local density), R is the radius of the elemental spherical vacancies, N_f and N_v are the number of the faces and vertices of the VP.

Results and discussion. Figure 3.12 shows the VP volume distribution, $P(V)$ along the liquid–gas coexistence curve and along the critical isochore. At low temperatures, the $P(V)$ distribution is of Gaussian shape. With increasing temperature, this distribution becomes broader due to the increasing volume fluctuation, and the main peak shifts to higher values due to thermal expansion of the system. More importantly, the shape of the $P(V)$ distribution increasingly deviates from the Gaussian curve, and develops an exponentially decaying tail at high volume values. This behaviour is clearly demonstrated in the inset of Figure 3.12, where the $P(V)$ distribu-

T/K	250	270	285	298	303	306	313
$\langle V \rangle / \text{\AA}^3$	69.7 ± 10.3	77.5 ± 13.8	87.1 ± 19.4	105.3 ± 31.1	114.4 ± 38.2	156.8 ± 68.8	156.8 ± 65.1
$\langle \rho \rangle / 10^{-2} \text{\AA}^{-3}$	1.47 ± 0.21	1.33 ± 0.22	1.20 ± 0.24	1.10 ± 0.26	0.96 ± 0.28	0.73 ± 0.26	0.74 ± 0.26
$\langle \eta \rangle$	1.54 ± 0.09	1.57 ± 0.10	1.60 ± 0.11	1.64 ± 0.13	1.66 ± 0.14	1.73 ± 0.18	1.73 ± 0.18
$\langle N_f \rangle$	14.9 ± 1.7	15.0 ± 1.9	15.1 ± 2.1	15.2 ± 2.4	15.2 ± 2.4	15.3 ± 2.7	15.2 ± 2.8
$\langle N_v \rangle$	5.22 ± 1.24	5.22 ± 1.29	5.22 ± 1.32	5.22 ± 1.36	5.23 ± 1.38	5.23 ± 1.44	5.2 ± 1.5
$\langle R \rangle / \text{\AA}$	3.21 ± 0.37	3.36 ± 0.43	3.54 ± 0.52	3.82 ± 0.68	3.95 ± 0.75	4.47 ± 0.97	4.5 ± 0.97

Table 3.3: Mean values and standard deviations of the properties of the Voronoi polyhedra of the CO₂ system along the liquid–gas coexistence curve (250 K–303 K) and along the critical isochore (306 K–313 K).

tion is shown on a logarithmic scale, and hence the exponential decay of the high volume tail is transformed to a linearly decreasing tail. It should be mentioned that the $P(V)$ distribution is not affected by the increase of the temperature along the critical isochore. The asymmetric shape of the VP volume distribution appears to be ubiquitous in published literature (Ruocco et al. 1993; Jedlovsky and Mezei 1999; Jedlovsky and Mezei 2000; Idrissi et al. 2008; Zaninetti 1992). The main idea in the interpretation of the asymmetric shape of $P(V)$ is that the molecules in the system are organised in more or less separated transient domains, resulting in the transient inhomogeneous distribution of the local densities. The molecules belonging to these dense transient domains contribute to the main peak of the $P(V)$ distribution (reflecting the limited availability of space around such molecules, the motion of which is thus restricted by the packing effect), whereas the molecules belonging to the boundary of these transient domains contribute to the highest volume part of the $P(V)$ distribution. Evidently, also the motion of such molecules is much less restricted.

It is obvious that in this physical picture, the local density around the molecules inside these transient domains is higher than that around the molecules in the boundary region of these transient domains. This fact can be correlated to the behaviour of the reciprocal volume of the VP (i.e., a measure of the local density around the molecules) $P(\rho)$. Indeed, as it is shown in Figure 3.13, at low temperatures this distribution is essentially of Gaussian shape (i.e., it can be sufficiently fitted by a single Gaussian function), indicating that the CO₂ molecules are homogeneously distributed. With increasing temperature the shape of the $P(\rho)$ distribution becomes

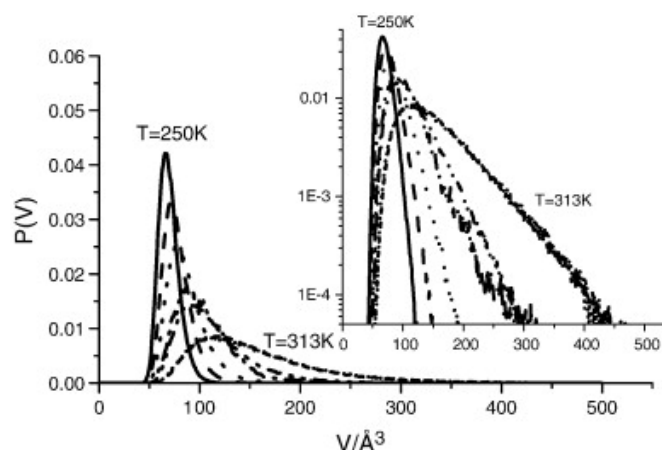


Figure 3.12: VP volume distribution of the CO_2 molecules along the liquid–gas coexistence curve ($250\text{ K} \leq T \leq 303\text{ K}$) and along the critical isochore ($306\text{ K} \leq T \leq 313\text{ K}$). The inset shows the same distributions on a logarithmic scale. Solid lines: 250 K, dashes: 273 K, dots: 285 K, dash–dots: 298 K, dash–dot–dots: 303 K, short dashes: 306 K, short dots: 313 K.

increasingly distorted, in particular, above the temperature of $T = 303\text{ K}$. Nevertheless, the obtained $P(\rho)$ distributions can still be fitted by the sum of two Gaussian functions even at these higher temperatures. To validate this finding we have used three criteria. First, the χ^2 value (χ being the deviation of the calculated distribution and the fitted analytical function at a given point of the distribution) dropped by a factor of at least two above 303 K upon adding a second Gaussian contribution to the fitting function. Second, the correlation matrix showed a significant decrease of correlation between the parameters (the addition of non pertinent parameters generally increases this correlation). Finally, the structure of the residue function (i.e., the difference between the calculated and fitted functions) is found to decrease considerably. Examples of this Gaussian fitting are given in Figure 3.14. In Figure 3.14a the $P(\rho)$ curve obtained at $T = 250\text{ K}$ is fitted by one single Gaussian function, whereas in Figure 3.14b the $T = 303\text{ K}$ curve is fitted by the sum of two Gaussians.

These findings indicate that, starting from the temperature of $T = 303\text{ K}$, besides the main peak of the $P(\rho)$ distribution a second peak develops at its low density side, although these two peaks are not resolved yet in the calculated distributions. The first of these peaks can be associated with the molecules that are in high local density environment, i.e., being inside the high density transient domains, whereas the other peak reflects the low local density around the molecules that belong to the boundary of such transient domains. This behaviour of the VP reciprocal volume distribution is a clear indication that the spatial distribution of the CO_2 molecules becomes increasingly inhomogeneous at the vicinity of the critical point.

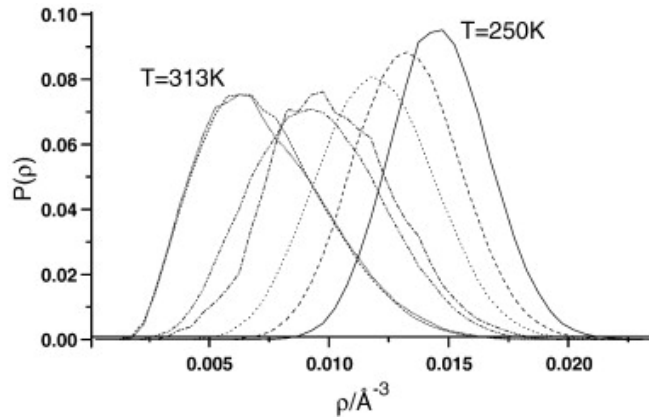


Figure 3.13: VP reciprocal volume (local density) distribution of the CO₂ molecules along the liquid–gas coexistence curve ($250\text{ K} \leq T \leq 303\text{ K}$) and along the critical isochore ($306\text{ K} \leq T \leq 313\text{ K}$). The legend is the same as in Figure 3.12

The $P(R)$ distribution of the radii of the elemental spherical cavities located among the CO₂ molecules (see Figure 3.15) is fully compatible with the above interpretation. Figure 3.15 shows that the $P(R)$ distribution broadens and shifts to larger R values with increasing temperature along the liquid–gas coexistence curve, whereas it is insensitive to the temperature along the critical isochore. Correspondingly, both the average value and the corresponding fluctuation of R increase along the coexistence line, but they remain almost constant along the critical isochore (see Table 1). Furthermore, a linear relation is observed between $\langle R \rangle$ and $\langle V \rangle$, as is clearly demonstrated in Figure 3.16. (The angled brackets $\langle \dots \rangle$ stand here for the mean value of the corresponding distribution.) This finding suggests that the observed shift and broadening of the $P(R)$ function can be traced back to the inhomogeneous distribution of the CO₂ molecules in the system at the vicinity of the critical point. In these cases (i.e., at $T \geq 303\text{ K}$) the low R part of the $P(R)$ distribution can be associated with the vacancies located among the CO₂ molecules inside the high density transient domains, while the appearance of the tail of $P(R)$ at high distances reflects the presence of large voids between the high density transient domains.

The change of the asphericity parameter distribution, $P(\eta)$, along the liquid–gas coexistence curve and along the critical isochore is shown in Figure 3.17. As is seen with increasing temperature the $P(\eta)$ distributions shift to higher values and become broader. This is also seen from the increase of the corresponding average values $\langle \eta \rangle$ and standard deviations (see Table 1). A careful inspection of the shape of the $P(\eta)$ distributions reveals that the temperature has a much larger effect at the high value side of its main peak than at its low value side. Following the interpretation of Ruocco et al. (Ruocco, Sampoli, and Vallauri 1992), the high value side of the $P(\eta)$ peak is associated with rather aspherical local arrangements of the neighbouring molecules,

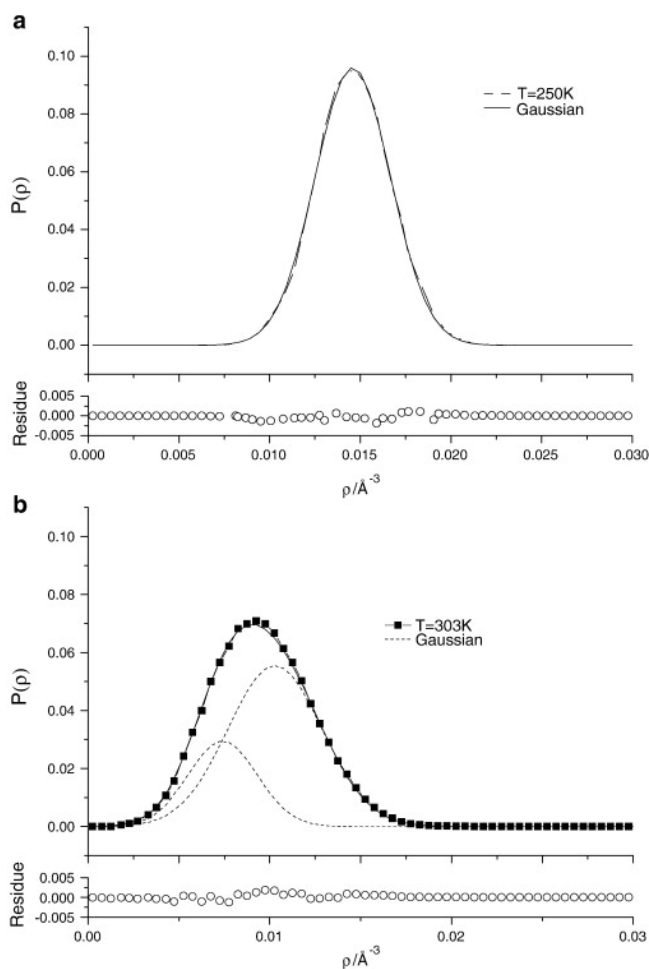


Figure 3.14: Illustration of the fitting of the obtained VP reciprocal volume distributions by Gaussians. (a) Data obtained at 250 K fitted by one single Gaussian. (b) Data obtained at 303 K fitted by the sum of two Gaussians. The simulation data and the fitting curve are shown by squares and solid line, respectively. The two elemental Gaussians are shown by dashed lines in b. The residue of the fitting (i.e., the difference of the data and the fitting function) is shown by open circles at the bottom of the figures.

and thus can be ascribed to those molecules belonging to the boundary of the high density transient domains, while the molecules located inside these transient domains contribute to the small value side of $P(\eta)$. Our finding indicates that the increase of the temperature increases the inhomogeneous character of the system as it makes the density fluctuations larger (and hence makes the local environment of the molecules at the boundary of the high density transient domains more and more

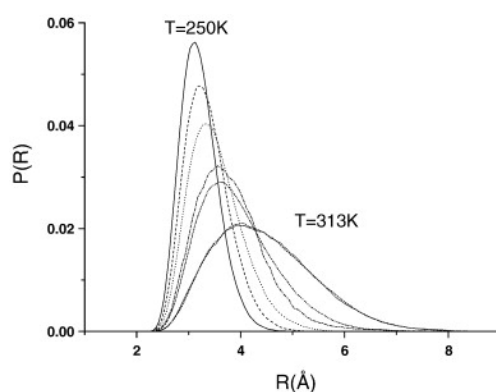


Figure 3.15: Distribution of the radius of the elemental spherical vacancies among the CO_2 molecules along the liquid–gas coexistence curve ($250 \text{ K} \leq T \leq 303 \text{ K}$) and along the critical isochore ($306 \text{ K} \leq T \leq 313 \text{ K}$). The legend is the same as in Figure 3.12.

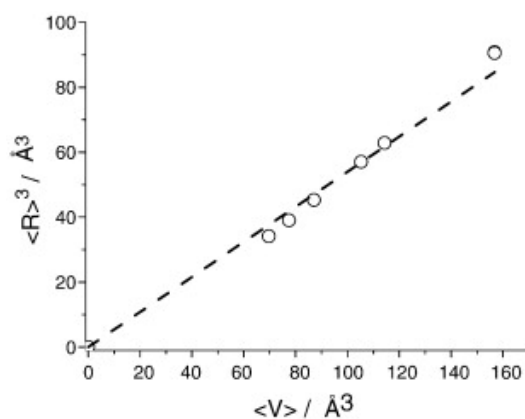


Figure 3.16: Correlation between the mean VP volume of the CO_2 molecules $\langle V \rangle$ and the cube of the mean radius of the elemental spherical vacancies among the molecules $\langle R \rangle^3$. The open circles show the calculated data point, whereas the dashed line is the straight line fitted to these data.

distorted), but it leaves the local structure inside these transient domains largely unchanged.

Conclusions. In this section we have presented a Voronoi polyhedra analysis of the local structure of CO_2 along the liquid–gas coexistence curve and along the critical isochore. Several properties (such as volume, local density, asphericity, radius of the elemental vacancies) associated with the Voronoi polyhedra have been calculated. The behaviour of these properties provided some insight into the changes of the local

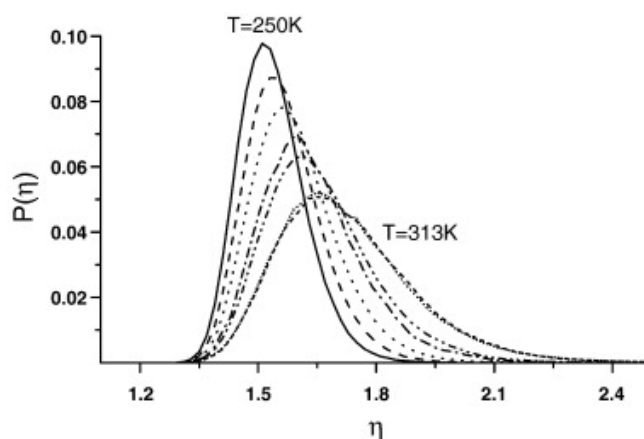


Figure 3.17: VP asphericity parameter distribution of the CO₂ molecules along the liquid–gas coexistence curve ($250 \text{ K} \leq T \leq 303 \text{ K}$) and along the critical isochore ($306 \text{ K} \leq T \leq 313 \text{ K}$). The legend is the same as in Figure 3.12.

structure with increasing temperature at the vicinity of the critical point. Thus, our results clearly indicate that upon approaching the critical isochore the distribution of the CO₂ molecules in the system becomes more and more inhomogeneous. This behaviour is evidenced by the development of a long, exponentially decaying tail of the VP volume distribution at high values, by the fact that the VP reciprocal volume (local density) distribution becomes the sum of two Gaussians of comparable amplitudes, and finally by the asymmetric broadening of the VP asphericity distribution.

3.1.2 Local structure and dynamics in supercritical ammonia

Investigation of the Local Structure in Sub and Supercritical Ammonia Using the Nearest Neighbor Approach: A Molecular Dynamics Analysis

Ammonia molecule (NH₃) has widespread use in many industrial sectors and is one of the most highly produced chemicals in the world (Ullmann 2003). Main uses are in industrial refrigeration systems, as well as in fertilizer, explosives, chemicals production (Wada et al. 2001; Desmoulins-Krawiec et al. 2004), and more recently in the CO₂ capture technology (Darde et al. 2009; Martin et al. 2007). By the same token, supercritical ammonia has been shown to provide advanced technological processes (such as separation, chemical reaction, material processing, waste treatment, plastic recycling, and others) (Darr and Poliakoff 1999). Although liquid ammonia has been the subject of numerous investigations both using experimental X-rays (Narten 1977; Sette et al. 2000; Giura et al. 2007), neutron scattering (Bausenwein et al. 1994; Chieux and Bertagnolli 1984; Thompson et al. 2003), infrared, Raman scattering (Buback and Schulz 1976; Schwartz and Wang 1973; Bradley, Zerda, and

Jonas 1985), nonlinear transient spectroscopy(Schafer et al. 2008) and theoretical simulations(Nelson, Fraser, and Klemperer 1985; Boese et al. 2003; Tongraar, Kerdcharoen, and Hannongbua 2006; Kiselev et al. 2000; Janeiro-Barral and Mella 2006; Spirko 1983; Spirko and Kraemer 1989; Rajamäki et al. 2004), a detailed understanding of the molecular structure of supercritical ammonia is still lacking. We then believe that some special features of supercritical ammonia are relevant to the understanding of supercritical phenomena. Indeed, NH_3 is a simple molecule where a subtle balance between hydrogen bonding and van der Waals interactions is expected to provide some peculiarities of its structure and dynamics in the supercritical domain. Understanding the local structure is one of the fundamental and essential problems for the successful use of supercritical technology using ammonia(Schafer et al. 2008; Kiselev et al. 2000). These considerations prompt us to characterize the change in the local structure of ammonia from the liquid state up to the supercritical fluid by means of molecular dynamics simulations. Indeed, computer simulations provide deep insight on the local structure and a successful use of this technique is based on two steps: the first one consists in the development of accurate potential model where the parameters are adjusted to available experimental data. The second step is to choose the adequate molecular simulation technique to estimate physical properties as efficiently as possible. Using computer simulations, the radial distribution function is a major means by which structure is usually described in fluids systems. However, this statistical property does not provide sufficient details on the nature of the local environment in terms of first-, second- or higher-order neighbors distributed around a central particle in fluids. In fact, even in cases where the dynamics differs by many orders of magnitude, the radial distribution function may reveal only minor differences. Indeed, the changes in the structure may occur at a level of nearest neighbors and averaging through the whole space volume reduces the effect of the change of thermodynamic conditions (pressure, temperature, etc.). Therefore to describe the change in the local structure, it is necessary to introduce statistical functions that are evaluated over small space volume. These statistical functions include the distribution of Voronoi polyhedra(Lavrik and Voloshin 2001), the mutual arrangement of Delaunay simplices(Medvedev, Geiger, and Brostow 1990), and the neighborhood approach(Mazur 1992; Keyes 1999; Bhattacharjee 2003; Simon, Dobrosavljevic, and Stratt 1991).

The purpose of this section is then to report molecular dynamics simulation investigations on the local structure in sub- and supercritical ammonia using the nearest neighbor approach. We started this work by the inspection of six simple interaction potential models of ammonia reported in the literature. The essential criterion that was adopted in the selection of these models is the simplicity of the expression of the intermolecular interaction potential. They are written in terms of a Lennard-Jones pair potential between atomic sites, plus a Coulomb interaction between dis-

tributed partial charges. Liquid gas-coexistence curve, critical temperature, densities, energies, and structural data (radial distribution functions) have been calculated for all models, and compared with the corresponding experimental data. These comparisons allow a classification of the different models in terms of their relative agreement with experimental data, particularly those properties of fluid ammonia near the critical point and under the supercritical conditions. After choosing the adequate potential model, we have investigated the local structure by analyzing the nearest neighbor radial distributions. The signature of the hydrogen bonding along the thermodynamic point considered here is discussed as well as the mutual orientation between ammonia molecules. Finally a conclusion is given.

Simulation Methodology.

Gibbs Ensemble Monte Carlo. To evaluate the liquid–gas coexistence curve and critical parameters for the different potential models, we performed Gibbs Ensemble Monte Carlo simulations (GEMC). This technique allows one to obtain the liquid–gas coexistence curve directly from the Monte Carlo run. Practically, two simulation boxes corresponding to the liquid and to the gas phase are considered. Standard Monte Carlo moves that include the center of mass translations, rotation around randomly chosen axes, are supplemented by trial moves that swap molecules between boxes and change volume of boxes. They are performed in such a way that overall volume of the boxes and the total number of molecules are kept constant. After several Monte Carlo cycles, one obtains the density corresponding to the liquid state in one box and the density of the gas in the other one. One can find a comprehensive description of this method in the original paper by Panagiotopoulos (Panagiotopoulos 1987) or in general courses on molecular simulations (Frenkel and Smith 2001). In this work, Monte Carlo simulations have been performed using the program Towhee (<http://towhee.sourceforge.net>). In each simulation step, a randomly chosen molecule has been randomly translated by no more than 0.5 Å and has been randomly rotated around a randomly chosen-fixed axis by no more than 0.05 radians, the probability of performing of the box interchanging move was chosen equal to 0.01. The edge length of the basic simulation boxes L1 (liquid density) and L2 (gas density) have been set in accordance with the experimental densities of liquid and gaseous ammonia respectively (Lemmon, McLinden, and Friend 2005). All interactions have been truncated to zero beyond the center–center cutoff distance of 12.5 Å. The long-range part of the electrostatic interaction has been accounted for using Ewald summation technique (Allen and Tildesley 1987). The system has been equilibrated by performing 50 000 Monte Carlo cycles. The production runs last 50 000 Monte Carlo cycles each.

Molecular Dynamics Simulations. After choosing the adequate potential model, molecular dynamics simulations of the NH_3 system has been performed in the isothermal-isobaric (N,P,T) ensemble at 135 bar and for the following temperatures 250, 300, 350, 380, 390, 394, 398, 400, 402, 406, 410, 420, 440, 460, and 500 K. The cubic simulation boxes contain 864 molecules. Standard periodic boundary conditions have been applied. All the models used here are the combination of the simple Lennard-Jones potentials with electrostatic potentials. The total potential thus writes where $r_{i\alpha j\beta}$ is the distance between a site α of molecule i and a site β of molecule j , $q_{i\alpha}$ is the charge on site α of molecule i , $q_{j\beta}$ is the charge on site β of molecule j . σ and ϵ are the LJ parameters. The simulations have been performed using the DL_POLY program (Smith and Forester 1996). The temperature and pressure of the systems have been kept constant by means of the weak coupling algorithms of Berendsen (Berendsen et al. 1984), using the coupling parameter values of 0.1 ps (temperature) and 0.5 ps (pressure). All site-site interactions have been truncated to zero beyond the center-center cut-off distance of 12.5 Å. The long-range part of the electrostatic interactions has been accounted for using the Ewald summation method. The equations of motion have been integrated using the leapfrog algorithm, employing an integration time step of 2 fs. The systems have been equilibrated by generating 5 ns long trajectories for each. Then, the production stage lasts 800 ps (400 000 configurations). The coordinates of molecules were stored each 8 fs and were used to calculate the relevant statistical properties.

Models of Ammonia. We have chosen to study six rigid potential models of ammonia proposed in the literature. The essential criterion we have adopted in the selection of the models is the simplicity of the expression for the intermolecular potential. The models we have selected were those written entirely in terms of a Lennard-Jones pair potential and Coulomb interaction between partial charges. Among the models that satisfy this criterion, we have chosen those proposed by (Impey and Klein 1984) and (Ferrario et al. 1990). They were developed to predict structural properties of liquid ammonia and are then good for describing of the experimental radial distribution functions and structure factors. At the same time, they fail to predict the thermodynamic parameters of the ammonia closely to the critical point and along liquid-gas coexistence curve (CC) in general. The model proposed by (Gao, Xia, and George 1993) was developed from pure quantum chemical considerations to take into account the bimolecular interactions and was reported to well predict the structure of the liquid ammonia and particularly the hydrogen bonds distribution. We have also used other recently developed potential models by (Kristof et al. 1999) which parameters were adjusted to reproduce the liquid-gas coexistence curve by means of the Grand Canonical Ensemble Monte Carlo simulations. However no molecular dynamics simulations using these models were reported.

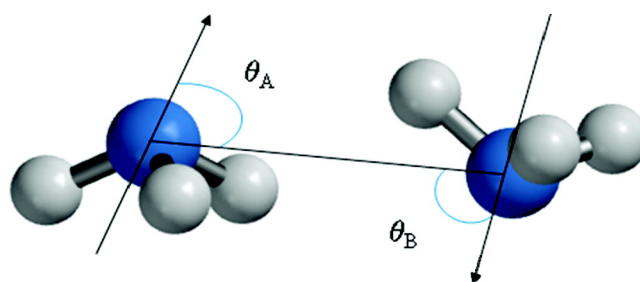


Figure 3.18: Pictorial representation of the orientation between a reference ammonia molecule and its first nearest neighbor. The angles θ_A is that between the molecular axis and that joining the nitrogen atoms of the two molecules. The angles θ_B is that between the neighbor molecular axis and that joining the nitrogen atoms of the two molecules.

In the remainder of the section, we use the following acronyms for the various ammonia models: IK for the model proposed by (Impey and Klein 1984) FHMK for the model proposed by (Ferrario et al. 1990), GXG for the model proposed by (Gao, Xia, and George 1993) and KRI1, KRI2, and KRI3 for the potential models proposed by (Kristof et al. 1999). It is worthy to mention that in the five-sites models (IK, FHMK, and KRI2), one additional site is introduced along the molecular axis between the nitrogen atom and the hydrogen atoms plane. The parameters of the six potentials models of ammonia are given in Table 3.4.

HNH is the angle between the NH axes of ammonia while HNM is the angle between the NH axis and that joining the N atom to the virtual site M; μ is the dipole moment.

Results and Discussion.

Structure. There are several experimental data available from X-ray diffraction (Narten 1977) and neutron scattering (Ricci et al. 1995) on ammonia and it is possible to establish the validity of a chosen potential model by comparing the calculated radial distribution function (rdf) and the experimental one. We compare in Figure 3.19a–c the calculated partial rdfs $g_{NN}(r)$, $g_{NH}(r)$, and $g_{HH}(r)$ with experimental ones measured at 273 K. It can be seen that all models have reasonable agreement with experiment. The shoulder in the $g_{NN}(r)$ at 2.7 Å is not reproduced by any model considered in the present study. But to our knowledge, no one could reproduce this feature even using such sophisticated methods as DFT, QM/MM, and path-integral molecular dynamics (Boese et al. 2003; Diraison, Martyna, and Tuckerman 1999). One should also mention that there is no contribution at this distance in the obtained $g_{NN}(r)$ from the X-ray experiment. The first solvation shell defined by the first minimum of $g_{NN}(r)$

site	ϵ (kcal)	σ (Å)	q(e)	r_{NH} (Å)	HNH	r_{NM} (Å)	HNM	μ (D)	acronyms
N	0.278	3.4	0	1.0124	106.7	0.156	67.8	1.50	IK ^{a)}
M	0	0	-1.386						
H	0	0	0.462						
N	0.278	3.4	0	1.0127	110.96	0.156	67.8	1.50	FHMK ^{b)}
M	0	0	-1.455						
H	0	0	0.485						
N	0.210	3.36	-1.026	1.0124	106.7			1.88	GXG ^{c)}
H	0	0	0.342						
N	0.348	3.4	-1.050	1.0124	106.7			1.92	KRI1 ^{d)}
H	0.35	0	0.350						
N	0.368	3.37	-1.275	1.0124	106.7	0.191	67.8	1.95	KRI2 ^{d)}
M	0	0	0.420						
H	0	0	0.285						
N	0.338	3.39	-1.035	1.0124	106.7			1.90	KRI3 ^{d)}
H	0	0	0.345						

Table 3.4: Geometrical and Energetical Parameters of the Six Potential Models of Ammonia

a. (Impey and Klein 1984)

b. (Ferrario et al. 1990)

c. (Gao, Xia, and George 1993)

d. (Kristof et al. 1999)

	IK	FHMK	GXG	KRI1	KRI2	KRI3	experiment ^a
T_C (K)	347	375	346	390	399	400	405.4
ρ_C (g/cm ³)	0.225	0.240	0.235	0.225	0.236	0.218	0.225

Table 3.5: Comparison between the Calculated Critical Temperature, T_C and Critical Density, ρ_C and the Corresponding Experimental Values

a. Lemmon, Mclinden, and Friend 2005.

contains 12–13 ammonia molecules. The peaks at distance less than 2 Å in the experimental NH and HH rdfs, correspond to the intramolecular contribution and of course cannot be seen from the MD simulations with rigid potential model. $g_{NH}(r)$ rdf has a noticeable shoulder at 2.25 Å that was considered to be a fingerprint of the hydrogen bonding in liquid ammonia (Ricci et al. 1995). This peak is more resolved for IK and FHMK potential models. Integration of this shoulder gives less than one hydrogen bond per one ammonia molecule (Ricci et al. 1995).

Liquid–Gas Coexistence Curve. To qualify one of the potential models for further analysis, we have also compared the calculated and experimental liquid–gas coexistence curves (CC). We have then performed Monte Carlo simulations in the Grand Canonical Ensemble using the Towhee program package (<http://towhee.sourceforge.net>). To calculate the critical density, ρ_C , and the critical temperature, T_C , the obtained T – ρ coexistence curves were fitted to the law of rectilinear diameters (2.27) and to the scaling law (2.28). The comparison between the experimental and calculated liquid–gas CC is drawn in Figure 3.20. It is obvious to notice that the KRI1, KRI2, KRI3, and IK models reproduce quite well the highest density side of the liquid state as well as the lowest density of the gas state. The FHMK and GXG potential models fail to reproduce the density of the liquid state of ammonia. As the temperature increases along the liquid–gas CC, the KRI1, KRI2, and KRI3 models give density values which are close to the experimental ones. Furthermore, the calculated critical temperature and the critical density are compared with the corresponding experimental values in Table 3.5. As one can see the IK, GXG, and FHMK models predict critical temperatures that are far from the experimental one compared with those predicted by KRI1, KRI2, and KRI3 potential models.

A good agreement was found between the experimental and calculated values using the KRI3 for quantities such as density, (Lemmon, Mclinden, and Friend 2005) thermal expansion (Lemmon, Mclinden, and Friend 2005) and diffusion coefficient (O’Reilly, Peterson, and Scheie 1973). We then chose to carry the analysis of the local structure of ammonia along the isobar 135 bar using the KRI3 potential model.

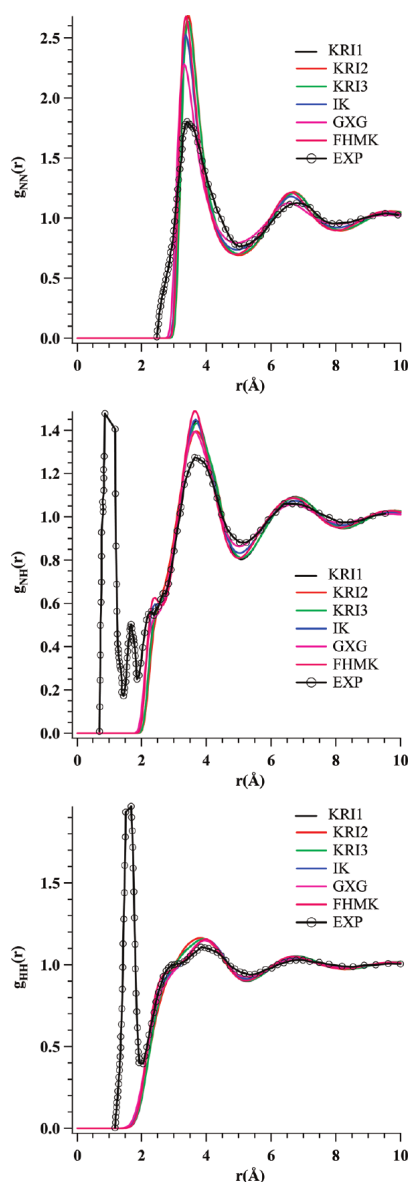


Figure 3.19: Comparison between the calculated radial distribution functions (top) $g_{NN}(r)$, (middle) $g_{NH}(r)$, and (bottom) $g_{HH}(r)$ with experimental ones measured at 273 K (Ricci et al. 1995).

Nearest Neighbor Radial Distributions. First we start by analyzing the connection between the $g_{NN}(r)$ and $g_{NH}(r)$ rdfs and the corresponding nearest neighbor radial distributions. The nearest neighbor radial distributions $p_{NN}(n, r, T = 250 \text{ K})$ and $p_{NH}(n, r, T = 250 \text{ K})$ are shown in , panels a and b, respectively. One can see here that up to the first minimum in the NN and NH rdfs, these functions are well repro-

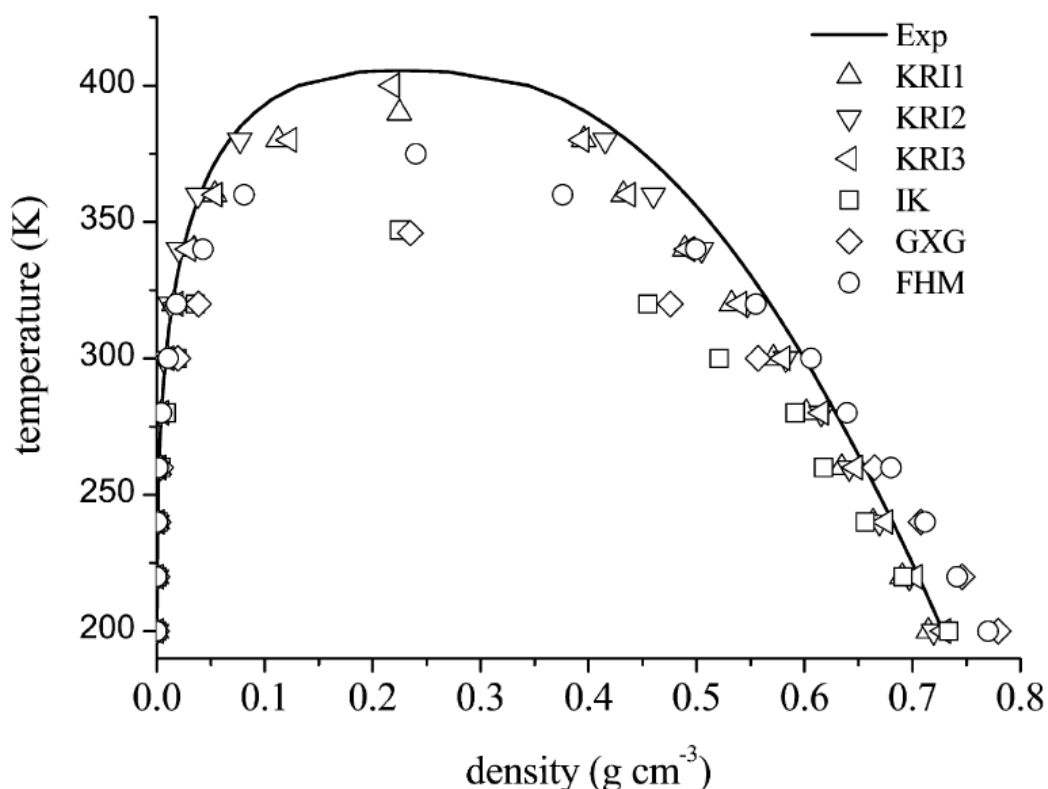


Figure 3.20: Comparison between the experimental and the calculated liquid-gas coexistence curves for the six potential models used in our simulations.

duced by the sum of the nearest neighbor radial distributions. The advantage of this approach can already be shown here. Indeed, as shown in Figure 3.22, the shoulder in the $g_{NH}(r)$ rdf at 2.25 Å is associated with the radial distribution contribution of the first nearest hydrogen atom to the nitrogen atom. Furthermore, the $p_{NH}(n=1, r, T=250\text{ K})$ distribution may be resolved in two contributions at distances $d1 = 2.40\text{ Å}$ and $d2 = 2.91\text{ Å}$. Using DFT calculations implemented in Spartan package(), we optimized the dimer geometry of two ammonia molecules under the constraints that the intermolecular distance between the nitrogen atoms of the two molecules is equal to $r_{N-N}(n=1, T=250\text{ K}) = 3.28\text{ Å}$ and that the intermolecular distance between nitrogen and one of the hydrogen atoms is equal to $d1$. The optimized geometry clearly shows that the intermolecular distance between the nitrogen and another hydrogen is equal to 2.92 Å, which may be associated with the contribution at $d2$ in $p_{NH}(n=1, r, T=250\text{ K})$.

Figure 3.22 shows that as the temperature increases, the contribution at short distance, $d1$ is drastically reduced indicating a weakening of hydrogen bond and the

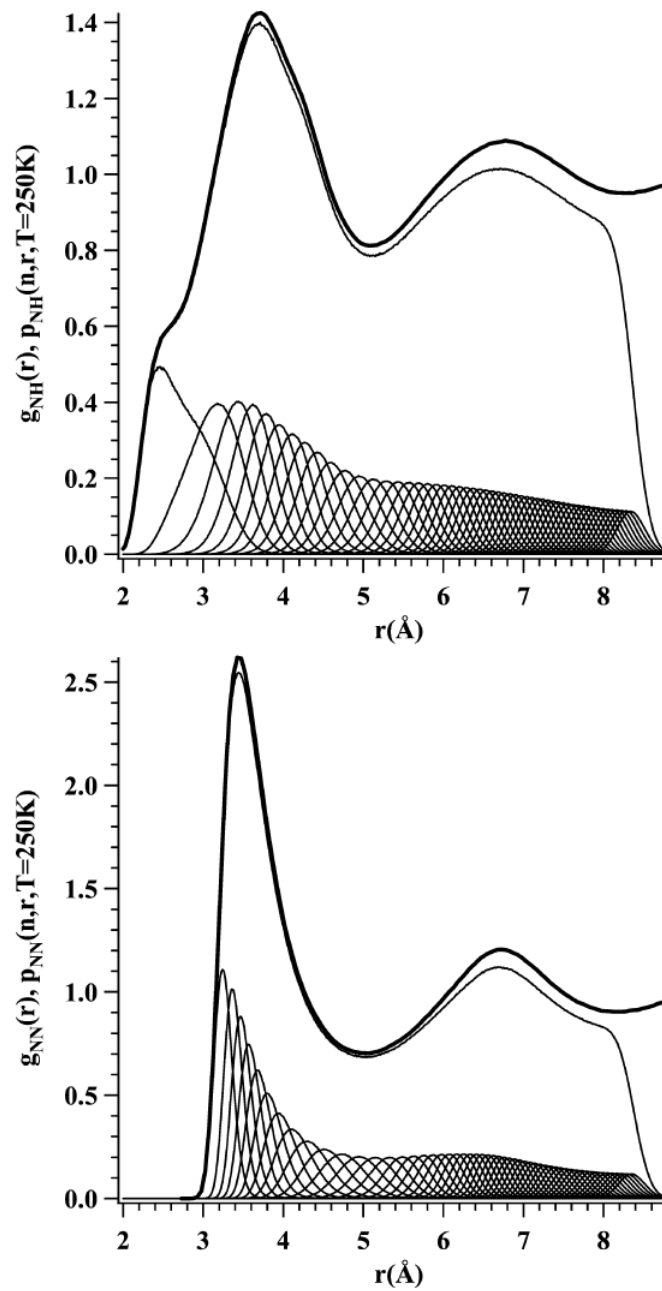


Figure 3.21: Nearest neighbor radial distributions for $n = 1-54$ (top) $g_{NN}(r)$, and $p_{NN}(n, r, T = 250 \text{ K})$ and (bottom) $g_{NH}(r)$ and $p_{NH}(n, r, T = 250 \text{ K})$. The sum $\sum_{i=154} p_{NN}(n, r, T)$ and $\sum_{i=154} p_{NH}(n, r, T)$ are also presented.

$p_{NH}(n = 1, r, T)$ distributions are then characterized by the occurrence of a large peak

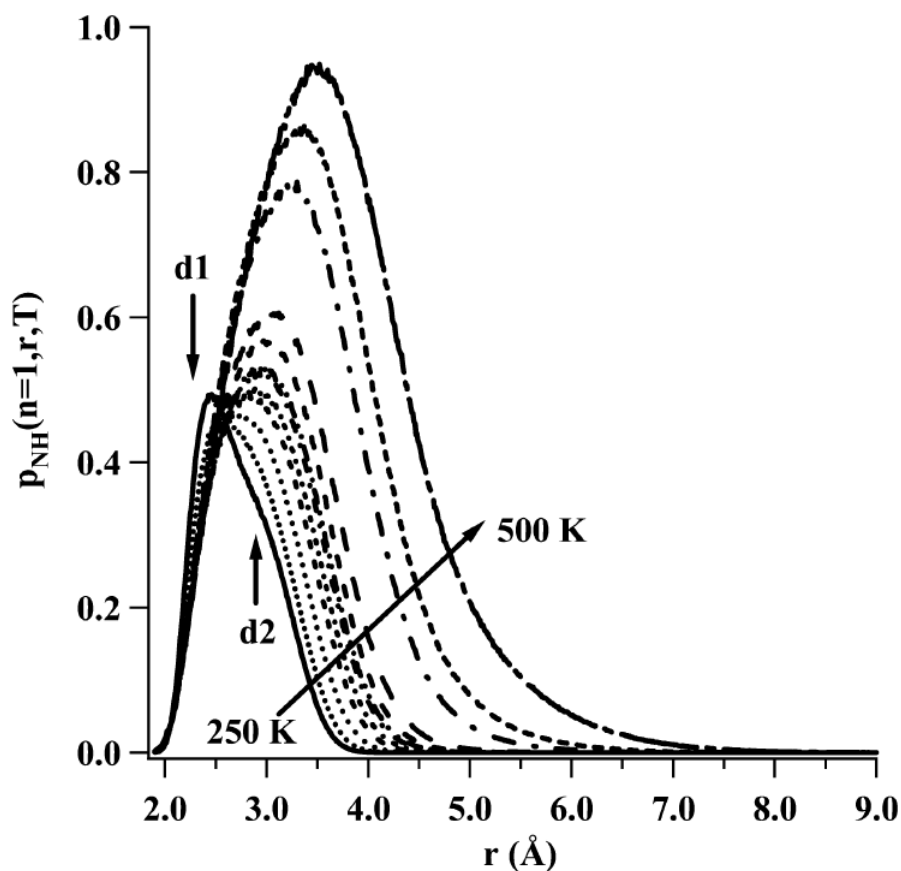


Figure 3.22: First nearest neighbor radial distributions $p_{NH}(n = 1, r, T)$ calculated along the isobar 50 bar and at various temperatures in the range between 259 and 500 K. The arrows indicate the position of the main contributions at distance $d1$ and $d2$ (see text).

centered at larger distance (higher than 3 Å). If we rely on the definition that the hydrogen bonding between an hydrogen atom and X atom is considered as weak when the $H \cdots X$ distance is typically between 2 and 3 Å (Jeffrey 1997), our results indicate that at higher temperature than 300 K the hydrogen bonding in ammonia may be considered as weak. To reinforce this conclusion, we have calculated the total interaction energy distributions, $p_{UTot}(n = 1, T)$ as well as the electrostatic $p_{UEI}(n = 1, T)$ and Lennard-Jones $p_{ULJ}(n = 1, T)$ contributions between a reference ammonia molecule and its first nearest neighbor. The corresponding average values are given in Figure 3.23. These results show that the weakening of the hydrogen bonding may be correlated with the balance between the rate of decrease of both the repulsive character of the LJ interactions and the attractive character of the electrostatic inter-

actions. These results also suggest that to analyze the signature of hydrogen bonding in ammonia using techniques (such as vibration spectroscopy, NMR, etc.) that probe the local structure one should carry the experiments in the range of temperature below 300 K.

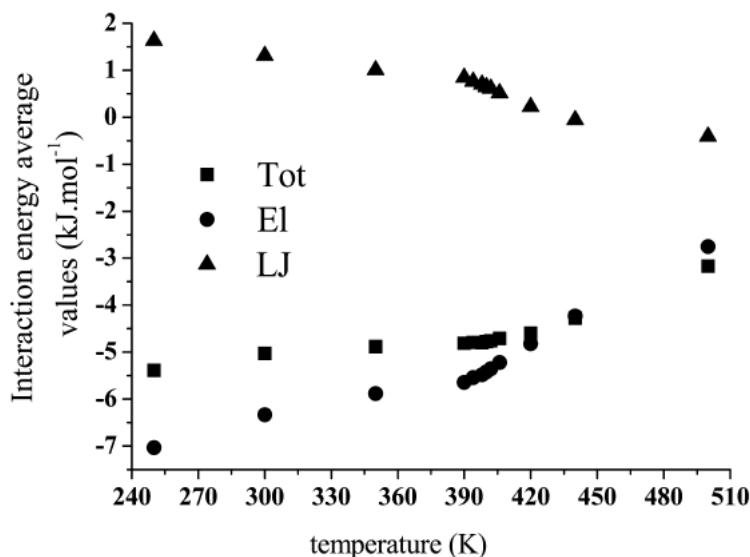


Figure 3.23: Average values of the interaction energy between a reference ammonia molecule and its first nearest neighbor, as a function of temperature.

At low temperature, the well-defined first minimum of the $g_{NN}(r)$ rdf defines the spatial extension of the first solvation shell and the integration of $g_{NN}(r)$ at this position gives the number of molecules (coordination number) in the first solvation shell. As the temperature increases, the position of the first minimum is not clearly defined (see Figure 3.25). The nearest neighbor approach allows to overcome this difficulty. Indeed the superimposition of the $g_{NN}(r)$ and $\Delta r_{N-N}(n, T = 250 \text{ K})$ (as a function of $r_{N-N}(n, T = 250 \text{ K})$) shows that the maximum of $\Delta r_{N-N}(n, T = 250 \text{ K})$ occurs in the region of the first minimum of $g_{NN}(r)$ (see Figure 3.25).

It is very interesting to note that such behavior was observed for other liquid systems such as water, carbon dioxide, acetone (Idrissi, Damay, and Kiselev 2007; Idrissi et al. 2009a; Idrissi et al. 2010). Therefore, the position of the maximum of $\Delta r_{N-N}(n, T = 250 \text{ K})$ provides a useful technique to find the border of the first solvation shell in fluids. We have plotted in Figure 3.26 the behavior of the average distance to each neighbor $r_{N-N}(n, T)$ and in Figure 10 the fluctuations of distance that are available for this neighbor $\Delta r_{N-N}(n, T)$. It can be seen that the increase of the average distance has a nonlinear character which is more pronounced at low temperatures. This feature is clearly seen in the behavior of the derivative of $r_{N-N}(n, T)$ with respect to n (see the inset of Figure 3.26). For instance, the derivative of $r_{N-N}(n, T)$ has a maximum

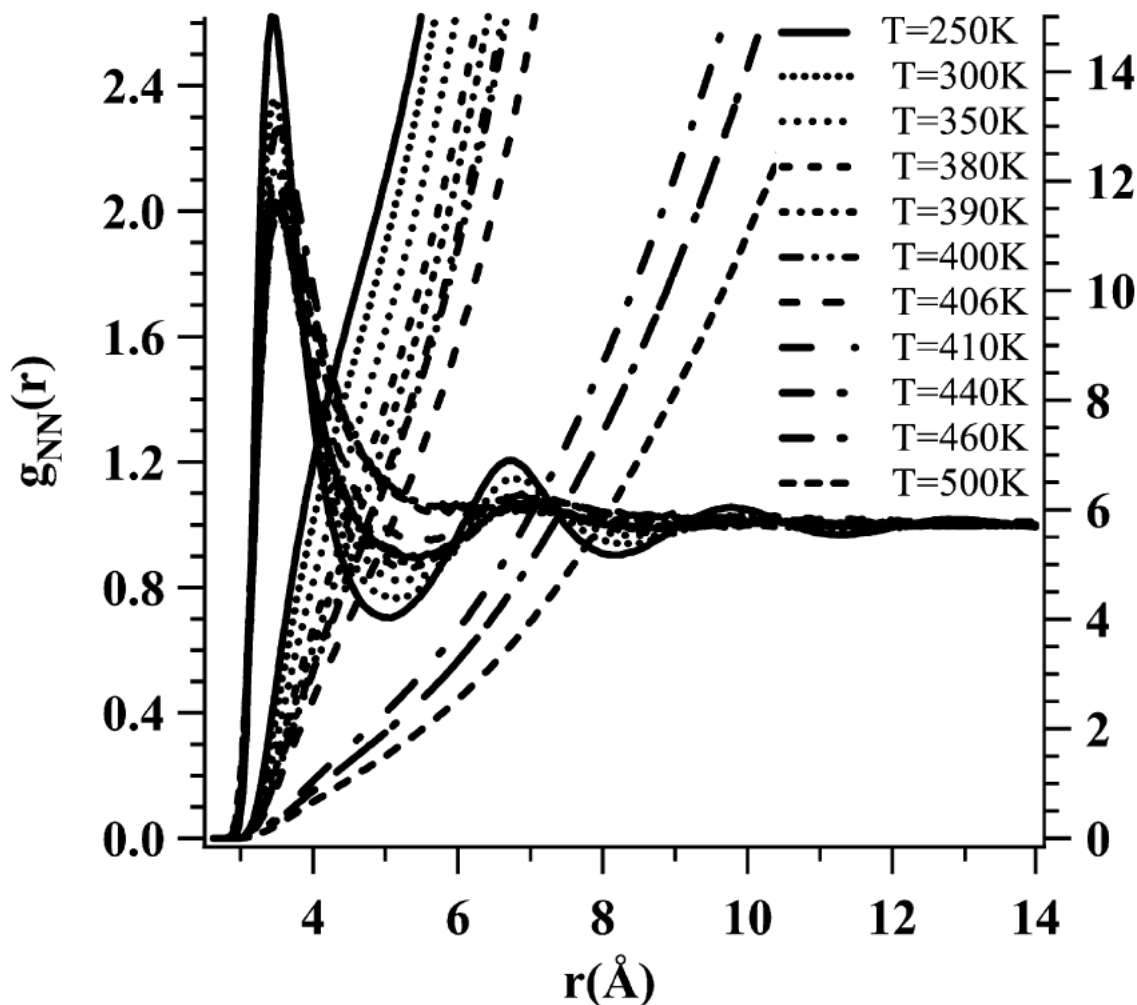


Figure 3.24: Radial distribution functions $g_{NN}(r)$ and coordination number (right axis) at various temperatures along the isobar 135 bar.

for the 11th nearest neighbor and the minimum for the third nearest neighbor. This behavior reflects the fact that the rate of increase of the average nearest neighbor distance with respect to the number of the neighbor depends on the local number density of the molecules in this region. For small n values (close nearest neighbors), the decrease of this rate (particularly the position of its minimum) is associated with high density regions and then with the dominance of the attractive component of the total interaction energy and the increase of this rate indicates the opposite situation. As the temperature increases along the isobar 135 bar, the minimum in the rate of increase of $r_{N-N}(n,T)$ disappears completely near the critical temperature (see

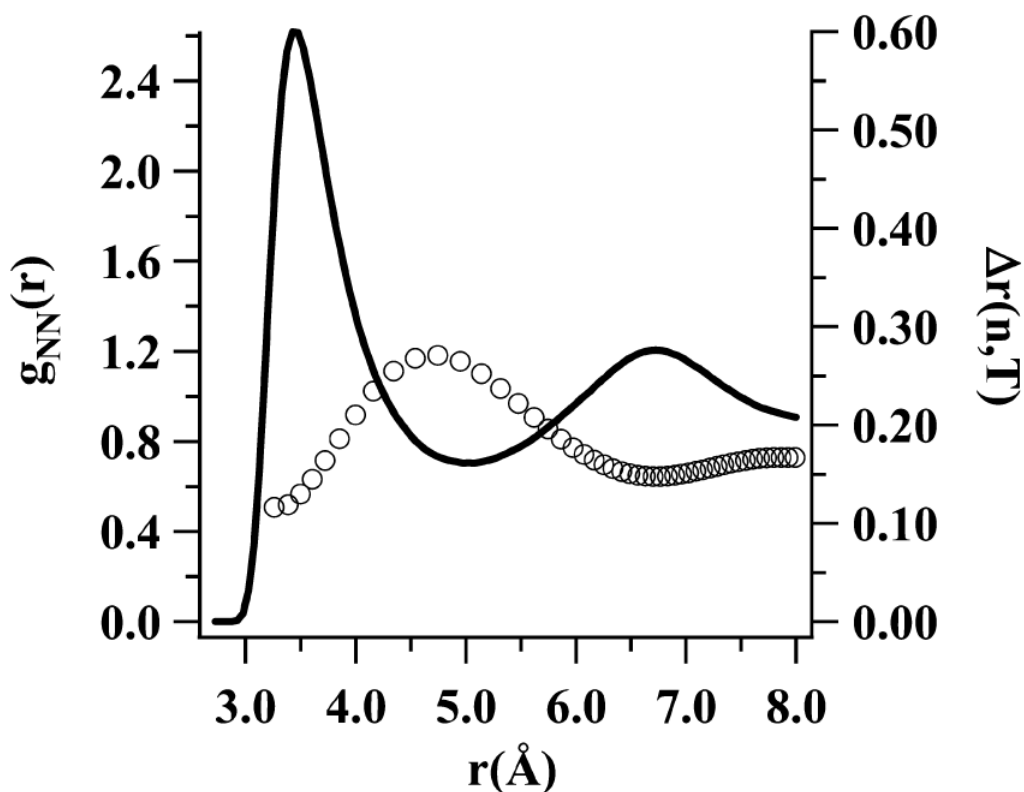


Figure 3.25: Radial distribution function $g_{NN}(r)$ and the fluctuations of distance of the nearest neighbors $\Delta r_{N-N}(n, T = 250 \text{ K})$.

the inset of Figure 3.26) indicating that the total interaction energy becomes less attractive. Furthermore, for higher temperatures, the rate of increase has a plateau shape indicating that these nearest neighbors are experiencing a homogeneous density distribution. At large n values, the rate of increase is almost the same for all the temperatures suggesting that a reference ammonia molecule sees these neighboring molecules randomly distributed.

An important role in the description of the nearest neighborhood of the reference molecule is given by the fluctuations of the average distances that describe the deviations of the distance between the reference molecule and its nearest neighbor from its average value. The effect of temperature on this parameter is given in Figure 3.27. The position of the maximum which defines the spatial extent of the first solvation shell shifts to occur for close nearest neighbors. The number of molecules in the first solvation shell then decreases from 11 to 7 near the critical temperature and down to only 5 for the highest temperatures considered here. The spatial extent of the first solvation increases from 4.7 to 6.5 \AA . The large gap in the behavior of $\Delta r_{\alpha-\beta}(n, T)$ near the critical temperature is associated with the maximum of the thermal expansion.

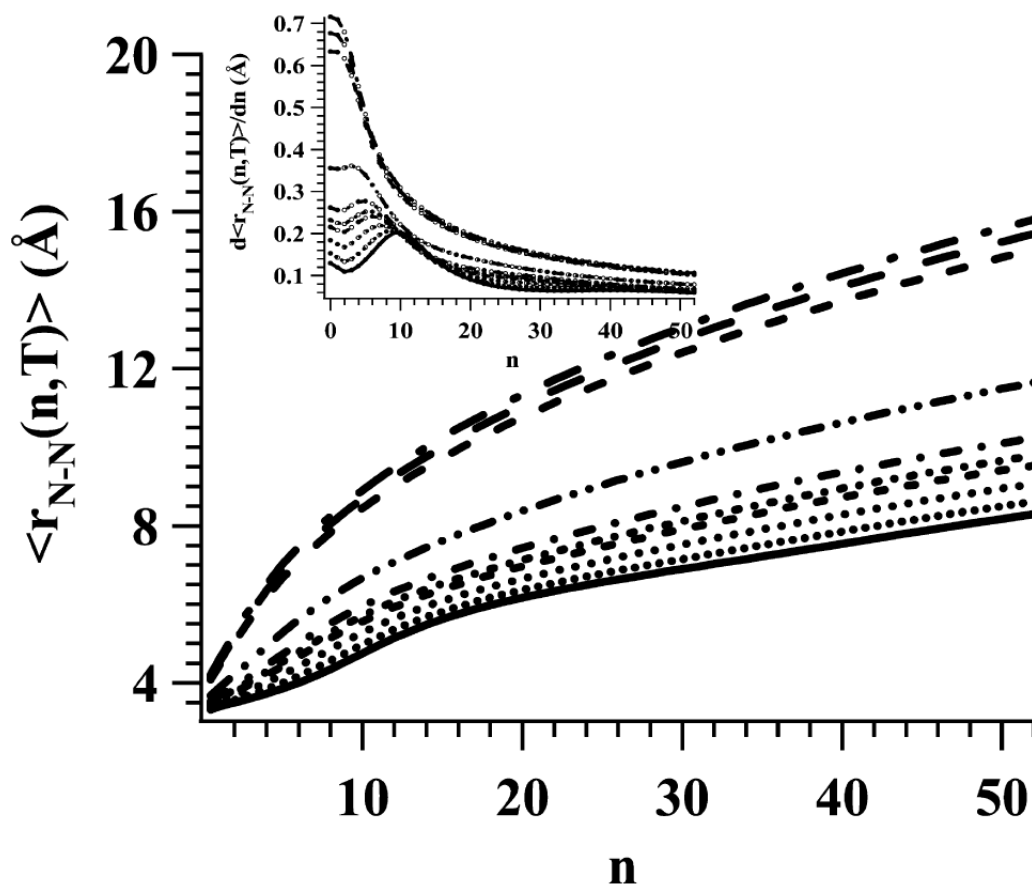


Figure 3.26: Average distance, $r_{N-N}(n, T)$, between a reference ammonia molecule and its nearest neighbors, n , along the isobar 50 bar and in the range of temperature between 250 and 500 K. The derivative of $r_{N-N}(n, T)$ with respect to n is given in the inset.

Nearest Neighbor Orientational Distributions. subsection 2.4.2 Previous findings (Gao, Xia, and George 1993) emphasize the importance of a detailed description of mutual orientation of the dimer of ammonia molecules to check the validity of the intermolecular potential model. We have used the nearest neighbor approach to analyze the mutual orientation distribution $P(\theta_A, \theta_B, n, T)$ between a reference ammonia molecule and its nearest neighbor. The angles θ_A and θ_B are defined in Figure 3.43. These distributions are depicted in Figure 3.28 for $T = 250, 380, 410$ and 500 K. The peaks positions of $P(\theta_A, \theta_B, n = 1, T = 250$ K) are at the values of $\theta_A = 40, 115^\circ$ and $\theta_B = 115, 40^\circ$ (the average distance $r_{N-N}(n = 1, T = 250$ K) = 3.26 Å).

The equilibrium geometry of the ammonia dimer has been the subject of a considerable body of experimental and theoretical studies and is then a subject of con-

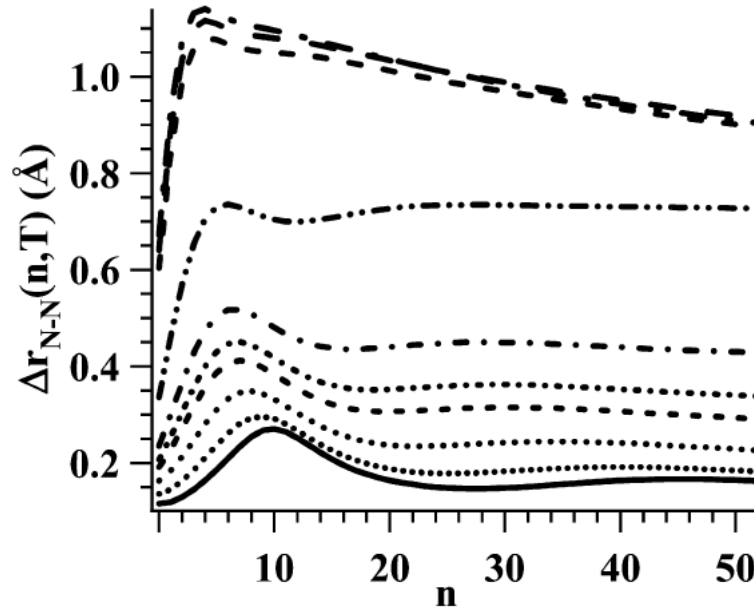


Figure 3.27: Fluctuation of the average distance $\Delta r_{\alpha-\beta}(n, T)$ along the isobar 50 bar and in the range of temperature between 250 and 500 K.

troversty. Indeed, using electric deflection method, Odutola et al. (Odutola et al. 1979) found the values $\theta_A = 50.6^\circ$ and $\theta_B = 66.5^\circ$; using high resolution microwave spectroscopy, Nelson et al. (Nelson, Fraser, and Klemperer 1985) found the average values of $\theta_A = 48.6^\circ$ and $\theta_B = 115.5^\circ$ for a distance between nitrogen atoms of two ammonia molecules r_{N-N} equal to 3.34 Å. Using quantum calculations, Olthof et al. (Olthof, Avoird, and Wormer 1994) found the values $\theta_A = 45^\circ$ and $\theta_B = 95^\circ$; Liu et al. (Liu et al. 1986) found the values $\theta_A = 13^\circ$ and $\theta_B = 102^\circ$ and $r_{N-N} = 3.34$ Å; Lee et al. (Lee and Park 2000) found the values $\theta_A = 36^\circ$ and $\theta_B = 95^\circ$ and $r_{N-N} = 3.24$ Å. Beu et al. (Beu and Buck 2001) report the values $\theta_A = 27^\circ$ and $\theta_B = 95^\circ$ for a distance $r_{N-N} = 3.26$ Å. Other values are compiled in the paper by Nelson et al. (Nelson, Fraser, and Klemperer 1985; Nelson, Fraser, and Klemperer 1987) Although the comparison between our results and those reported in the literature cited before is not easy since in our case the mutual orientation is environment dependent (many body interactions), our results seem to correlate with the experimental data reported by Nelson et al. (Nelson, Fraser, and Klemperer 1985; Nelson, Fraser, and Klemperer 1987) The effect of temperature on the mutual orientation between a reference ammonia molecule and the first nearest neighbor is illustrated in Figure 3.28. The behavior of $P(\theta_A, \theta_B, n = 1, T)$ clearly indicates that the mutual orientation defined by the angles $\theta_A = 40, 115^\circ$ and $\theta_B = 115, 40^\circ$ remains the most probable although the associated probability decreases with increasing the temperature.

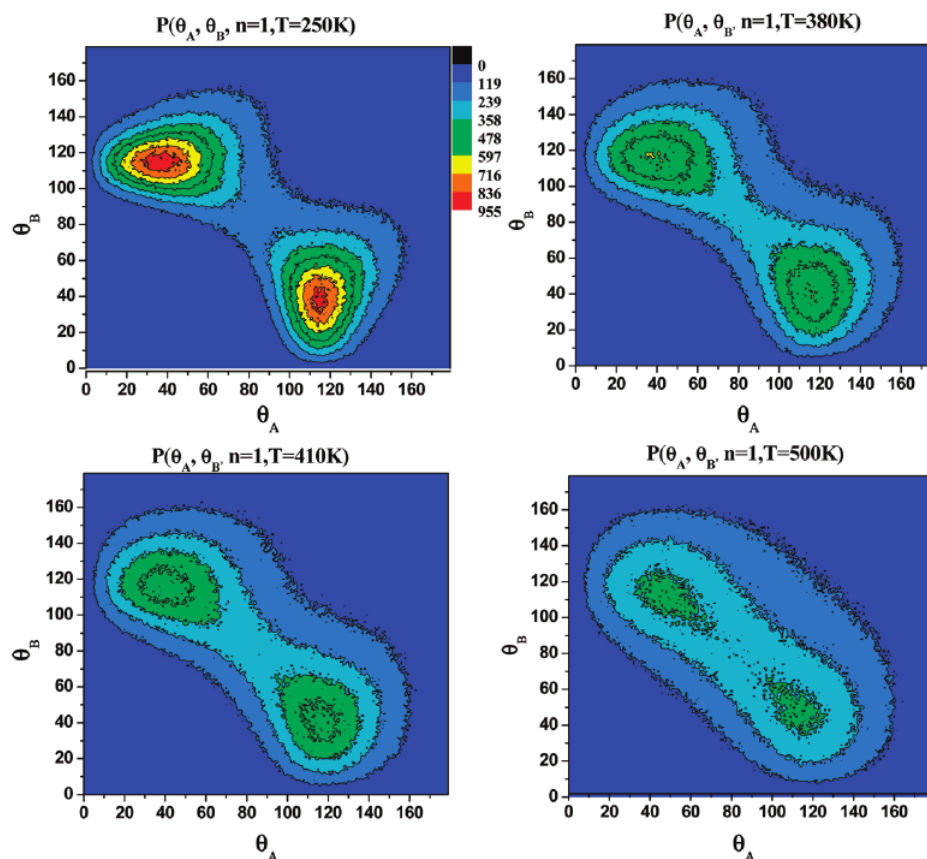


Figure 3.28: Nearest neighbor relative orientational distribution. The angles θ_A and θ_B are defined in 3.18. For comparison purposes the color scaling has been preserved.

Conclusion. In this section, we report the results of a number of molecular dynamics and Monte Carlo simulations of sub and supercritical ammonia system along the isobar 135 bar. In the first step, we promote one of six potential models proposed in the literature on the basis of a favorable comparison of the calculated and experimental data such as the liquid–gas coexistence curve, the partial structure factors and the density. The analysis of the local structure along the isobar 135 bar was carried out using the nearest neighbor approach. The change of the local structure was traced back to the change in the behavior of both the average distance between a reference ammonia molecule and its subsequent nearest neighbors, and the corresponding fluctuation. Our results show that the average distance has a nonlinear behavior with an occurrence of a minimum and maximum in the rate of increase of the average distance. The minimum coincides with the position of the third nearest neighbor and was interpreted as indication of high density region and a dominance

of attractive character of the interaction potential energy. The maximum coincides with the position of the eleventh nearest neighbor that was associated with a low density region and a reduced contribution of the attractive contribution to the total interaction energy. Furthermore, we suggest to use the position of the maximum in the fluctuation of the average distance to define the spatial extent of the first solvation shell, showing then that this spatial extent increases and that the number of the involved ammonia molecules is reduced. At low temperature (far from the critical one), hydrogen bonding was inferred from the occurrence of short distance peak in the first nearest neighbor radial distribution between nitrogen and hydrogen atoms. The position of this peak coincides with that observed in the $g_{NH}(r)$ radial distribution function. As this peak disappears with increasing the temperature (higher than 300 K) in favor of high distance peak, this suggests that the hydrogen bonding in ammonia becomes weak. This result is in accordance with Buback conjecture that hydrogen bond in ammonia is weak at and above room temperature and, in particular, under supercritical conditions. (Buback 1974) Furthermore our results provide unambiguous information on the change of the mutual orientation between a reference ammonia molecule and its first nearest neighbor, upon the change in the thermodynamic points considered in this work. Indeed, our results clearly show that the angles between each molecular axis and the axis joining the two nitrogen atoms are equal respectively to 40 and 115° for a distance of 3.26 Å between the two nitrogen atoms. When increasing the temperature, this mutual orientation remains the most probable, however, the associated probability decreases drastically.

Heterogeneity of the Local Structure in Sub- and Supercritical Ammonia: A Voronoi Polyhedra Analysis.

Introduction. One of the most important properties of supercritical fluids (SCFs) is the drastic increase of the thermodynamic response functions (e.g., thermal expansion, compressibility, heat capacity) near the critical point. As a consequence, the properties of supercritical fluids can be varied continuously from gaslike to liquidlike values by small changes in the pressure or/and temperature. This feature makes SCFs attractive alternatives to liquid solvents for use in the development of new chemical processes. From the microscopic point of view, the increase of the response functions near the critical point is associated with the heterogeneous character of the distribution of the local density. The information on the local structure is then indispensable for understanding the precise structural changes when the thermodynamic states are close to the critical point. In several previously reported experimental and theoretical studies, the importance of the local density inhomogeneity in the determination of SCF properties has been clearly underlined (Musso et al. 2004; Tucker 1999; Rovere, Heermann, and Binder 1990). The main problem is that independent physical techniques that can give direct characterization of such

inhomogeneity are not available. Indeed, although the radial distribution function, being one of the most widely used tools to investigate the local structure, gives important information on the structure of supercritical fluids, this statistical property is too much averaged to be able to describe in detail the changes of the local structure. In characterizing the local environment of the molecules when the temperature and/or the pressure is varied, the analysis of their Voronoi polyhedra (VP) is an efficient tool. VP is the generalization of Wigner–Seitz cells of crystals for disordered structures (Okabe 2000). The VP of a given molecule is the locus of the spatial points that are closer to this selected molecule than to any other molecule. The geometry (i.e., shape, volume, etc.) of the polyhedron belonging to a given molecule in a liquid rapidly fluctuates due to molecular motion. The distributions of the metric and topological properties of these polyhedra can be calculated in simulations, and their shape, the position of its maximum, and their width give insight into the local molecular structure. The use of VP was suggested earlier by Finney (Finney 1970; Finney 1977) to analyze the topology of the local structure. Since then several publications have appeared in the literature, and the local structure of various disordered systems, such as hard spheres (Oger et al. 1996; Lavrik and Voloshin 2001; Sastry, T. M. Truskett, and Stillinger 1998; Yang, Zou, and Yu 2002; Richard et al. 1998), Lennard-Jones liquids (Ruff et al. 1986; Montoro et al. 1994; Voloshin, Beaufils, and Medvedev 2002), molten (Baranyai et al. 1986; Pusztai and al. 1988) and hydrated salts (Montoro et al. 1994), liquid metals (Luchnikov et al. 1996; Brostow et al. 1998; Hoare 1978; Aparicio and Cocks 1995; Maruyama et al. 2009), glass-forming liquids (Starr et al. 2002), water (Ruocco, Sampoli, and Vallauri 1992; Ruocco et al. 1993; Shih, Sheu, and Mou 1994; Jedlovszky and Mezei 2000; Yeh and Mou 1999; Mountain 1999; Jedlovszky et al. 2008a; Etzler, Ross, and Halcomb 1991; Rapaport 1983; Soyer et al. 2000) under different thermodynamic conditions, including supercritical (Jedlovszky and Mezei 2000; Jedlovszky and Mezei 1999) and supercooled states (Jedlovszky et al. 2008a; Jedlovszky and Mezei 1999; Okabe 2000), other hydrogen bonding liquids (Jedlovszky and Mezei 2000), grafted (Tokita et al. 2004) and soft polymers, (Sega et al. 2004) hydrated phospholipid membranes, (Alinchenko et al. 2005) and colloidal particle packing (Sega et al. 2004; Alinchenko et al. 2005; Schenker et al. 2009; Varadan and Solomon 2003) have been successfully characterized by means of VP analysis. It should also be noted that the VP analysis has numerous applications in other fields of sciences (Okabe 2000) from biophysics (Soyer et al. 2000) to astrophysics (Weygaert and V. Icke 1989) and from neurosciences (Ahnelt et al. 2000) to bioinformatics (Karch et al. 2003; Tsai and Gerstein 2002). In the present study the local structure of ammonia is investigated in detail on the basis of long molecular dynamics (MD) calculations, performed under both sub- and supercritical conditions at temperatures ranging from 250 to 500 K along the 135 bar isobar. The topological and metric properties of VP, such as the number of the faces, face area, and volume of the polyhedron, have been quantified.

The effect of increasing temperature on the shape, width, and intensity of the associated distributions allows quantifying, on the molecular level, the local structural changes accompanying the approaching and crossing the critical point of ammonia. This section is organized as follows. In paragraph 3.1.2, details on the performed calculations are given. In paragraph 3.1.2, the analysis of the obtained VP results is discussed in detail, whereas in section the conclusions drawn are given.

Computational Details.

Molecular Dynamics Simulation. Molecular dynamics simulations have been performed on the isothermal–isobaric (N, p, T) ensemble along the 135 bar isobar, using a cubic simulation box consisting of 864 ammonia molecules under periodic boundary conditions. The potential model of ammonia proposed by Kristof et al. was used (Kristof et al. 1999). In our previous work (Vyalov et al. 2010) we have shown that there is good agreement between the calculated values, such as the density (Bone and Handy 1990), liquid–gas coexistence curve, thermal expansion (Bone and Handy 1990), and diffusion coefficient (O’Reilly, Peterson, and Scheie 1973), of this model and the corresponding experimental data. The interaction potential between two ammonia molecules contains two parts, namely a Lennard-Jones (LJ) term and a Coulomb term. The simulations have been performed using the DL_POLY program (Tsuzuki et al. 1996). The temperature and pressure of the system have been kept constant by means of the weak coupling algorithms of Berendsen (Berendsen et al. 1984), using the coupling parameter values of 0.1 ps (temperature) and 0.5 ps (pressure). All site–site interactions have been truncated to zero beyond the center–center cutoff distance of 14.5 Å. The long-range part of the electrostatic interactions has been accounted for using the Ewald summation method implemented in the DL_POLY package (Smith and Forester 1996). The equations of motion have been integrated using the leapfrog algorithm, employing an integration time step of 1.0 fs. A typical simulation run was composed of two stages: first, the system was equilibrated during 5 ns at a given temperature and pressure; second, the trajectory of particles was saved at every 10 fs during the 500 ps long production run. Seventeen temperatures, ranging from 250 to 500 K have been chosen along the 135 bar isobar. These thermodynamic states as well as the experimental coexistence curve are shown in Figure 3.29. The filled circles of Figure 1 show the thermal expansion coefficient, calculated by numerical differentiation of the $V(T)$ function at the 135 bar isobar. The maximum of the calculated thermal expansion coefficient occurs at $T = 410$ K. Throughout this section this temperature is referred to as T_α .

Voronoi Polyhedra Analysis. In this study the coordinates of nitrogen atoms have been considered to be the representative points of the ammonia molecules in order

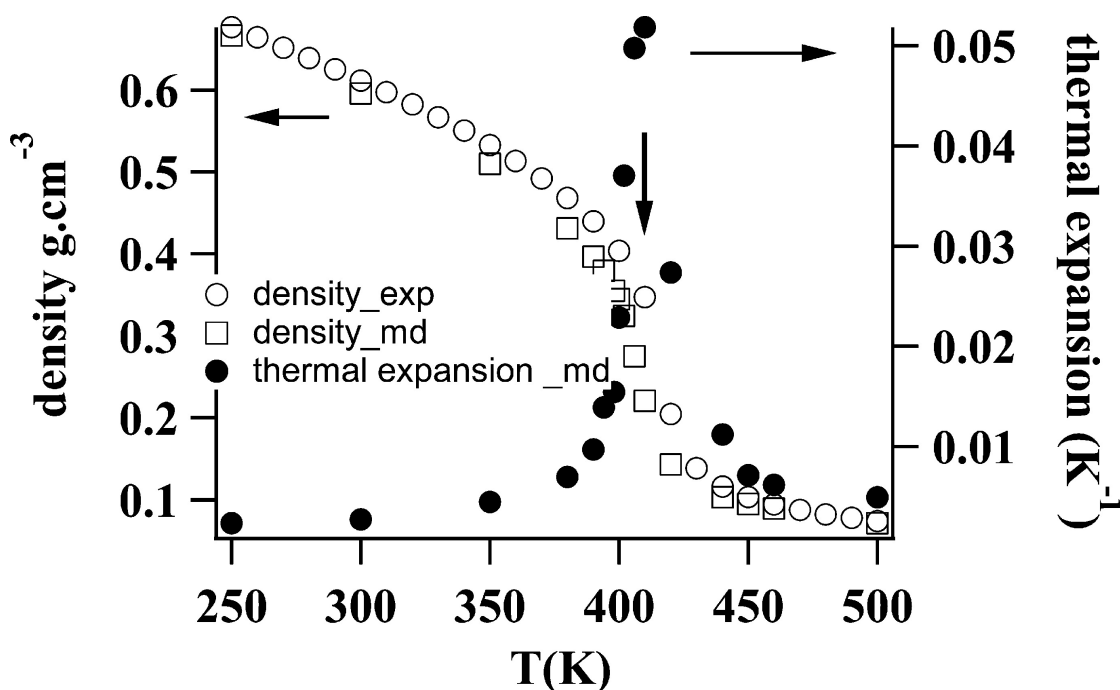


Figure 3.29: Experimental (open circles) and simulated (open squares) liquid–vapor coexistence curves of ammonia along the 135 bar isobar. The thermal expansion coefficients obtained in the present MD simulations by numerical differentiation of the $V(T)$ data along this isobar are also shown (filled circles). The maximum of the thermal expansion coefficient occurs at $T_{\alpha} = 410$ K.

to construct the VP. The VP of a given molecule is the region of space containing all the spatial points that are closer to this molecule than to any other one. The tessellation of the VP is constructed by partitioning the space around the molecules into N polyhedra, formed by the planes bisecting the sections connecting the molecules with their nearest neighbors. The VP of the molecules can be characterized by the number of its edges (NE), vertices (NV), and faces (NF), the area of its individual faces (A), its total surface area (S), volume (V), and reciprocal volume, characterizing the local density around the molecules, ρ . The first three of these properties are typical topological characteristics, while the last four are the most widely used metric properties. Further, the VP vertices are the locations of the largest empty spheres (spherical vacancies) present between the molecules. These vacancies can be characterized by their radius R , which is the distance of the given vertex from the central molecule of the VP. These properties are characterized here by their full statistical distributions as well as by the mean values and standard deviations of these distributions. The distribution, mean value, and standard deviation of the quantity X are denoted here as $P(X)$, X , and $\sigma(X)$, respectively.

Results and Discussion. Distribution of Various VP Properties We computed the distribution of several VP properties, including the reciprocal volume, characteristic of the local density (ρ), volume (V), total surface area (S), area of the individual faces (A), number of faces (NF), and radius of the empty spheres, centered at the VP vertices (R). Figure 3.19 illustrates the change in the VP density distribution $P(\rho)$ with increasing temperature between 250 and 500 K along the 135 bar isobar. At low temperatures, far from T_α , $P(\rho)$ has a well-defined peak. As the temperature increases, (i) this peak shifts to lower values, (ii) it broadens, and (iii) the corresponding intensity decreases. Finally, as the temperature increases above T_α , the $P(\rho)$ distribution becomes significantly narrower and, at the same time, the intensity increases substantially. The dependence of the average density, ρ , and the corresponding standard deviation, σ_ρ , on the temperature is shown in Figure 3.31. It is clearly seen that the rate of decrease of ρ increases drastically when the temperature is around 390 K. Further, the standard deviation, σ_ρ , goes through a maximum near the temperature of 410 K, i.e., T_α . This behavior clearly indicates that the local density, as described by the VP reciprocal volume, becomes increasingly inhomogeneous upon approaching the T_α temperature, and it becomes less inhomogeneous when the temperature increases above T_α .

Figure 3.32 shows the behavior of the VP volume distribution, $P(V)$. At low temperatures, the distribution of $P(V)$ is rather sharp around the mean volume value. With increasing temperature the distribution broadens and its peak shifts to higher volume values. Furthermore, an asymmetric tail develops on the large volume side of the $P(V)$ distribution peak, particularly near T_α . As has been explained in many previous works, the asymmetry of $P(V)$ is a consequence of the fact that in inhomogeneous systems there is no upper limit for the maximum volume of VP, while this quantity has a lower limit due to the excluded volume interaction (Montoro, Gil, and Abascal 1993). Thus, the presence of such a long, exponential-like tail is a clear sign of inhomogeneous distribution of the molecules (Zaninetti 1992). A quantity of interest is thus the standard deviation of this distribution, σ_V , since it measures the amplitude of the VP volume fluctuation. The behavior of σ_V has been reported as a function of the temperature in Figure 3.33. It shows that the rate of increase of the fluctuation in the VP volume increases drastically when the temperature is close to T_α . This behavior can be interpreted as a microscopic change, occurring at the molecular level, which results in increased thermal expansion. The physical picture emerging from this finding is that some of the geometric neighbors (i.e., the ones sharing a common VP face) with the central ammonia molecule are located, due to their increasing thermal motion, at larger distances from the central molecule, which leads to an increasing thermal expansion of the system.

The volume of a VP is closely related to the area and number of its faces. Therefore, here we analyze also the behavior of the corresponding distributions in order to

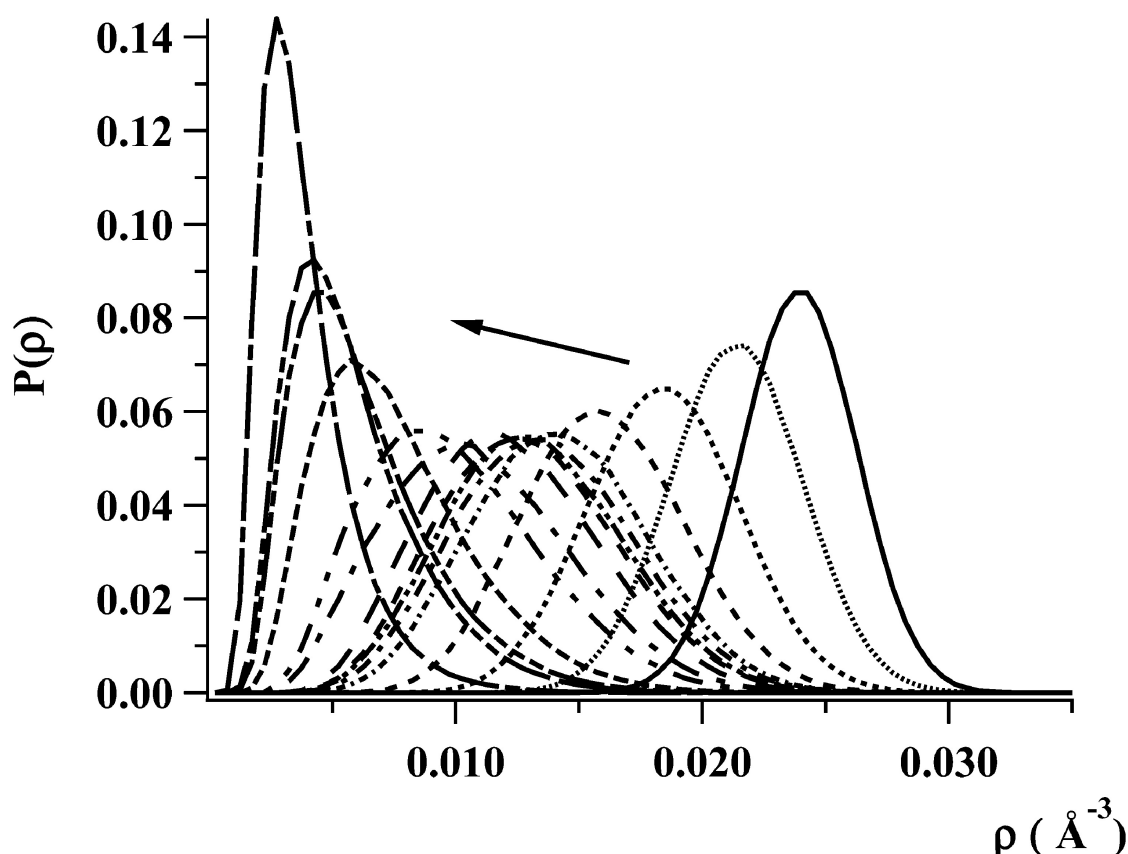


Figure 3.30: Density distribution of the VP of the ammonia molecules, as obtained along the 135 bar isobar at various temperatures in the range between 250 and 500 K. The arrow indicates the increase of the temperature.

get more insight into the change of the local structure of ammonia along the thermodynamic path chosen in our study. The first property characterizing the local structure around the ammonia molecules is the $P(NF)$ distribution of the number of VP faces, which is given in Figure 3.34. The mean number of the face area of the VP resulted in around 14.7 at the lowest temperature and around 15.5 at the highest temperature considered (see the upper inset of Figure 3.34), can be interpreted as the number of geometric neighbors of each ammonia molecule. It should be mentioned that in the present work the faces are not weighted by their area, which is probably the main reason for the misleading occurrence of large values in such distributions (Xu, Yang, and Hu 2009; Dong and al. 2009; Jullien and al. 1996). Indeed, the distance of the 15th nearest neighbor from the central molecule is clearly larger than the position of the first minimum of the nitrogen–nitrogen radial distribution function, which defines the spatial extent of the first coordination shell. This confirms that the behavior of the VP face number distribution is shaped by the neighbor molecules located at

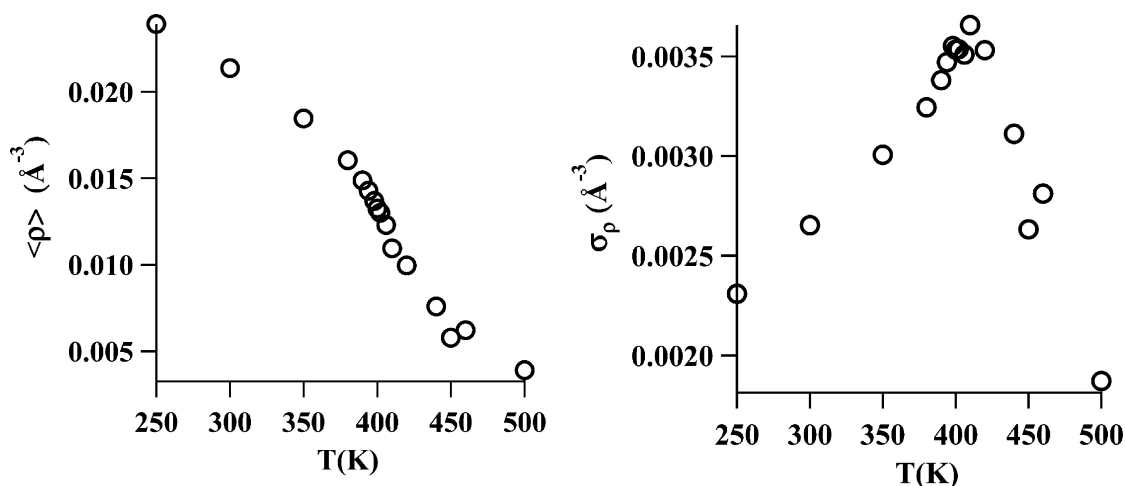


Figure 3.31: Mean value of the reciprocal VP volume, characterizing the local density ρ (left) and the corresponding standard deviation σ_ρ (right) of the $P(\rho)$ distribution as a function of the temperature.

distances beyond the first coordination shell. We notice a drastic decrease of the intensity of the maximum and some broadening of the $P(\text{NF})$ distribution as the temperature increases. Further, the $P(\text{NF})$ distributions are more skewed toward large values of NF at the higher temperatures. This increase of the contribution of large NF values to the total $P(\text{NF})$ distribution can be interpreted as a sign of the geometric rearrangement of distant neighbors when the temperature increases. Indeed, the large fluctuation of the position of the farthest neighbors forming the polyhedra (distant neighbors will cease to be neighbors if their positions are slightly perturbed) induces an increase of the fluctuation in the number of faces. The correlation between the average volume of the VP and the average number of its faces is illustrated in Figure 3.35. As is clearly seen, at temperatures near T_α a small change in the value of NF is accompanied by large changes in the mean VP volume.

The second parameter that helps to characterize the VP properties is the distribution of the area of its faces, $P(A)$. The behavior of this distribution is illustrated in Figure 3.36. At low temperatures there are two peaks in the face area distribution $P(A)$. The first, high, trivial peak around the surface area value of 0 is given by the large number of distant neighbors, sharing only tiny VP faces with the central molecule (Brostow et al. 1998). This peak is rather insensitive to the temperature and provides no information on the local arrangement of the molecules around each other. The second peak is located at higher values of the face area distribution. The position of this peak shifts slightly toward higher face area values and gradually flattens out as the temperature approaches T_α . The change in the intensity of the second peak of $P(A)$ results from the change of the number of closest neighbor

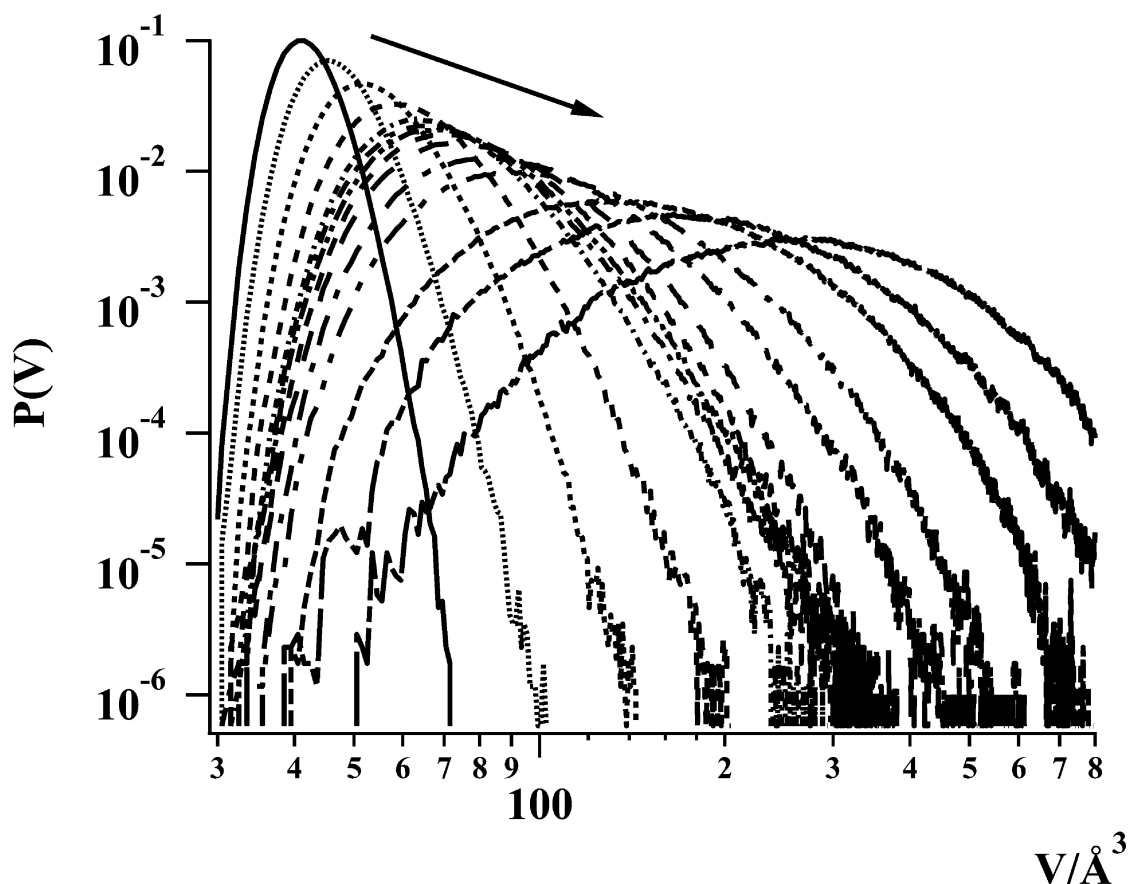


Figure 3.32: Volume distribution of the VP of ammonia molecules, as obtained along the 135 bar isobar at various temperatures in the range between 250 and 500 K. The arrow indicates the increase of the temperature.

molecules (Yang, Zou, and Yu 2002). Furthermore, the distance between two vertices of the VP face must be larger than a certain minimum value due to the excluded volume (repulsive interaction) of the corresponding neighbor molecules. It is therefore logical to expect that this peak would be much narrower and sharper at low temperatures (small fluctuation of the position of the neighboring molecules that determine the VP). The shift and flattening of this peak are associated with the increase of the distance of some vertices belonging to this face from the central molecule due to the thermal expansion of the system. This information can also be obtained from the behavior of the vacancy radius $P(R)$ distribution, which is illustrated in Figure 3.37. $P(R)$ has a well-defined peak at low temperatures (i.e., high densities). When the temperature increases above T_α the intensity of the distribution reduces substantially, and a concomitant broadening of the distribution and a shift of its peak to higher R values are observed. All these changes can be associated with the formation of large voids.

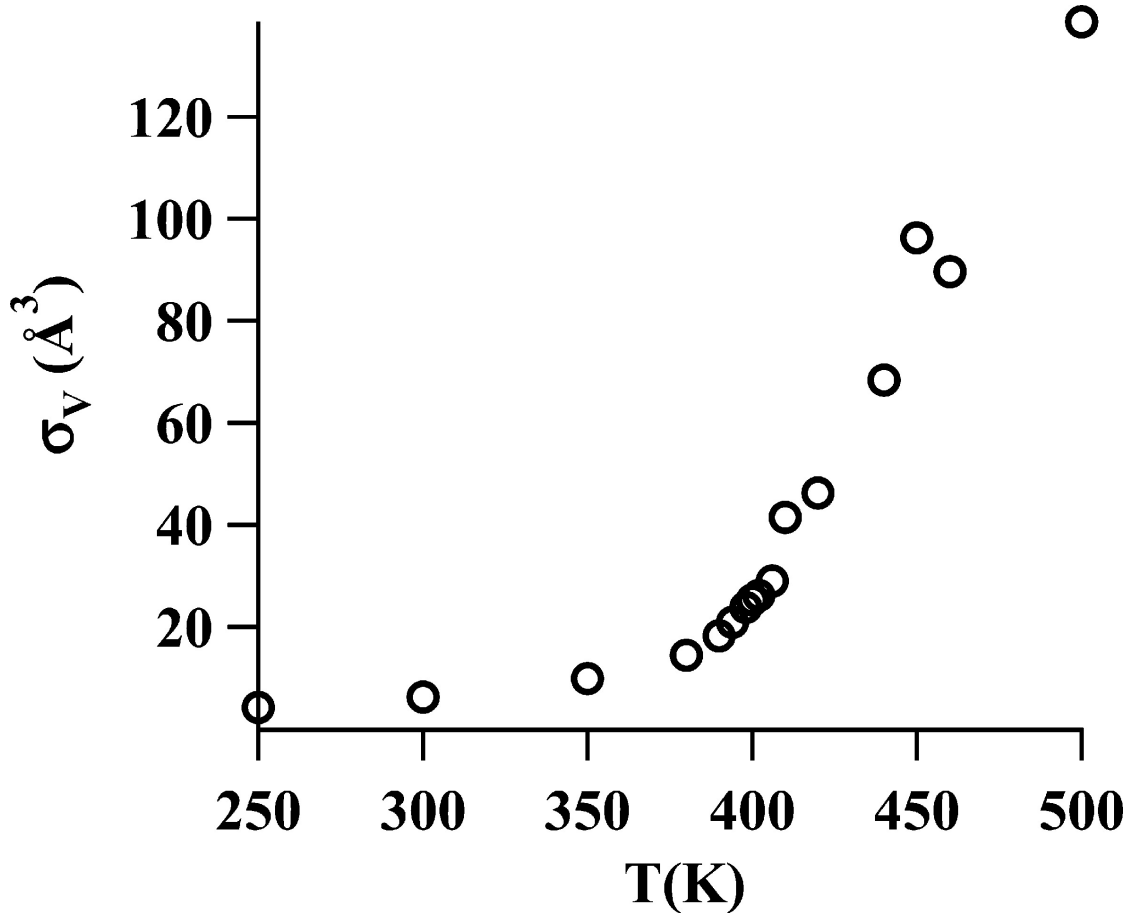


Figure 3.33: Standard deviation σ_V of the volume of the VP distribution as a function of the temperature.

The increase of temperature leads to an increase of the average void size, as R shifts upward large values. The rate of increase of R becomes particularly high near the temperature T_α (see Figure 3.38a). The local structure responds to an increase of the temperature by creating large voids, the distribution of which becomes increasingly heterogeneous, as indicated by the increase of its fluctuation σ_R (see Figure 3.38b). These results support the physical picture that the maximum of the thermal expansion coefficient is associated with the transition from the situation when small voids of rather uniform size dominate the $P(R)$ distribution to that when rather large voids also appear besides these small, uniformly sized ones. The observed increase of the void radius is also illustrated by Figure 3.39, showing equilibrium snapshots of ammonia as taken from the simulations performed at the temperatures of $T = 250$ K and $T = 420$ K, respectively.

As there is a strong correlation between the volume and the total surface area (S)

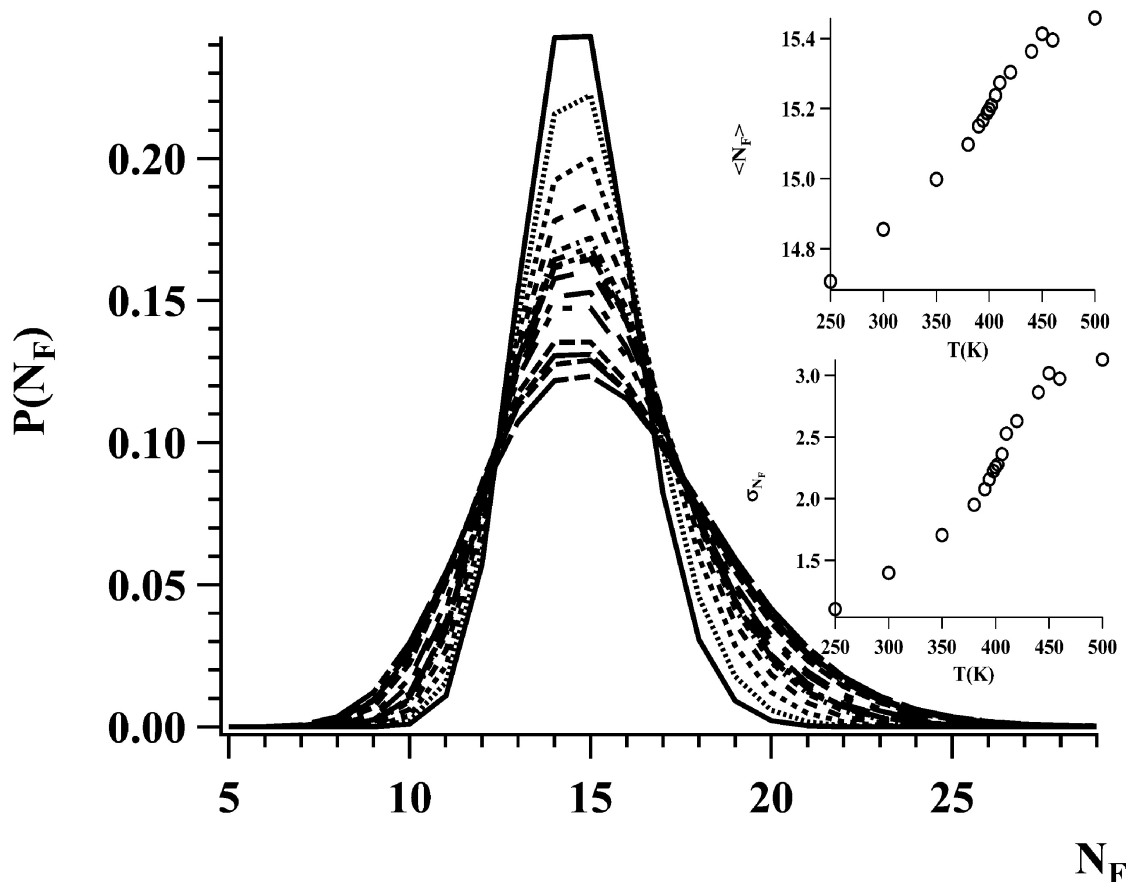


Figure 3.34: Number of faces distribution of the VP of ammonia molecules, as obtained along the 135 bar isobar at various temperatures in the range between 250 and 500 K. The mean value $\langle N_F \rangle$ and the corresponding standard deviation σ_{N_F} of the $P(N_F)$ distribution are given in the upper and lower insets, respectively, as a function of the temperature.

of the VP, the same qualitative behavior is found for the $P(S)$ distribution as what was also observed for $P(V)$. Indeed, at low temperatures, the $P(S)$ distribution is peaked around the mean surface area value (see Figure 3.40). As the temperature increases, we notice a decrease of the intensity of the maximum of $P(S)$ and a concomitant shift and broadening of this peak. The behavior of S and σ_S with increasing temperature is similar to that of V and σ_V in the sense that a change in the rate of increase of the mean value of both parameters as well as a maximum of both standard deviations can be noticed when the temperature is close to T_α . The information concerning the change in the volume and the surface of the VP may be gathered in the asphericity parameter, which combines volume and surface area into a single descriptor to measure how far the shape of the polyhedron is from that of a perfect sphere. The

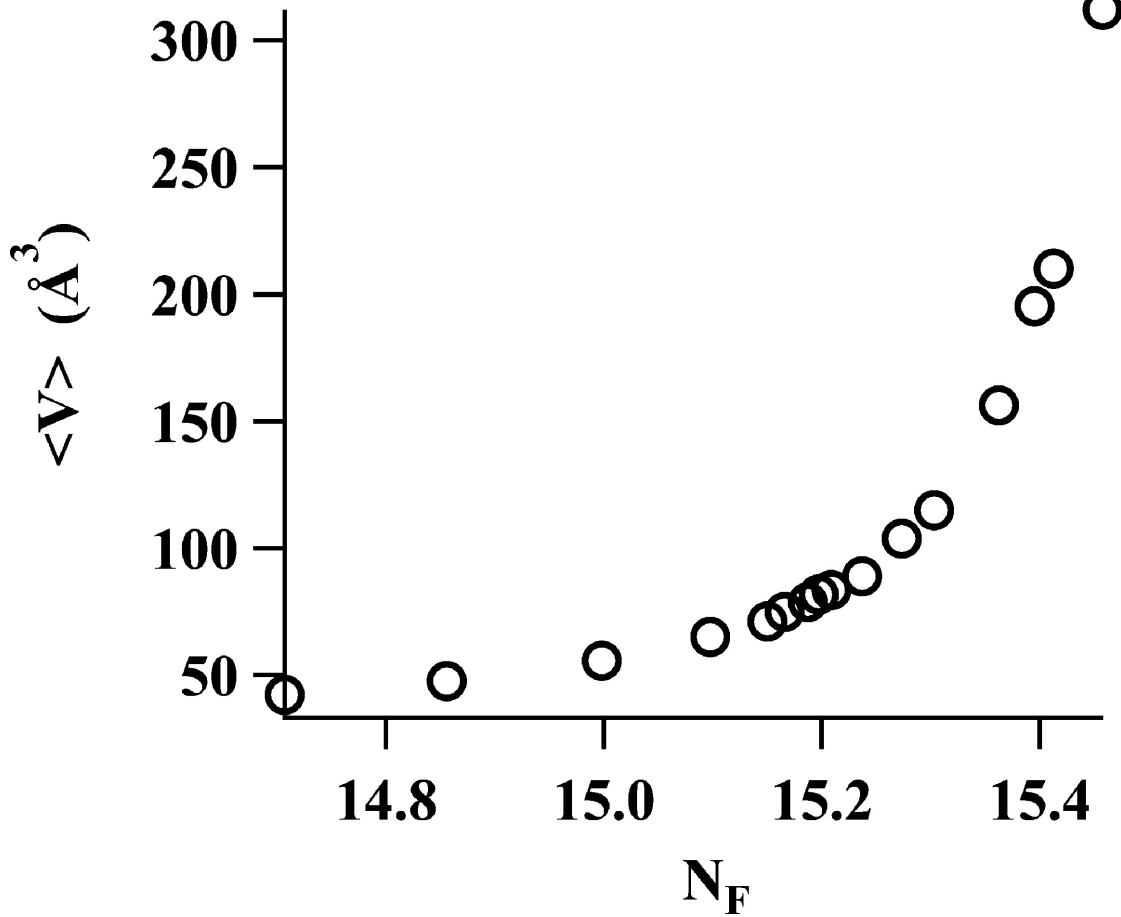


Figure 3.35: Correlation between average VP volume, V , and average number of VP faces, N_F .

asphericity parameter, defined as (Jedlovszky and Mezei 2000):

$$\eta = \frac{S^3}{36\pi V^2} \quad (3.1)$$

approaches unity if the VP is less distorted in its shape (the three principal axes of the VP have almost equal length); otherwise it is considerably larger than unity. Therefore, the asphericity parameter can be used to characterize the VP anisotropy. At low temperatures, the distribution is defined by a narrow and symmetric peak, centered at around 1.51 (see Figure 3.41). As the temperature increases, $P(\eta)$ shifts to higher values with a concomitant decrease of its intensity and a broadening of its shape. The largest gradient of the average value of the asphericity parameter as function of temperature is observed around T_α .

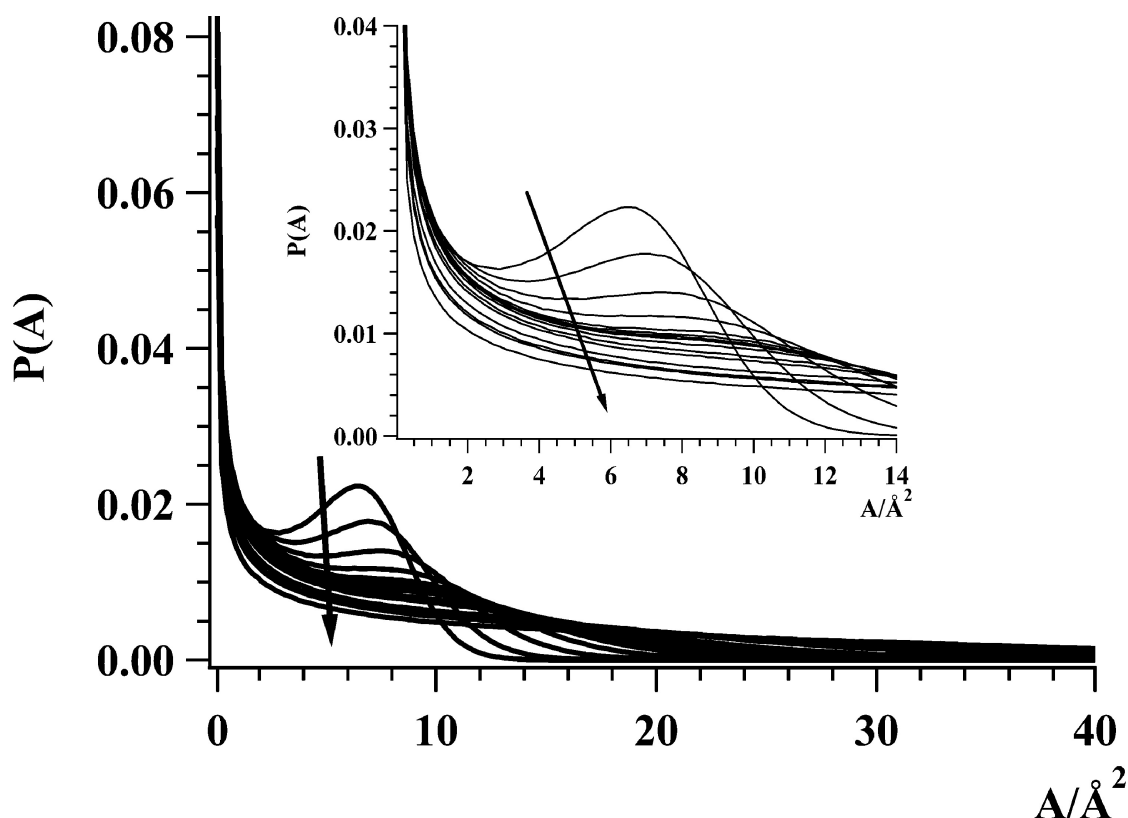


Figure 3.36: Face area distribution of the VP, as obtained along the 135 bar isobar at various temperatures in the range between 250 and 500 K. The inset shows the region of the second, nontrivial peak on a magnified scale. The arrows indicate the increase of temperature.

Diffusion Coefficient and the VP Analysis. The changes in the topological properties of the system with increasing temperature are expected to lead to changes also in several physical properties. In the following, we discuss the correlation between the local structure, as revealed by the VP analysis, and a macroscopic property, namely the diffusion coefficient, D , the temperature dependence of which along the 135 bar isobar is illustrated in Figure 3.42. The diffusion coefficients have been calculated from the mean square displacement. The rate of increase of D undergoes a drastic change near the temperature T_α . One can expect that the dynamics of a single molecule is largely determined by its nearest neighbors, the spatial distribution of which is described by the VP properties. Indeed, our results suggest that as far as small VP volumes and small vacancy radii dominate their respective total distributions, the large number of nearby neighbors imposes a strong caging effect, which reduces the diffusion of the molecules. The increasing temperature has a “softening” effect on these cages formed by the nearest neighbors, and at higher temperatures

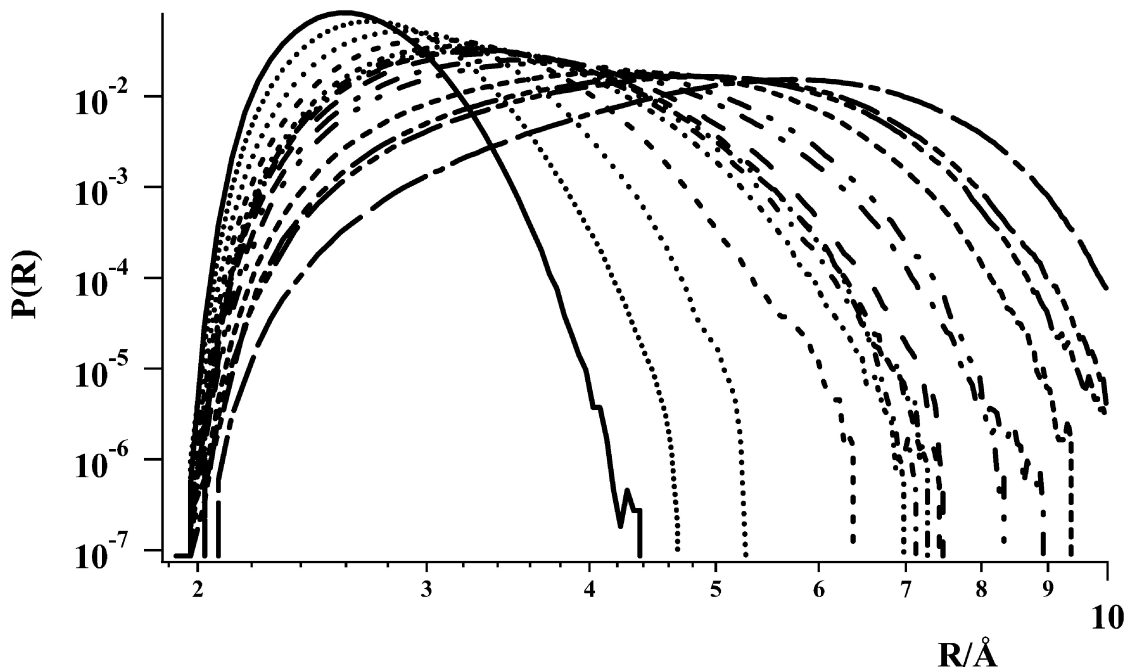


Figure 3.37: Distribution of the radius of the spherical voids present in ammonia, as obtained along the 135 bar isobar at various temperatures in the range between 250 and 500 K. The two axes are on logarithmic scale.

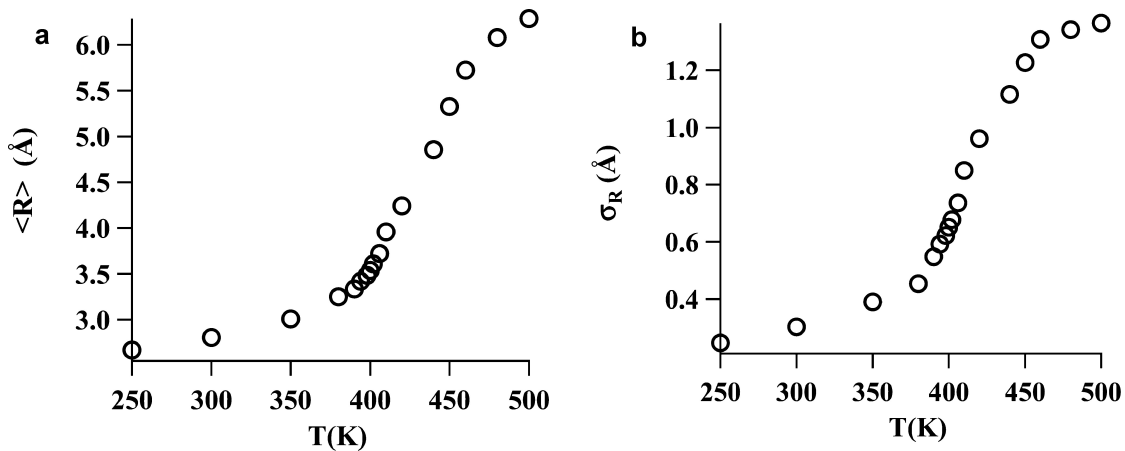


Figure 3.38: Behavior of (a) the void radius average distance and (b) the corresponding fluctuation as a function of temperature. figure

the cage should even disappear, indicating a translational diffusion regime. The softening of the cage is associated with the observed increase of the VP volumes and radii of the spherical voids among the molecules. This results in a change of the rate

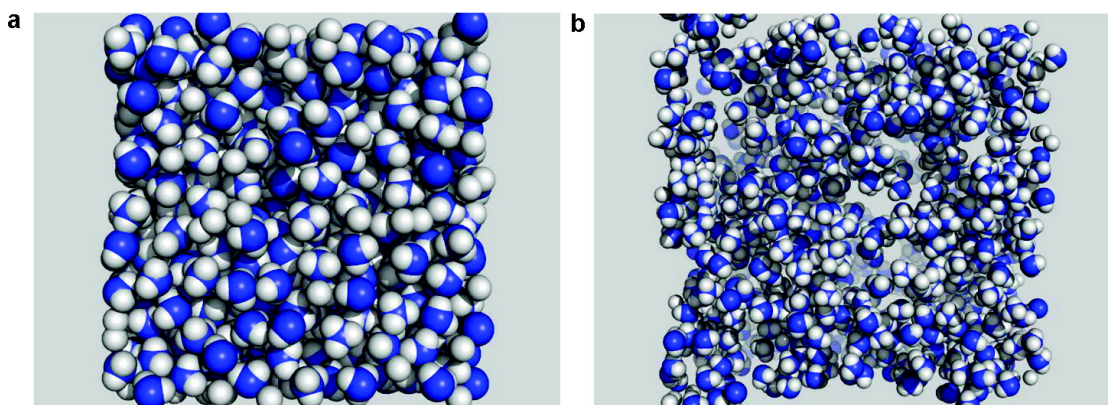


Figure 3.39: Equilibrium snapshots of ammonia, as taken from the simulations performed at (a) $T = 250$ K and (b) $T = 420$ K.

of increase of the diffusion coefficient, as seen from Figure 3.42.

Conclusions. We have reported results of a statistical analysis of Voronoi polyhedra in sub- and supercritical ammonia in a wide temperature range, between 250 and 500 K, along the 135 bar isobar. Typical topological and metric properties have been quantified as functions of the temperature. Our results led to the following main conclusions.

- The distributions of the VP volume and total surface area, and of the radius of the spherical voids located at the VP vertices, are characterized by a single peak at low temperatures, and as the temperature increases, these distributions increasingly broaden, in particular, near T_α (i.e., where the maximum of the thermal expansion coefficient occurs). This behavior is interpreted as a signature of the inhomogeneity of the spatial distribution of the ammonia molecules.
- The inhomogeneity of the spatial distribution of the ammonia molecules is strongly correlated with the change in the rate of increase of the average value of the VP volume, surface area, area, and number of the individual VP faces, and radius of the spherical voids between the molecules.
- The behavior of some macroscopic properties, such as the diffusion coefficient, is strongly correlated with changes in the local structure. Indeed, for temperatures below T_α the local structure is characterized by the dominance of small and rather uniform values contributing to the respective distributions of the VP volume and surface area as well as of the void radius. The dominance of these small values is associated with the occurrence of the strong caging effect of the nearest neighbors, which results in relatively small values of the diffusion coefficient. As the temperature increases, the contribution of large values to these distributions becomes gradually dominant, in accordance with a soft-

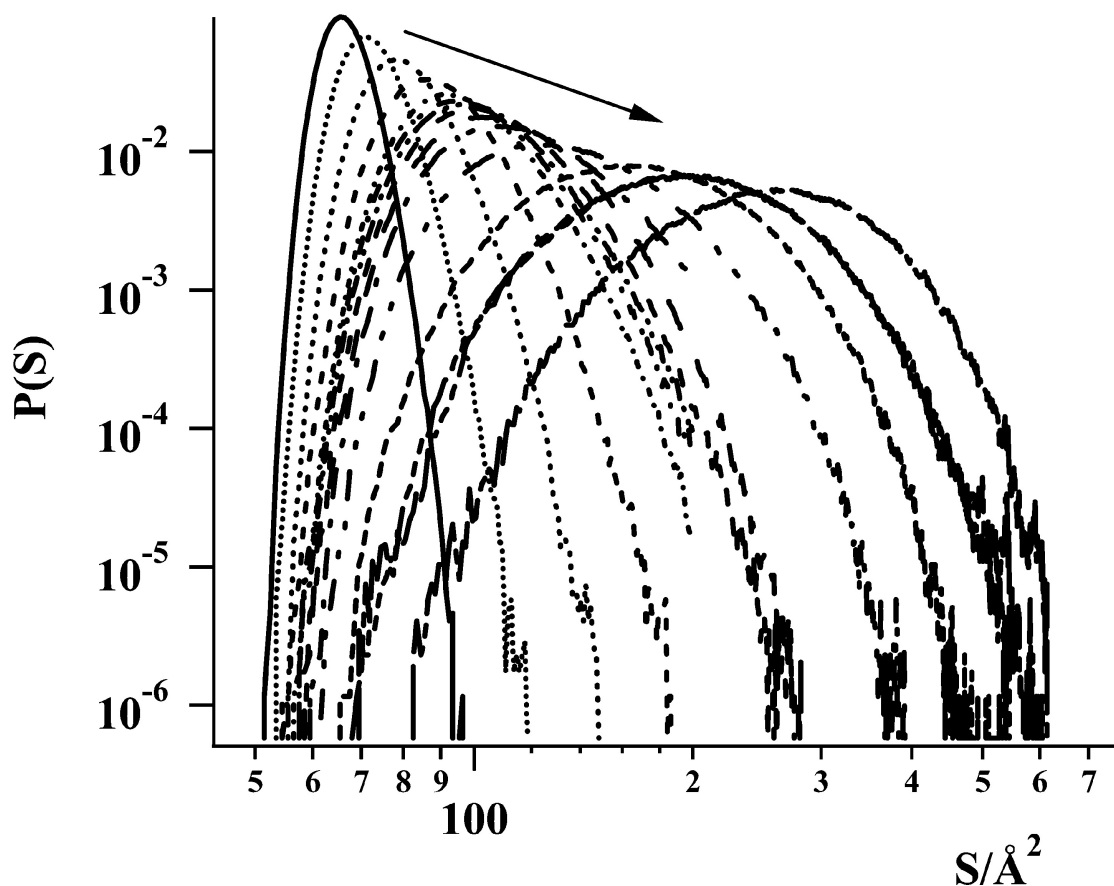


Figure 3.40: Distribution of the total surface area of the VP distributions, as obtained along the 135 bar isobar at various temperatures in the range between 250 and 500 K. The arrow indicates the increase of the temperature. The two axes are on logarithmic scale.

ening of the cage formed by the neighboring molecules, which correlates with the observed drastic increase of the diffusion coefficient.

Reorientation relaxation in supercritical ammonia

Introduction. Ammonia is an important compound with many industrial applications e.g., uses such as in the manufactures of fertilizers, explosives and pharmaceuticals (Ullmann 2003). Moreover, liquid ammonia is an important solvent and special interest exists in the solutions of solvated electron (Rodriguez, Skaf, and Laria 2003). As liquid ammonia is an important example of weak hydrogen bond system, the properties of ammonia in supercritical conditions are of fundamental interest. Indeed, a number of experimental investigations have been performed using X-rays

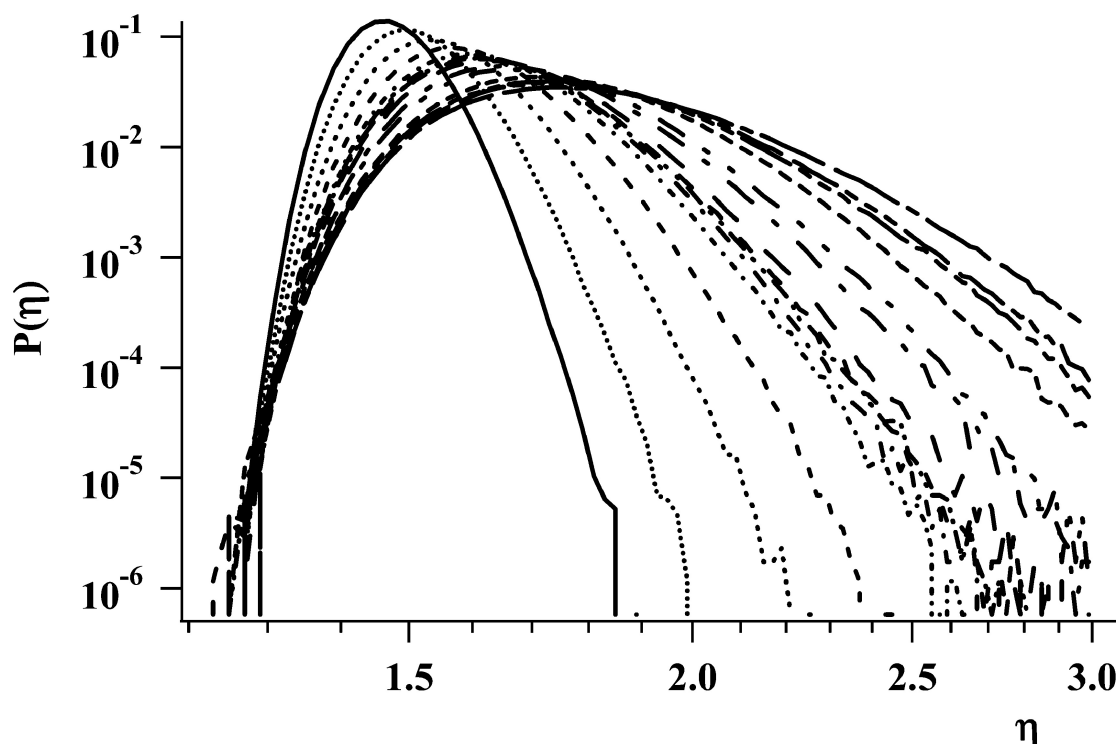


Figure 3.41: Distribution of the asphericity parameter of the VP, as obtained along the 135 bar isobar at various temperatures in the range between 250 and 500 K.

(Giura et al. 2007; Narten 1977), neutron scattering (Bausenwein et al. 1994; Chieux and Bertagnolli 1984), infrared, Raman scattering (Buback and Schulz 1976; Schwartz and Wang 1973; Bradley, Zerda, and Jonas 1985) and more recently non linear transient spectroscopy (Schafer et al. 2008) as well as theoretical simulations (Nelson, Fraser, and Klemperer 1985; Boese et al. 2003; Tongraar, Kerdcharoen, and Hannongbua 2006; Kiselev et al. 2000; Janeiro-Barral and Mella 2006; Spirko 1983; Spirko and Kraemer 1989; Rajamäki et al. 2004). This section has two main goals. Firstly, it concerns the analysis of the time behavior of the reorientation and the angular velocity correlation functions of ammonia and secondly it is an investigation of the relationship between this time behavior and the changes in the local structure particularly while approaching the critical regime. Indeed, the molecule reorientation should be affected by an effective friction arising from the intermolecular interactions. Therefore, the reorientation correlation should be sensitive to the local density fluctuations on molecular level and particularly to the density inhomogeneities near the critical regime. To some extent, the reorientation dynamics may be described as an interplay between two extreme regimes: one is the Debye diffusion describing the molecular reorientation at long time which is associated with an exponential time behavior

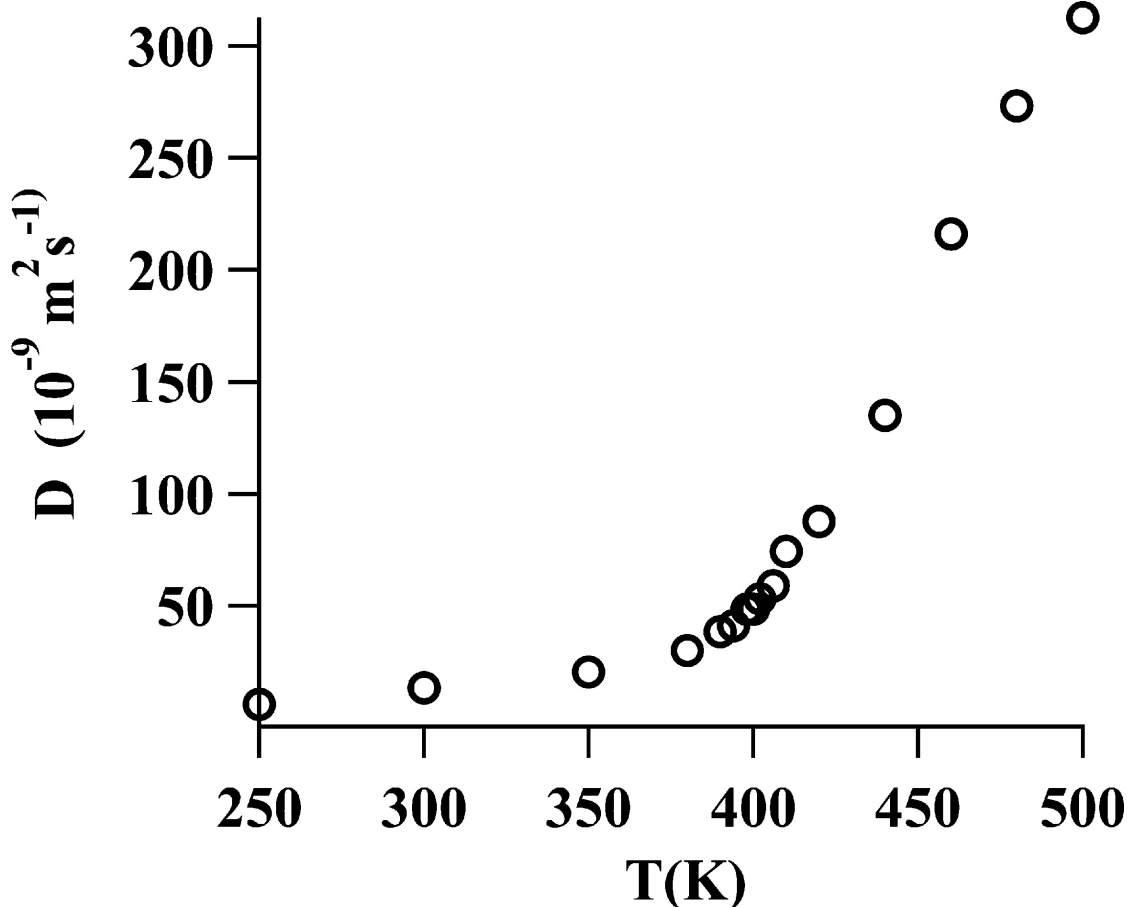


Figure 3.42: Diffusion coefficient of ammonia as function of temperature.

(Matubayasi, Nakao, and Nakahara 2001). The other one occurs at short time and is associated with inertial motion. The analysis of the intermediate time behavior of the reorientation correlation, which connects the inertial and the diffusive situations, is of particular interest, since it is directly connected to the change in the local structure. We then carried out molecular dynamics simulations of neat NH_3 over wide range densities, along the 135 bar isobar as a function of temperature and in a wide density range between 0.666 g/cm^3 and 0.074 g/cm^3 .

Simulations methodology. Molecular dynamics (MD) simulations of the NH_3 system have been performed in the isothermal-isobaric (N,p,T) ensemble on cubic basic simulation boxes containing 864 molecules. Standard periodic boundary conditions have been applied. The force field used in our simulation was consisting of Lennard-Jones (LJ) and charge-charge Coulombic interactions and the corresponding param-

Site	ϵ (kcal)	σ (Å)	q(e)	r_{NH} (Å)	$\angle HNH$ (degree)	μ (D)
N	0.338	3.385	-1.035	1.0124	106.7	1.90
H	0	0	0.345			

Table 3.6: Parameters of the molecular potential model of ammonia. r_{NH} is the distance between nitrogen and hydrogen atom. $\angle HNH$ is the angle between H–N and N–H axes. μ is the molecular dipole moment.

eters are given in Table 1. The total potential is written as follow:

$$U_{nb} = \sum_{i < j} \left\{ 4\epsilon \left[\left(\frac{\sigma}{r} \right)^{12} - \left(\frac{\sigma}{r} \right)^6 \right] + \frac{q_i q_j}{r} \right\} \quad (3.2)$$

where r_{ij} is the distance between a site i a site j , q_i is the charge on site i , q_j is the charge on site j . ϵ and σ are the LJ parameters. The potential model used in this analysis was proposed by Kristof et al (Kristof et al. 1999). The calculated critical temperature, T_C , and the critical density, ρ_C of this model are $T_c = 400$ K, $\rho_c = 0.218$ g/cm³ which are quite close to the experimental values $T_c = 405.4$ K, $\rho_c = 0.225$ g/cm³ (Lemmon, Mclinden, and Friend 2005). The simulations have been performed using the DL_POLY program (Smith and Forester 1996). The temperature and pressure of the system have been kept constant by means of the weak coupling algorithms of Berendsen, using the coupling parameter values of 0.1 ps (temperature) and 0.5 ps (pressure). The van der Waals interactions have been truncated to zero beyond the center-center cut-off distance of 14 Å. And the long range part of the electrostatic interactions has been accounted for using the Ewald summation method. The equations of motion have been integrated using the leap-frog algorithm using a time step of 1.0 fs. The systems have been equilibrated by generating 5 ns long trajectories for each thermodynamic point.

A good agreement was found between the experimental and calculated values for quantities such as the heat of vaporization, the structure, the liquid–gas coexistence curve (Kristof et al. 1999), the density (Lemmon, Mclinden, and Friend 2005) (see Figure 3.43), the thermal expansion (Lemmon, Mclinden, and Friend 2005) (see Figure 3.43) and the diffusion coefficient (O’Reilly, Peterson, and Scheie 1973) and (Grob et al. 1997) (see Figure 3.45).

The relevant dynamical quantities computed in this work are the reorientation correlation function, and the angular velocity correlation function $\Omega(t)$ which are defined as follows:

$$C_\ell^u(t) = \langle P_\ell(u(t) \cdot u(0)) \rangle$$

and

$$\Omega(t) = \langle (\omega(t) \cdot \omega(0)) \rangle$$

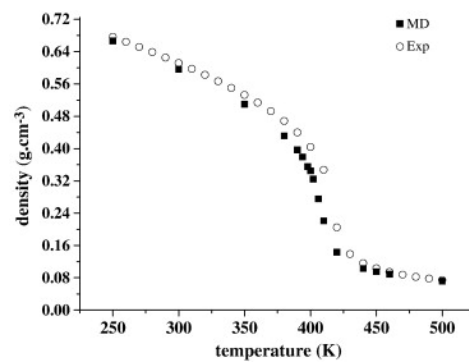


Figure 3.43: Comparison between the calculated and experimental densities along the isobar 135 bar (Lemmon, Mclinden, and Friend 2005).

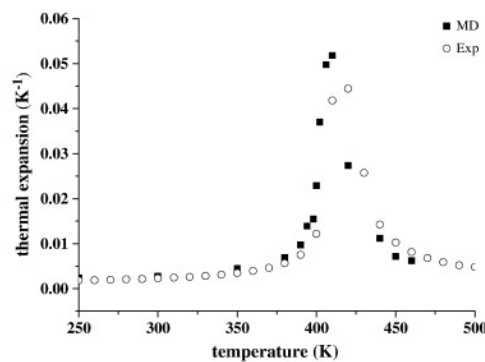


Figure 3.44: Comparison between the calculated and experimental thermal expansion (Lemmon, Mclinden, and Friend 2005).

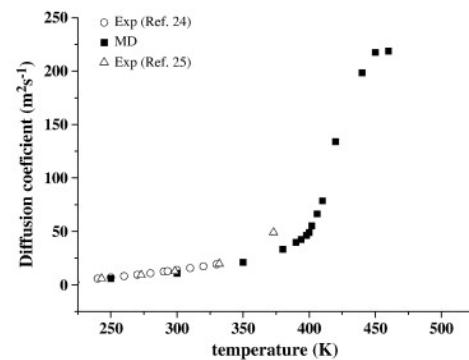


Figure 3.45: Comparison between the calculated and experimental diffusion coefficient (O'Reilly, Peterson, and Scheie 1973; Grob et al. 1997).

u is a unit vector along one of the principal axes of the molecule (see Figure 3.46), $\omega(t)$ is the angular velocity and P is the Legendre Polynomial with order ℓ . As the x

and y axes are equivalent by symmetry, we will discuss only the reorientation correlation of the x and z axes as well as the angular velocity around these axes (see below). The order ℓ of the Legendre polynomial being 1 if the MD results are compared with those obtained by infrared absorption experiment and being 2 if the comparison is done with those obtained by Raman scattering, NMR or fluorescence depolarization experiments. For a molecule having a permanent dipole moment, it is usually appropriate that u be taken in the direction of the principal axis of symmetry (here is the z axis). To quantify the reorientation dynamics of ammonia molecule, the reorientation correlation time τ_ℓ^u (u = x,z) of the x and z axes were calculated as follow:

$$\tau_\ell^u = \int_0^{+\infty} C_\ell^u(t) dt \quad (3.3)$$

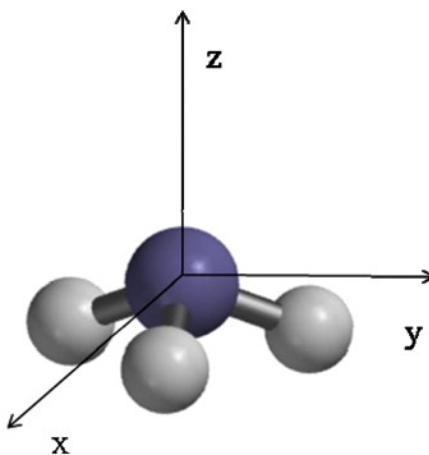


Figure 3.46: Definition of the principal axes of ammonia.

Results.

Reorientation. The behavior of the reorientation correlation functions $C_\ell^u(t)$ (u = x,z) of the z and x molecular axes are given in Figure 3.47A and B, respectively. One sees that upon a density decrease, it takes progressively smaller time for a reorienting principal axes to move to any particular displacement angle and thus the reorientation correlation function will decay on a smaller time. This is confirmed by the behavior of the associated reorientation correlation times (see Figure 3.48). It is worthy to mention that the reorientation relaxation of the x axis is faster than that of the z axis. This indicates that the reorientation of the x axis is less hindered with respect to that of the z axis suggesting an anisotropic character of the intermolecular interaction as seen by an ammonia probe molecule.

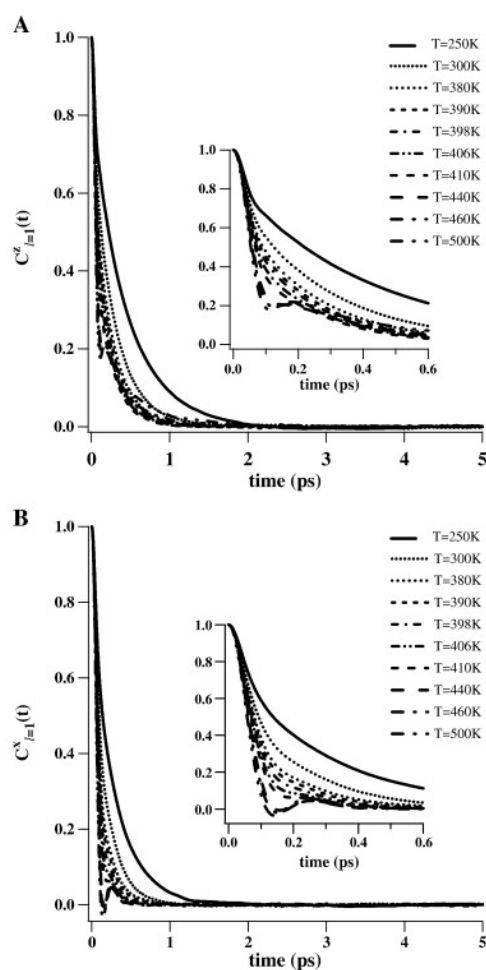


Figure 3.47: A: Reorientation correlation functions of the z axis (dipole axis). The short time behavior of these functions is shown in the inset. B: Reorientation correlation functions of the x axis. The short time behavior is given in the inset. The same legend as in A.

At intermediate time, between 0.05 and 0.15 ps (see the inset of Figure 3.47A, B), the time decay behavior of both $C_{\ell(t)}^z = 1$ and $C_{\ell(t)}^x = 1$ are characterized by an occurrence of a glitch (a sudden increase of the reorientation correlation) occurring in the temperature range where the thermal expansion has its maximum. This behavior is a characteristic of a free rotor obtained theoretically by averaging the first Legendre polynomial over a Boltzmann distribution of rotational velocities (Berne and Harp 1970).

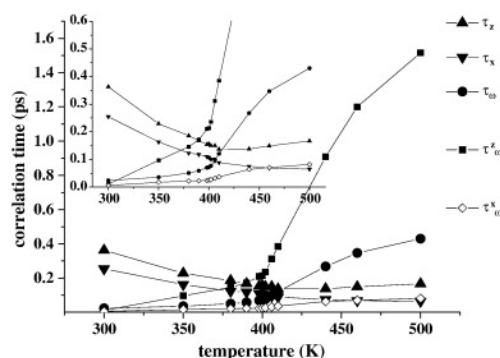


Figure 3.48: Temperature behavior of the reorientation and rotation correlation times. τ_z and τ_x are the reorientation correlation times of the z and x axes. τ_ω is the angular velocity correlation time, τ_ω^z and τ_ω^x are the component of the angular velocity correlation time around the z and x axes.

Angular velocity. To have complementary information on the dynamics leading to the time decay of the reorientation correlation functions discussed above, we focus now on the angular velocity correlation function $\Omega(t)$. As it is seen in Figure 3.49, it is obvious to notice that the decay time of $\Omega(t)$ is much strongly dependent on the density (the temperature) than that was found for $C_{\ell(t)}^u = 1$ ($u = x, z$). At low temperatures, the time decay of $\Omega(t)$ is the fastest (the more hindered) and it is characterized by an occurrence of a negative region. As the temperature increases, this negative region disappears progressively in favor of a positive minimum which depth decreases and disappears completely in the temperature range where a maximum in the thermal expansion occurs. The short time behavior indicates that the rotation motion is more and more hindered with decreasing the temperature. This behavior may be associated with the strengthening of specific interaction (at low temperature), indicating an increase of the effective inertia moment (some sort of rotation dragging process), the consequence is that ammonia molecule rotation becomes more hindered.

At low temperatures, the negative minimum in $\Omega(t)$ indicates a complete reversal of the direction of rotation of the angular velocity. It is then expected that the time behavior of the reorientation correlation of the z (direction of the dipole moment) and of the x (or y) axes should display signatures of the occurrence of this minimum in $\Omega(t)$. Figure 3.47A and B show that only an inflexion point (kink) occurs in the time behavior of $C_{\ell(t)}^z = 1$, however almost an exponential decay characterizes the time decay of $C_{\ell(t)}^x = 1$. It is obvious that the reversal in the direction of angular velocity is not translated in an isotropic way on the reorientation dynamics of the x (or y) and z molecular axes. In order to rationalize the connection between the time behavior of the reorientation and angular velocity correlation functions, we then calculated the

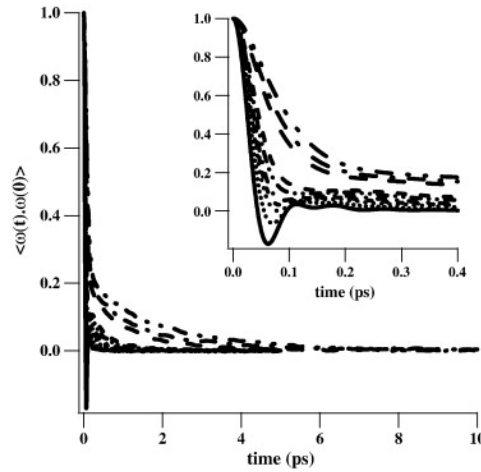


Figure 3.49: Angular velocity correlation functions. The short time behavior is given in the inset. The same legend as in Figure 3.47

angular velocity correlation function around the principal axes (x, z) of ammonia as follow:

$$\Omega_i(t) = \langle \omega(t) \cdot \omega(0) \rangle$$

where $i = x, z$. Note that $\Omega_x(t)$ and $\Omega_y(t)$ are equal. $\Omega_x(t)$ and $\Omega_z(t)$ are given in Figure 3.50A and B and the corresponding correlation times are given in Figure 3.48. As the temperature increases, the time difference between $\tau_{\omega z}$ and $\tau_{\omega x}$ is increases smoothly and it increases drastically for the temperature higher than the critical one.

The correlation function $\Omega_z(t)$ never undergoes a complete reversal of rotation direction. Indeed, at low temperature, a sudden increase of the angular velocity correlation characterizes the intermediate time decay of $\Omega_z(t)$. As the temperature increases, an exponential decay characterizes its long time behavior. However, $\Omega_x(t)$ is characterized by an occurrence of negative minimum (indicating a reversal in the direction of rotation of ω_x) which depth decreases and shifts to occur at longer time when the temperature increases. For temperatures higher than 410 K, the negative minimum disappears and an exponential decay is observed. These results show that the time behavior of $\Omega(t)$ (particularly the negative region) is mainly associated with that occurring in $\Omega_x(t)$.

The analysis of the intermediate time behavior (0.05–0.15 ps) of $C_{\ell(t)}^u = 1$ ($u = x, z$) and $\Omega_i(t)$ ($i = x, z$) suggests that they are connected. Indeed, at low temperatures, the negative minimum of $\Omega_x(t)$ occurs in the intermediate time region (0.05–0.15 ps) where $C_{\ell(t)}^z = 1$ is characterized by a kink, whereas, $\Omega_z(t)$ is characterized by a sudden increase of the correlation where $C_{\ell(t)}^x = 1$ is characterized by an exponential decay. At high temperatures, $\Omega_x(t)$ and $\Omega_z(t)$ have an exponential decay and $C_{\ell(t)}^x = 1$ and $C_{\ell(t)}^z = 1$ are characterized by a sudden increase of the correlation (glitch) indicating

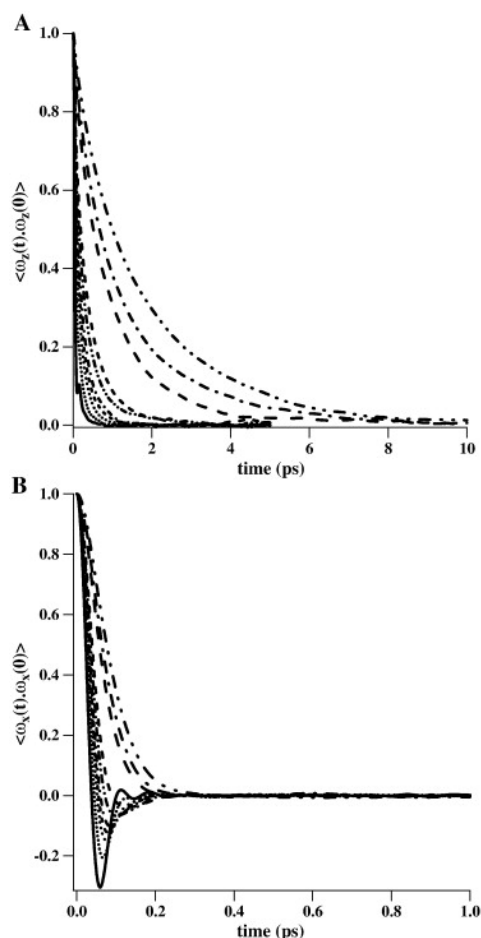


Figure 3.50: A: Angular velocity correlation functions about the principal molecular axis z. The same legend as in Fig. 5A. B: Angular velocity correlation functions about the principal molecular axis x. The same legend as in Figure 3.47

a free reorientation behavior.

Structure. In order to reveal some information relative to the local intermolecular structure in ammonia, we have calculated the radial distribution functions (RDFs), g_{N-N} , g_{N-H} and g_{H-H} as a function of temperatures (density). These functions are given in Figure 3.51A, B and C. By inspecting these functions, we may observe that a gap is observed between the RDFs calculated at temperatures below and higher than 410 K. The occurrence of this gap coincides with the range of temperature at which the maximum of the thermal expansion occurs. Furthermore, starting from this temperature, the exact location of the first minimum becomes undefined and as a consequence the spatial extent of the first shell is difficult to define. In order

to get more insight on the subtle changes induced by increasing the temperature on the g_{N-N} RDF, we used the generalized two-dimensional correlation approach (Noda 1990). The aim of this mathematical tool is to emphasize in phase (synchronous signal) and out of phase (asynchronous signal) correlation between the change in g_{N-N} values occurring at different distance r that are induced by the increase of the temperature. The intensity of the synchronous 2D correlation signal $\varphi(r_1, r_2)$ represents the simultaneous or coincidental changes of two separate intensity variations of g_{N-N} measured at r_1 and r_2 during the measurement interval of the external perturbations (here is the temperature T), while the intensity of the asynchronous signal $\psi(r_1, r_2)$ represents sequential or successive, but not coincidental changes of the intensity variation of g_{N-N} measured separately at r_1 and r_2 . The equations used to obtain these two quantities are given in reference (Noda 1990). The synchronous $\varphi(r_1, r_2)$ and asynchronous $\psi(r_1, r_2)$ signals are given in Figure 3.52A and B, respectively. The two diagonal peaks in the synchronous signal located respectively at 3.25 Å and 4.5 Å represent the susceptibility of these distance regions of g_{N-N} to change as the temperature increases. The asymmetric shape of the diagonal peak corresponding to the range of distance between 4.0 and 5.5 Å indicates that the temperature induces a large effect on the structural arrangement particularly in the distance region located between the first and second solvation shells (distance region of the minimum). The negative sign (red color) of the cross peak indicates that the g_{N-N} values of the first peak (3.5 Å) is decreasing while those of the second peak (between 4 and 5.5 Å) are increasing. The cross negative peak (red color) in the asynchronous signal suggests that the changes of the g_{N-N} values occur predominantly at the distance region of the first peak before the distance region of the second peak in a sequential order of increasing the temperature. Furthermore, at low temperature, the first small peak in g_{N-H} at about 2.47 Å is associated with the occurrence of hydrogen bond (Tongraar, Kerdcharoen, and Hannongbua 2006). The values of the coordination number $n_{N-H}(r)$ indicate that in average one nitrogen atom is hydrogen bonded to one hydrogen atom. This is in good agreement with previous simulations (Hannongbua 2000). This number is relatively small, especially when compared to that in liquid water. As the temperature increases the first small peak in g_{N-H} is smeared out indicating the weakening of hydrogen bond involving nitrogen atom. This decrease is also indicated by the behavior of the microscopic density (Tucker 1999) of hydrogen atoms around nitrogen which is calculated using the expression :

$$\rho_m(r) = \frac{n_{N-H}(n)}{\frac{4}{3}\pi(r^3 - R_C^3)} \quad (3.4)$$

where $n_{N-H}(r)$ is the coordination number of hydrogen atoms around a nitrogen atom at distance r between two atoms given by the expression:

$$n_{N-H}(r) = \rho_m \int_0^r g_{N-H}(r') 4\pi r' dr' \quad (3.5)$$

where, ρ_m is the macroscopic density and g_{N-H} is the nitrogen–hydrogen radial distribution function.

In (3.4), the term $\frac{4}{3}\pi r^3$ is a volume of a sphere of radius r , and $\frac{4}{3}\pi R_c^3$ is the volume occupied by a probe molecule. R_c is the distance at which g_{N-H} starts to be different from zero and is estimated to equal to 1.83 Å.

As shown in Figure 3.53, $\rho_m(r)$ is higher than the macroscopic density in the range of the first shell of neighbour molecules; particularly around a distance indicated by an arrow, one may notice the decrease of the microscopic density of hydrogen atoms around a nitrogen atom. This result is to be correlated with the behavior of the rotation relaxation about the x axis which becomes less and less hindered when the temperature increases.

Concluding remarks. Molecular dynamics simulations have been performed to analyze the changes in the intermediate time behavior of the reorientation correlation function along the 135 bar isobar and in a density range between 0.666 g/cm³ and 0.074 g/cm³. It has been shown that this intermediate time behavior is correlated with that of the angular velocity. Indeed, at low temperatures, it has been shown that the negative minimum that appears in the intermediate time of the angular velocity correlation around the x axis, displays a signature as kink in that of the reorientation of the dipole axis (z), while the sudden increase of the angular velocity correlation around the dipole axis, displays a signature as an exponential decay in that of the reorientation of the x axis. At higher temperatures than the critical one, the exponential decay behavior of the angular velocity correlation functions around the x and z displays a signature as a sudden increase of the reorientation correlation of the x and z axes, indicating a free reorientation behavior.

The time behavior of the reorientation and angular velocity correlation functions is traced back to the changes occurring at a level of the local environment. Indeed, at low temperatures, the analysis of the first nearest radial distribution function of hydrogen atoms around a reference nitrogen atom as well as the corresponding microscopic density indicate that the hydrogen bond interactions are enough strong (although weak as a comparison with water) to affect the time behavior of the reorientation and angular velocity correlation functions.

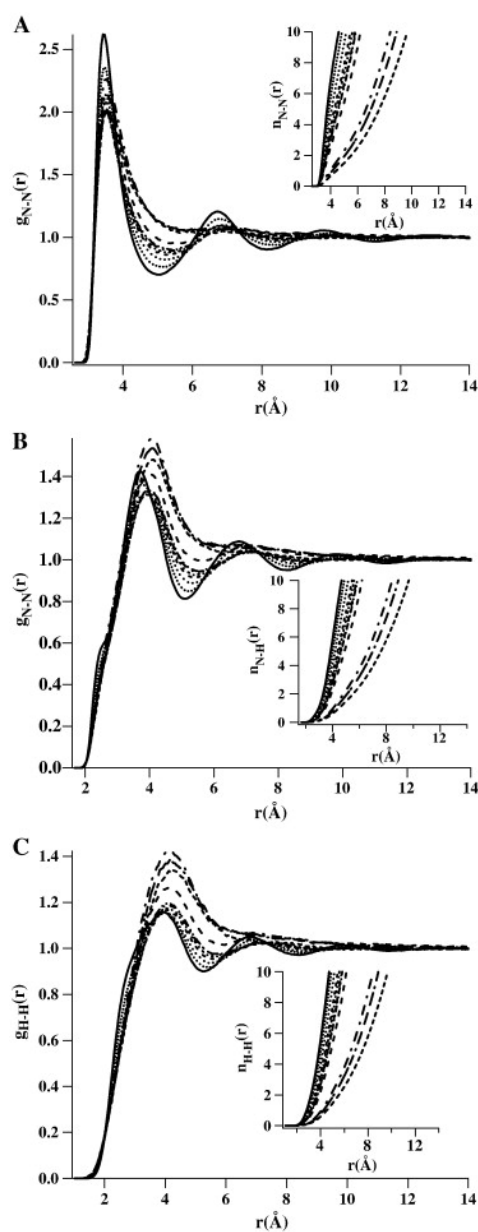


Figure 3.51: A: Radial distribution functions g_{N-N} and the corresponding coordination number is given in the inset. The same legend as in Figure 3.47A. B : Radial distribution functions g_{N-H} and the corresponding coordination number is given in the inset. The same legend as in Figure 3.47A. C: Radial distribution functions g_{H-H} and the corresponding coordination number is given in the inset. The same legend as in Figure 3.47

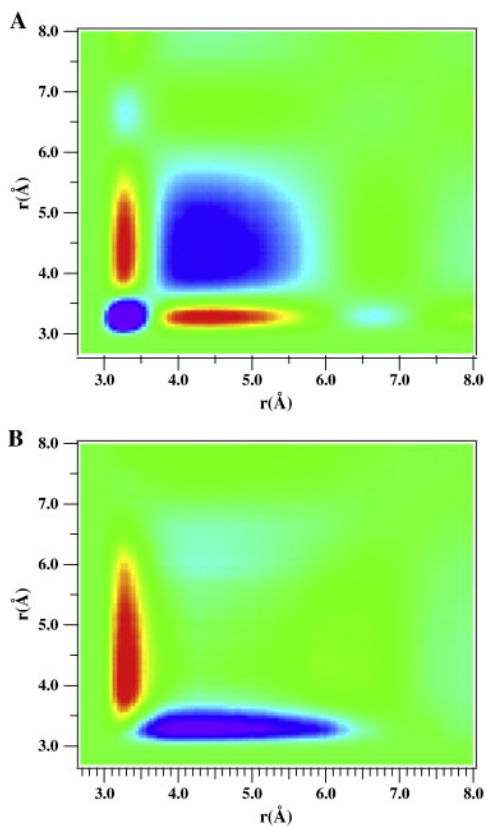


Figure 3.52: A: Synchronous 2D correlation signal of the g_{N-N} radial distribution function. Positive peaks are in blue, negative ones are in red. B: Asynchronous 2D correlation signal of the g_{N-N} radial distribution function. The same legend as for A.

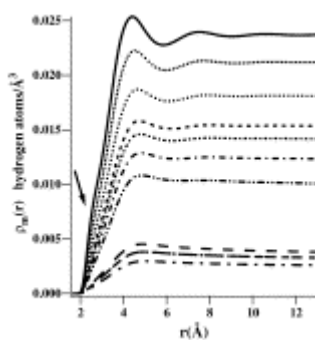


Figure 3.53: Behavior of the microscopic density.

3.2 Properties of mixtures of carbon dioxide with cosolvents

3.2.1 Thermodynamic integration for carbon dioxide–ethanol and carbon dioxide–acetone systems

In the present section we present computer simulations of binary mixtures of CO₂ with acetone and ethanol above the critical point of CO₂ in the entire composition range from neat CO₂ to neat acetone or ethanol. From the number of existing models of CO₂ (Murthy, Singer, and McDonald 1981; Harris and Yung 1995; Potoff and Siepmann 2001; Zhang and Duan 2005) we have chosen that of Zhang and Duan (Zhang and Duan 2005) because this model is claimed to reproduce most accurately (Zhang and Duan 2005) the experimental critical point of CO₂ of $T_c = 304.13$ K, $\rho_c = 0.4676$ g/cm³, $p_c = 7.377$ MPa (Duschek, Kleinrahm, and Wagner 1990) and provides an excellent description of the thermodynamic, structural and transport properties of neat CO₂ in a broad range of supercritical states (Zhang and Duan 2005). It should, however, also be noted that this claim has later been challenged by Merker et al. (Merker, Vrabec, and Hasse 2008). For acetone and ethanol we have tested models belonging to three different potential families, namely to the Transferable Potentials for Phase Equilibria (TraPPE) (Chen, Potoff, and Siepmann 2001; Stubbs, Potoff, and Siepmann 2004) Optimized Potential for Liquid Simulations (OPLS) (Jorgensen, Madura, and Swenson 1984; Jorgensen 1986; Jorgensen, Briggs, and Contreras 1990), and Anisotropic United Atom 4 (AUA4) (Ungerer et al. 2000; Ferrando et al. 2009; Ferrando, Lachet, and Boutin 2010) force fields. Finally, the simulations involving the TraPPE models of acetone and ethanol have also been repeated using the TraPPE model of CO₂ (Potoff and Siepmann 2001) instead of that of Zhang and Duan.

To characterize the mixtures of various different models of acetone and ethanol with those of scCO₂ we calculate the change of various thermodynamic properties accompanying the mixing of the two neat components. Thus, volume, energy, entropy and Helmholtz free energy of mixing of the two components are evaluated in the entire composition range, and are compared for the different model pairs and, whenever possible, also with experimental data. However, while the calculation of the energy and volume of mixing of two neat components is rather straightforward, that of the free energy (and, consequently, also the entropy) of mixing is far from being a trivial task. The Helmholtz free energy change accompanying the mixing of two miscible neat components is, however, a key thermodynamic quantity, because under constant volume conditions spontaneous mixing occurs only if this free energy change is negative. Therefore, reproducing at least the sign of the free energy change of mixing of two neat components in a computer simulation is an obvious prerequisite of considering the corresponding potential model pair as a reliable rep-

resentation of the system of interest. (Jedlovsky, Idrissi, and Jancsó 2009)

Like other free energy calculation methods, thermodynamic integration (TI) (Mezei and Beveridge 1986; Leach 2001) proved to be a suitable tool to determine the excess Helmholtz free energy of a given (condensed) phase relative to the ideal gas state (Jedlovsky, Idrissi, and Jancsó 2009; Mezei and Beveridge 1986; Leach 2001; Mezei, Swaminathan, and Beveridge 1978; Mezei 1989; Mináry et al. 2000; Jedlovsky et al. 2008b). Based on this fact, recently we proposed a way of calculating the Helmholtz free energy of mixing of two neat phases using thermodynamic integration (Darvas, Jedlovsky, and Jancsó 2009). This method is based on a thermodynamic cycle, in which the mixing of the two neat components is achieved by (a) bringing them separately to the ideal gas state; (b) mixing them in the ideal gas state; and (c) finally bringing the mixed system back from the ideal gas state to the state of interest. Thus, the free energy change accompanying steps (a) and (c) can be obtained by performing TI calculations on the neat systems and on the mixture, respectively, while step (b) is accompanied by the free energy change of ideal mixing, i.e., $RT(x_A \ln x_A + x_B \ln x_B)$, where R is the gas constant, T is the absolute temperature, and x_A and x_B are the mole fractions of the respective components (see Fig.1 of ref. (Darvas, Jedlovsky, and Jancsó 2009)). This method is used here for the calculation of the Helmholtz free energy (and thus also the entropy) of mixing of scCO₂ with acetone and ethanol.

The section is organized as follows. In subsection 3.2.1 a detailed description of the calculations performed is given. Thus, the calculated thermodynamic properties are summarized, the potential models considered are described in detail, the method of thermodynamic integration is reminded and details of the performed simulations are presented. The obtained results are presented and discussed in detail in subsection 3.2.1. Finally, in subsection 3.2.1 the main conclusions of this study are summarized.

Calculated properties

In characterizing the thermodynamic properties of the acetone/CO₂ and ethanol/CO₂ mixtures simulated we have calculated the change of the molar volume, internal energy, Helmholtz free energy and entropy accompanying the mixing of the two components, as

$$V^{mix} = V_{AB} - x_A V_A - x_B V_B, \quad (3.6)$$

$$U^{mix} = U_{AB} - x_A U_A - x_B U_B, \quad (3.7)$$

$$F^{mix} = F_{AB} - x_A F_A - x_B F_B + RT(x_A \ln x_A + x_B \ln x_B), \quad (3.8)$$

$$S^{mix} = S_{AB} - x_A S_A - x_B S_B - R(x_A \ln x_A + x_B \ln x_B). \quad (3.9)$$

In these equations V , U , F and S stand for the volume, internal energy, free energy and entropy of one mole of the corresponding system at the pressure of vapour-liquid

coexistence, indices A, B and AB of these molar quantities refer to the neat systems of components A (standing here for acetone or ethanol) and B (i.e., CO₂) and to that of their mixture, respectively, x_A and x_B are the mole fractions of components A and B, respectively, in their mixture (and, hence, $x_A + x_B = 1$), and the term $R(x_A \ln x_A + x_B \ln x_B)$ in eqn Equation 3.8 and Equation 3.9 is the molar entropy of ideal mixing.

All calculations have been performed at the temperature of $T = 313$ K for mixtures consisting of 5, 10, 20, 30, 40, 50, 60, 70, 80 and 90 mol% acetone or ethanol. Since our preliminary results indicated some peculiar features of the systems of low acetone/ethanol content, V^{mix} has also been evaluated for systems consisting of 15 mol% acetone or ethanol. The pressure of the saturated vapour of the various systems has been taken from the literature. (Brennecke and Chateauneuf 1999; NIST 1962; Chiu, Lee, and Lin 2008) In the case of neat CO₂, which is already above its critical temperature of 304.13 K (Duschek, Kleinrahm, and Wagner 1990), the pressure corresponding to the supercritical extension of the vapour–liquid coexistence curve according to the Clausius–Clapeyron equation has been used. The pressure values used in the calculations are collected in Table 3.7.

The molar volume and internal energy of the various mixed systems as well as of the neat components have been determined by Monte Carlo simulations performed on the isothermal–isobaric (N,p,T) and canonical (N,V,T) ensembles, respectively, their molar free energy has been calculated by the method of thermodynamic integration, whereas the molar entropy has simply been obtained as

$$S = \frac{U - F}{T} \quad (3.10)$$

for the considered systems.

Potential models

In describing both the acetone and the ethanol molecules in the calculations we have used three different potential models, belonging to the TraPPE, (Stubbs, Potoff, and Siepmann 2004; Chen, Potoff, and Siepmann 2001), OPLS (Jorgensen, Madura, and Swenson 1984; Jorgensen 1986; Jorgensen, Briggs, and Contreras 1990) and AUA4 (Ungerer et al. 2000; Ferrando et al. 2009; Ferrando, Lachet, and Boutin 2010) force fields, respectively. According to these models hydrogens bound to a C atom have not explicitly been described; the CH₂ and CH₃ groups have been treated as united atoms. In the case of the TraPPE and OPLS potentials the interactions are centred on the atomic sites, whereas in the case of the AUA4 potential, following the original idea of Toxvaerd (Toxvaerd 1990) the centre of the Lennard–Jones interaction corresponding to the CH₂, CH₃, (Ungerer et al. 2000) and alcoholic OH groups (Ferrando et al. 2009) is displaced from the C or O atom toward the center-of-mass of the entire group. For CO₂ we have used the potential model proposed by Zhang and Duan (Zhang

Acetone/ ethanol mole fraction	Number of CO ₂	Number of acetone/ ethanol	Acetone/CO ₂		Ethanol/CO ₂	
			p/bar ^a	ϵ ^b	p/bar ^a	ϵ ^c
0.00	512	0	105.1 ^{d,e}	1.37 ^c	105.1 ^{d,e}	1.37
0.05	486	26			81.5	1.72
0.10	461	51	72.0	2.03	79.8	2.13
0.15	435	77			78.9	2.77
0.20	410	102	61.8	3.10	77.7	3.38
0.30	358	154	53.4	4.54	75.7	5.05
0.40	307	205	44.7	6.16	72.5	6.93
0.50	256	256	35.3	7.96	67.2	9.02
0.60	205	307	27.5	9.86	59.8	11.22
0.70	154	358	19.7	11.84	49.7	13.52
0.80	102	410	12.2	13.83	36.4	15.82
0.90	51	461	3.25 ^f	16.35	18.6	18.75
1.00	0	512	0.53 ^d	19.6 ^g	0.18 ^d	22.52

Table 3.7: Characteristics of the simulated systems

a. (Chiu, Lee, and Lin 2008)

b. Data obtained by assuming the same composition dependence of the dielectric constant between the values for the two neat components as in the CO₂/ethanol mixtures.

c. (Wesch, Dahmen, and Ebert 1996)

d. (NIST 1962)

e. Value along the supercritical extension of the vapour-liquid coexistence curve

f. (Day, Chang, and Chen 1996)

g. (Khimenko M. T. And N.N. 1973)

and Duan 2005) as it was claimed to accurately reproduce the critical point of CO₂ although this claim was later questioned by other authors. However, since our present results indicate that this model fails in reproducing the experimental molar volume of CO₂ at 313 K, we have also calculated the mixing properties of CO₂ with acetone and ethanol using the TraPPE potential for CO₂ (Potoff and Siepmann 2001) as well as for the other component. (Chen, Potoff, and Siepmann 2001; Stubbs, Potoff, and Siepmann 2004). All molecular models used have been rigid and the interaction sites have been arranged in a planar (acetone and ethanol) or co-linear (CO₂) way. The bond lengths and bond angles of these models as well as the interaction offset parameters δ of the AUA4 models are collected in Table 3.8. The systems described by the above combinations of the potential models are referred to as TraPPE/Zhang, OPLS/Zhang, AUA4/Zhang, and TraPPE/TraPPE systems, respectively, throughout this paper.

Thermodynamic integration

The method of thermodynamic integration (TI) (Mezei and Beveridge 1986; Leach 2001) can provide the Helmholtz free energy difference of the system of interest between its thermodynamic states X and Y, where Y denotes the state of interest and X is an appropriately chosen reference state. When applying the method for the calculation of the entire free energy characterizing a given phase the reference state X is usually chosen to be the ideal gas state of the system. In this way, the method yields the excess Helmholtz free energy of the system at state Y (relative to the ideal gas state). Mathematics of the method is explained in subsection 2.5.2 In our case a simulation is performed with the potential function $U(\lambda)$ at the temperature T is technically equivalent with a simulation performed using the full U_Y potential at the temperature T^* . It should be emphasized that the simulations performed at the various T^* virtual temperatures do not directly correspond to any physically meaningful system, in accordance with the fact that the coupling parameter λ connects the real physical systems X and Y along a continuous path of fictitious states.

In the present study we have determined the integrand at five different λ values corresponding to the five point Gaussian quadrature, i.e., at 0.046911, 0.230765, 0.5, 0.769235 and 0.953089, respectively, by performing Monte Carlo simulations on the canonical (N,V,T) ensemble. In order to calculate also the molar potential energy (and, hence, the molar entropy) of the different systems, an additional simulation of each system has also been performed at $\lambda = 1$. The integral of eqn (2.59) has been calculated by fitting a fourth order polynomial to the integrand values calculated at the quadrature points and performing the integration of this fitted function analytically. The integrand values and the polynomials fitted to them are shown in Figure 3.54 for the AUA4/Zhang systems of selected compositions.

Integrand of the thermodynamic integration performed for the AUA4/Zhang systems of ethanol/CO₂ (top) and acetone/CO₂ (bottom) mixtures of selected composi-

Molecule	Potential model	Bond between sites	Bond length/Å	Angle formed by sites	Bond angle/deg	Offset from sites/Å	Interaction offset/Å
Acetone	TraPPE ^a	C=O	1.229	CH ₃ -C=O	121.4		
		C-CH ₃	1.520	CH ₃ -C-CH ₃	117.2		
	OPLS ^b	C=O	1.222	CH ₃ -C=O	121.4		
		C-CH ₃	1.507	CH ₃ -C-CH ₃	117.2		
	AUA4 ^c	C=O	1.229	CH ₃ -C=O	120.4	CH ₃	0.216 ^d
		C-CH ₃	1.522	CH ₃ -C-CH ₃	119.2		
Ethanol	TraPPE ^e	CH ₃ -CH ₂	1.535	CH ₃ -CH ₂ -O	109.47		
		CH ₂ -O	1.430	CH ₂ -O-H	108.50		
		O-H	0.945				
	OPLS ^f	CH ₃ -CH ₂	1.530	CH ₃ -CH ₂ -O	108.00		
		CH ₂ -O	1.430	CH ₂ -O-H	108.50		
		O-H	0.945				
	AUA4 ^g	CH ₃ -CH ₂	1.535	CH ₃ -CH ₂ -O	109.47	CH ₃	0.216
		CH ₂ -O	1.430	CH ₂ -O-H	108.50	CH ₂	0.384
		O-H	0.945			O	0.010
CO ₂	Zhang ^h	C=O	1.163	O=C=O	180.00		
	TraPPE ⁱ	C=O	1.160	O=C=O	180.00		

Table 3.8: Geometry parameters of the potential models used

- a.* (Stubbs, Potoff, and Siepmann 2004)
b. (Jorgensen, Briggs, and Contreras 1990)
c. (Ferrando, Lachet, and Boutin 2010)
d. (Ungerer et al. 2000)
e. (Chen, Potoff, and Siepmann 2001)
f. (Jorgensen 1986)
g. (Ferrando et al. 2009)
h. (Zhang and Duan 2005)
i. (Potoff and Siepmann 2001)

Molecule	Potential model	Site	$\sigma/\text{\AA}$	$\epsilon/\text{kJ}\cdot\text{mol}^{-1}$	q/e
Acetone	TraPPE ^a	CH ₃	3.790	0.8144	0
		C	3.820	0.3324	0.424
		O	3.05	0.6565	-0.424
	OPLS ^b	CH ₃	3.910	0.6696	0.062
		C	3.750	0.4394	0.300
		O	2.960	0.8788	-0.424
	AUA4 ^c	CH ₃	3.607d	0.9985d	0.000
		C	3.020	0.5143	0.490
		O	2.981	0.8020	-0.490
Ethanol	TraPPE ^d	CH ₃	3.750	0.8144	0
		CH ₂	3.950	0.3823	0.265
		O	3.020	0.7729	-0.700
		H	—	—	0.435
	OPLS ^e	CH ₃	3.905 ^f	0.7327 ^f	0
		CH ₂	3.905g	0.4940g	0.265
		O	3.070	0.7118	-0.700
		H	—	—	0.435
	AUA4 ^g	CH ₃	3.607	0.9985	0
		CH ₂	3.461	0.7171	0.265
		O	3.081	1.0389	-0.700
		H	—	—	0.435
CO ₂	Zhang ^h	C	2.792	0.2398	0.5888
		O	3.000	0.6869	-0.2944
	TraPPE ⁱ	C	2.800	0.2244	0.70
		O	3.050	0.6566	-0.35

Table 3.9: Interaction parameters of the potential models used

a. (Stubbs, Potoff, and Siepmann 2004)

b. (Jorgensen, Briggs, and Contreras 1990)

c. (Ungerer et al. 2000)

d. (Chen, Potoff, and Siepmann 2001)

e. (Zhang and Duan 2005)

f. (Jorgensen, Madura, and Swenson 1984)

g. (Ferrando et al. 2009)

h. (Zhang and Duan 2005)

i. (Potoff and Siepmann 2001)

tions. The values calculated at the quadrature points for the systems containing 0%, 20%, 40%, 60%, 80% and 100% ethanol or acetone are shown by asterisks, squares, circles, up triangles, down triangles and diamonds, respectively, while the fourth order polynomials fitted to these data are shown by solid curves.

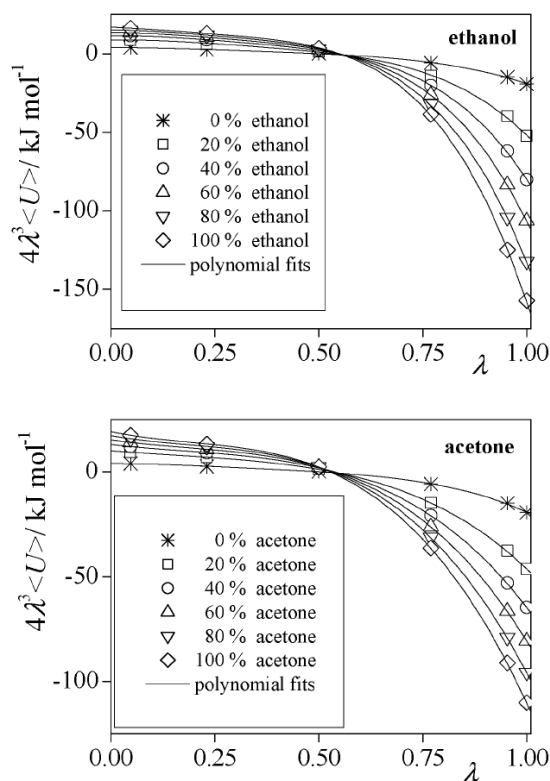


Figure 3.54: Integrand of the thermodynamic integration performed for the AUA4/Zhang systems of ethanol/ CO_2 (top) and acetone/ CO_2 (bottom) mixtures of selected compositions. The values calculated at the quadrature points for the systems containing 0%, 20%, 40%, 60%, 80% and 100% ethanol or acetone are shown by asterisks, squares, circles, up triangles, down triangles and diamonds, respectively, while the fourth order polynomials fitted to these data are shown by solid curves.

Monte Carlo simulations

Simulations on the (N,V,T) ensemble. In order to evaluate the ensemble average in (2.59) Monte Carlo simulations have been performed on the canonical (N,V,T) ensemble at the virtual temperatures corresponding to the λ values at which the integrand is calculated. The volume of the cubic basic simulation box has been chosen in accordance with the molar volume of the given system at the pressure of its saturated

vapour. The volume values to be used in these simulations have been determined by preliminary Monte Carlo simulations performed on the isothermal–isobaric (N,p,T) ensemble. The systems consisted of 512 molecules. Standard periodic boundary conditions have been applied.

The energy of the systems has been calculated according to (2.14). All interactions have been truncated to zero beyond the molecule-based cut-off distance of 12.5 Å. The long range part of the electrostatic interactions has been accounted for by means of the reaction field correction method (Allen and Tildesley 1987; Barker and Watts 1973; Neumann 1985). For the dielectric constant ϵ of the ethanol/CO₂ systems we used the experimental data of Wesch et al. measured at 313.15 K.⁶⁶ The dielectric constant of the acetone/CO₂ systems has been estimated by assuming the same composition dependence of λ as in the case of the ethanol/CO₂ systems, using the dielectric constant of neat acetone (Khimenko M. T. And N.N. 1973). The dielectric constant values used in the simulations are summarized in Table 3.7.

The simulations have been performed using the program MMC. (*MMC: Monte Carlo program for simulation of molecular assemblies.*) In each simulation step a randomly chosen molecule has randomly been translated by no more than 0.25 Å and has randomly been rotated around a randomly chosen space-fixed axis by no more than 10°. In this way, at least 50% of the tried moves have been successful in every case. The systems have been equilibrated by performing $5 \cdot 10^7$ Monte Carlo steps. The ensemble average of has then been calculated over 10^8 equilibrium sample configurations in the production stage of the simulations.

Simulations on the (N,p,T) ensemble. In order to evaluate the molar volume of the different systems and also to determine the volume of the basic box to be used in the (N,V,T) ensemble simulations we have also performed a Monte Carlo simulation of each system on the isothermal–isobaric (N,p,T) ensemble prior to the canonical ensemble simulations used for the thermodynamic integration. These simulations have been done in the same way as those on the (N,V,T) ensemble. The pressure has been set to the saturated vapour pressure of the corresponding system (Day, Chang, and Chen 1996; NIST 1962; Chiu, Lee, and Lin 2008) (see Table 3.7). In the simulations every 512 particle displacement steps have been followed by a volume change trial, in which the volume of the basic box has been attempted to be randomly altered by no more than 1000 Å³. The ratio of the accepted and tried volume changes has been at least 0.6 in every case. Following an equilibration period of $5 \cdot 10^7$ Monte Carlo steps the molar volume of the systems has been evaluated by averaging over 10^8 equilibrium sample configurations.

Results and discussion

Molar volume. The composition dependence of the molar volume of the ethanol/CO₂ and acetone/CO₂ mixtures obtained with different model pairs is shown and compared with experimental data (Day, Chang, and Chen 1996; Span and Wagner 1996; Seifried and Temelli 2010; Sih and Foster 2008) in Figure 3.55. As is seen, the molar volume of neat CO₂ is considerably better reproduced by the TraPPE potential than by the model of Zhang and Duan, as it results in only 12%, whilst the Zhang–Duan model results in 44% higher molar volume than the experimental value of 70 (Liu and Kiran 2007). cm³/mol. (Span and Wagner 1996) For ethanol, the experimental molar volume of 59.83 cm³/mol 70 is reproduced within about 1% both by TraPPE and AUA4 (being slightly overestimated by the former, and underestimated by the latter one), whereas the deviation of the OPLS result from the experimental value is considerably larger, being about 5%. In the case of acetone, however, AUA4 performs significantly better than the other two models considered, as it reproduces the experimental molar volume of 75.40 cm³/mol 71 within 2%, whilst this deviation is about 6–7% for TraPPE and OPLS.

Composition dependence of the molar volume of the ethanol/CO₂ (top) and acetone/CO₂ (bottom) systems simulated. The data obtained with the TraPPE/Zhang, OPLS/Zhang, AUA4/Zhang and TraPPE/TraPPE model combinations are shown by open squares, open circles, open triangles and asterisks, respectively. The lines connecting the symbols are just guides to the eye. For comparisons, experimental data obtained by (Day, Chang, and Chen 1996) (full circles) and (Sih and Foster 2008) (full squares) are also shown. The insets show the large x_A part of the data on a magnified scale.

As far as the mixtures are concerned, above the ethanol or acetone mole fraction of 0.3 the AUA4/Zhang model pair performs the best. The advantage of this model combination over the other ones considered here is evident in the case of acetone (see the lower inset of Figure 3.55), whereas for ethanol/CO₂ mixtures the TraPPE ethanol model provides nearly as good results with both CO₂ potentials as the AUA4/Zhang model pair.

The most dramatic feature of the calculated $V(x_A)$ curves is clearly the huge peak at low ethanol or acetone mole fraction values, around $x_A = 0.05$. Clearly, with the exception of the AUA4 acetone model, the highest molar volume is always obtained at this x_A value. Further, at $x_A = 0.1$ (in the case of acetone) and at $x_A = 0.15$ (in the case of ethanol) the resulting molar volume values are always already smaller than what is obtained for neat CO₂. Although the height of this narrow molar volume peak turns out to be strongly model dependent, its existence is clearly predicted by all model combinations considered for ethanol/CO₂ mixtures, and by all but one (i.e., AUA4/Zhang) combination for acetone/CO₂ mixtures.

Although the accurate prediction of this peak could be a stringent test of the different model combinations, unfortunately, we are not aware of any experimental

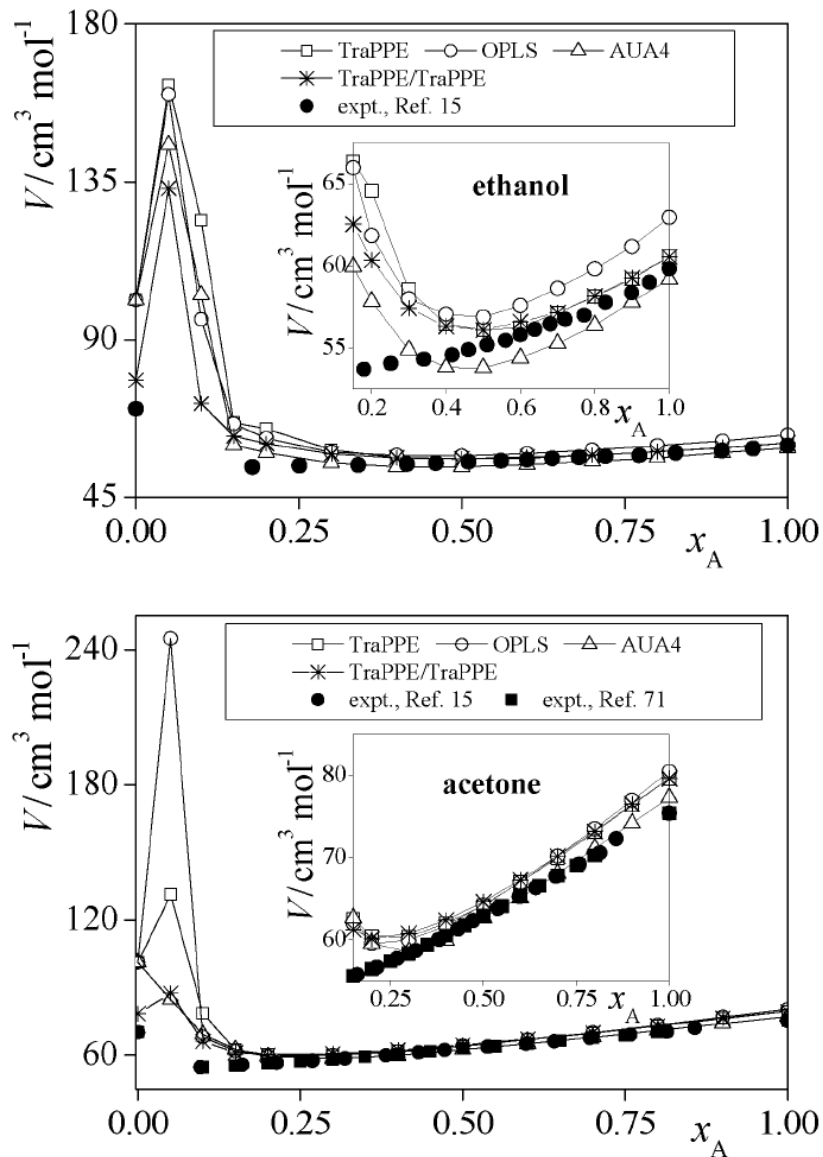


Figure 3.55: Composition dependence of the molar volume of the ethanol/CO₂ (top) and acetone/CO₂ (bottom) systems simulated. The data obtained with the TraPPE/Zhang, OPLS/Zhang, AUA4/Zhang and TraPPE/TraPPE model combinations are shown by open squares, open circles, open triangles and asterisks, respectively. The lines connecting the symbols are just guides to the eye. For comparisons, experimental data obtained by Day et al. (Day, Chang, and Chen 1996) (full circles) and Sih and Foster (Sih and Foster 2008) (full squares) are also shown. The insets show the large x_A part of the data on a magnified scale.

data in this composition range, i.e., below the x_A values of 0.18 (for ethanol/ CO_2 mixtures) and 0.1 (for acetone/ CO_2 mixtures). The observed large molar volume peak at very low ethanol or acetone mole fractions is probably related to the fact that these molecules, forming a liquid phase at the simulated temperature of 313 K, are dispersed in a supercritical phase in this composition range. Conversely, the decay of this peak, i.e., the sudden sharp increase of the density around the x_A values of 0.1–0.15, indicates the transformation of the supercritical system to a liquid mixture.

To check whether the appearance of the molar volume peak at low solute mole fractions is indeed related to the transition of the system from the supercritical to the liquid state, Voronoi polyhedra (VP) analysis (Voronoi 1908; N. 2000) is an appropriate tool. The VP of a particle is the locus of points that are closer to this particle than to any other one in the system. Thus, the volume V of a VP represents the space available for its central particle, whereas reciprocal VP volume is a measure of the local density around this particle. Therefore, the distribution of the VP volume in a system is a quite sensitive indicator of the presence and extent of local density fluctuations. Namely, in the case of homogeneous spatial distribution of the particles, the VP volume distribution has a narrow, symmetric peak, whereas in the presence of large density fluctuations the peak develops a long, exponentially decaying tail at its high volume side. (Zaninetti 1992) We have performed VP analysis of the ethanol/ CO_2 system described by the TraPPE/Zhang model pair at the ethanol mole fraction values of 0, 0.05, 0.1 and 0.2. The positions of the CO_2 and ethanol molecules have been represented by their C atoms and CH_2 groups, respectively. The resulting VP volume distributions are shown in Figure 3.56. As is seen, in the case of neat CO_2 the $P(V)$ distribution already has a rather asymmetric peak, reflecting the fact that the system is not far from the critical point. The presence of ethanol at the mole fraction of 0.05 significantly enhances the asymmetric character of the peak, but further increase of the ethanol mole fraction brings back the peak rapidly to a nearly symmetric shape, indicating the gradual decrease of the density fluctuations upon going farther from the critical point. Thus, at the ethanol mole fraction of 0.1 the peak is still slightly more asymmetric than in neat CO_2 (the exponential character of its decay at large volumes is illustrated in the inset of the figure, which shows this distribution on a logarithmic scale, transforming this decay to linear), whereas at the ethanol mole fraction of 0.2 already a narrow and nearly symmetric peak characteristic of liquid phases is obtained.

Voronoi polyhedra volume distribution of the molecules in the ethanol/ CO_2 mixtures described by the TraPPE/Zhang model pair at the ethanol mole fractions of 0 (solid line), 0.05 (open circles), 0.1 (filled circles), and 0.2 (dash-dotted line). The inset shows the VP volume distribution of all the molecules (filled circles) and that of only the ethanol, disregarding the CO_2 molecules (asterisks) at $x_A = 0.1$ on a logarithmic scale, to emphasize the exponential character of the decay of the peak at large

volumes.

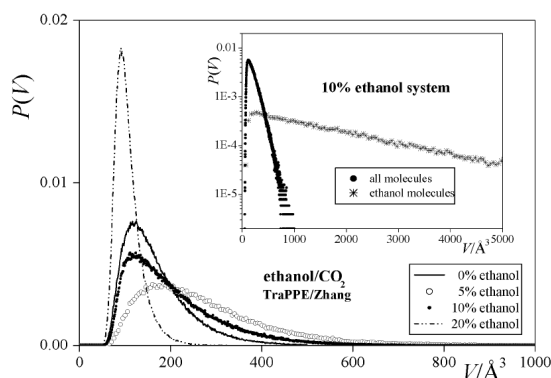


Figure 3.56: Voronoi polyhedra volume distribution of the molecules in the ethanol/ CO_2 mixtures described by the TraPPE/Zhang model pair at the ethanol mole fractions of 0 (solid line), 0.05 (open circles), 0.1 (filled circles), and 0.2 (dash-dotted line). The inset shows the VP volume distribution of all the molecules (filled circles) and that of only the ethanol, disregarding the CO_2 molecules (asterisks) at $x_A = 0.1$ on a logarithmic scale, to emphasize the exponential character of the decay of the peak at large volumes.

Furthermore, besides the density fluctuations accompanying the supercritical-to-liquid transition, the presence of the molar volume peak suggests the possible existence of a gap in the miscibility of the two components here. The lack of experimental data in the corresponding composition range could also be related to this presumed immiscibility, although we did not find any evidence or even claim of this fact in the literature. The problem of this potential existence of this miscibility gap is further addressed in the following sub-section. Nevertheless, the present results clearly stress the need of accurate experimental data on these mixtures at low acetone/ethanol mole fractions.

The molar volume change accompanying the mixing of the two components, V_{mix} , is plotted against x_A in Figure 3.57. When comparing the volumes of mixing rather than the volumes themselves, the advantage of the TraPPE/TraPPE model pair over the other combinations considered becomes evident. Thus, this model pair is able to accurately reproduce experimental data in the entire composition range of its existence, whilst the model pairs containing the Zhang–Duan potential of CO_2 perform considerably worse. This fact can be clearly related to the much better performance of the TraPPE than the Zhang–Duan CO_2 model, as the volume of mixing values are also affected by the possible inaccuracy of the molar volume of neat CO_2 in the entire composition range see (3.6). Considering also the fact that the OPLS model of ethanol proved to be considerably, and that of acetone slightly, worse than

either TraPPE or AUA4 as far as the total volume of the systems of large x_A values is concerned, we can predict that the combination of the AUA4 models of acetone or ethanol with the TraPPE model of CO₂ might be as good as the TraPPE/TraPPE model combinations, whereas model pairs involving either the OPLS acetone/ethanol or the Zhang–Duan CO₂ potential provide less accurate results.

Composition dependence of the change of the molar volume accompanying the mixing of ethanol (top) and acetone (bottom) with CO₂ as obtained in the different systems simulated. The data obtained with the TraPPE/Zhang, OPLS/Zhang, AUA4/Zhang and TraPPE/TraPPE model combinations are shown by open squares, open circles, open triangles and asterisks, respectively. The lines connecting the symbols are just guides to the eye. For comparisons, experimental data obtained by Day et al. (Day, Chang, and Chen 1996) (full circles) and Sih and Foster (Sih and Foster 2008) (full squares) are also shown.

Energetic properties The molar energy, free energy and entropy obtained for the different systems considered at different compositions are shown in Figure 3.58, whilst the composition dependence of the change of these quantities accompanying the mixing of ethanol and acetone with CO₂ is plotted in Figure 3.59 and Figure 3.60, respectively. As is seen, unlike in the case of the molar volume, the energy, free energy and entropy values obtained with the different model combinations are rather close to each other. Thus, surprisingly, the volumetric properties of these mixtures clearly proved to be much more sensitive to the details of the potential models than the energetic properties. It is also seen that the energetic properties change nearly smoothly with the composition, the huge peak of the $V(x_A)$ curves present at $x_A = 0.05$ is only reflected in a small ripple of the $U(x_A)$, $F(x_A)$ and $S(x_A)$ functions.

Composition dependence of the molar energy (top panels), free energy (middle panels) and entropy (bottom panels) of the ethanol/CO₂ (left) and acetone/CO₂ (right) systems simulated. The data obtained with the TraPPE/Zhang, OPLS/Zhang, AUA4/Zhang and TraPPE/TraPPE model combinations are shown by open squares, open circles, open triangles and asterisks, respectively. The lines connecting the symbols are just guides to the eye.

Composition dependence of the change of the molar energy (top panel), free energy (middle panel) and entropy (bottom panel) accompanying the mixing of ethanol with CO₂ as obtained in the different systems simulated. The data obtained with the TraPPE/Zhang, OPLS/Zhang, AUA4/Zhang and TraPPE/TraPPE model combinations are shown by open squares, open circles, open triangles and asterisks, respectively. The lines connecting the symbols are just guides to the eye. The dashed lines show the free energy and entropy contributions of the ideal mixing (see (3.8), (3.9)).

Composition dependence of the change of the molar energy (top panel), free energy (middle panel) and entropy (bottom panel) accompanying the mixing of ace-

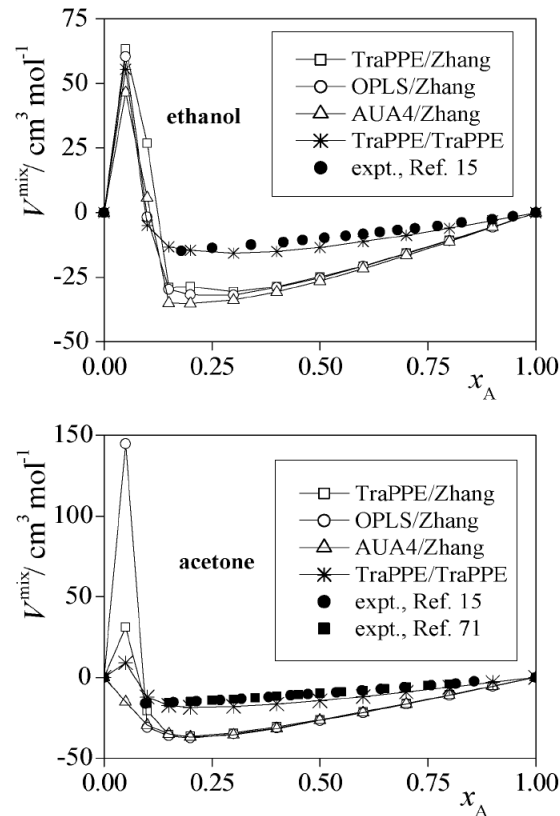


Figure 3.57: Composition dependence of the change of the molar volume accompanying the mixing of ethanol (top) and acetone (bottom) with CO_2 as obtained in the different systems simulated. The data obtained with the TraPPE/Zhang, OPLS/Zhang, AUA4/Zhang and TraPPE/TraPPE model combinations are shown by open squares, open circles, open triangles and asterisks, respectively. The lines connecting the symbols are just guides to the eye. For comparisons, experimental data obtained by Day et al. (Day, Chang, and Chen 1996) (full circles) and Sih and Foster (Sih and Foster 2008) (full squares) are also shown.

tone with CO_2 as obtained in the different systems simulated. The data obtained with the TraPPE/Zhang, OPLS/Zhang, AUA4/Zhang and TraPPE/TraPPE model combinations are shown by open squares, open circles, open triangles and asterisks, respectively. The lines connecting the symbols are just guides to the eye. The dashed lines show the free energy and entropy contributions of the ideal mixing (see eqn (3.8), (3.9)).

This ripple is, however, magnified when calculating the change of these quantities accompanying mixing of the two components (see Figure 3.59 and Figure 3.60). As is seen, the mixing of the two components at $x_A = 0.05$ is energetically highly

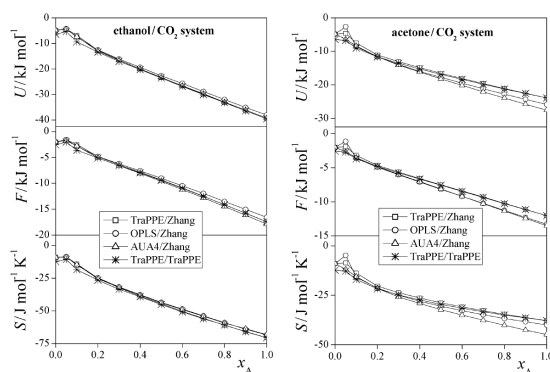


Figure 3.58: Composition dependence of the molar energy (top panels), free energy (middle panels) and entropy (bottom panels) of the ethanol/CO₂ (left) and acetone/CO₂ (right) systems simulated. The data obtained with the TraPPE/Zhang, OPLS/Zhang, AUA4/Zhang and TraPPE/TraPPE model combinations are shown by open squares, open circles, open triangles and asterisks, respectively. The lines connecting the symbols are just guides to the eye.

unfavourable. Although the mixing is accompanied by a larger entropy gain than what would simply correspond to ideal mixing, in the case of the ethanol/CO₂ system this entropy gain is clearly not enough to compensate the increase of the energy. Thus, the free energy of mixing ethanol and CO₂ is found to be positive with every model combinations tested at $x_A = 0.05$ (in the case of the TraPPE/Zhang system even at $x_A = 0.1$), indicating demixing of the system at these compositions. The observed demixing is also illustrated in Figure 3.61, showing equilibrium snapshots of the TraPPE/Zhang system with the ethanol mole fraction values of 0.05 and 0.1, as taken out from the simulation performed at the temperature of 313 K (i.e., with the λ value of 1). Further, we have also calculated the size distribution of the ethanol clusters in these systems. Two ethanol molecules are regarded to be bound to each other if their CH₂ groups are closer than 7.4 Å, i.e., the first minimum position of their pair correlation function. The size n of a cluster is simply the number of molecules belonging to it. The obtained $P(n)$ cluster size distributions, plotted in Figure 3.62, clearly show that ethanol molecules form as large clusters in both cases that their size is often comparable with the total number of ethanol molecules in the systems (i.e., (Houndonougbo et al. 2007) and (Ferrando, Lachet, and Boutin 2010), respectively). The extreme clustering of the ethanol molecules is further demonstrated by showing the VP volume distribution of the ethanol molecules, calculated by disregarding the CO₂ molecules in the system of 0.1 ethanol mole fraction (see the inset of Figure 3.56), and comparing it with the VP volume distribution obtained by considering all molecules, regardless of whether they are ethanol or CO₂, in the same system. As is seen, ethanol molecules are distributed in the system showing extremely large

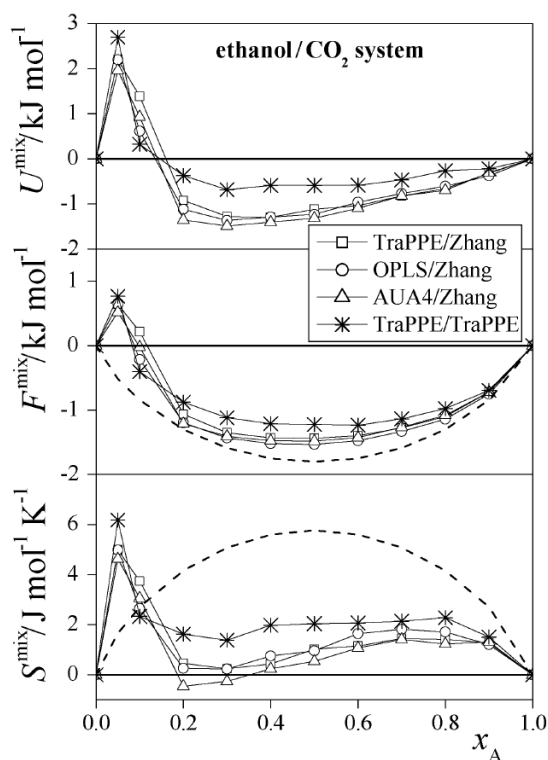


Figure 3.59: Composition dependence of the change of the molar energy (top panel), free energy (middle panel) and entropy (bottom panel) accompanying the mixing of ethanol with CO_2 as obtained in the different systems simulated. The data obtained with the TraPPE/Zhang, OPLS/Zhang, AUA4/Zhang and TraPPE/TraPPE model combinations are shown by open squares, open circles, open triangles and asterisks, respectively. The lines connecting the symbols are just guides to the eye. The dashed lines show the free energy and entropy contributions of the ideal mixing (see eqn (3.8),(3.9)).

density inhomogeneities. All these results confirm that phase separation, already seen from the positive value of the free energy of mixing, is already detectable in the rather small systems simulated under periodic boundary conditions.

Equilibrium snapshots of the ethanol/ CO_2 mixed systems containing (a) 5% and (b) 10% ethanol, illustrating the demixing of the components, as taken out from the simulations performed at 313 K with the TraPPE/Zhang model pair. The C, O and H atoms are marked by grey, red and white colours, respectively. For clarity, atoms belonging to the ethanol molecules are shown by large, space-filling balls, whilst those belonging to the CO_2 molecules by sticks.

Size distribution of the ethanol clusters in the TraPPE/Zhang system containing ethanol at mole fractions of 0.05 (solid lines) and 0.1 (dashed lines). The inset shows

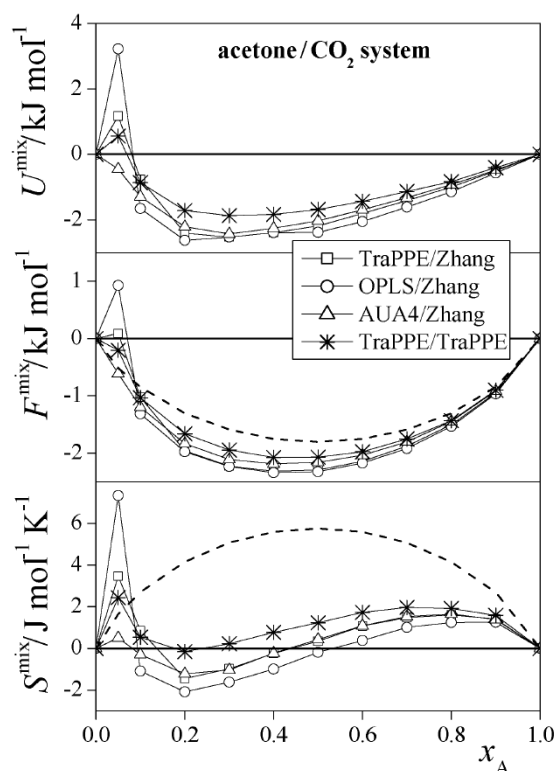


Figure 3.60: Composition dependence of the change of the molar energy (top panel), free energy (middle panel) and entropy (bottom panel) accompanying the mixing of acetone with CO_2 as obtained in the different systems simulated. The data obtained with the TraPPE/Zhang, OPLS/Zhang, AUA4/Zhang and TraPPE/TraPPE model combinations are shown by open squares, open circles, open triangles and asterisks, respectively. The lines connecting the symbols are just guides to the eye. The dashed lines show the free energy and entropy contributions of the ideal mixing (see eqn (3.8),(3.9)).

the same distributions on a logarithmic scale, for emphasizing the presence of large clusters.

The picture is somewhat more complicated in the case of the acetone/ CO_2 mixtures. Thus, the OPLS/Zhang and TraPPE/Zhang systems show demixing at $x_A = 0.05$, as F_{mix} is positive for these systems here, whilst the free energy of mixing values obtained for the AUA4/Zhang and TraPPE/TraPPE model pairs are negative in the entire composition range, indicating full miscibility of these models, at least at 313 K. The fact that different model pairs predict even qualitatively different behaviour of the acetone/ CO_2 system strongly points out the urgent need of performing experiments that should be decisive in this respect. The fact that the two model combinations

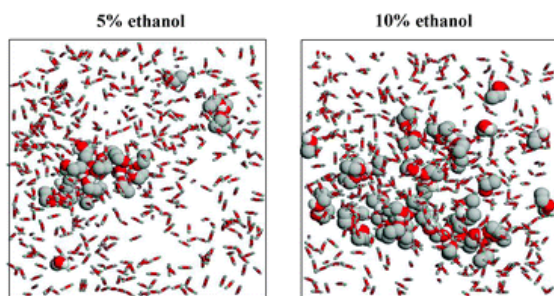


Figure 3.61: Equilibrium snapshots of the ethanol/ CO_2 mixed systems containing (a) 5% and (b) 10% ethanol, illustrating the demixing of the components, as taken out from the simulations performed at 313 K with the TraPPE/Zhang model pair. The C, O and H atoms are marked by grey, red and white colours, respectively. For clarity, atoms belonging to the ethanol molecules are shown by large, space-filling balls, whilst those belonging to the CO_2 molecules by sticks.

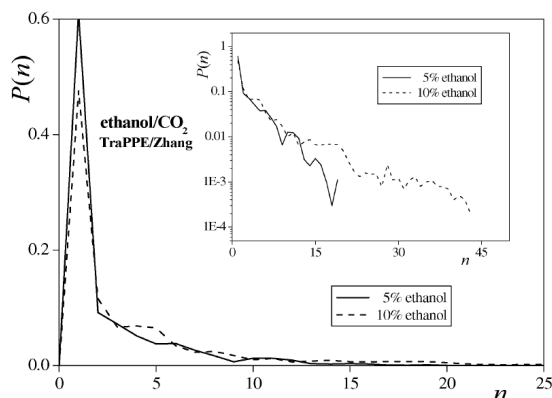


Figure 3.62: Size distribution of the ethanol clusters in the TraPPE/Zhang system containing ethanol at mole fractions of 0.05 (solid lines) and 0.1 (dashed lines). The inset shows the same distributions on a logarithmic scale, for emphasizing the presence of large clusters.

predicting full miscibility have previously been proven to be the best ones provides us an argument supporting the scenario of full miscibility. However, in interpreting the obtained data the possible immiscibility of even the AUA4/Zhang and TraPPE/-TraPPE systems cannot be excluded if this miscibility gap is located at $0 < x_A < 0.05$. In other words, it is still quite possible that the only difference between the different model combinations in this respect concerns the composition range of immiscibility, and the composition grid we used here could simply be too crude to see this immiscibility for certain systems.

Summary and conclusions

In this paper we presented a detailed computer simulation investigation, including extensive free energy calculations, to investigate the properties of ethanol/ CO_2 and acetone/ CO_2 mixtures above the critical point of CO_2 . Several combinations of various potential models have been tested by comparing the volumetric behaviour of the systems simulated with experimental data. The results revealed that the Zhang–Duan potential of CO_2 , proved to be an accurate model in many respects, fails in reproducing the molar volume of CO_2 at the supercritical temperature of 313 K. On the other hand, the TraPPE model of CO_2 turned out to be much better in this respect. Concerning the molar volume of neat acetone and ethanol the AUA4 force field was found to give the best and OPLS the worst results. Among the four model pairs tested, the AUA4/Zhang and TraPPE/TraPPE combinations turned out to be the best ones, the former giving a slightly better reproduction of the molar volume of the mixed systems, and the latter giving a considerably better reproduction of the molar volume change accompanying the mixing of the two components above the acetone/ethanol mole fraction of 0.2. The results obtained for the neat and mixed systems also suggest that the AUA4/TraPPE model pair might be similarly successful in this respect.

Around the acetone/ethanol mole fraction of 0.05 all model pairs, with the exception of the AUA4/Zhang model of the acetone/ CO_2 system, predicted a huge and narrow peak of the molar volume. This molar volume peak is limited to a rather narrow composition range, up to the x_A value of 0.1–0.15, above which the mixed system is no longer in the supercritical state. The sharp increase of the molar volume around $x_A = 0.05$ is accompanied by the immiscibility of the components, evidenced by the positive values of the free energy of mixing, with the exception of the TraPPE/TraPPE model of the acetone/ CO_2 system. (Full miscibility is also seen for the AUA4/Zhang acetone/ CO_2 system; however, here no peak of the molar volume was observed either.) Although the two best model pairs predict full miscibility of the acetone/ CO_2 system, this result should be interpreted with care, as immiscibility of even these systems might still occur below $x_A = 0.05$. On the other hand, all model combinations predicted limited miscibility of the ethanol/ CO_2 system. The present results clearly point out the urgent need for new experimental data that could unambiguously clarify the problem of miscibility of these binary systems.

Chapter **4**

CELLOBIOSE SOLVATION

4.1 Cellobiose solvation

As it was mentioned in introduction to the Part II, one of the approaches to selection of a solvent for polymer dissolution is to take the monomer and to check its affinity to the solvent. Molecular simulations approach is suitable for this and well-known techniques such as thermodynamic integration or free energy perturbation methods can be applied. Free energy of solvation of monomer can be a measure of thermodynamic affinity of monomer (cellobiose in our case) to solvent.

We used molecular dynamics simulations to obtain the solvation free energy of cellobiose in water, 1-ethyl,3-methylimidazolium chloride ionic liquid (EMIMCl), pure supercritical CO₂ and its mixtures with acetone, ethanol, water and water+ethyleneglycol as well as with ammonia in liquid and supercritical state. Interestingly, there is no data on solvation free energy of cellobiose in water in the literature at present moment and it was useful to calculate it and compare to other solvents. The water is the most common solvent in nature that is not able to dissolve cellulose at ambient conditions and one would like to achieve higher cellobiose affinity to potential solvent than to water. EMIMCl ionic liquid is well established cellulose solvent and its choice was obvious for testing purposes.

Our ultimate goal would be the selection of co-solvent in addition to scCO₂ that dissolves cellulose. To achieve this goal we should compare solvation free energy of scCO₂/co-solvent mixtures with pure carbon dioxide. Two supercritical solvation systems for cellulose acetate dissolution were developed in the following works (Pöhler and Kiran 1997b; Pöhler and Kiran 1997a; Kiran and Pöhler 1998). These mixtures found to be a good solvents for cellulose acetate, however no data on possible cellulose dissolution was published. In order to check this mixtures with respect to cellobiose solvation we performed FEP simulations on CO₂, CO₂ + ethanol, CO₂ + acetone systems.

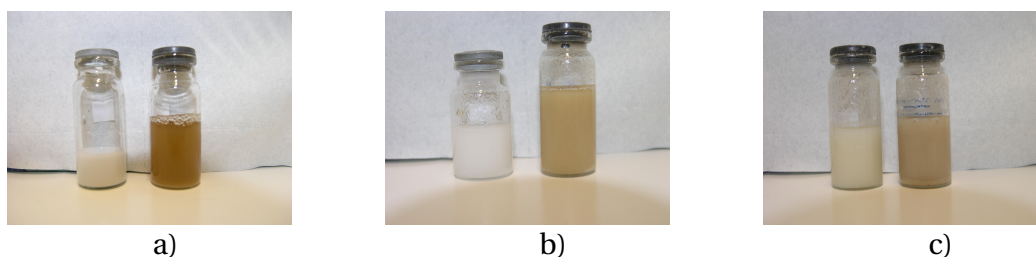


Figure 4.1: The macroscopic changes of cellulose models after treatment by supercritical mixture of solvents (for every picture: left-hand side is the picture of sample before treatment and the right-hand side—after treatment): a) cellobiose, b) wood cellulose, c) cotton cellulose.

Another systems were chosen on the basis of experiments performed in Institute

of Solution Chemistry of Russian Academy of Science. In the frame of collaborative project co-financed by the CNRS and the Russian Academy of Science the dissolution of model of celluloses such as cellobiose, wood cellulose, and cotton cellulose in a co-solvent/scCO₂ was analyzed (Dyshin A.A. 2007). Figure 4.1 shows the macroscopic changes occurring after the treatment of the cellulose samples. Methods of differential scanning calorimetry (DSC) mass spectrometry, Infrared, NMR and scanning electron microscope (SEM) have been used to characterize the structural changes in the treated cellulose. The DSC method indicates difference between curves of initial microcrystalline cellulose and after treating by co-solvent/scCO₂. It has been found that for region of temperatures between 100–150°C treated cellulose has chemical transformation which is connected with breaking of intramolecular hydrogen bonds. Figure 4.1 shows the macroscopical changes in cellulose obtained from different sources after treatment in CO₂ with co-solvents.

Our final system for cellobiose solvation was liquid and supercritical ammonia under several conditions. Ammonia is well-known in wood industry for its ability to soften the wood. It has been reported that both liquid ammonia, gaseous ammonia and its water solutions have a plasticizing influence on wood while the latter is much less effective (Pentoney 1966; “Wood Softening and Forming with Ammonia”). From the other hand, to our knowledge, there were no studies on influence of supercritical ammonia on crystalline cellulose and/or wood. Thus, we decided to close this gap.

Data on thermodynamical conditions and compositions of solvents are summarized in the Table 4.1.

Free energy perturbation (FEP) method (see subsection 2.5.1) allows one to get free energy differences between two states. In our case these states are solvated and non-solvated cellobiose. However, straightforward application of FEP to large solutes is questionable because they can possess conformational degrees of freedom which usually affect free energy differences (Hodel et al. 1993). Thus, at first we needed to estimate the influence of conformational degrees of freedom on free energy perturbation calculation of solvation free energy.

Simulation details. FEP and metadynamics simulations were performed using NAMD molecular dynamics program (Phillips et al. 2005). All the systems were first equilibrated in NPT ensemble. Then simulations in NVT ensemble were performed where the number of particles was chosen to fit the density with box cell length equal to 40 Å. Usage of this box length is sufficient to sample large density fluctuations particularly for the thermodynamic points near the critical point. In each case we used Langevin thermostat with an addition of Langevin barostat in NPT ensemble. The information on the studied solvent, the total number of particles, the thermodynamic conditions is summarized in Table 4.1.

The choice of particular parametrizations of Lennard-Jones force fields pursued

Solvent	N_{mol}	P, bar	T, K	state
water	2130	1	298	liquid
EMIMCl	251	1	373	liquid
CO ₂	407	100	313	supercritical
CO ₂ + EtOH	229+92	120	420	supercritical
CO ₂ + Acetone	237+77	153	420	supercritical
CO ₂ + H ₂ O	600+400	300	420	supercritical
CO ₂ + H ₂ O + ethyleneglycol	600+300+100	300	420	supercritical
ammonia	1500	135	243	liquid
ammonia	1042	135	390	liquid
ammonia	829	135	420	supercritical
ammonia	243	135	450	supercritical

Table 4.1: Systems for cellobiose solvation simulations

several reasons for each solvent system. In case of water we have chosen SPC/E model (Berendsen, Grigera, and Straatsma 1987) which well describes the structure of liquid water and reproduces density and diffusion coefficient of water better compared to SPC model (Berendsen 1981). Its another advantage is that it is simple enough and includes only three point charges.

Many interaction potential models for EMIMCl were proposed in literature (Cadena et al. 2004; Canongia Lopes, Deschamps, and Pádua 2004; Liu, Huang, and Wang 2004; Bhargava and Balasubramanian 2007; Sambasivarao and Acevedo 2009; Chaban, Voroshylova, and Kalugin 2011). All abovementioned force fields are “all-atoms” what means that alkyl chains will include all hydrogens. In order to reduce computational time one could make use of “united atoms” approach where CH₂ and CH₃ groups are treated as the single point, in fact, this was done by (Liu, Wu, and Wang 2006) who proposed such model of ionic liquid representing imidazolium cation by 11 atoms instead of 19. Their results show that this does not influence the structure of ionic liquid and this model can be easily used in larger scale modelings. Finally, in order to reduce computational time we have chosen this model of ionic liquid.

United atoms approach was used for many substances in another force field, a namely TraPPE: Transferable Potentials for Phase Equilibria For. This family of potentials was parametrized by means of Gibbs ensemble Monte Carlo in order to reproduce the liquid-gas coexistence curve of not complicated fluids. The potential models of CO₂ (Chen, Potoff, and Siepmann 2001), of ethanol (Potoff and Siepmann 2001) and of acetone (Stubbs, Potoff, and Siepmann 2004) used here were taken from TraPPE family. These potentials not only represent the coexistence curve, they also successfully predict the binary mixtures equilibria (Stubbs, Potoff, and Siepmann

2004). For special cases that we used we also tested the compatibility of these models by means of thermodynamic integration.

Case of potential models for ammonia was considered in details in paragraph 3.1.2 and here we just precise that we used KRI3 parametrization of Kristof et al. 1999.

Perhaps, the most important part of this discussion is the choice of the potential model for cellobiose and cellulose models. There are several well-known force fields available in the literature, a namely: GROMOS 45A4(Schuler, Daura, and Gunsteren 2001; Chandrasekhar et al. 2003; Soares et al. 2005; Lins and Hnenberger 2005), GLYCAM(Kirschner et al. 2008) and CHARMM(Guvench et al. 2008; Guvench et al. 2009). Many papers on conformational properties of disaccharides, including cellobiose, in water are also known, the most recent, for instance, are (Perić-Hassler et al. 2010; Hatcher et al. 2011). The former work considers conformations of the whole family of disaccharides in water due to its obvious importance for natural disaccharides. The latter is devoted to the testing of CHARMM (Guvench et al. 2008; Guvench et al. 2009) force field with respect to experimental data. Perfect quality of this force field was found. Particularly, conformations of cellobiose were found very well predicted compared to NMR experiment. The advantage of this force field is in its compatibility with other CHARMM force fields which is achieved by using very general methodology in development of this force field.

Details of free energy calculations. In order to obtain free energy of solvation of cellobiose we performed FEP simulations according to following the standard scheme: We took 10 evenly spaced λ -windows for annihilation (as it was explained in subsection 2.5.1). For each λ -window we carried out 10ns molecular dynamics simulation. The increase of λ values represents the gradual decrease of the interactions between cellobiose and solvent, what is illustrated in Figure 4.2. This procedure is called the forward direction (annihilation) of calculation of solvation free energy, however, in this direction one usually overestimates the free energy (Chipot and Pohorille 2007). We also performed the backward transformation(λ decreases) where solute gradually appears in the solvent(the interactions between cellobiose and solvent increase). The appearance of the hysteresis in the forward and backward of FEP calculations is an indication of poor sampling of the configurational space.

4.1.1 Conformational sampling of cellobiose

The sampling of various conformations of cellobiose may influence the calculated free energy values. We then decided to use the metadynamics approach. It allows to construct the free energy surface spanned by conformational degrees of freedom φ and ψ (see subsection 4.1.1) and also to escape free energy minima, which allow an efficient sampling of the various conformations. In practice, we combine

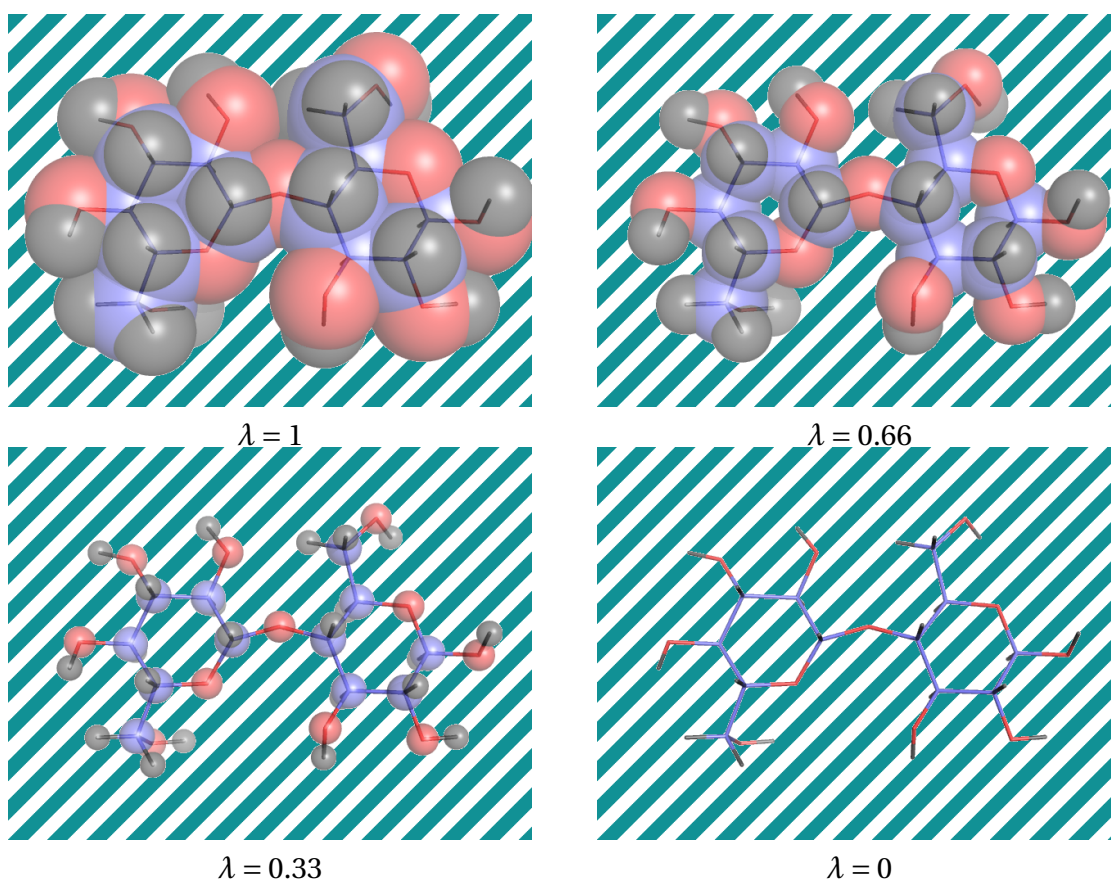


Figure 4.2: Illustration of switching off of the interactions between cellobiose and solvent media.

metadynamics approach with FEP calculation and bias the dynamics in order to sample all the conformations. Important conformations of cellobiose that may be observed in NMR experiment are defined by dihedral angles φ and ψ shown in the Figure 4.3. These angles are similar to Ramachandran angles (Ramachandran, Ramakrishnan, and Sasisekharan 1963). In order to build the free energy map of conversion of conformers into each other, metadynamics (see subsection 2.5.3) approach was used.

As a reference we calculated the free energy surface of cellobiose along the φ and ψ in vacuum Figure 4.4. We can distinguish three main conformers that correspond to three free energy minima marked “A”, “B” and “C”. Such maps are well-known for oligosaccharides in vacuum and were studied intensively by various methods (Lieth, Kozár, and Hull 1997). As it was mentioned before, the changes of cellobiose conformations in water were studied by (Perić-Hassler et al. 2010; Hatcher et al. 2011). From the other hand, change of conformations of cellobiose in non-aqueous media were

not studied, especially solvents chosen in this thesis (see section 1.2).

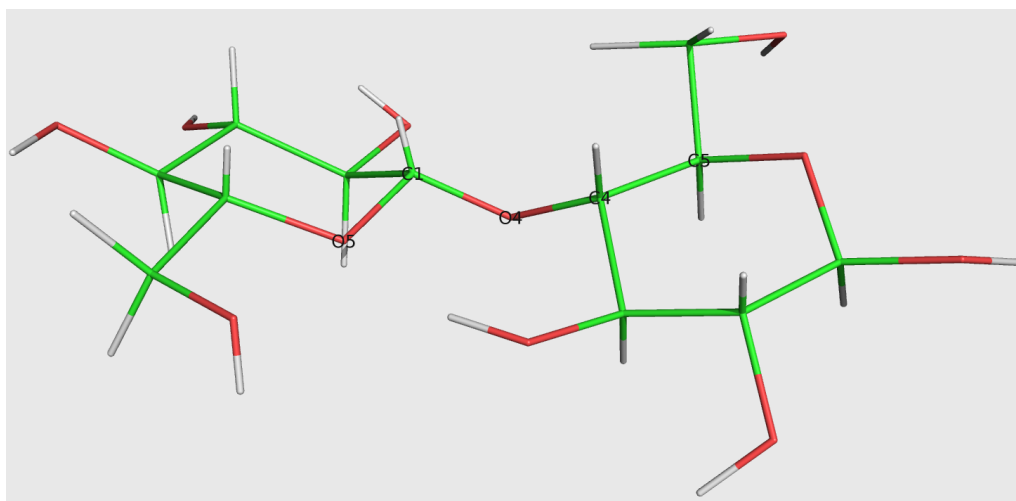


Figure 4.3: Definition of conformational degrees of freedom of cellobiose: Dihedral angles φ (O5-C1-O4-C4) and ψ (C1-O4-C4-C5)

It should be mentioned that the time duration of the transition between two conformations is too large (about hundreds of nanosecond) and using standard simulation it was not possible to sample correctly these rare events. Thus, until the development of accelerated sampling techniques the problem of free energy calculations of large molecules was difficult to address. Indeed, in Figure 4.4 the free energy barriers between cellobiose conformers varies from 5 to 8 kcal/mol which is too long for conventional MD simulation to overcome.

We studied the conformational changes in the thermodynamic conditions listed in Table 4.1 for the different solvents and then compared the free energy surfaces (positions of minima, heights of the transition barriers) for these solvents. For instance, in the case of ammonia Figure 4.5 shows that the barriers become smaller by 1 kcal/mol for higher density (and lower temperature). Another feature of high-density maps is that minima in regions A and B are more pronounced and separated: For liquid ammonia one can see two profound minima in region A separated by 1 kcal/mol barrier (at points with coordinates $(100^\circ, 50^\circ)$ and $(50^\circ, 100^\circ)$) and in case of supercritical ammonia at 450 K there is only one minimum. Pictures corresponding to intermediate states illustrate gradual disappearing of minimum at $(100^\circ, 50^\circ)$. Thus we can observe two processes here: Distinguishing conformers in regions A and B, and lowering the barriers of the transition between regions A, B and C. However, our interest to ammonia is mostly limited to sub- and supercritical conditions (it will become clear later why). The analysis of the change of conformations did not allow us to draw any correlation with the possible dissolution of cellulose in this solvent.

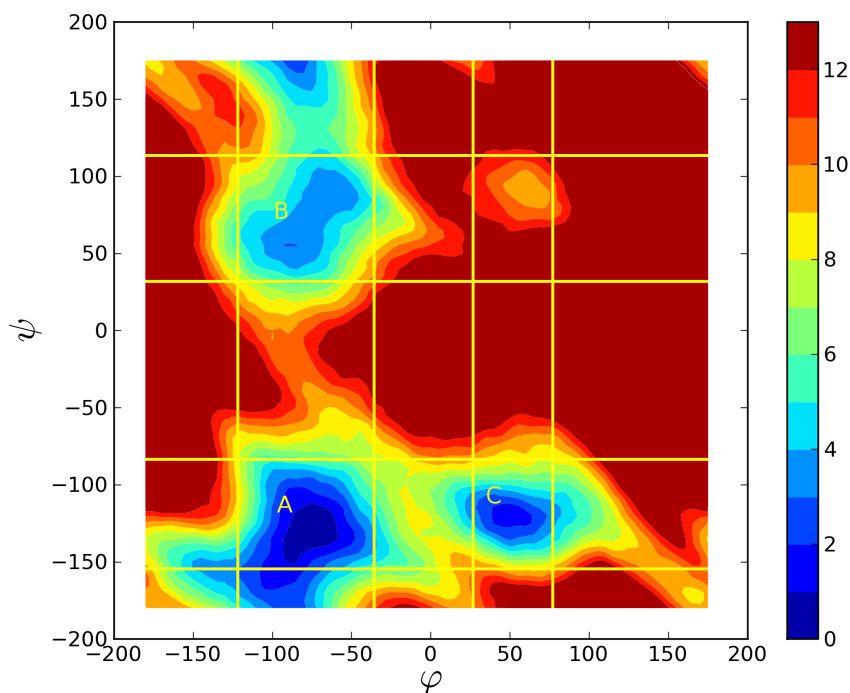


Figure 4.4: Free energy map of cellobiose in vacuum along φ and ψ coordinates.

The same free energy maps were obtained for cellobiose in other solvents. They are given on Figure 4.6. Again, we see similar picture and even though we can not compare these pictures directly in light of data on free energy of solvation (see Figure 4.10 and Figure 4.11). Ionic liquid induces the increase of the barrier of transition between the conformations in region B. It also shifts the position of the minimum in region A and, on the other hand, it reduces the transition barriers between the various conformational regions A, B and C.

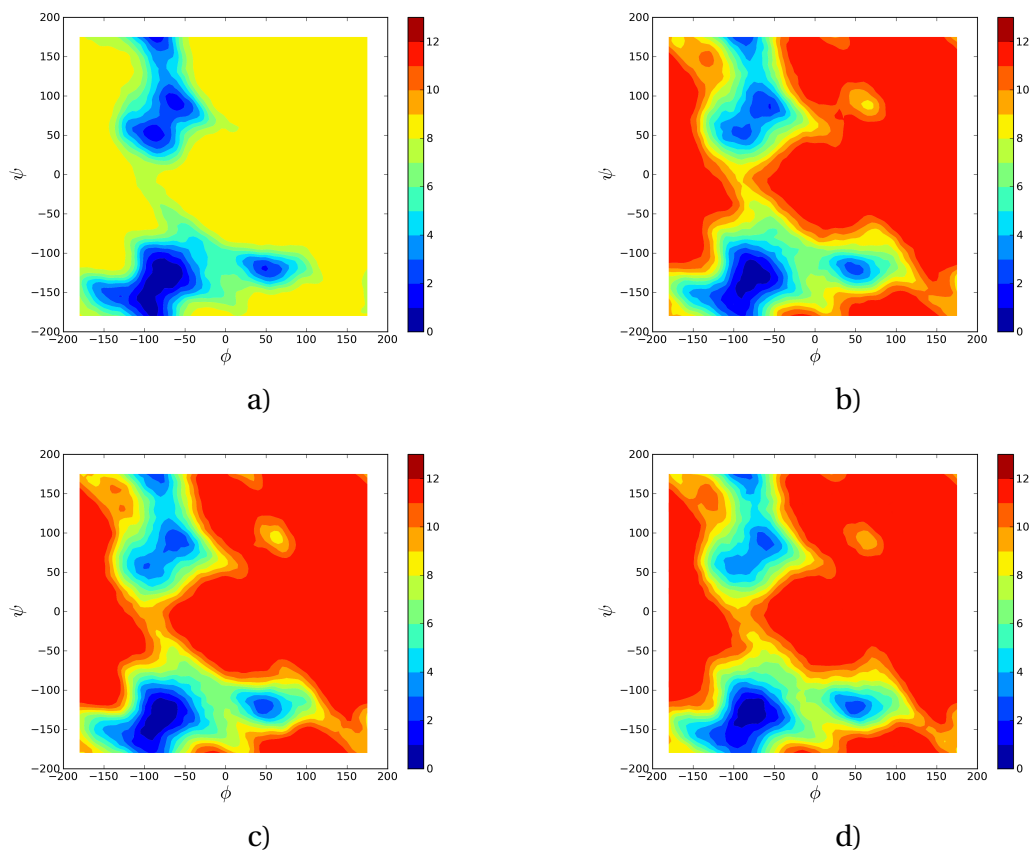


Figure 4.5: Free energy maps of cellobiose in ammonia for: a) 243 K, b) 390 K, c) 420 K, d) 450 K.

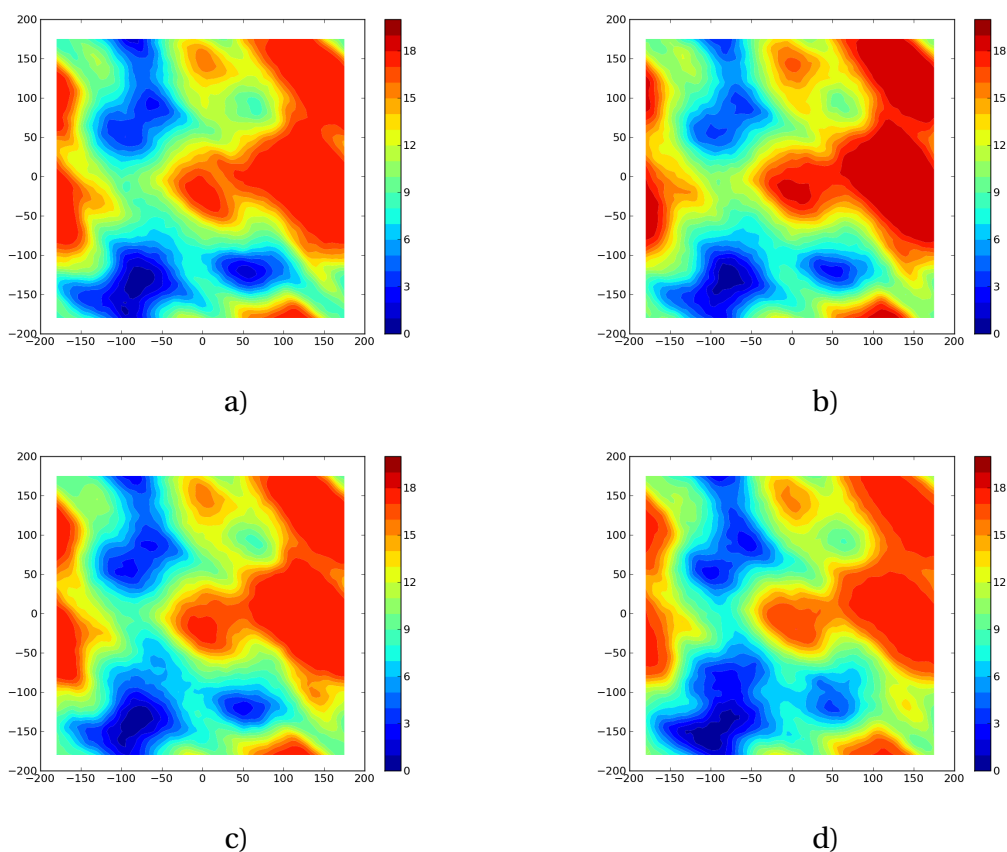


Figure 4.6: Free energy maps of cellobiose for: a) CO₂, b) CO₂-acetone c) CO₂-ethanol d) EMIMCl

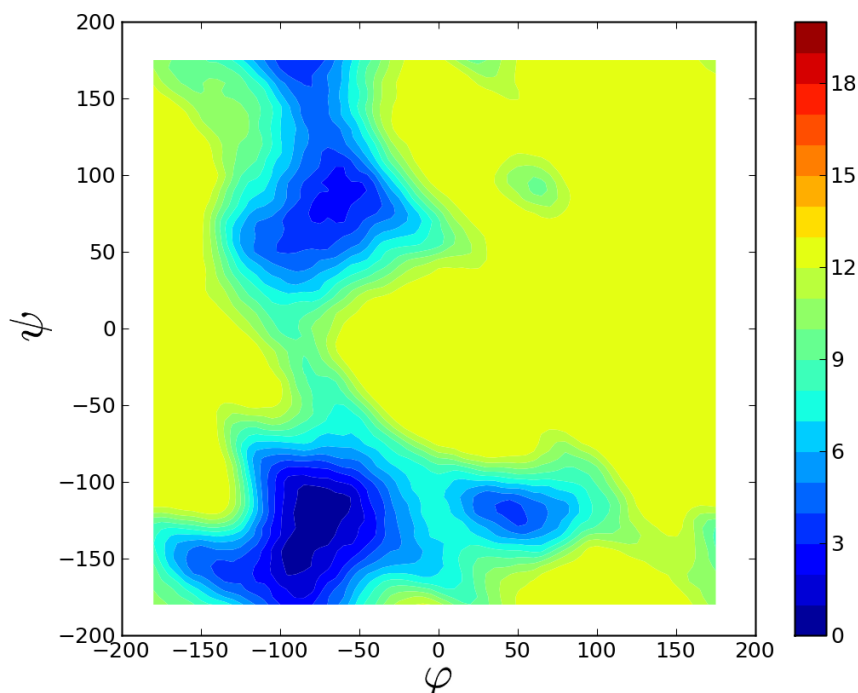


Figure 4.7: Cut of free energy surface of cellobiose in water along φ and ψ coordinates

4.1.2 Solvation free energies from FEP simulations

In order to check the influence of the conformational sampling on the solvation free energy, we compared the FEP calculations with and without the metadynamics. In the first stage we used water and ionic liquid as a benchmark for such a comparison. The free energy surface of cellobiose in water along φ and ψ is given in Figure 4.7, while in Figure 4.8 free energies surfaces (left-hand panel) and probabilities to observe φ and ψ angles directly from MD trajectories (right-hand panel) for several λ stages of FEP simulation are shown. The values of solvation free energy are -32.1 kcal/mol and -31.3 kcal/mol with and without conformational sampling respectively. This means difference in less than 0.8 kcal/mol and the error is about 2.5%. Our another observation is that conformational sampling does not decrease the hysteresis in forward-backward transformation directions in this particular case. However, if we analyze the free energy annihilation and creation paths given in Figure 4.9, even in the case of ordinary FEP we notice that there is a small hysteresis indicating that here we do not need metadynamics.

For ionic liquid the comparison of free energy annihilation and creation paths

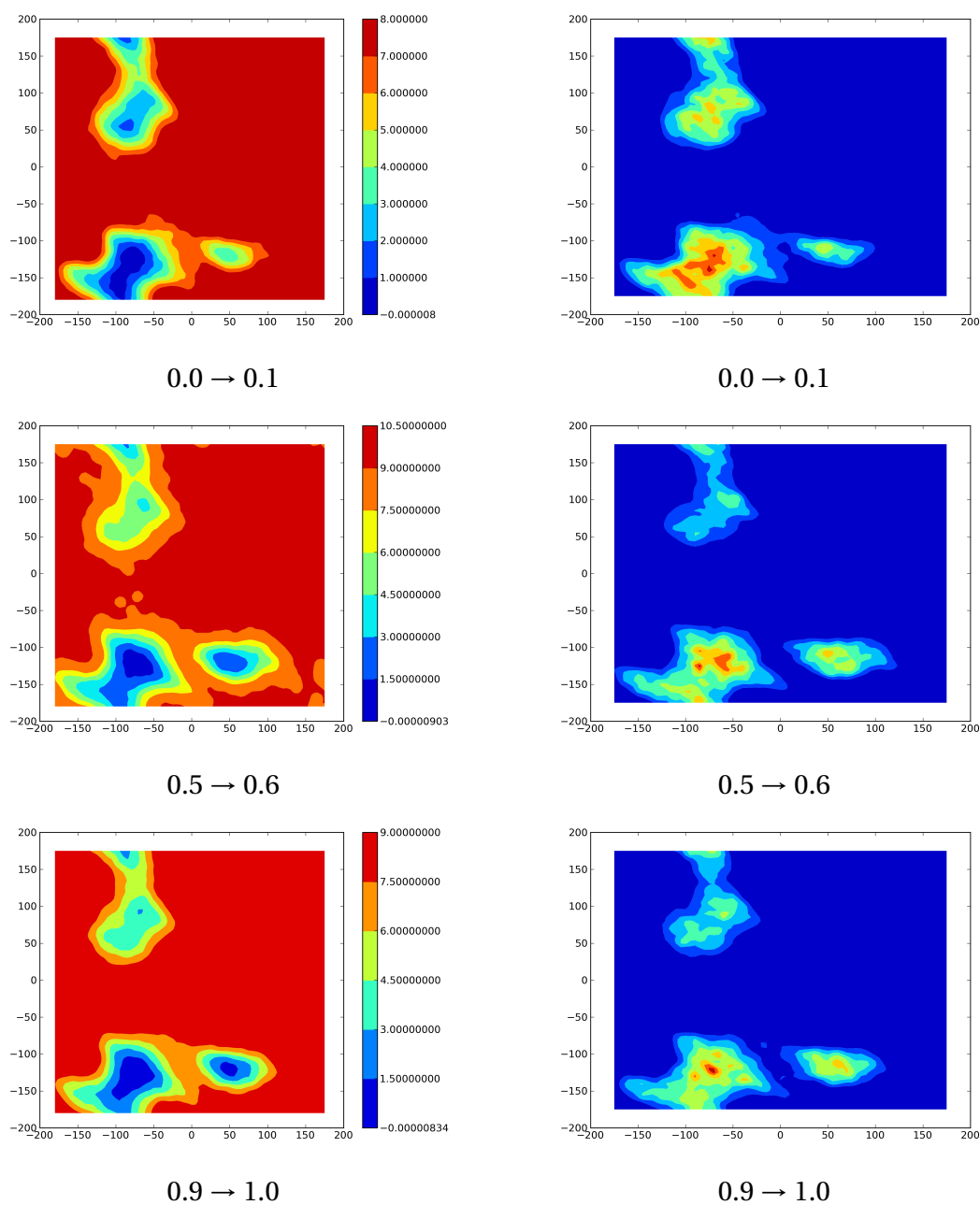


Figure 4.8: Cut of free energy surfaces along φ and ψ coordinates(left-hand column) and probabilities to observe φ and ψ from MD-trajectories(right-hand column)

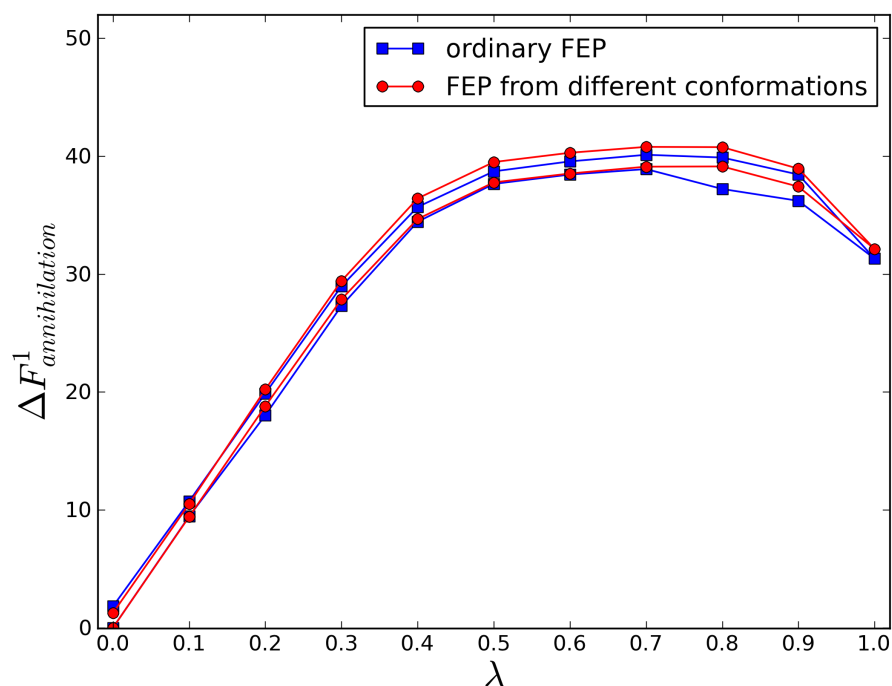


Figure 4.9: FEP graphs with and without conformational sampling for cellobiose in water

with and without metadynamics is illustrated in (Figure 4.10). The difference between the free energy determined in the frame of the two situations, differs by 3.2 kcal/mol (37.9 and 41.1 kcal/mol with and without conformational sampling respectively) what gives a relative error of about 8.4%. Furthermore, the forward-backward transformation hysteresis decreases sufficiently to 1.8 kcal/mol with conformational sampling from 5.4 kcal/mol in ordinary sampling. These results indicate clearly the presence of hysteresis in the case where only FEP is used which points out the poor sampling.

From these values we can see that ionic liquid to cellobiose affinity is stronger than that of water to cellobiose. However, this difference is not very striking and is in agreement with previous work devoted to the subject of carbohydrate dissolution (Liu et al. 2010). For instance, the total interaction energies between cellobiose and the solvents were found to be ≈ 1.35 times larger for ionic liquid than that for water in. In our case the free energy of solvation in ionic liquid is 1.23 times larger than in water.

A methodological observation can be made here about the accuracy of FEP method in application to large solute molecules. Obviously, the bigger the solvent the more

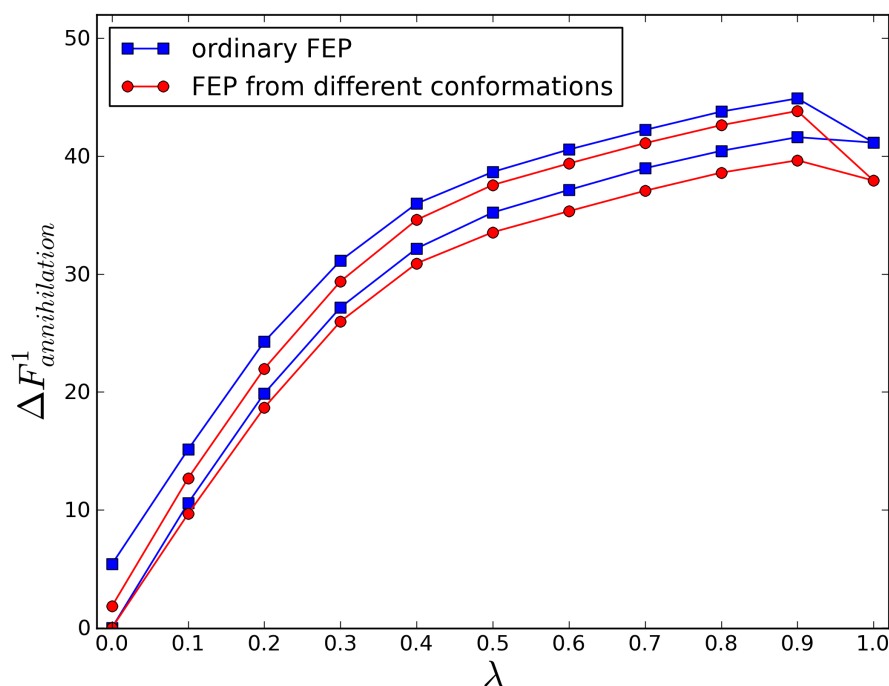


Figure 4.10: FEP graphs with and without conformational sampling for cellobiose in EMIMCl

time we need to sample the configurations of solvent surrounding solute molecules. However, in our case we have got rid of sufficient amount of hysteresis employing the accelerated conformational sampling. This could be explained in such a way that instead of waiting for natural dynamics of ionic liquid, in metadynamics we artificially move cellobiose molecule with respect to solute and thus got the enhanced sampling of configurations of solvent near solute.

After these tests were performed FEP calculations on solvation of cellobiose in $scCO_2$ and its mixtures with cosolvents. Figure 4.11 and Figure 4.12 show again normal and conformational sampling augmented FEP calculations results. From the methodological point of view conformational sampling almost does not affect the final values of solvation free energies while it reduces values of hysteresis.

It is considered to be a common knowledge that addition of polar cosolvents in $scCO_2$ increases the solubility of polar solute (Staff, Sun, and Corporation 2002). However, from our studies of cellobiose solvation we can see an interesting result: An addition of polar cosolvent—acetone—increases the free energy of solvation (makes it less negative) compared to pure $scCO_2$ (at least for taken mole fraction). This is quite an unexpected result as an addition of polar entrainer is believed to increase

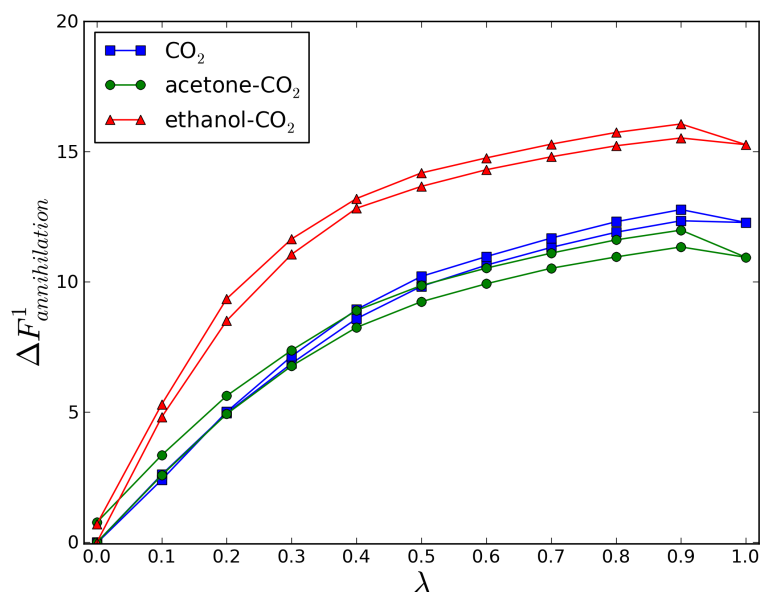


Figure 4.11: FEP graphs for cellobiose in scCO₂ and its mixtures with acetone and ethanol

solubility of substances in supercritical mixtures and thus the solvation free energy. For ethanol more usual situation is observed and the free energy of solvation decreases for this cosolvent.

Finally, we analyzed the solvation of cellobiose in liquid and supercritical ammonia by means of FEP simulations. Figure 4.13 shows that solvation free energy at $T = 243$ K is comparable to that in ionic liquid. However, liquid ammonia does not dissolve cellulose without additions of salts (see subsection 1.2.5). This brings us to the main conclusion of this part of the work. The analysis of the dissolution process of monomer of cellulose (cellobiose) using the criteria of solvation free energy is not sufficient to obtain the dissolution of cellulose itself. Indeed, cellulose has a developed crystalline structure due to intra- and intersheet hydrogen bonds and one can see that considering only the interactions between monomer and solvent without studying the influence of crystal packing and hydrogen bonds formed between monomers and fibers formed by them is not enough to give a reasonable conclusions.

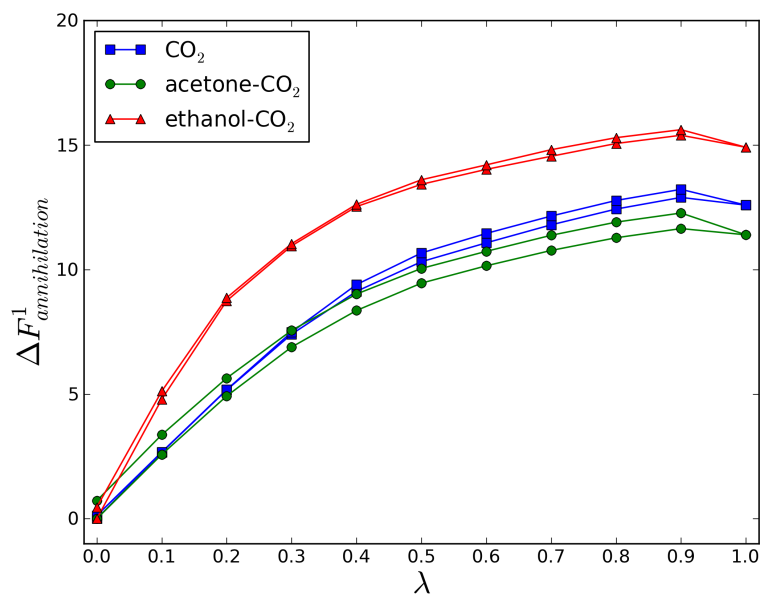


Figure 4.12: FEP graphs with conformational sampling for cellobiose in scCO₂ and its mixtures with acetone and ethanol

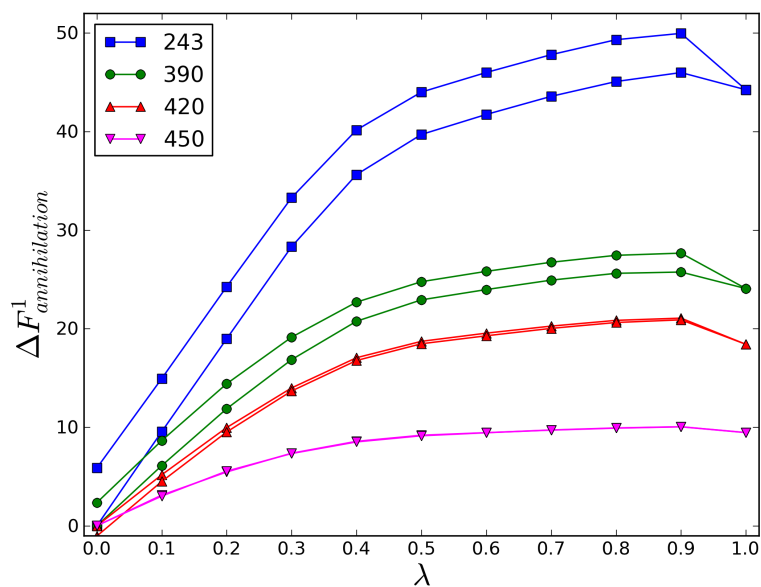


Figure 4.13: FEP graphs of cellobiose solvation in ammonia for thermodynamical parameters corresponding to those in Table 4.1

Chapter **5**

**CELLULOSE NANOCRYSTALS
DISSOLUTION**

5.1 Introduction

As we showed in the previous chapter one has to consider a crystal to study cellulose dissolution and this chapter is devoted to modeling of cellulose dissolution in various solvent systems. When the dissolution of cellulose is discussed one should take into account the structure of this polymer. One can subdivide cellulose existing in nature into two main types: Amorphous and crystalline. As it was discussed in section 1.3, there exist seven cellulose polymorphs with different unit cells and different arrangement of hydrogen bonds network and hence different stability and crystal lattice energies. Starting from the experimental geometries and using the CHARMM force field for cellulose we calculated the nonbonded interaction energies of six nanocrystals of polymorphs of cellulose. The results normalized for one unit cell are given in Table 5.1. From these simple preliminary calculations one can already see that the most stable polymorph should be I_β and the least stable is IV_I . Furthermore, the energy values indicate that polymorph III_I is more than polymorph II. Noticing this, we can compare these data with the results of the very recent calculations devoted to depolymerization studies of cellulose in water (Beckham et al. 2011). The authors studied tearing off of one cellulose fiber from a crystal applying umbrella sampling method. The main conclusion was that the pulling one fiber from the others goes easier when the non-natural polymorphs (II, III_I) are considered. The series of free energy barriers, ΔG , corresponding to this process correlates with the crystal lattice energies given in Table 5.1: $\Delta G_{II} < \Delta G_{III_I} < \Delta G_{I_\alpha} < \Delta G_{I_\beta}$.

Polymorph	Energy, kcal/mol
I_β	188
I_α	172
III_I	164
II	152
IV_{II}	138
IV_I	133

Table 5.1: Nonbonded interaction energy of cellulose polymorphs in CHARMM carbohydrates force field, normalized by one unit cell.

In the first stage of our analysis, we studied of various nanocrystal polymorphs of cellulose in 1-methyl,3-ethylimidazolium chloride ionic liquid (EMIMCl). In the second stage we studied the dissolution of nanocrystals in CO_2 -ethanol and CO_2 -acetone supercritical mixtures. Finally, different various cosolvents were considered. The choice of these cosolvents was based on previous studies mentioning these cosolvents as potential solvents to dissolve cellulose. The principal property of these cosolvents is their ability to form strong hydrogen bond with the oxygens of cellulose.

lose. The cosolvents considered in this work are the following: trimethylamine oxide(TMAO), triethylamine oxide(TEAO) and urea. Finally, we prospect the dissolution of cellulose in liquid and supercritical ammonia.

Simulation details. In all our simulations in this section we equilibrated the box of solvent molecules for 1ns and then add each of the polymorph form of cellulose inside the box. The geometries of unit cells of microcrystals were taken directly from the experimental data collected in (Zugenmaier 2007). Cellulose nanocrystals were modeled within CHARMM carbohydrates force field (Guvench et al. 2008; Guvench et al. 2009). The cellulose microcrystals were not as large as in works of (Bellesia et al. 2011; Beckham et al. 2011) but our goal was to represent inter- and intramolecular hydrogen bonds' patterns. It can be seen in Figure 5.1 that the nanocrystals taken represent two unit cells in height(three sheets) and two unit cells in width. The length of the nanocrystals was equal to three cellobiose units corresponding to three unit cells. Thus we had 21 cellobiose units in total for each polymorph used in our simulations. They formed totally 7 hexaose fibers. For all simulations we took the initial box length to be equal to 80 Å to avoid interaction of cellulose with its own periodic images.

Interaction potential models of CO₂, ethanol, acetone, EMIMCl and ammonia were the same as in the previous chapter.

Analysis of the results was made by means of common dynamical quantities of molecular dynamics: RMSD and ROG analysis(see section 2.4). In our simulations we choose term "dissolution" to describe phenomena when the radius of gyration of cellulose crystal shows unlimited fast growth. Actually, what we should observe in case of cellulose dissolution is the expansion of initially bounded cellulose fibers till the border of the box. There the growth should stop due to the periodic boundary conditions. This means that system approaches an equilibrium that is characterized by the limit of the radius of gyration value. However, due to several limitations of data analysis we really observe not this picture but rather unlimited growth of r_g as it was discussed in section 2.4.

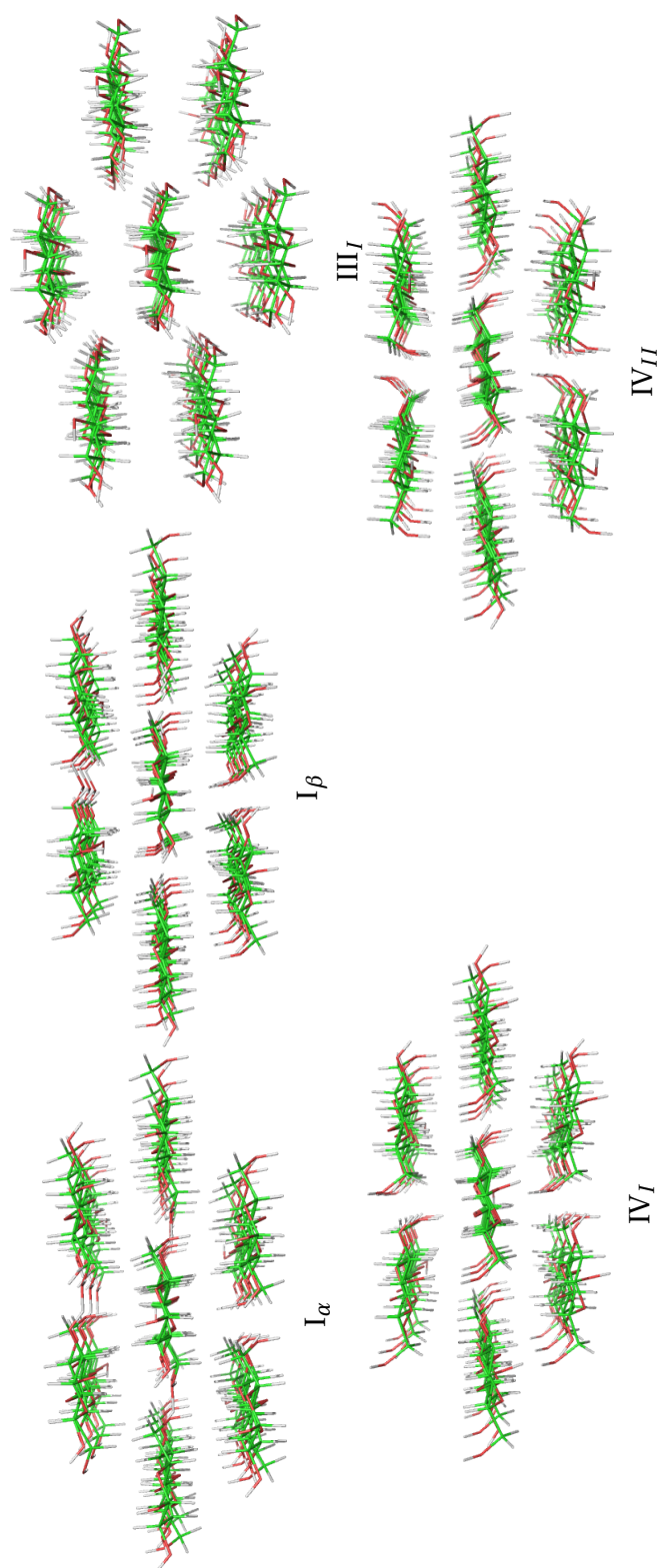


Figure 5.1: Side-view of cellulose polymorphs nanocrystals that were used for simulations. Polymorph types are subscribed directly on the figure.

5.2 Cellulose nanocrystals in ionic liquid.

To our knowledge until now there were no attempts to model dissolution of cellulose microcrystals in ionic liquid to observe directly the dissolution of cellulose. This is partly due to long time scales on which such a dissolution should be observed. For large systems (in computational sense) the time duration to observe changes can reach micro or even milliseconds which is beyond our capabilities at present moment. However, even for such large systems that are tremendously difficult to simulate another rather theoretical problem arises. When we deal with periodic system such as the system we are studying in MD simulations we need only to take care that size of the box is larger than the correlation length of this system (Tucker 1999). Things become more complicated if we want to obtain proper thermodynamics from the finite small system simulation.

Having mentioned this, we start our studies of the behaviour of cellulose nanocrystals in different solvents with an ionic liquid that dissolves all kinds of cellulose (Pinkert et al. 2009), a namely 1-methyl,3-ethylimidazolium chloride. We studied cellulose nanocrystals of five polymorphs (I_α , I_β , III_I , IV_I , IV_{II}). Each of these polymorphs has been added in the box containing equilibrated ionic liquid (1465 molecules). The runs last 80 ns.

The initial configurations of ionic liquid box were generated by PACKMOL program (Martínez et al. 2009), equilibrated for 1 ns and then cellulose nanocrystal was added inside the box and the molecules of ionic liquid that clashed with cellulose were removed. Initial configuration of molecules within the box are shown in Figure 5.2 for polymorphs I_β and III_I .

Results and Discussion. On the accessible time scale of 100 ns, we observed only the dissolution of cellulose nanocrystals of polymorphs IV_I and IV_{II} , although EMIMCl is known to dissolve all kinds of cellulose. This result is correlated with the values of nonbonded interaction energies of crystals given in Table 5.1.

Figure 5.3 shows the time behaviour of radii of gyration of the five nanocrystals of cellulose. We can clearly see the expansion of nanocrystal in case of polymorphs IV_I and IV_{II} . The process starts after ≈ 20 ns for cellulose IV_{II} and after ≈ 30 ns for cellulose IV_I .

Another quantity that we measured was the RMSD. It is presented on the Figure 5.4. One can notice that the RMSD for nanocrystals of cellulose IV_I and IV_{II} starts to increase from the beginning of the simulation while for the other nanocrystals the RMSD remains almost constant during the whole 80 ns simulation run. In the case of ionic liquid the behaviour of ROGs and RMSDs are correlated. We interpret this correlation as the signature of the expansion (dissolution) of nanocrystal of cellulose.

The long time simulation runs to dissolve cellulose nanocrystals in ionic liquid

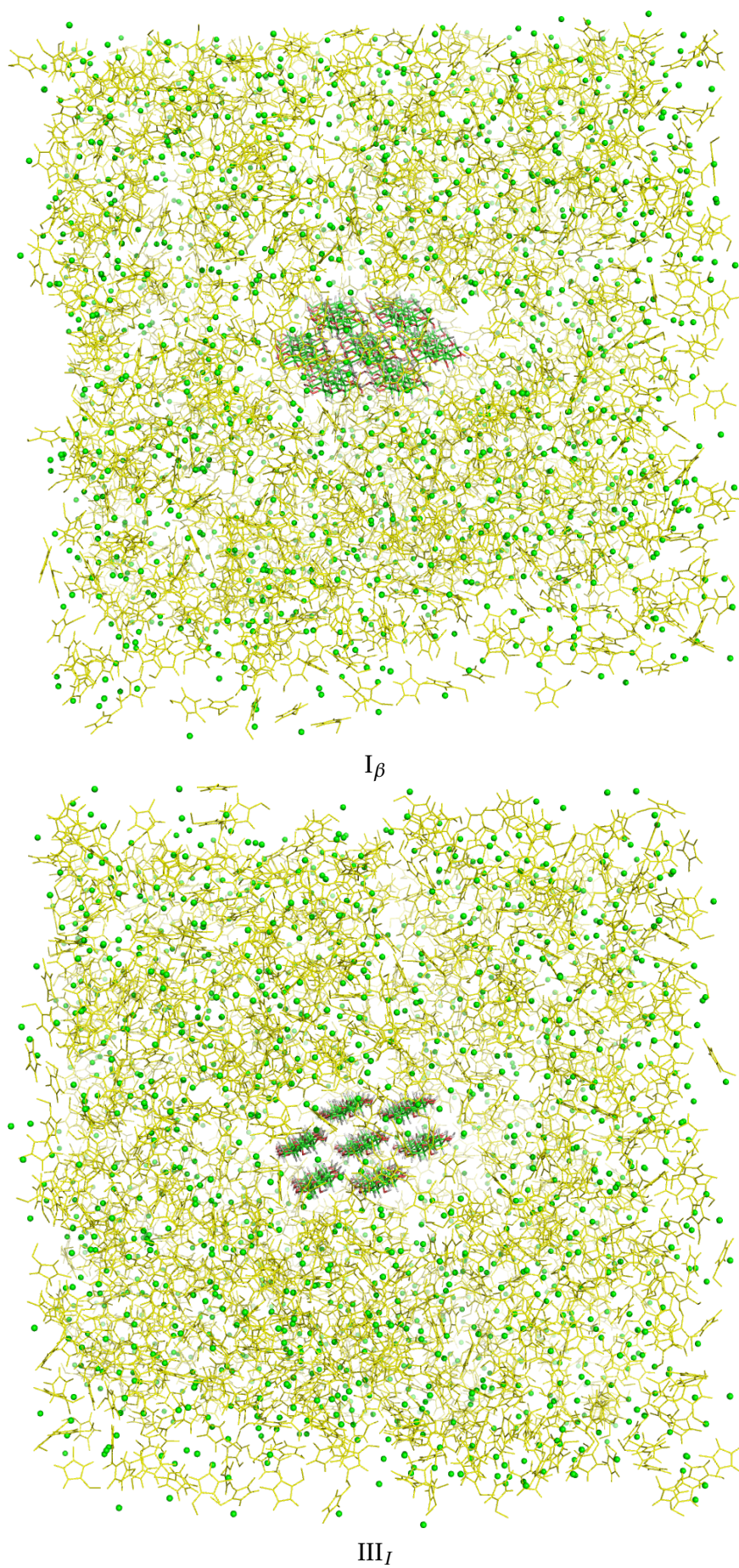


Figure 5.2: Snapshots of the first timesteps of cellulose simulation of polymorphs I_β and III_I in EMIMCl ionic liquid.

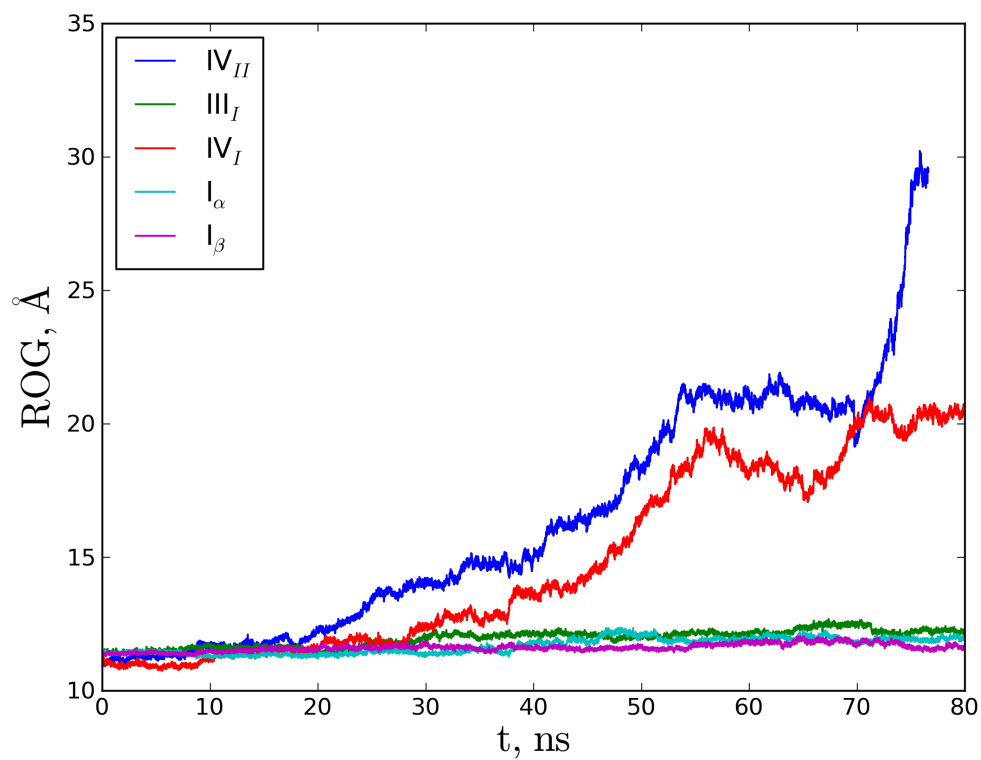


Figure 5.3: Radii of gyration of cellulose polymorphs in emim.

can be justified not only by the high crystallinity of cellulose but also by very low diffusion coefficients of ionic liquid that were reported to be equal to 0.60 ± 0.58 for anion and 1.79 ± 0.54 for cation (Rey-Castro and Vega 2006). Thus, for other solvent systems that potentially dissolve cellulose and having higher diffusion coefficient, we can expect shorter times to dissolve cellulose.

From these figures one may conclude that EMIMCl can dissolve only polymorphs IV_I and IV_{II} as only they show expansion of the fibers. Nevertheless, the analysis of the snapshots on the final timesteps of the simulations show that the time duration is the limiting factor to observe the dissolution of the other polymorphs nanocrystals. Indeed, the last snapshots of the calculations are shown in Figure 5.5. One can see that the cellulose of polymorphs IV_I and IV_{II} are spread all over the simulation box. The other polymorphs are still compact but they are sufficiently distorted and molecules of ionic liquid are located inside the nanocrystals' fibers. These two structural facts suggest that the dissolution process of these polymorphs is in its initial stage and one needs larger time scale calculations to observe the dissolution process of these polymorphs. For instance, Figure 5.5 shows that in the case of polymorph III_I one fiber is being detached from the rest of the nanocrystal. One may interpret this as the first step in the dissolution of polymorph III_I . These results may be correlated with the work of (Beckham et al. 2011) where they calculated the free energy of tearing off of one fiber from the crystal of cellulose. The reaction coordinate was defined as the distance between the ends of the given fiber and the end of the rest of crystal. We believe that there are many choices of reaction coordinate (ROGs, for instance) that can be used for description of free energy of dissolution.

5.3 Cellulose nanocrystals in supercritical mixtures of $scCO_2$ /acetone and $scCO_2$ /ethanol

In this section we present the results on long-time simulations of cellulose polymorphs in supercritical mixtures of $scCO_2$ /acetone and $scCO_2$ /ethanol. The thermodynamical parameters of these mixtures were established in previous works by (Pöhler and Kiran 1997b; Pöhler and Kiran 1997a). In the work by (Kiran and Pöhler 1998) these mixtures were used to dissolve cellulose acetate. Here we discuss their influence on nanocrystals polymorphs of cellulose applying the same methodology as in the previous section.

5.3.1 Cellulose in $scCO_2$ /acetone mixture.

It follows from (Pöhler and Kiran 1997a) that the critical point of $scCO_2$ /acetone mixture lies at the following parameters: $P_C = 120$ bar, $T_C = 402$ K, $x_C^{acet} = 30\text{mass}\%$.

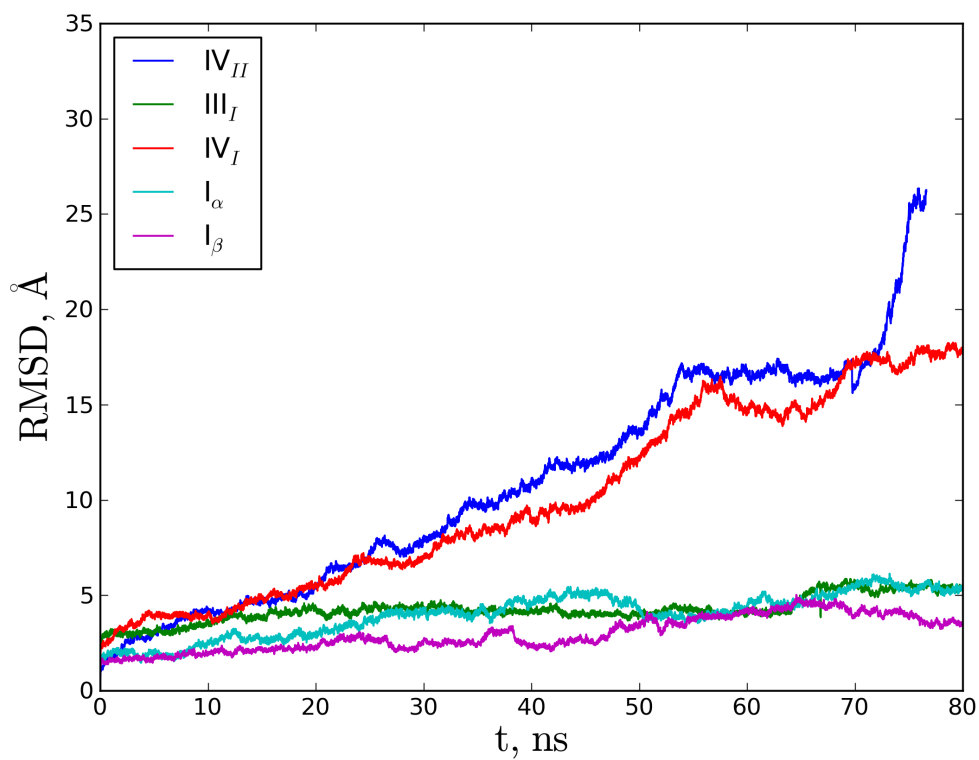


Figure 5.4: RMSDs of cellulose polymorphs.

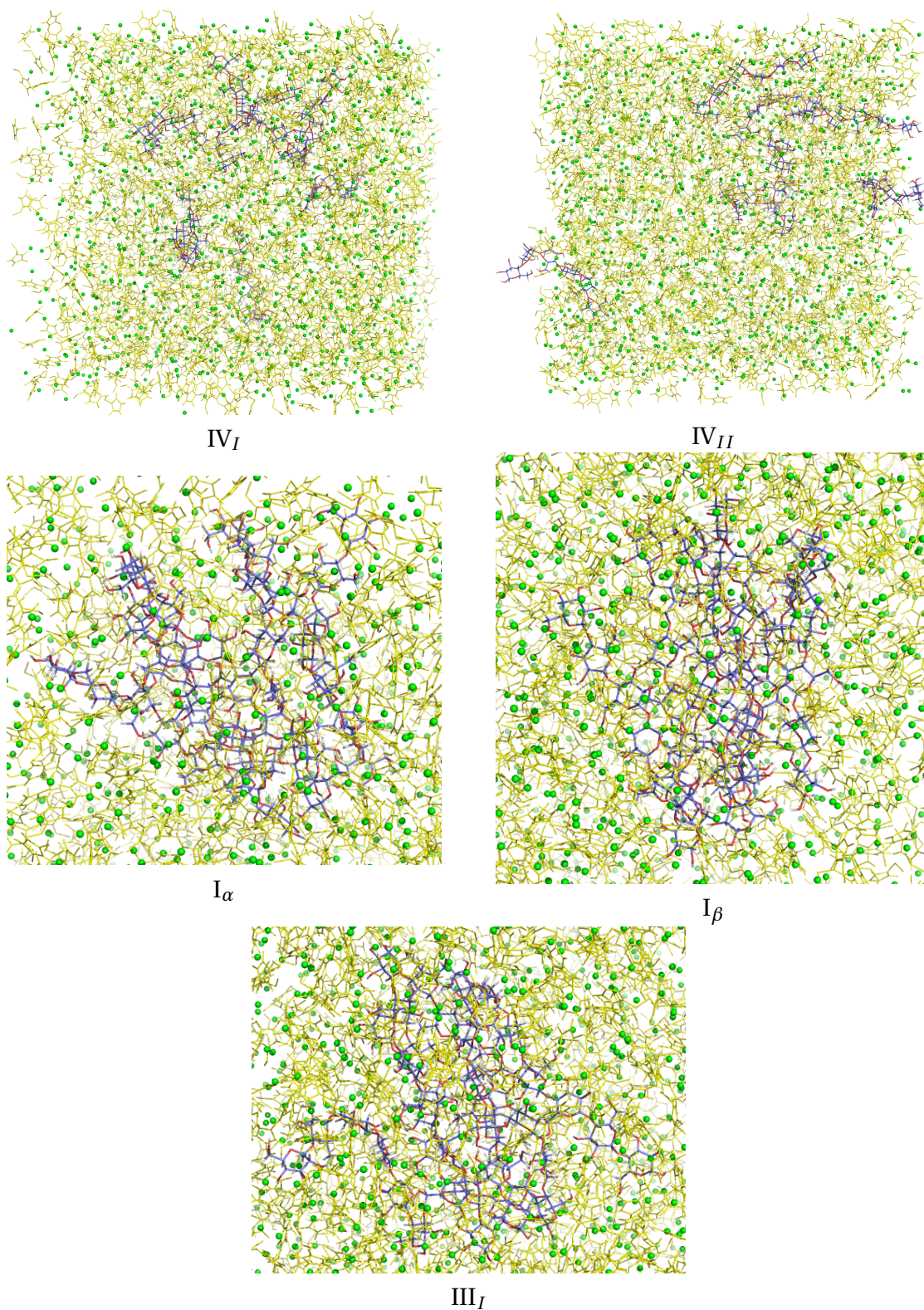


Figure 5.5: Final snapshots of simulations of cellulose polymorphs in EMIMCl. Polymorph types are subscribed directly on the figure.

According to these data we put all polymorphs in a box with cell length 80 Å and the solvent included 1629 molecules of CO₂ and 529 molecules of acetone. The procedure of preparation was exactly the same as in case of ionic liquid including preparation of the box by PACKMOL program (Martínez et al. 2009), equilibrating of the solvent box and inserting the cellulose microcrystals inside the equilibrated box. As before we carried out NPT-simulations during 80 ns. Figure 5.6 shows the first frames of polymorphs I_α and IV_I in the simulation boxes.

Results and Discussion. To our knowledge, there is no reports in the literature mentioning neither the dissolution of any kind of cellulose, nor the dissolution of its polymorph forms in CO₂/acetone mixture. We consider this result as stringent test to the methodology and the potential model used in our simulations.

Figure 5.8a shows the time behaviour of radii of gyration of 5 polymorphs of cellulose in CO₂/acetone mixture. One can see that the radii of gyration do not exceed much their initial values. From the other hand we can observe relatively large peak at ≈ 44 ns. ROG values can be suitable tool to check if the given system is expanding. However, if this is not the case ROG is not suitable observable to assess the dynamics of the nanocrystal. In order to understand what is happening in the nanocrystal when it is not expanding we will need RMSD values. Here, they are somewhat independent on ROG, because if one fiber of cellulose crystal moves with respect to others it will almost not affect the ROG but will sufficiently change the RMSD. Figure 5.8b shows the RMSD values of polymorphs in CO₂/acetone mixture. Compared to ROGs, RMSDs change sufficiently, especially for the the cases of polymorphs IV_I and IV_{II}. Thus we can conclude that rather sufficient peaks on ROG of polymorph IV_I are related to internal rearrangements of fibers with respect to each other. In order to illustrate this interpretation the direct atomistic picture is given in the Figure 5.7. One can observe lack of any structure and it is even possible that the blue fibers are almost perpendicular to green ones.

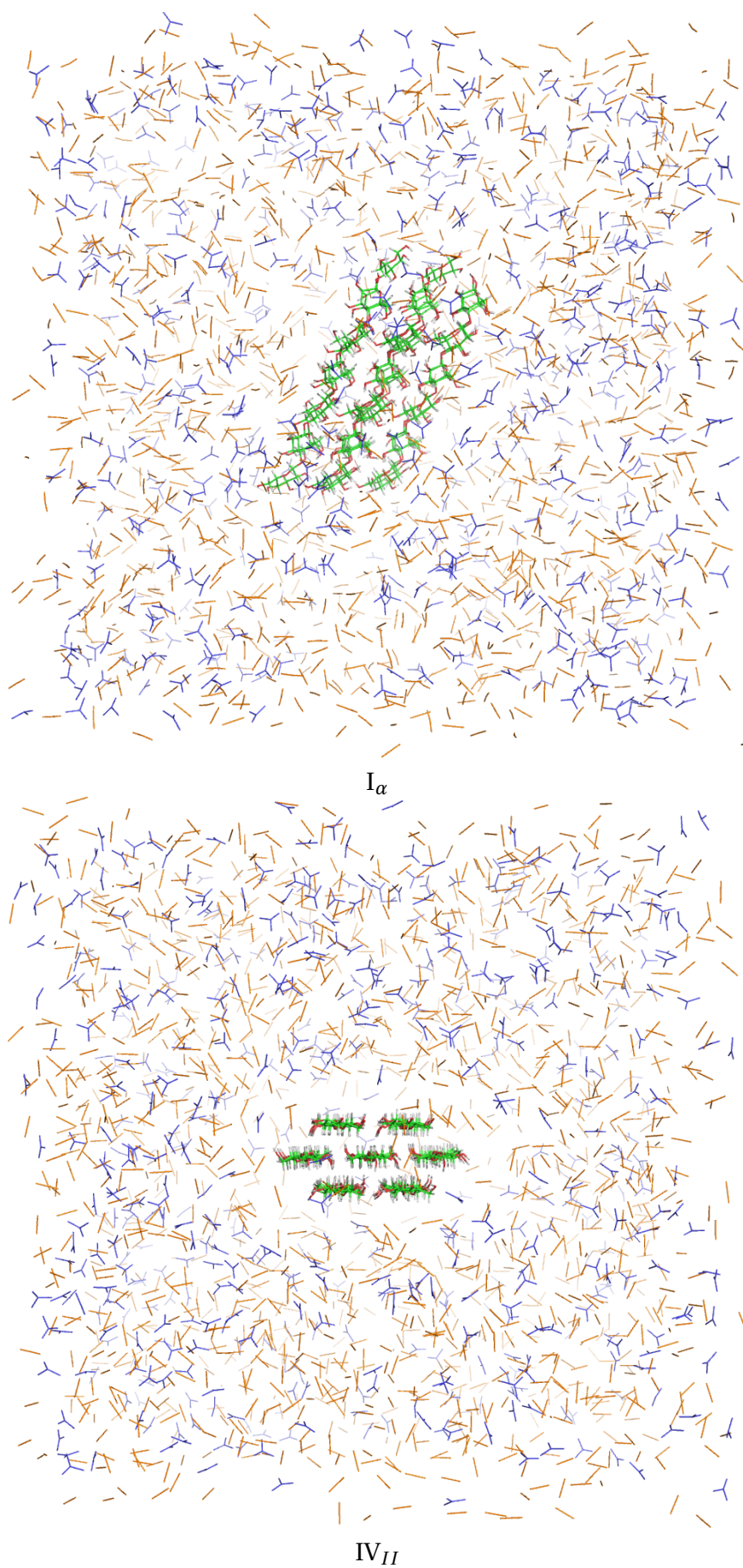


Figure 5.6: Snapshots of the first timestep of cellulose simulation of polymorphs I_α and IV_{II} in $scCO_2$ /acetone mixture.

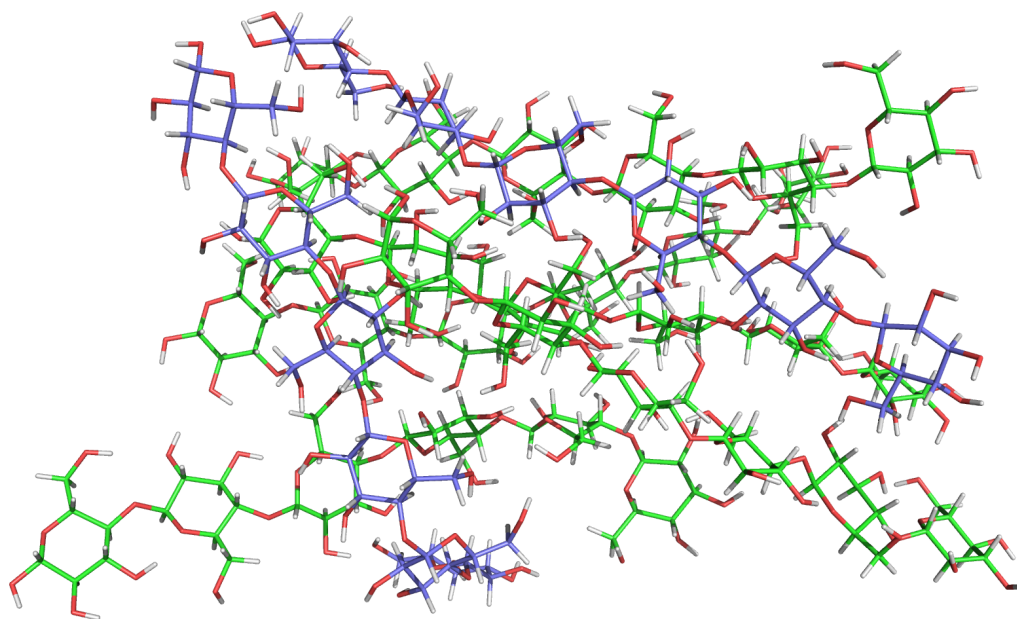
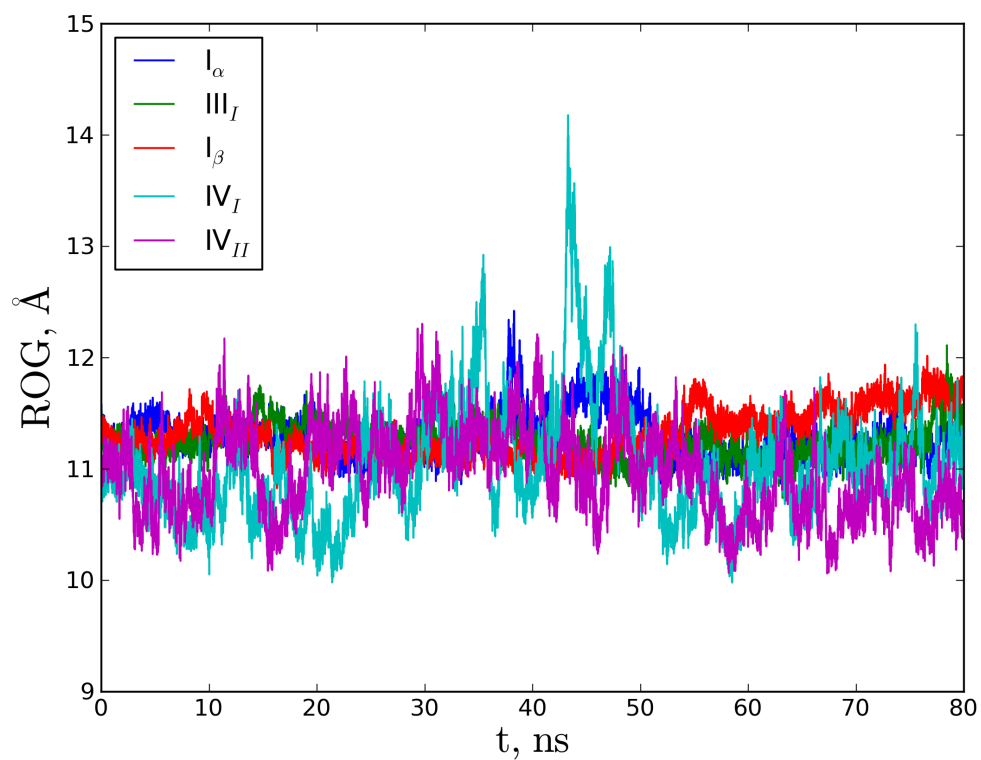


Figure 5.7: Cellulose snapshot in the moment of internal rearrangement. The solvent molecules are removed in order to facilitate the perception. One can see that the crystalline structure is completely lost and blue cellulose fibers are almost perpendicular to green ones.

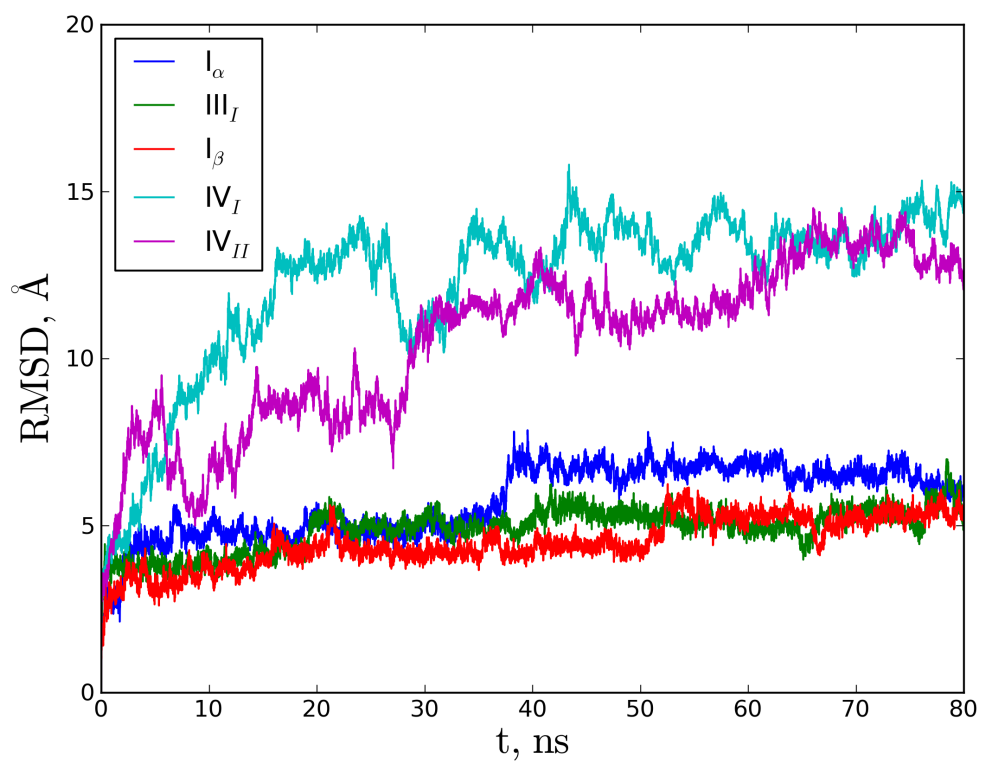
5.3.2 Cellulose in scCO₂/Ethanol Mixture.

Properties of supercritical mixtures of CO₂ with ethanol were reported in work by (Pöhler and Kiran 1997b). Critical parameters of one of compositions are as follows: $P_C = 153$ bar, $T_C = 393$ K, $x_C^{\text{etoh}} = 30\text{mass}\%$. Using these data we set up 5 systems with the same polymorphs and 80ns-long simulations were performed. Initial configurations look pretty much the same and we will do not present them here, instead, the final configurations will be shown in the end of this subsection.

Results and Discussion. CO₂/ethanol supercritical mixture was not used as a cellulose solvent until now. However, ethanol forms much stronger hydrogen bonds and it is very interesting to observe the influence of this fact on the cellulose behaviour inside the box filled with CO₂/ethanol mixture. If ethanol can compete for hydrogen bonds with cellulose fibers then more interesting behaviour can be expected. Figure 5.9 shows radii of gyration and RMSDs of cellulose polymorphs in CO₂/ethanol mixture media. Again we see the behaviour resembling the case of acetone but somewhat intensified: Fluctuating r_G and growing RMSDs. This time the picture is observed not only for one but for several polymorphs and even the most stable— I_β is



a



b

Figure 5.8: Radii of gyration (a) and RMSDs (b) of cellulose polymorphs in scCO_2 /acetone mixture.

affected. Another interesting fact to observe is the large fluctuation of $r_G^{I\beta}$ at 40 ns that is accompanied by the sharp growth of RMSD. It can be attributed to internal rearrangement and destruction of the crystal structure of cellulose. Indeed, Figure 5.10 shows cellulose microcrystal after 43 ns from the beginning of the simulation. Again, we see that the cellulose loses its crystallinity and several fibers are perpendicular to their neighbors.

However, such structure can be only considered as transitional and already in few nanoseconds new equilibrium is achieved characterized by parallel arrangement of fibers, see for instance Figure 5.11. This situation is perfectly illustrated by RMSD, where, for instance, for polymorph I_β one observes the formation of a plateau starting at ≈ 50 ns and characterizing the non-changing of the structure. In fact, after 80 ns one obtains the same picture—not a crystalline but definitely ordered cellulose with fibers arranged in parallel way.

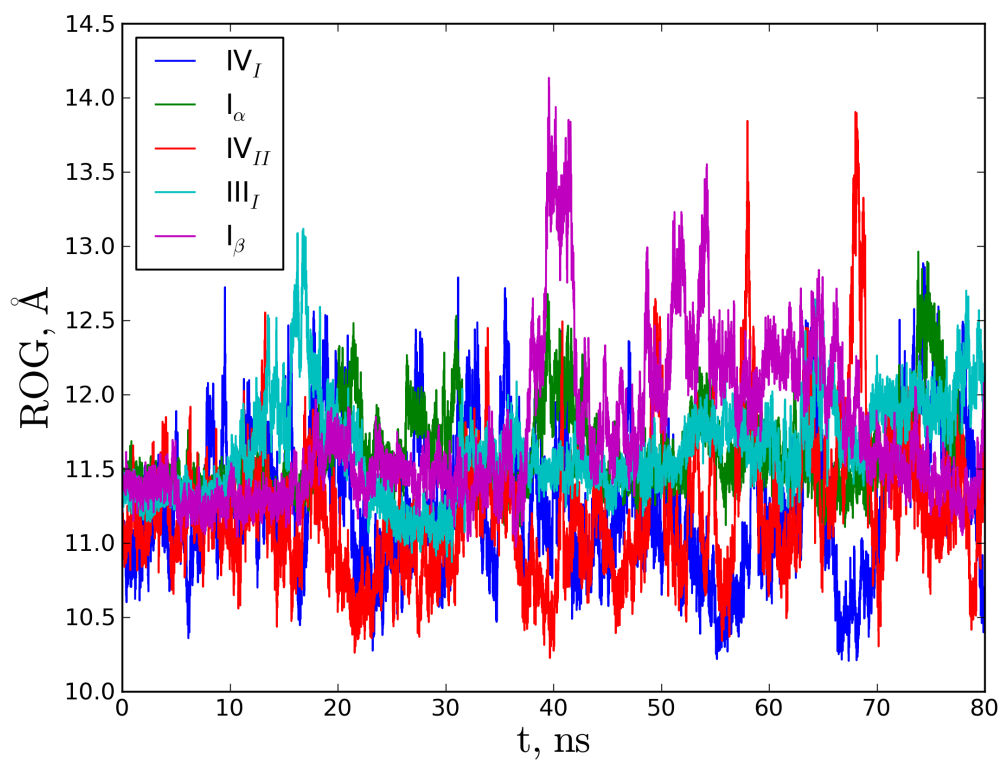
Thus, we can conclude that ethanol entrainer helps to cause more sufficient changes in crystalline cellulose structure than acetone and even relatively stable polymorphs are affected.

We notice that the ionic liquid dissolves the polymorphs IV_I and IV_{II} and structural changes indicate that it may dissolve the other polymorphs. In the case of CO₂/ethanol mixture we did not observe the dissolution of any polymorph of cellulose. Thus, for our subsequent studies of the dissolution of cellulose in other solvents we will only use polymorph IV_{II} in order to reduce computational efforts. However, in case of a success of dissolution with a given solvent we will repeat the simulations for most stable polymorph—I_β.

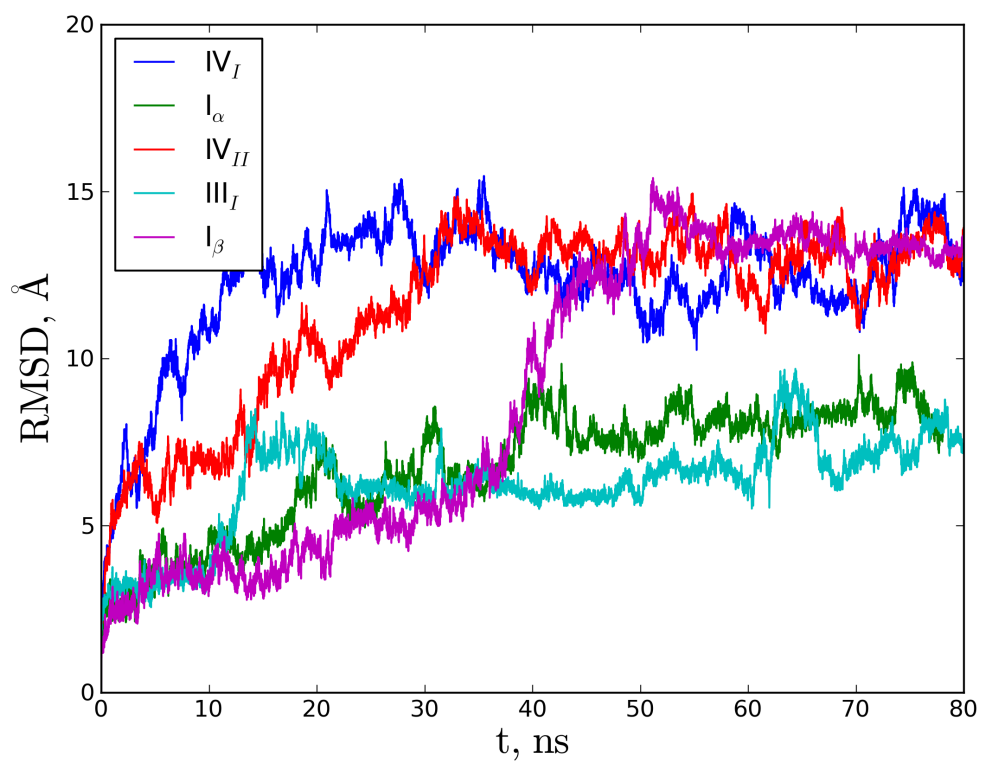
5.3.3 Influence of a second cosolvent on the process of cellulose dissolution.

In previous subsection we saw that supercritical CO₂ even with addition of polar cosolvents such as ethanol and acetone can not dissolve cellulose. From the other hand scCO₂ mixture can dissolve other polar cosolvents that could compete with cellulose for its hydrogen bonds. Our strategy here was to take already known cosolvents such as trimethylamine N-oxides and urea and to check the ability of these ternary mixtures to dissolve cellulose.

One of the motivations of these simulations was the existence of patent (CORPORATION 2003) (which was finally rejected) describing the method for dissolution of cellulose in supercritical mixtures containing CO₂, ethanol and one of the tertiary amine oxides, for instance triethylamine N-oxide. The choice of urea was due to, first of all, its ability to form numerous strong hydrogen bonds with OH- groups. The other reason was the recently proposed process of dissolution of cellulose in basic urea solutions (ZHOU and ZHANG 2000). From the other hand scCO₂/ethanol/urea



a



b

Figure 5.9: Radii of gyration (a) and RMSDs (b) of cellulose polymorphs in scCO_2 /ethanol mixture.

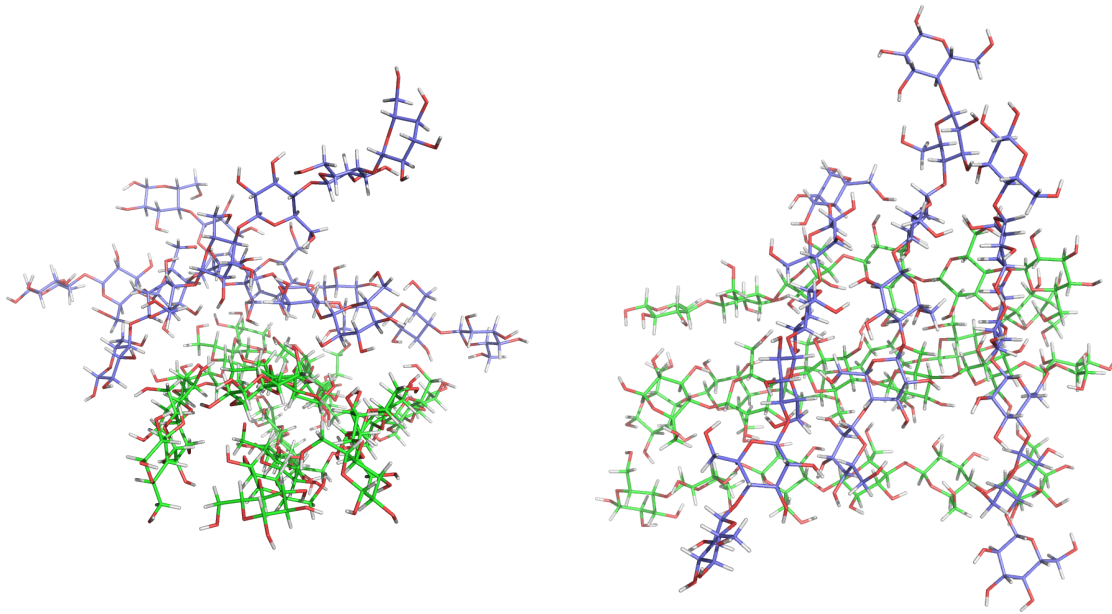


Figure 5.10: Structural rearrangement in cellulose crystal in scCO₂/ethanol mixture. Left-hand side: View from the side; right-hand side: view from the top.

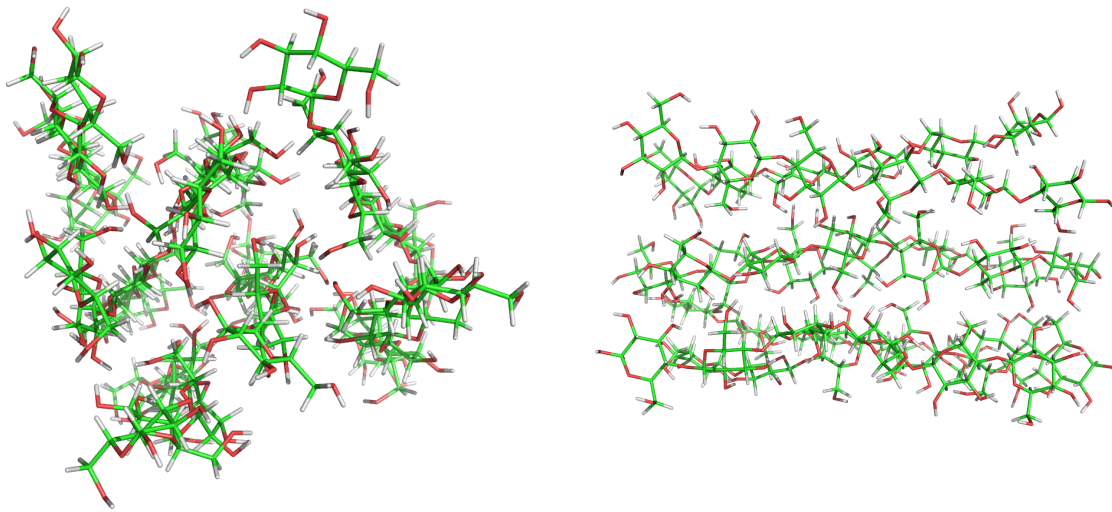


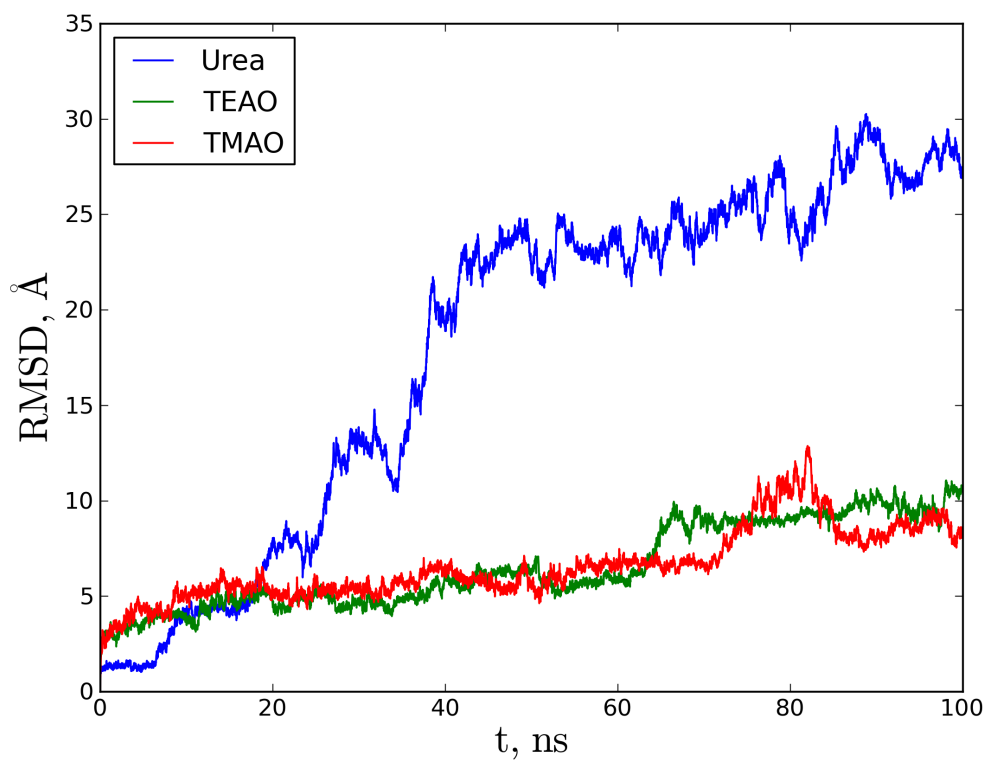
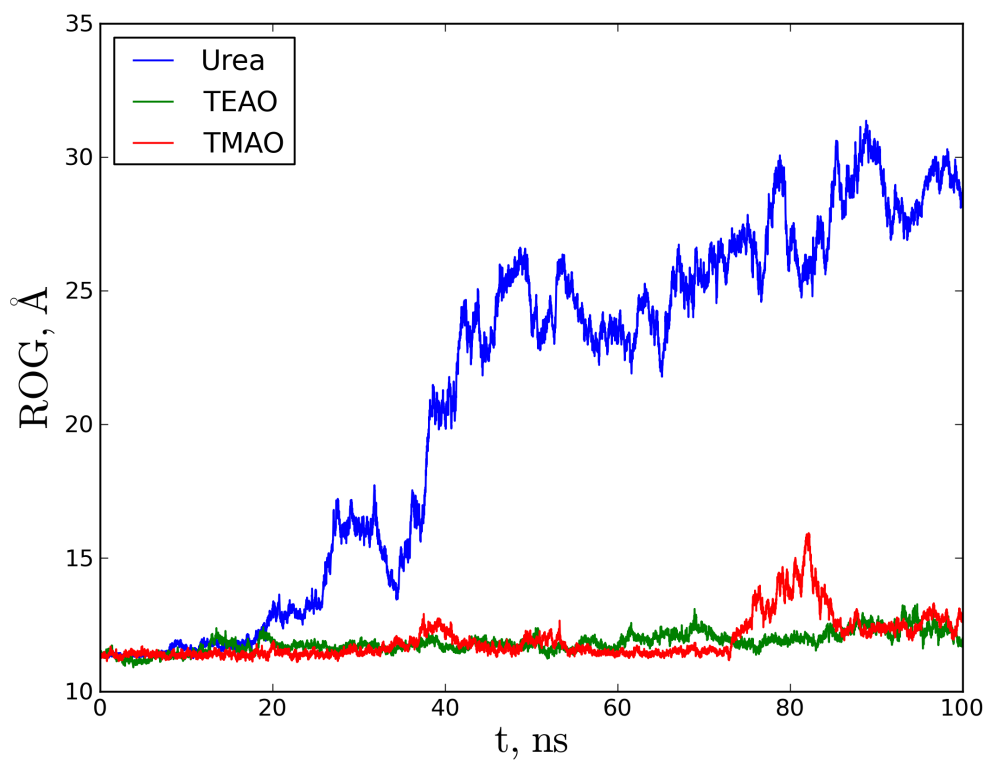
Figure 5.11: Final snapshots of cellulose I_β (solvent molecules were removed for better perception). Cellulose fibers are packed in parallel.

mixture was already used in the process of preparation of cellulose carbamate. The impregnation of cellulose at 120°C was reported and chemical conversions of cellulose at temperature of 130–150°C. Experimental method of samples preparing, however, would not allow authors to observe dissolution of cellulose even if it was the

case. Urea itself can be dissolved in supercritical carbon dioxide and addition of ethanol increases the solubility in up to 1000 times (Catchpole et al. 2005).

Details of Simulations. To check the ability of these ternary mixtures we set up the systems in the following way. For all the simulations we took the nanocrystal of cellulose IV_{II} as it is the less stable compared to other polymorphs. The mixture of CO₂ with ethanol always contained 2042 CO₂ molecules and 820 molecules of ethanol. The amount of a second cosolvent was 120 molecules in case of trialkylamine N-oxides and 200 molecules in case of urea. The interaction potential models for TMAO, TEAO and urea were taken from the “CHARMM general force field” (Vanommeslaeghe et al. 2010). Each solvent system was equilibrated for 1 ns and then the cellulose nanocrystal was inserted inside the box. This procedure was followed by the 100 ns run and the coordinates snapshots were gathered every 10 ps.

Results and Discussion. Figure 5.12 shows the changes of ROGs of cellulose nanocrystal with time. In case of systems containing trialkylamine N-oxides one can observe almost constant ROG during the whole simulation time duration. In case of TMAO a sharp increase of ROG is observed about 80 ns which quickly disappears for the subsequent time. In case of urea we observe the increase of the ROG that grows till the end of simulation. However, there was a problem caused by jumping of parts of the crystal from one periodic image to another and we continued our simulations in order to check the results. Figure 5.13 shows the extension of the simulation scale till 200 ns. One can see that the radius of gyration stops growing and even decreases by the end of simulation. Thus, we do not believe that cellulose shows the dissolution in case of urea being the second cosolvent.



ertiary mixtures.]Radii of gyration and RMSDs of cellulose polymorph IV_{II} in scCO_2 /ethanol/[urea|TMAO|TEAO] tertiary mixtures.

Figure 5.12: t

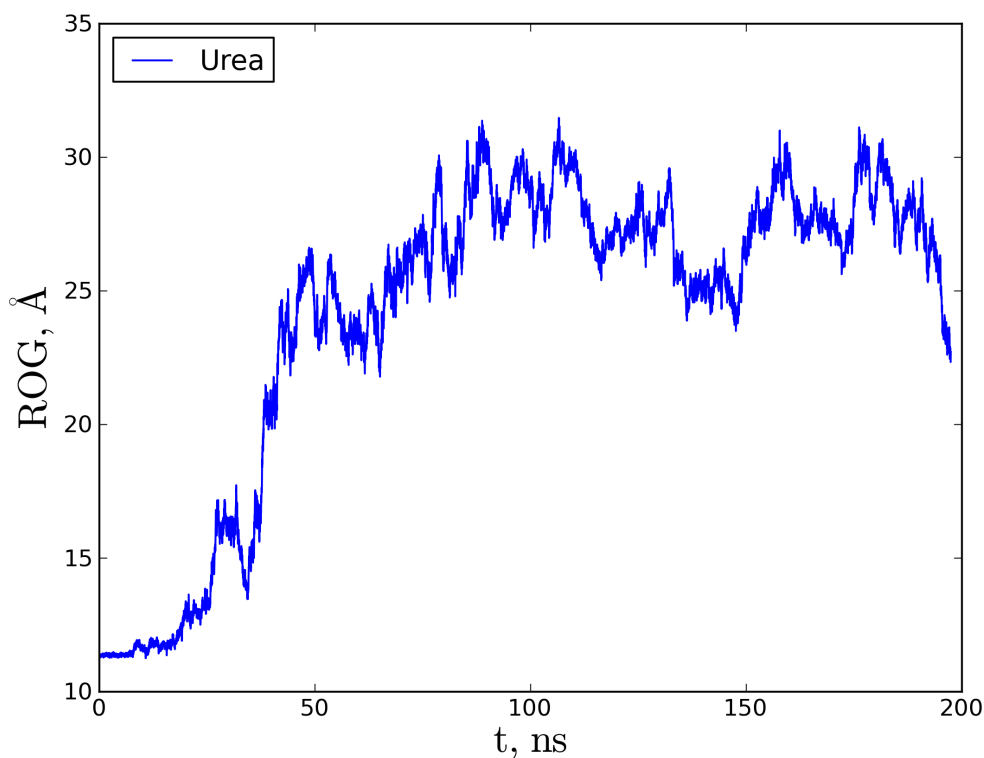


Figure 5.13: Changes of ROG during the 200ns–long run in scCO_2 /ethanol/urea tertiary mixture.

5.4 Cellulose nanocrystals in liquid and supercritical ammonia.

Application of ammonia to cellulose chemistry has a long history. It begins in the beginning of XXth century when it was recognized that liquid ammonia with combinations with organic salts dissolves cellulose (Scherer 1931). After that the role of supercritical ammonia in cellulose polymorphism was discovered as simultaneously showed (Hess and Trogus 1935; Barry, Peterson, and King 1936). These aspects were already discussed in section 1.2 and in section 1.3.

Current trends in cellulose chemistry lead researchers to find the paths for conversion of cellulose into biofuel. Enzymatic hydrolysis is considered to be as one of the most perspective ways to convert cellulose into bioethanol. The enzymatic hydrolysis is found to be more efficient where the cellulose was pretreated and converted into less stable crystalline form. For instance during the course of treatment of

cellulose III_I the yield of the cellobiose was more than 8 times larger than for case of cellulose I_α (Igarashi, Wada, and Samejima 2007). Recently several papers were published devoted to simulations of processes happening in cellulose under the influence of liquid and gaseous ammonia (Bellesia et al. 2011; Wada et al. 2011). Indeed, it would be very interesting to study the dynamics of cellulose polymorphs transformations. These rearrangements happen at elevated temperatures and were observed, for example, in (Wada et al. 2011) at 140°C. Capturing of ammonia was observed in those simulations and the structure ammonia–cellulose III_I was refined, a namely, formation of cellulose–ammonia hydrogen bonds. However, there is an unclear moment related to the following fact. The potential model of ammonia used in simulations by (Bellesia et al. 2011; Wada et al. 2011) was taken from the work of (Gao, Xia, and George 1993). These parametrization of conventional Lennard-Jones + Electrostatics interactions was found to be good with respect to prediction of structure of liquid ammonia, however, the liquid-gas equilibrium was found to be not well-predicted by this model (see subparagraph 3.1.2) while such properties of fluid can be crucial when one deals with supercritical state. For instance, it was shown that nucleation pathways can be changed due to critical fluctuations in the fluid (Wolde and Frenkel 1997).

Results and Discussion. As it was discussed in the previous section, CO₂-based supercritical mixtures do not dissolve cellulose. We came to the idea to use supercritical ammonia as a solvent. We believe that most likely, this is due to small affinity of cellulose monomer to such mixtures. From the other hand, even though liquid ammonia has a large affinity, comparable to that of the well-known cellulose solvent—EMIMCl, it does not dissolve cellulose. But what will we observe in case of ammonia in the vicinity of the critical point? What will be the influence of critical fluctuations?

In our work we studied the influence of sub- and supercritical ammonia on cellulose nanocrystals. We used the interaction potential model of ammonia proposed by (Kristof et al. 1999) that became well-recommended in prediction of properties of ammonia near the critical point and liquid structure as well. Figure 5.14 visually shows the conditions at which we performed our simulations. In order to represent liquid, sub- and supercritical we choose four points along the isobar $P = 135$ bar that lies above the coexistence curve: One point is to model liquid ammonia at 243 K, one point is for subcritical ammonia at 390 K, one point is for supercritical ammonia slightly above both the critical point and the point of maximum of isobaric compressibility (subsubsection 3.1.2) of ammonia at $T = 420$ K and the final point is at gas-like density at 450 K.

We chose to analyse the nanocrystals of cellulose IV_{II} because it is the least stable polymorph and this will allow to reduce the time of the simulation. Figure 5.15 shows the time evolution of ROGs. The remarkable result is the growth of the ROG in the

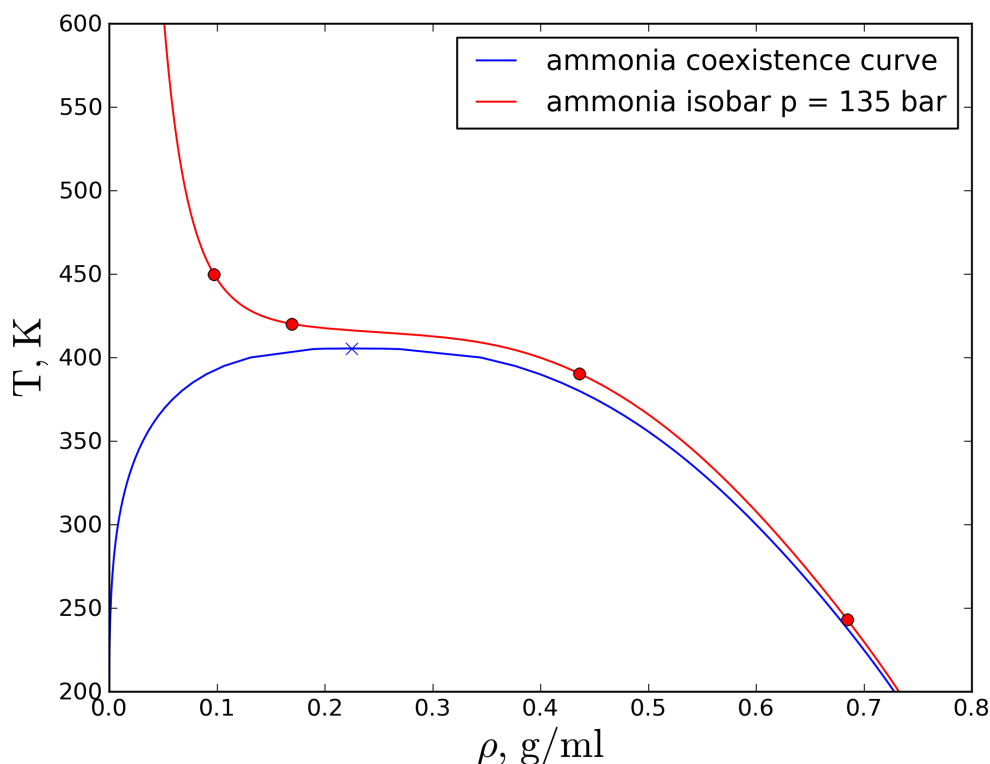


Figure 5.14: Blue line stands for coexistence curve at which top the critical point marked as a blue cross. Red line is an isobar at $P = 135$ bar, red points, lying on the isobar, represent the thermodynamical conditions used in our simulations of cellulose dissolution in liquid, sub- and supercritical ammonia. Temperatures (from bottom to top): 243, 390, 420 and 450 K

thermodynamical conditions near the critical point ($T = 390$ K and $T = 420$ K) as a comparison with those for the conditions far from the critical point ($T = 243$ K and $T = 450$ K). This result clearly shows that the cellulose is dissolved in ammonia near the critical point. In fact, we even stopped the simulations in case of temperatures 390 and 420 K to save the computational time: Already in 10 ns at temperature 390 K we obtained the same value of ROG as in EMIMCl after 80 ns. At the same time ROGs for liquid ammonia remains constant showing us that crystal remains unaltered. ROG of cellulose in ammonia at gas-like density fluctuates and in the box we can visually observe the penetration of ammonia molecules inside the crystal, however, no rapid increase of ROG was observed and we put forth the conclusion that ammonia will not dissolve under these conditions. The penetration of ammonia molecules can be clearly seen by RMSD of cellulose IV_{II} shown in Figure 5.16. It grows with time for

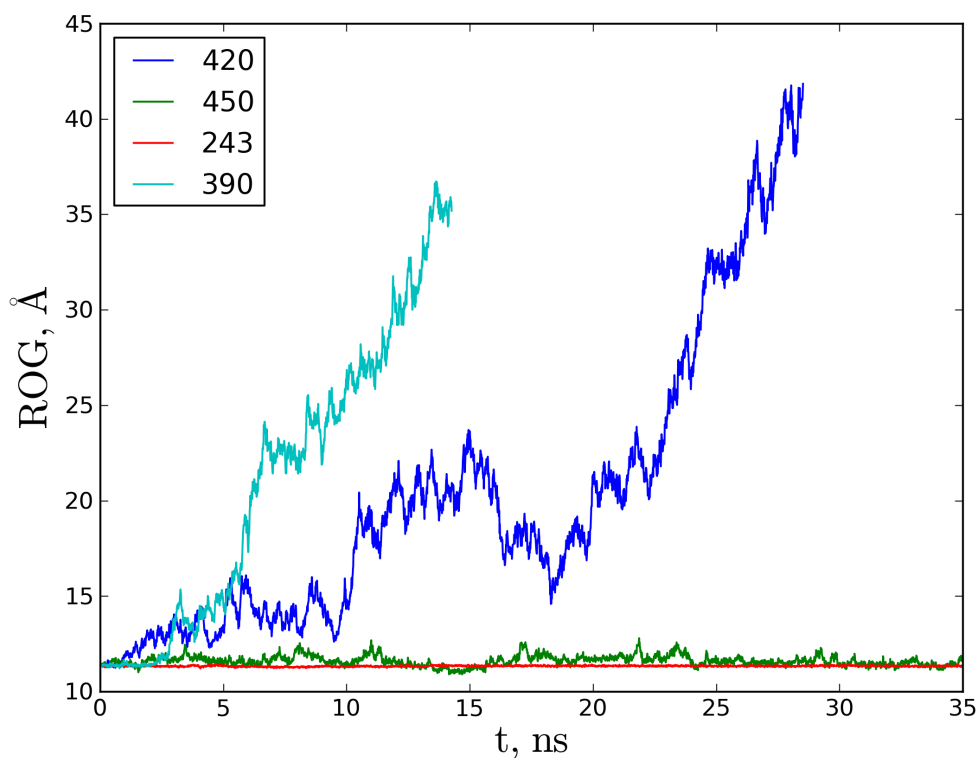


Figure 5.15: Radii of gyration of cellulose IV_{II} polymorph in ammonia along the iso-bar 135 bar.

gas-like density but not as rapidly as for near-critical region and does not exceed the limit of 10 Å. In fact, this means that cellulose fibers perform mutual rearrangements but remain stucked to each other.

In order to verify that the observed effect does not depend on the polymorph of cellulose we have taken a nanocrystal of the most stable polymorph— I_{β} and performed the same simulations with it. Figure 5.17 shows the time evolution of radii of gyration for this system. The main features remain the same: We observe rapid increase of the ROG in near-critical(390 K and 420 K) region while far from the critical point (243 K and 450 K) we see that the ROG does not change sufficiently.

Summarizing results on simulation of cellulose in ammonia we can clearly state that we have shown the dissolution of cellulose in supercritical ammonia and studied the influence of thermodynamic parameters on this process.

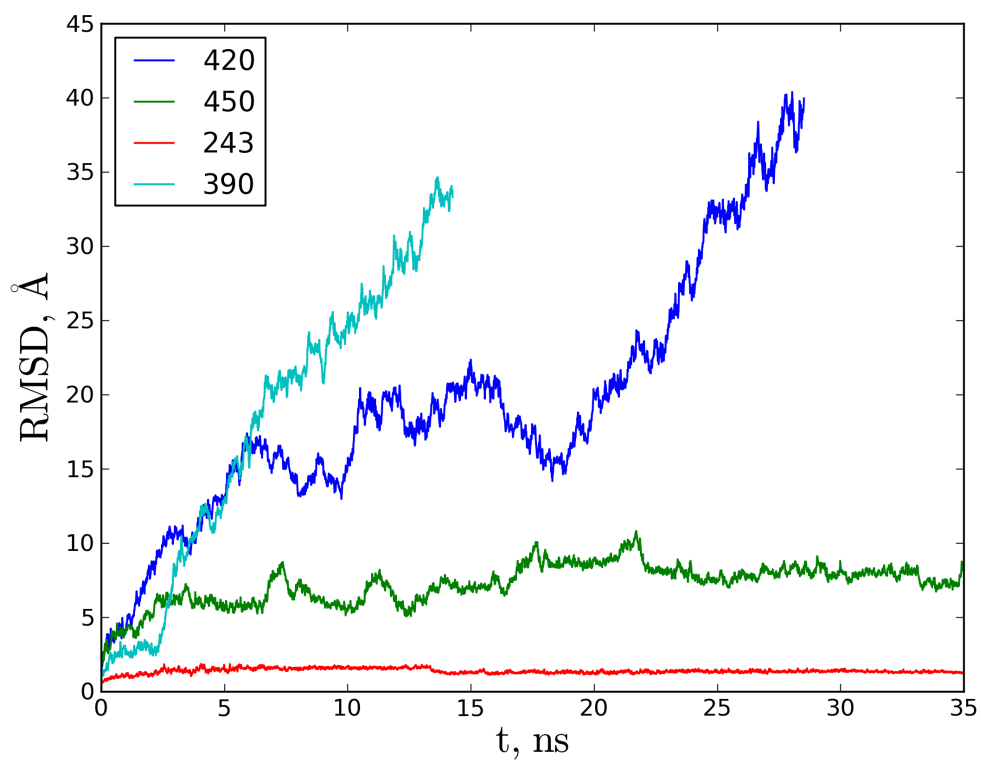


Figure 5.16: RMSDs of cellulose IV_{II} polymorph in ammonia along the isobar 135 bar.

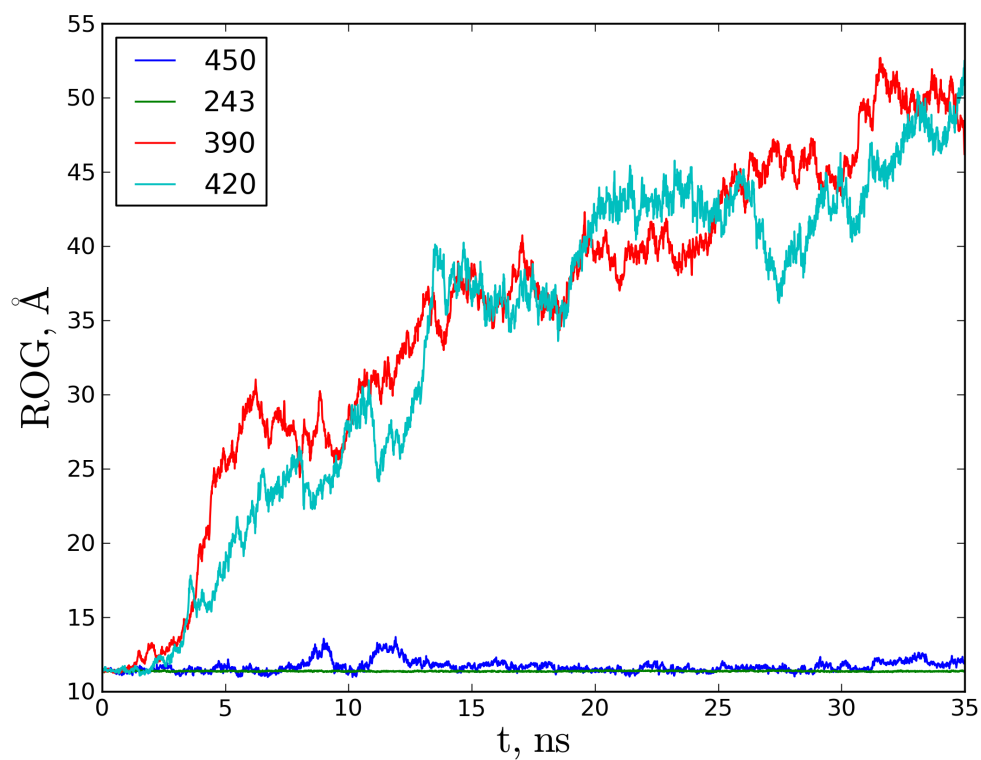


Figure 5.17: Radii of gyration of cellulose I_{β} polymorph in ammonia along the isobar 135 bar.

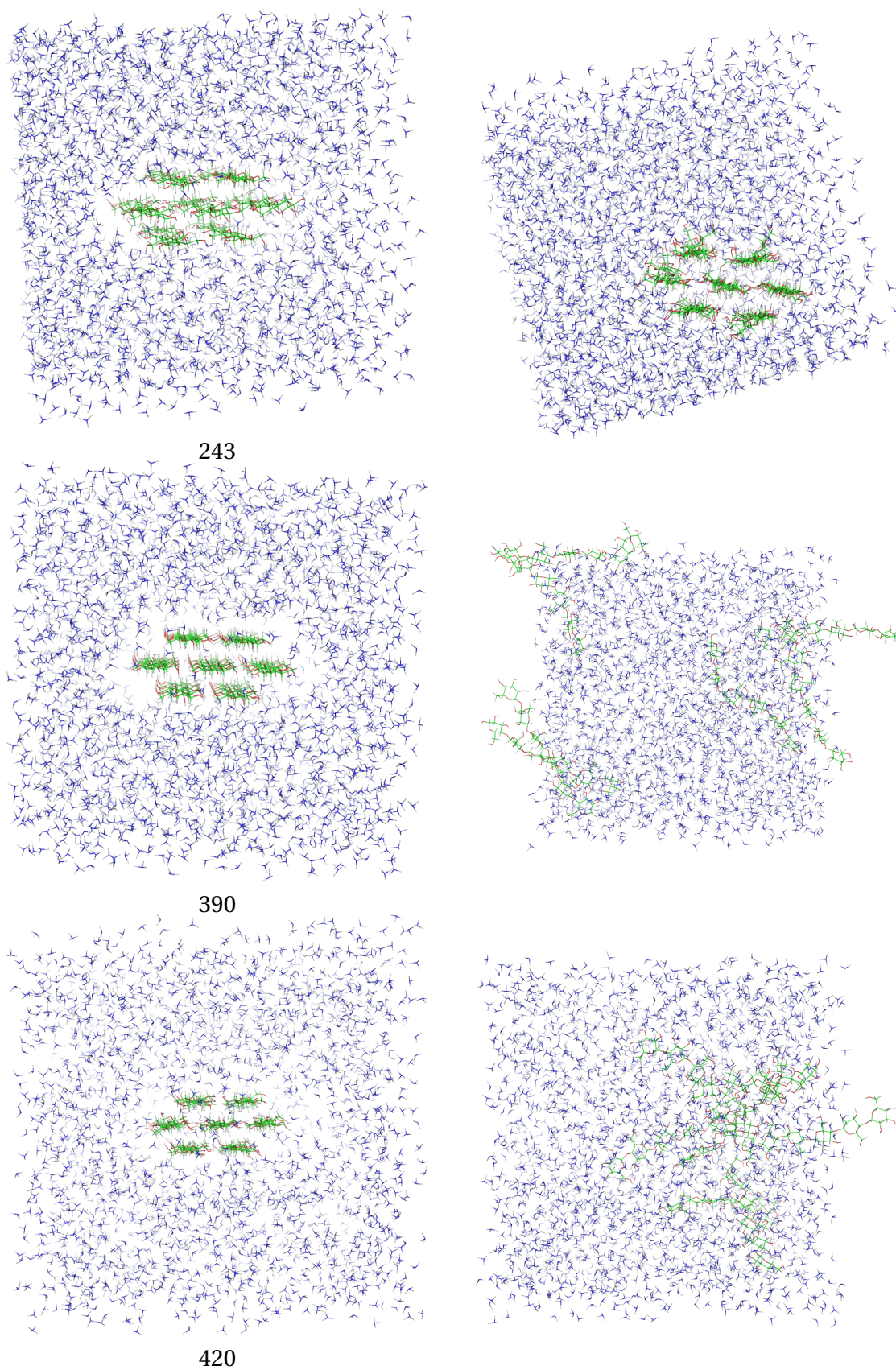


Figure 5.18: Initial snapshots of cellulose in liquid and supercritical ammonia. Temperatures are subscribed below the figures.

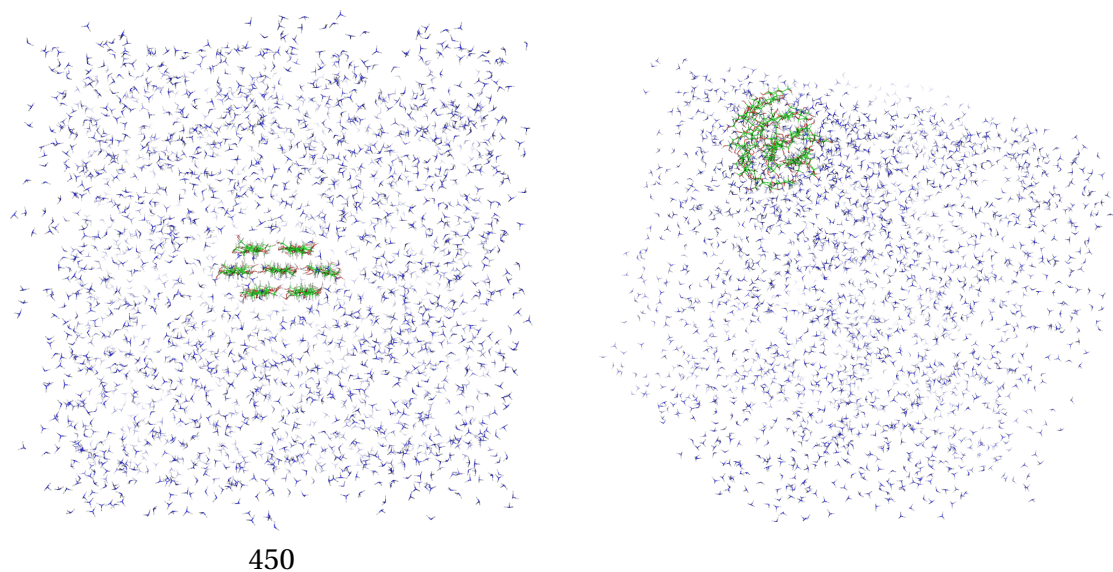


Figure 5.18: Figure 5.18–Continuation. Initial(left-hand side) and final(right-hand side) snapshots of configurations of cellulose nanocrystals in ammonia. Temperatures are subscribed under the figures.

Chapter **6**

CONCLUSIONS AND PERSPECTIVES

6.1 Conclusions.

The present thesis was carried out in the frame of the project which aim is to explore the possibility of supercritical fluids technologies application in the dissolution of cellulose. The progress in this field may lead to economically and more attractive process and to alleviate environmental constraints. For this propose it is necessary to further improve the knowledge in this area on fundamental level. We used extensive molecular dynamic simulations on pure supercritical fluids, on various co-solvents/supercritical fluids mixtures and on models of cellulose and finally on nanocrystal polymorph of cellulose. The principal objective of the study on pure supercritical fluids was to characterize the locale structure (radial and orientation distribution of molecules) along the liquid gas coexistence curve. We carried then molecular dynamics simulation to quantify in an unambiguous way these subtle local changes around the atoms involved in hydrogen bond interactions using adequate statistical functions. Indeed, the radial distribution function (as obtained by neutron scattering and molecular dynamics simulations) is a major means by which the locale structure is usually described in liquid systems. However, this statistical property does not provide sufficient details on the nature of the local environment in these systems around a probe atom. Particularly, when analyzing the locale structure in the studied system using this standard statistical approach, one is faced with a major problem: the subtle changes of the locale structure occur only near the probe molecule and averaging through all of thermodynamic ensemble diminishing all effect sometimes closely to zero. Therefore, in order to understand the changes of the locale structure around a probe molecule, it is important to use appropriate statistical functions for studying the local structure in the studied system. The main idea then is to used statistical geometry and the nearest neighbour distribution approaches as an indicator of the local structure around the probe moelcule. In the statistical geometry method, the local structure is characterized by the statistical analysis of irregular polyhedra obtained by a specific tessellation (in our case the Voronoi tessellation) of the three dimensional space. The neighbour-ship approach allows calculating the density probability of nearest neighbour distribution. The neighbours of a central atom are sorted by distance into the first neighbours, second neighbours, etc. Separate radial distribution functions, $p_{\alpha\beta}(n,r)$ may be defined for each set of nearest neighbours atoms β (indicated by n), and at distance r from the central atom α . These functions are less averaged and contain then more information than the corresponding $g_{\alpha\beta}(r)$ (the radial distribution of atom β around atom α). The main results of this analysis may be summarized in the flowing points:

- The local structure may be resolved into two components or sub shells: one is characterized by small radial fluctuations, and a dominance of the contribution of the attractive part of both the electrostatic (EL) and Lennard-Jones (LJ)

to the total interaction energy. Conversely, the second sub shell is characterized by large radial fluctuations and by a concomitant increase of the repulsive contribution of the EL interaction and a shift to less attractive character of the LJ contribution. When the temperature increases along the liquid-gas CC, the first sub shell undergoes large changes which are characterized by an obvious increase of the radial fluctuations, by an increase of the random character of the orientation distribution except for the first nearest neighbor which almost maintains its orientation with respect to the probe molecule.

- This analysis of the local structure based on the behavior of distributions of metric and topological properties of the Voronoi polyhedra (VP) show that by increasing the temperature, the volume, surface and face area distributions of the Voronoi polyhedra as well as the vacancy radius distribution broaden, particularly near the critical temperature, where the thermal expansion coefficient has its maximum. Furthermore, the rate of increase of the corresponding mean values and fluctuations increases drastically when approaching the critical point. This behavior clearly indicates that the local structure, as described by the VP, becomes increasingly heterogeneous upon approaching this temperature. This heterogeneous distribution of supercritical fluid molecules is traced back to the increase of the large voids with increasing the temperature, and is also clearly seen in the behavior of the fluctuation of the local density, as measured by the Voronoi polyhedra. More interestingly, the maximum in the heterogeneity coincide with the maximum of the fluctuation in the density of the VP.
- From the point of methodological point of view, our results point out the importance of choosing an adequate potential of the simulated supercritical fluid. The liquid gas-coexistence curve, critical temperature, densities, energies, and structural data (radial distribution functions) should be calculated for the various interaction potential models of the studied supercritical fluid, and compared with the corresponding experimental data. This comparison allows a classification of the different models in terms of their relative agreement with experimental data, particularly, those properties of the studied supercritical fluid near the critical point and under the supercritical conditions. Furthermore when dealing with binary mixtures of CO₂ with cosolvent, although the intermolecular potentials models of CO₂ and co-solvent could be individually “good” (they are parameterized to reproduce the structure and dynamics of the CO₂ in supercritical conditions and the co-solvent, respectively), the combination of these two intermolecular potentials does not necessarily reproduce the structure and dynamics of the mixture. Our results suggest the systematic comparisons of the molar volume of the different systems as well as of the change of their molar volume accompanying the mixing of the two components with

experimental data to predict the experimental miscibility of these compounds, as seen from the negative values of the free energy change accompanying their mixing.

The study of the dissolution process of cellulose was carried out at two different levels. In the first level, we started from the hypothesis that information on the dissolution process of cellulose may be obtained by considering only its monomer (the cellobiose molecule). We studied then in the chapter 4, the process of dissolution of cellobiose in various solvents and various thermodynamic points. These solvents were water and ionic liquid, mixtures of supercritical CO₂ with ethanol, and acetone, supercritical ammonia. The choice of the potential models for these solvents as well as for cellobiose was justified by the agreement of the calculated and experimental results of the physical and chemical properties of these molecules. We used the free energy of solvation of cellobiose as a measure of the thermodynamic affinity of cellobiose to the solvent. The free energy was estimated using the free energy perturbation method which allows one to get the free energy differences between two states. In our case these two states were the solvated and non solvated cellobiose. The calculation of the free energy of solvation by means of free energy perturbation (FEP) were carried out in the forward and backward (annihilation-creation) scheme which allows to estimate the hysteresis associated with a bad sampling of the conformational changes of the cellobiose molecules. The conformations of cellobiose was quantified by the change in the dihedral angles φ and ψ (similar to Ramachandran angles). The free energy maps along these two angles were calculated for the various solvents listed before. Three conformers that correspond to three free energy minima were found. The conformations of cellobiose were affected by the solvent (thermodynamic states) as indicated by the shift of the positions of the minima, the reduction of the barriers between the minima, however, we didn't found any indication how these changes may influence the dissolution of cellulose. We also addressed in this chapter the problem of the application of FEP to large flexible solutes. Indeed, these solutes possess conformational degrees of freedom which affect the free energy differences. However, using standard molecular dynamics simulations is not sufficient to sample correctly these various conformations. Indeed, the time duration of the transition between two conformers may last several nanoseconds and large simulation time scale should be used. We decided to combine the free energy perturbations calculations with the metadynamics approach which allows an efficient sampling of the various conformers of cellobiose. We used first water and ionic liquid, for which previous simulation data are available, as benchmarks to the comparison between FEP calculations (without metadynamics) and the combination of FEP and metadynamics approach. This approach was used to analyse the free energy of solvation of cellobiose in a mixtures of supercritical CO₂ with acetone and ethanol and in supercritical ammonia. The main conclusion of this chapter is that the analysis of the

dissolution process of monomer of cellulose (cellobiose) using the criteria of solvation free energy is not sufficient to get information on the dissolution of cellulose itself. Indeed, cellulose has a crystalline structure which is due to intra and intersheet of hydrogen bonds and one can see that considering only the interactions between monomer and the solvent without studying the influence of the crystal packing and hydrogen bonds formed between monomers (the fibre structure) is not enough to give reasonable conclusions.

In Chapter 5, we studied the dissolution process of the five nanocrystal polymorphs of cellulose (I_α , I_β , III_I , IV_I and IV_{II}) in various solvents systems including supercritical fluids. The calculations of the interaction energy of these nanocrystal polymorphs of cellulose allow classifying them with respect to their stability. This result allows us to test first the dissolution of the less stable nanocrystal polymorph of cellulose in a given solvent and in the case of success we went further and analyse the dissolution of the least stable polymorph. The statistical observables we used to characterise the dissolution were the radius of gyration (ROG) and root-mean square displacement (RMSD). The TraPPE forcefield was used to model CO_2 , acetone and ethanol. Kristof's ammonia interaction potential was chosen with the same purpose—to predict the liquid-gas coexistence curve and to represent the properties of ammonia near the critical point. The CHARMM general force field for small bioactive molecules was used for trimethylamine N-oxide (TMAO), triethylamine N-oxide (TEAO) and urea. The CHARMM carbohydrates interaction potential model was used for the nanocrystal polymorphs of cellulose as it was proven to be good in predicting of features of carbohydrates. Our results show, that none of the nanocrystal polymorph of cellulose is dissolved in supercritical mixture with both acetone and ethanol. Although, some structural changes in the polymorphs of cellulose are observed in the case of ethanol due to its ability to form hydrogen bond with cellulose. The time behaviour of the ROG of polymorphs IV_I and IV_{II} indicates clearly the dissolution of these polymorphs in the ionic liquid. These findings are supported by the analysis of the snapshot of the simulations which show a spreading of the cellulose molecules forming these polymorphs in the whole simulation box. Structural changes in the other polymorphs suggest that the dissolution process is in its first stages, and the increase of the simulation time duration (which we could not afford) would show it clearly.

In addition to ethanol and acetone other co-solvents were considered, such as urea, TMAO, TEAO. They have the common ability to form hydrogen bonds with cellulose. We have then studied the dissolution of the nanocrystal polymorphs of cellulose in ternary systems scCO_2 /ethanol/urea, scCO_2 /ethanol/TMAO and scCO_2 /ethanol/TEAO. Only the first system shows interesting results. Indeed, the time behaviour of the ROG indicates the dissolution ability of this ternary mixture, however, to check this result, we carried out long simulation run which lasts 200 ns. The radius of gyration stops

growing and even starts to decrease in the final steps. We have then doubt about the ability of this ternary mixture to dissolve cellulose.

Our final promising results concern the dissolution of cellulose in supercritical ammonia. We show that nanocrystal of cellulose dissolve in ammonia near its critical point (maximum of thermal expansion) while for thermodynamic point far from the critical point, the dissolution for the various polymorphs was not observed. Experiment will be carried out in order to test the validity of this finding.

6.2 Perspectives.

Perspectives of the following research can be summarized as follows:

1. Further studying of the scCO_2 -based solvent mixtures in order to check the pressure, temperature and mixture composition influence on the possible dissolution of cellulose;
2. Further clarifying simulation of the dissolution of cellulose in ternary mixture scCO_2 /ethanol/urea by increasing the simulation box size and analyse the effect of pressure, temperature and mixture composition;
3. Experimentally checking the dissolution of cellulose in supercritical ammonia near the critical point;
4. Applications of free energy methods to the dissolution process of cellulose along various reaction coordinates such as: the radius of gyration (to study expansion of crystals), the distance between fibers' ends (to study the tearing off of one fiber from the others), etc.
5. A good connection of our simulations with experiment will be the modeling of the recrystallization of cellulose from ammonia solution and obtaining the polymorph transition in crystalline cellulose $I_\beta \rightarrow \text{III}_I$.
6. Moreover, one should go further in details and analyze the local structure of ammonia solutions of cellulose, applying standard techniques of molecular simulations such as RDFs and newly developed nearest neighbours approach as well as Voronoi tessellations.

Bibliography

- Ahnelt, Peter Kurt et al. (2000). "Irregular S-cone mosaics in felid retinas. Spatial interaction with axonless horizontal cells, revealed by cross correlation". In: *J. Opt. Soc. Am. A* 17.3, pp. 580–588.
- Alinchenko, Marina G. et al. (2005). "Effect of Cholesterol on the Properties of Phospholipid Membranes. 4. Interatomic Voids". In: *J. Phys. Chem. B* 109.34. doi: 10.1021/jp051832s, pp. 16490–16502.
- Allen, M. P. and D. J. Tildesley (1987). *Computer Simulation of Liquids*. Oxford: Clarendon.
- Allen, M.P. and D.J. Tildesley (1999). *Computer simulation of liquids*. Clarendon Press. ISBN: 9780198556459. URL: <http://books.google.com/books?id=032VXB9e5P4C>.
- Aparicio, N. D. and A. C. F. Cocks (1995). "On the representation of Random Packings of Spheres for sintering Simulations". In: *Acta. metall. mater.* 43.
- Arakcheev, V. G. et al. (2003). "Linewidths and shifts of carbon dioxide CARS spectra near the critical point". In: *J. Raman. Spectroscopy* 34.12. 10.1002/jrs.1098, pp. 952–956.
- Balesku, Radu (1975). *Equilibrium and Nonequilibrium Statistical Mechanics*. John Wiley & Sons.
- Baranyai, Andras et al. (1986). "Statistical geometry of molten alkali halides Ionic association in electrolyte solutions: A Voronoi polyhedra analysis Voronoi polyhedra analysis of the local structure of water from ambient to supercritical conditions Structural and thermodynamic properties of different phases of supercooled liquid water The local structure of various hydrogen bonded liquids: Voronoi polyhedra analysis of water, methanol, and HF Voronoi space division of a polymer: Topological effects, free volume, and surface end segregation A Voronoi analysis of lipid area fluctuation in a bilayer Computer simulation study of intermolec-

- ular voids in unsaturated phosphatidylcholine lipid bilayers". In: *J. Chem. Phys.* 85.1, pp. 365–373.
- Barker, J.A. and R.O. Watts (1973). "Monte Carlo studies of the dielectric properties of water-like models". In: *Molecular Physics* 26.3, pp. 789–792. DOI: 10.1080/00268977300102101. eprint: <http://www.tandfonline.com/doi/pdf/10.1080/00268977300102101>. URL: <http://www.tandfonline.com/doi/abs/10.1080/00268977300102101>.
- Barry, A. J., F. C. Peterson, and A. J. King (1936). "x-Ray Studies of Reactions of Cellulose in Non-Aqueous Systems. I. Interaction of Cellulose and Liquid Ammonia". In: *Journal of the American Chemical Society* 58.2, pp. 333–337. DOI: 10.1021/ja01293a043. eprint: <http://pubs.acs.org/doi/pdf/10.1021/ja01293a043>. URL: <http://pubs.acs.org/doi/abs/10.1021/ja01293a043>.
- Bausenwein, T. et al. (1994). "Structure and intermolecular interactions in fluid ammonia: An investigation by neutron diffraction at high pressure, statistical-mechanical calculations and computer simulations". In: *J. Chem. Phys.* 101.1, pp. 672–682.
- Beckham, Gregg T. et al. (2011). "Molecular-Level Origins of Biomass Recalcitrance: Decrystallization Free Energies for Four Common Cellulose Polymorphs". In: *The Journal of Physical Chemistry B* 115.14, pp. 4118–4127. DOI: 10.1021/jp1106394. eprint: <http://pubs.acs.org/doi/pdf/10.1021/jp1106394>. URL: <http://pubs.acs.org/doi/abs/10.1021/jp1106394>.
- Bellesia, Giovanni et al. (2011). "Probing the Early Events Associated with Liquid Ammonia Pretreatment of Native Crystalline Cellulose". In: *The Journal of Physical Chemistry B* 115.32, pp. 9782–9788. DOI: 10.1021/jp2048844. eprint: <http://pubs.acs.org/doi/pdf/10.1021/jp2048844>. URL: <http://pubs.acs.org/doi/abs/10.1021/jp2048844>.
- Berendsen, H. J. C., J. R. Grigera, and T. P. Straatsma (1987). "The missing term in effective pair potentials". In: *The Journal of Physical Chemistry* 91.24, pp. 6269–6271. DOI: 10.1021/j100308a038. eprint: <http://pubs.acs.org/doi/pdf/10.1021/j100308a038>. URL: <http://pubs.acs.org/doi/abs/10.1021/j100308a038>.
- Berendsen, H. J. C. et al. (1984). "Molecular dynamics with coupling to an external bath". In: 81.8, pp. 3684–3690. ISSN: 00219606. DOI: DOI: 10.1063/1.448118. URL: <http://dx.doi.org/10.1063/1.448118>.
- Berendsen H. J. C.; Postma, J. P. M.; van Gunsteren W. F.; Hermans J. (1981). *Intermolecular forces*. Ed. by B Pullmann. Reidel: Dordrecht, p. 331.
- Berg, B.A. (2004). *Markov chain Monte Carlo simulations and their statistical analysis: with web-based Fortran code*. World Scientific. ISBN: 9789812389350. URL: <http://books.google.com/books?id=ZAX-wg0WjDoC>.
- Berne, B. J. and G. D. Harp (1970). Vol. 17. *Advances in Chemical Physics*. New York: Wiley.

- Beu, Titus A. and Udo Buck (2001). "Structure of ammonia clusters from $n = 3$ to 18". In: *J. Chem. Phys.* 114.18, pp. 7848–7852.
- Bhargava, B. L. and S. Balasubramanian (2007). "Refined potential model for atomistic simulations of ionic liquid [bmim][PF₆]" . In: *The Journal of Chemical Physics* 127.11, pp. 114510–6.
- Bhattacharjee, Biplob (2003). "nth-nearest-neighbor distribution functions of an interacting fluid from the pair correlation function: A hierarchical approach" . In: *Phys. Rev. E* 67.4. Copyright (C) 2010 The American Physical Society Please report any problems to prola@aps.org PRE, p. 041208.
- Binder, K. and D.W. Heermann (2010). *Monte Carlo Simulation in Statistical Physics: An Introduction*. Graduate Texts in Physics. Springer Verlag. ISBN: 9783642031625. URL: <http://books.google.com/books?id=y6oDME582TEC>.
- Boчек, A. M. (2003). "Effect of Hydrogen Bonding on Cellulose Solubility in Aqueous and Nonaqueous Solvents" . In: *Russian Journal of Applied Chemistry* 76 (11). 10.1023/B:RJAC.0000018669.88546.56, pp. 1711–1719. ISSN: 1070-4272. URL: <http://dx.doi.org/10.1023/B:RJAC.0000018669.88546.56>.
- Boese, A. Daniel et al. (2003). "From ab initio quantum chemistry to molecular dynamics: The delicate case of hydrogen bonding in ammonia" . In: *The Journal of Chemical Physics* 119.12, pp. 5965–5980. DOI: 10.1063/1.1599338. URL: <http://link.aip.org/link/?JCP/119/5965/1>.
- Bone, R. G. A. and N. C. Handy (1990). In: *Theor. Chim. Acta.* 78, p. 133.
- Bradley, M., T. W. Zerda, and J. Jonas (1985). "High pressure Raman study of vibrational relaxation of the Fermi coupled modes of ammonia" . In: 82.9, pp. 4007–4011. ISSN: 00219606. DOI: DOI: 10.1063/1.448840. URL: <http://dx.doi.org/10.1063/1.448840>.
- Brennecke, Joan F. and John E. Chateaufneuf (1999). "Homogeneous Organic Reactions as Mechanistic Probes in Supercritical Fluids" . In: *Chemical Reviews* 99.2, pp. 433–452. DOI: 10.1021/cr970035q. eprint: <http://pubs.acs.org/doi/pdf/10.1021/cr970035q>. URL: <http://pubs.acs.org/doi/abs/10.1021/cr970035q>.
- Brostow, Witold et al. (1998). "Voronoi polyhedra and Delaunay simplexes in the structural analysis of molecular-dynamics-simulated materials" . In: *Phys. Rev. B* 57.21. Copyright (C) 2010 The American Physical Society Please report any problems to prola@aps.org PRB, p. 13448.
- Buback, M. (1974). In: *Ber. Bunsenges. Phys. Chem.* 78.22. doi: 10.1021/j100563a0100022-3654 doi: 10.1021/j100563a010, p. 1230.
- Buback, M. and K. R. Schulz (1976). "Raman scattering of pure ammonia at high pressures and temperatures" . In: *J. Phys. Chem.* 80.22. doi: 10.1021/j100563a0100022-3654 doi: 10.1021/j100563a010, pp. 2478–2482.

- Cabaço, M. I et al. (2007). “Local Density Enhancement in Supercritical Carbon Dioxide Studied by Raman Spectroscopy”. In: *J. Phys. Chem. A*.
- Cabaco, M. Isabel et al. (2008). “Transient dimer formation in supercritical carbon dioxide as seen from Raman scattering”. In: *J. Chem. Phys.* 128.7, pp. 074507–10.
- Cadena, Cesar et al. (2004). “Why Is CO₂ So Soluble in Imidazolium-Based Ionic Liquids?” In: *Journal of the American Chemical Society* 126.16, pp. 5300–5308. DOI: 10.1021/ja039615x. eprint: <http://pubs.acs.org/doi/pdf/10.1021/ja039615x>. URL: <http://pubs.acs.org/doi/abs/10.1021/ja039615x>.
- Canongia Lopes, José N., Johnny Deschamps, and Agílio A. H. Pádua (2004). “Modeling Ionic Liquids Using a Systematic All-Atom Force Field”. In: *The Journal of Physical Chemistry B* 108.6, pp. 2038–2047. DOI: 10.1021/jp0362133. eprint: <http://pubs.acs.org/doi/pdf/10.1021/jp0362133>. URL: <http://pubs.acs.org/doi/abs/10.1021/jp0362133>.
- Catchpole, O.J. et al. (2005). “Measurement and modelling of urea solubility in supercritical CO₂ and CO₂+ethanol mixtures”. In: *Fluid Phase Equilibria* 237.1-2, pp. 212–218. ISSN: 0378-3812. DOI: DOI: 10.1016/j.fluid.2005.09.004. URL: <http://www.sciencedirect.com/science/article/pii/S0378381205003511>.
- Chaban, Vitaly V., Iuliia V. Voroshylova, and Oleg N. Kalugin (2011). “A new force field model for the simulation of transport properties of imidazolium-based ionic liquids”. In: *Phys. Chem. Chem. Phys.* 13 (17), pp. 7910–7920. DOI: 10.1039/C0CP02778B. URL: <http://dx.doi.org/10.1039/C0CP02778B>.
- Chandrasekhar, Indira et al. (2003). “A consistent potential energy parameter set for lipids: dipalmitoylphosphatidylcholine as a benchmark of the GROMOS96 45A3 force field”. In: *European Biophysics Journal* 32 (1). 10.1007/s00249-002-0269-4, pp. 67–77. ISSN: 0175-7571. URL: <http://dx.doi.org/10.1007/s00249-002-0269-4>.
- Chen, Bin, Jeffrey J. Potoff, and J. Ilja Siepmann (2001). “Monte Carlo Calculations for Alcohols and Their Mixtures with Alkanes. Transferable Potentials for Phase Equilibria. 5. United-Atom Description of Primary, Secondary, and Tertiary Alcohols”. In: *The Journal of Physical Chemistry B* 105.15, pp. 3093–3104. DOI: 10.1021/jp003882x. eprint: <http://pubs.acs.org/doi/pdf/10.1021/jp003882x>. URL: <http://pubs.acs.org/doi/abs/10.1021/jp003882x>.
- Chieux, P. and H. Bertagnolli (1984). “Deuterated liquid ammonia and lithium.ammonia-d₃ (7Li.4ND₃) solution. A neutron scattering investigation”. In: *The Journal of Physical Chemistry* 88.17, pp. 3726–3730. DOI: 10.1021/j150661a009. eprint: <http://pubs.acs.org/doi/pdf/10.1021/j150661a009>. URL: <http://pubs.acs.org/doi/abs/10.1021/j150661a009>.

- Chipot, C. and A. Pohorille (2007). *Free energy calculations: theory and applications in chemistry and biology*. Springer series in chemical physics. Springer. ISBN: 9783540384472. URL: <http://books.google.com/books?id=XTE5eejRTCOC>.
- Chiu, Hung-Yu, Ming-Jer Lee, and Ho-mu Lin (2008). "Vapor-Liquid Phase Boundaries of Binary Mixtures of Carbon Dioxide with Ethanol and Acetone". In: *Journal of Chemical & Engineering Data* 53.10, pp. 2393–2402. DOI: 10.1021/jc800371a. eprint: <http://pubs.acs.org/doi/pdf/10.1021/jc800371a>. URL: <http://pubs.acs.org/doi/abs/10.1021/jc800371a>.
- CORPORATION, HYOSUNG (2003). "Preparation method of homogeneous cellulose solution using supercritical fluid". Korean. Pat. 035633.
- D, Ben-Amotz. et al. (1992). In: *Proceedings of the supercritical Fluids Technology*. Ed. by V Bright. F and M. E. McNanly. Vol. No. 488. Washington, DC, p. 18.
- Darde, Victor et al. (2009). "Chilled ammonia process for CO₂ capture". In: *Energy Procedia* 1.1, pp. 1035–1042. ISSN: 1876-6102. DOI: 10.1016/j.egypro.2009.01.137. URL: <http://www.sciencedirect.com/science/article/pii/S1876610209001386>.
- Darr, Jawwad A. and Martyn Poliakoff (1999). "New Directions in Inorganic and Metal-Organic Coordination Chemistry in Supercritical Fluids". In: *Chem. Rev.* 99.2. doi: 10.1021/cr970036i0009-2665 doi: 10.1021/cr970036i, pp. 495–542.
- Darvas, M., P. Jedlovszky, and G. Jancsó (2009). "Free Energy of Mixing of Pyridine and Its Methyl-Substituted Derivatives with Water, As Seen from Computer Simulations". In: *The Journal of Physical Chemistry B* 113.21. PMID: 19413281, pp. 7615–7620. DOI: 10.1021/jp901649r. eprint: <http://pubs.acs.org/doi/pdf/10.1021/jp901649r>. URL: <http://pubs.acs.org/doi/abs/10.1021/jp901649r>.
- Day, Chany-Yih, Chiehming J. Chang, and Chiu-Yang Chen (1996). "Phase Equilibrium of Ethanol + CO₂ and Acetone + CO₂ at Elevated Pressures". In: *Journal of Chemical & Engineering Data* 41.4, pp. 839–843.
- Desmoulins-Krawiec, Sophie et al. (2004). "Synthesis of nanostructured materials in supercritical ammonia: nitrides, metals and oxides". In: *J. Mater. Chem.* 14.2. 10.1039/b310806f, pp. 228–232.
- Diraison, M., G. J. Martyna, and M. E. Tuckerman (1999). "Simulation studies of liquid ammonia by classical ab initio, classical, and path-integral molecular dynamics". In: *J. Chem. Phys.* 111.3, pp. 1096–1103.
- Dong, K. J. and et al. (2009). "Critical states and phase diagram in the packing of uniform spheres". In: *EPL (Europhysics Letters)* 86.4, p. 46003.
- Drozdo, A. N. and S. C. Tucker (2001). In: *J. Chem. Phys.* 114, p. 4912.
- Duschek, W., R. Kleinrahm, and W. Wagner (1990). In: *J. Chem. Thermodyn* 22, p. 841.
- Dyshin A.A. Kiselev M.G., Idrissi A. (2007). "The study of solubility of cellulose in a mixture of co-solvent and supercritical carbon dioxide". In: *Proceedings of the conference on "Supercritical fluids technologies" Rostov on Don, Russia*.

- Etzler, F. M., R. F. Ross, and R. A. Halcomb (1991). “The structure and properties of vicinal waer : Lessons from statistical geometry”. In: *Physica A* 172.
- Ferrando, Nicolas, Véronique Lachet, and Anne Boutin (2010). “Monte Carlo Simulations of Mixtures Involving Ketones and Aldehydes by a Direct Bubble Pressure Calculation”. In: *The Journal of Physical Chemistry B* 114.26. PMID: 20540589, pp. 8680–8688. DOI: 10.1021/jp1031724. eprint: <http://pubs.acs.org/doi/pdf/10.1021/jp1031724>. URL: <http://pubs.acs.org/doi/abs/10.1021/jp1031724>.
- Ferrando, Nicolas et al. (2009). “Transferable Force Field for Alcohols and Polyalcohols”. In: *The Journal of Physical Chemistry B* 113.17. doi: 10.1021/jp810915z 1520-6106 doi: 10.1021/jp810915z, pp. 5985–5995.
- Ferrario, Mauro et al. (1990). “Molecular-dynamics simulation of aqueous mixtures: Methanol, acetone, and ammonia”. In: *The Journal of Chemical Physics* 93.7, pp. 5156–5166. DOI: 10.1063/1.458652. URL: <http://link.aip.org/link/?JCP/93/5156/1>.
- Finney, J. L. (1970). “Random Packings and the Structure of Simple Liquids. I. The Geometry of Random Close Packing”. In: *Proc. R. Soc. Lond.* 319, p. 479.
- Finney, J. L (1977). “Modelling the structures of amorphous metals and alloys”. In: *Nature* 266, p. 309.
- Frenkel, D. and B. Smit (2002). *Understanding molecular simulation: from algorithms to applications*. Computational science. Academic Press. ISBN: 9780122673511. URL: <http://books.google.com/books?id=5qTzldS9R0IC>.
- Frenkel, D. and B. Smith (2001). *Understanding Molecular simulation*. Orlando: Academic Press, Inc.
- Gao, Jiali, Xinfu Xia, and Thomas F. George (1993). “Importance of bimolecular interactions in developing empirical potential functions for liquid ammonia”. In: *The Journal of Physical Chemistry* 97.36, pp. 9241–9247. DOI: 10.1021/j100138a028. eprint: <http://pubs.acs.org/doi/pdf/10.1021/j100138a028>. URL: <http://pubs.acs.org/doi/abs/10.1021/j100138a028>.
- Giura, P. et al. (2007). “High frequency dynamics and structural relaxation process in liquid ammonia”. In: *J. Chem. Phys.* 127.8, pp. 084508–9.
- Goodyear, Grant, Michael W. Maddox, and Susan C. Tucker (July 2000a). “Domain-Based Characterization of Density Inhomogeneities in Compressible Supercritical Fluids”. In: *The Journal of Physical Chemistry B* 104.26, pp. 6240–6247. ISSN: 1520-6106. URL: <http://dx.doi.org/10.1021/jp000378j>.
- (2000b). “The correlation between local and long-range structure in compressible supercritical fluids”. In: *The Journal of Chemical Physics* 112.23, pp. 10327–10339. DOI: 10.1063/1.481670. URL: <http://link.aip.org/link/?JCP/112/10327/1>.

- Grob, T. et al. (1997). "The p,T-Dependence of Self-Diffusion in Fluid Ammonia". In: *J. Mol. Liq.* 73,74, pp. 433–444.
- Guvench, Olgun et al. (2008). "Additive empirical force field for hexopyranose monosaccharides". In: *Journal of Computational Chemistry* 29.15, pp. 2543–2564. ISSN: 1096-987X. DOI: 10.1002/jcc.21004. URL: <http://dx.doi.org/10.1002/jcc.21004>.
- Guvench, Olgun et al. (2009). "CHARMM Additive All-Atom Force Field for Glycosidic Linkages between Hexopyranoses". In: *Journal of Chemical Theory and Computation* 5.9, pp. 2353–2370. DOI: 10.1021/ct900242e. eprint: <http://pubs.acs.org/doi/pdf/10.1021/ct900242e>. URL: <http://pubs.acs.org/doi/abs/10.1021/ct900242e>.
- Hannongbua, Supot (2000). "The best structural data of liquid ammonia based on the pair approximation: First-principles Monte Carlo simulation". In: *The Journal of Chemical Physics* 113.11, pp. 4707–4712. DOI: 10.1063/1.1289145. URL: <http://link.aip.org/link/?JCP/113/4707/1>.
- Harris, J. G. and K. H. Yung (1995). In: *J. Phys. Chem.* 99, p. 12021.
- Hatcher, Elizabeth et al. (2011). "Conformational Properties of Methyl β -Maltoside and Methyl α and β -Cellobioside Disaccharides". In: *The Journal of Physical Chemistry B* 115.3, pp. 597–608. DOI: 10.1021/jp109475p. eprint: <http://pubs.acs.org/doi/pdf/10.1021/jp109475p>. URL: <http://pubs.acs.org/doi/abs/10.1021/jp109475p>.
- Heinze, Thomas et al. (2000). "Effective preparation of cellulose derivatives in a new simple cellulose solvent". In: *Macromolecular Chemistry and Physics* 201.6, pp. 627–631. ISSN: 1521-3935. DOI: 10.1002/(SICI)1521-3935(20000301)201:6<627::AID-MACP627>3.0.CO;2-Y. URL: [http://dx.doi.org/10.1002/\(SICI\)1521-3935\(20000301\)201:6<627::AID-MACP627>3.0.CO;2-Y](http://dx.doi.org/10.1002/(SICI)1521-3935(20000301)201:6<627::AID-MACP627>3.0.CO;2-Y).
- Hess, K. and C. Trogus (1935). "Über Ammoniak-Cellulose". In: *Ber Dtsch Chem Ges* 70, p. 1788.
- Hoare, M. R. (1978). "Packing models and structural specificity". In: *J. Non-Cryst. Solids* 31.
- Hodel, Alec et al. (1993). "Conformational substates and uncertainty in macromolecular free energy calculations". In: *The Journal of Physical Chemistry* 97.13, pp. 3409–3417. DOI: 10.1021/j100115a054. eprint: <http://pubs.acs.org/doi/pdf/10.1021/j100115a054>. URL: <http://pubs.acs.org/doi/abs/10.1021/j100115a054>.
- Houndonougbo, Y. et al. (2007). "Prediction of phase equilibria and transport properties in carbon-dioxide expanded solvents by molecular simulation". In: *Molecular Simulation* 33.9-10, pp. 861–869. DOI: 10.1080/08927020701310923. eprint: <http://www.tandfonline.com/doi/pdf/10.1080/08927020701310923>. URL: <http://www.tandfonline.com/doi/abs/10.1080/08927020701310923>.

<http://towhee.sourceforge.net>.

- Idrissi, A., P. Damay, and M. Kiselev (2007). "Nearest neighbor assessments of spatial distribution in CO₂: A molecular dynamics analysis". In: *Chemical Physics* 332.1, pp. 139–143. ISSN: 0301-0104. DOI: DOI : 10 . 1016 / j . chemphys . 2006 . 11 . 037. URL: <http://www.sciencedirect.com/science/article/B6TFM-4MHX7H1-4/2/1e25b3e2f044a0673db33e3c75cb404d>.
- Idrissi, A. et al. (2005). "Low-frequency Raman spectra of sub- and supercritical CO₂: Qualitative analysis of the diffusion coefficient behavior". In: *J. Chem. Phys.* 123.9, pp. 094501–6.
- Idrissi, A. et al. (2006). "Analysis of the transverse and the longitudinal pseudodiffusion of CO₂ in sub- and supercritical states: A molecular-dynamics analysis". In: *J. Chem. Phys.* 125.22, pp. 224501–9.
- Idrissi, A. et al. (Dec. 2009a). "Assessment of the Spatial Distribution in Sub- and Supercritical CO₂ Using the Nearest Neighbor Approach: A Molecular Dynamics Analysis". In: *The Journal of Physical Chemistry B* 113.48, pp. 15820–15830. ISSN: 1520-6106. URL: <http://dx.doi.org/10.1021/jp9042107>.
- Idrissi, A. et al. (2009b). "Local structure in sub and supercritical ammonia: a molecular dynamics analysis". In: *EMLG/JMLG Annual Meeting: Intermolecular Interactions and Liquid Structure*.
- Idrissi, A. et al. (2010). "Local structure in sub- and supercritical CO₂: A Voronoi polyhedra analysis study". In: *J. Mol. Liq.* 153.1, pp. 20–24.
- Idrissi, A. et al. (2011a). "Assessment of the potential models of acetone/CO₂ and ethanol mixtures by computer simulation and thermodynamic integration." In: *"Supercritical fluids (SCF): fundamentals, technologies, innovations", 4–7 July, Listvyanka, lake Baykal*.
- Idrissi, A. et al. (2011b). "Heterogeneity of the Local Structure in Sub- and Supercritical Ammonia: A Voronoi Polyhedra Analysis". In: *The Journal of Physical Chemistry B* 115.31, pp. 9646–9652. DOI: 10 . 1021 / jp204078u. eprint: <http://pubs.acs.org/doi/pdf/10.1021/jp204078u>. URL: <http://pubs.acs.org/doi/abs/10.1021/jp204078u>.
- Idrissi, Abdenacer et al. (2008). "Self-association of urea in aqueous solutions: A Voronoi polyhedron analysis study". In: *The Journal of Chemical Physics* 129.16, pp. 164512–9.
- Idrissi, Abdenacer et al. (2011c). "Assessment of the potential models of acetone/CO₂ and ethanol/CO₂ mixtures by computer simulation and thermodynamic integration in liquid and supercritical states". In: *Phys. Chem. Chem. Phys.* 13 (36), pp. 16272–16281. DOI: 10 . 1039 / C1CP21042D. URL: <http://dx.doi.org/10.1039/C1CP21042D>.
- Igarashi, Kiyohiko, Masahisa Wada, and Masahiro Samejima (2007). "Activation of crystalline cellulose to cellulose III_I results in efficient hydrolysis by cellobiohy-

- drolase". In: *FEBS Journal* 274.7, pp. 1785–1792. ISSN: 1742-4658. DOI: 10.1111/j.1742-4658.2007.05727.x. URL: <http://dx.doi.org/10.1111/j.1742-4658.2007.05727.x>.
- Impey, Roger W. and Michael L. Klein (1984). "A simple intermolecular potential for liquid ammonia". In: *Chemical Physics Letters* 104.6, pp. 579–582. ISSN: 0009-2614. DOI: 10.1016/0009-2614(84)80031-7. URL: <http://www.sciencedirect.com/science/article/B6TFN-44GGRC-DJ3/2/0cc64b069564f272783916b7c44ffffee>.
- Ishii, R et al. (1995a). "A neutron scattering study of the structure of supercritical Carbon dioxide". In: *Chem. phys. Lett* 240, p. 84.
- Ishii, R et al. (1995b). "Structural Study of supercritical Carbon dioxide by neutron diffraction". In: *Fluid Phase Equilibria* 104, p. 291.
- Ishii, R et al. (1996). "Density dependence of structure of supercritical carbon dioxide along an isotherm". In: *J. Chem. Phys.* 105, p. 7011.
- Ishikawa, Yoichi and Shiro Saka (2001). "Chemical conversion of cellulose as treated in supercritical methanol". In: *Cellulose* 8 (3). 10.1023/A:1013170020469, pp. 189–195. ISSN: 0969-0239. URL: <http://dx.doi.org/10.1023/A:1013170020469>.
- Ivanov, D.Y. (2008). *Critical behavior of non-ideal systems*. Wiley-VCH. ISBN: 9783527406586. URL: <http://books.google.com/books?id=hxAmm9ruQ38C>.
- Janeiro-Barral, P. E. and M. Mella (2006). "Study of the Structure, Energetics, and Vibrational Properties of Small Ammonia Clusters (NH₃)_n (n = 2-5) Using Correlated ab Initio Methods". In: *J. Phys. Chem. A* 110.39, pp. 11244–11251.
- Jedlovsky, P. and M. Mezei (1999). In: *J. Chem. Phys.* 111.null, p. 10770.
- (2000). In: *J. Am. Chem. Soc.* 122.null, p. 5125.
- Jedlovsky, Pál, Abdenacer Idrissi, and Gábor Jancsó (2009). "Can existing models qualitatively describe the mixing behavior of acetone with water?" In: *The Journal of Chemical Physics* 130.12, 124516, p. 124516. DOI: 10.1063/1.3086859. URL: <http://link.aip.org/link/?JCP/130/124516/1>.
- Jedlovsky, Pál et al. (2008a). "Structural and thermodynamic properties of different phases of supercooled liquid water". In: *J. Chem. Phys.* 128.24, pp. 244503–12.
- Jedlovsky, Pál et al. (2008b). "Structural and thermodynamic properties of different phases of supercooled liquid water". In: 128.24, p. 244503. ISSN: 00219606. DOI: 10.1063/1.2939119. URL: <http://dx.doi.org/doi/10.1063/1.2939119>.
- Jeffrey, G. A. (1997). *An introduction to hydrogen Bonding*. New York: Oxford University.
- Jorgensen, William L. (1986). "Optimized intermolecular potential functions for liquid alcohols". In: *The Journal of Physical Chemistry* 90.7, pp. 1276–1284. DOI: 10.

- 1021/j100398a015. eprint: <http://pubs.acs.org/doi/pdf/10.1021/j100398a015>. URL: <http://pubs.acs.org/doi/abs/10.1021/j100398a015>.
- Jorgensen, William L., James M. Briggs, and M. Leonor. Contreras (1990). "Relative partition coefficients for organic solutes from fluid simulations". In: *The Journal of Physical Chemistry* 94.4, pp. 1683–1686. DOI: 10.1021/j100367a084. eprint: <http://pubs.acs.org/doi/pdf/10.1021/j100367a084>. URL: <http://pubs.acs.org/doi/abs/10.1021/j100367a084>.
- Jorgensen, William L., Jeffrey D. Madura, and Carol J. Swenson (1984). "Optimized intermolecular potential functions for liquid hydrocarbons". In: *Journal of the American Chemical Society* 106.22, pp. 6638–6646. DOI: 10.1021/ja00334a030. eprint: <http://pubs.acs.org/doi/pdf/10.1021/ja00334a030>. URL: <http://pubs.acs.org/doi/abs/10.1021/ja00334a030>.
- Jullien, R. and et al. (1996). In: *Phys. Rev. E* 54.6, p. 6035.
- Karch, Rudolf et al. (2003). "Voronoi Polyhedra Analysis of Optimized Arterial Tree Models". In: *Annals of Biomedical Engineering* 31.5, pp. 548–563.
- Kast, Kristine M. et al. (2003). "Binary Phases of Aliphatic N-Oxides and Water: A Force Field Development and Molecular Dynamics Simulation". In: *The Journal of Physical Chemistry A* 107.27, pp. 5342–5351. DOI: 10.1021/jp027336a. eprint: <http://pubs.acs.org/doi/pdf/10.1021/jp027336a>. URL: <http://pubs.acs.org/doi/abs/10.1021/jp027336a>.
- Keyes, T. (1999). "Neighborhood structure and dynamics in supercooled liquids". In: *J. Chem. Phys.* 110.2, pp. 1097–1105.
- Khimenko M. T., Aleksandrov V.V. and Gritsenko N.N. (1973). In: *Zh. Fiz. Khim.* 47, p. 2914.
- Kiran, Erdogan and Holger Pöhler (1998). "Alternative solvents for cellulose derivatives: Miscibility and density of cellulosic polymers in carbon dioxide+acetone and carbon dioxide+ethanol binary fluid mixtures". In: *The Journal of Supercritical Fluids* 13.1-3, pp. 135–141. ISSN: 0896-8446. DOI: DOI: 10.1016/S0896-8446(98)00090-4. URL: <http://www.sciencedirect.com/science/article/pii/S0896844698000904>.
- Kirschner, Karl N. et al. (2008). "GLYCAM06: A generalizable biomolecular force field. Carbohydrates". In: *Journal of Computational Chemistry* 29.4, pp. 622–655. ISSN: 1096-987X. DOI: 10.1002/jcc.20820. URL: <http://dx.doi.org/10.1002/jcc.20820>.
- Kiselev, M. et al. (2000). "The structure of supercritical ammonia as studied by molecular dynamics simulations". In: *Chemical Physics Letters* 327.5-6, pp. 425–428. ISSN: 0009-2614. DOI: DOI: 10.1016/S0009-2614(00)00836-8. URL: <http://www.sciencedirect.com/science/article/B6TFN-414WS22-V/2/52fd7b0d2bcb0602127dc09065d4f671>.

- Klemm, D. (1998). *Comprehensive Cellulose Chemistry: Functionalization of cellulose*. Comprehensive Cellulose Chemistry. Wiley-VCH. ISBN: 9783527294893. URL: <http://books.google.com/books?id=UjRRAAAAMAAJ>.
- Klemm, D. and T. Heinze (1998). *Comprehensive Cellulose Chemistry: Fundamentals and analytical methods*. Comprehensive Cellulose Chemistry. Wiley-VCH. ISBN: 9783527294138. URL: <http://books.google.com/books?id=1TNRAAAAMAAJ>.
- Kristof, T. et al. (1999). "A simple effective pair potential for the molecular simulation of the thermodynamic properties of ammonia". In: *Molecular Physics* 97.10, pp. 1129–1137. URL: <http://www.informaworld.com/10.1080/002689799163073>.
- Lavrik, N. L. and V. P. Voloshin (2001). "Calculation of mean distances between the randomly distributed particles in the model of points and hard spheres (the method of Voronoi polyhedra)". In: *J. Chem. Phys.* 114.21, pp. 9489–9491.
- Leach, Andrew R. (2001). *Molecular modelling: principles and applications*. Pearson Education. Prentice Hall. ISBN: 9780582382107. URL: <http://books.google.com/books?id=kB7jsbV-uhkC>.
- Lee, Jae Shin and Sun Yong Park (2000). "Ab initio study of (NH₃)₂: Accurate structure and energetics". In: *J. Chem. Phys.* 112.1, pp. 230–237.
- Lemmon, W., M. O. McLinden, and D. G. Friend (2005). *Thermophysical Properties of Fluid Systems*. WebBook de Chimie NIST, Base de Données Standard de Référence NIST Numéro 69. Gaithersburg MD, 20899: National Institute of Standards and Technology, (<http://webbook.nist.gov>).
- Lieth, Claus-Wilhelm von der, Tibor Kozár, and William E. Hull (1997). "A (critical) survey of modelling protocols used to explore the conformational space of oligosaccharides". In: *Journal of Molecular Structure: THEOCHEM* 395-396.0. <ce:title>Carbohydrate Modeling</ce:title>, pp. 225–244. ISSN: 0166-1280. DOI: 10.1016/S0166-1280(96)04953-6. URL: <http://www.sciencedirect.com/science/article/pii/S0166128096049536>.
- Lins, Roberto D. and Philippe H. Hnenberger (2005). "A new GROMOS force field for hexopyranose-based carbohydrates". In: *Journal of Computational Chemistry* 26.13, pp. 1400–1412. ISSN: 1096-987X. DOI: 10.1002/jcc.20275. URL: <http://dx.doi.org/10.1002/jcc.20275>.
- Liu, Hanbin et al. (2010). "Understanding the Interactions of Cellulose with Ionic Liquids: A Molecular Dynamics Study". In: *The Journal of Physical Chemistry B* 114.12. PMID: 20218725, pp. 4293–4301. DOI: 10.1021/jp9117437. eprint: <http://pubs.acs.org/doi/pdf/10.1021/jp9117437>. URL: <http://pubs.acs.org/doi/abs/10.1021/jp9117437>.
- Liu, Kun and Erdogan Kiran (2007). "Viscosity, Density and Excess Volume of Acetone + Carbon Dioxide Mixtures at High Pressures". In: *Industrial & Engineering Chemistry Research* 46.16, pp. 5453–5462. DOI: 10.1021/ie070274w. eprint: <http://pubs.acs.org/doi/abs/10.1021/ie070274w>.

- //pubs.acs.org/doi/pdf/10.1021/ie070274w. URL: <http://pubs.acs.org/doi/abs/10.1021/ie070274w>.
- Liu, Shi-Yi et al. (1986). "Electrical properties of ammonia and the structure of the ammonia dimer". In: *The Journal of Chemical Physics* 85.4, pp. 2077–2083. DOI: 10.1063/1.451151. URL: <http://link.aip.org/link/?JCP/85/2077/1>.
- Liu, Zhiping, Shiping Huang, and Wenchuan Wang (2004). "A Refined Force Field for Molecular Simulation of Imidazolium-Based Ionic Liquids". In: *The Journal of Physical Chemistry B* 108.34, pp. 12978–12989. DOI: 10.1021/jp048369o. eprint: <http://pubs.acs.org/doi/pdf/10.1021/jp048369o>. URL: <http://pubs.acs.org/doi/abs/10.1021/jp048369o>.
- Liu, Zhiping, Xiaoping Wu, and Wenchuan Wang (2006). "A novel united-atom force field for imidazolium-based ionic liquids". In: *Phys. Chem. Chem. Phys.* 8 (9), pp. 1096–1104. DOI: 10.1039/B515905A. URL: <http://dx.doi.org/10.1039/B515905A>.
- Longelin, S. (2003). "thesis". PhD thesis.
- Luchnikov, V. A. et al. (1996). "Medium-range structure of amorphous silicon studied by the Voronoi-Delaunay method". In: *Mol. Phys.* 88, p. 1337.
- M., BARISKA and SCHUERCH C. "Wood Softening and Forming with Ammonia". In: *Wood Technology: Chemical Aspects*. Chap. 22, pp. 326–347. DOI: 10.1021/bk-1977-0043.ch021. eprint: <http://pubs.acs.org/doi/pdf/10.1021/bk-1977-0043.ch021>. URL: <http://pubs.acs.org/doi/abs/10.1021/bk-1977-0043.ch021>.
- Marhoefer, Richard J. et al. (2000). "Molecular dynamics simulations of tertiary systems of cellohexaose/aliphatic N-oxide/water". In: *Macromolecular Chemistry and Physics* 201.15, pp. 2003–2007. ISSN: 1521-3935. DOI: 10.1002/1521-3935(20001001)201:15<2003::AID-MACP2003>3.0.CO;2-A. URL: [http://dx.doi.org/10.1002/1521-3935\(20001001\)201:15<2003::AID-MACP2003>3.0.CO;2-A](http://dx.doi.org/10.1002/1521-3935(20001001)201:15<2003::AID-MACP2003>3.0.CO;2-A).
- Martin, A. et al. (2007). "Neues umweltfreundliches Herstellungsverfahren für primäre Amine durch Hydroaminomethylierung von Olefinen in Überkritischem Ammoniak". In: *Chemie Ingenieur Technik* 79.6. 10.1002/cite.200700035, pp. 891–900.
- Martinez, Hernan L., R. Ravi, and Susan C. Tucker (1996). "Characterization of solvent clusters in a supercritical Lennard-Jones fluid". In: *The Journal of Chemical Physics* 104.3, pp. 1067–1080. DOI: 10.1063/1.470762. URL: <http://link.aip.org/link/?JCP/104/1067/1>.
- Martínez, JoséMario and Leandro Martínez (2003). "Packing optimization for automated generation of complex system's initial configurations for molecular dynamics and docking". In: *Journal of Computational Chemistry* 24.7, pp. 819–825. ISSN: 1096-987X. DOI: 10.1002/jcc.10216. URL: <http://dx.doi.org/10.1002/jcc.10216>.
- Martínez, L. et al. (2009). "PACKMOL: A package for building initial configurations for molecular dynamics simulations". In: *Journal of Computational Chemistry* 30.13,

- pp. 2157–2164. ISSN: 1096-987X. DOI: 10.1002/jcc.21224. URL: <http://dx.doi.org/10.1002/jcc.21224>.
- Maruyama, Kenji et al. (2009). “Void structure and intermediate-range fluctuations in the metal-nonmetal transition range in expanded liquid Hg”. In: *Phys. Rev. B* 80.1. Copyright (C) 2010 The American Physical Society Please report any problems to prola@aps.org PRB, p. 014201.
- Matubayasi, Nobuyuki, Naoko Nakao, and Masaru Nakahara (2001). “Structural study of supercritical water. III. Rotational dynamics”. In: *J. Chem. Phys.* 114.9, pp. 4107–4115.
- Mazur, Stephen (1992). “Neighborhood partition of the radial distribution function for simple liquids”. In: *The Journal of Chemical Physics* 97.12, pp. 9276–9282. DOI: 10.1063/1.463302. URL: <http://link.aip.org/link/?JCP/97/9276/1>.
- Medvedev, N. N., A. Geiger, and W. Brostow (1990). In: *J. Chem. Phys.* 93.null, p. 8337.
- Merker, Thorsten, Jadran Vrabec, and Hans Hasse (2008). “Comment on “An optimized potential for carbon dioxide? [*J. Chem. Phys.* 122, 214507 (2005)]””. In: 129.8, p. 087101. ISSN: 00219606. DOI: DOI : 10.1063/1.2965899. URL: <http://dx.doi.org/doi/10.1063/1.2965899>.
- Mezei, M. *MMC: Monte Carlo program for simulation of molecular assemblies*. URL: <http://inka.mssm.edu/~mezei/mmc/mmc.html>.
- Mezei, M. and D.L. Beveridge (1986). “Free Energy Simulations”. In: *Ann. Acad. Sci N.Y.* 486, pp. 1–23.
- Mezei, Mihaly (1989). “Direct Calculation of the Excess Free Energy of the Dense Lennard-Jones Fluid”. In: *Molecular Simulation* 2.3, pp. 201–207. DOI: 10.1080/08927028908031368. eprint: <http://www.tandfonline.com/doi/pdf/10.1080/08927028908031368>. URL: <http://www.tandfonline.com/doi/abs/10.1080/08927028908031368>.
- Mezei, Mihaly, S. Swaminathan, and David L. Beveridge (1978). “Ab initio calculation of the free energy of liquid water”. In: *Journal of the American Chemical Society* 100.10, pp. 3255–3256. DOI: 10.1021/ja00478a070. eprint: <http://pubs.acs.org/doi/pdf/10.1021/ja00478a070>. URL: <http://pubs.acs.org/doi/abs/10.1021/ja00478a070>.
- Mináry, P. et al. (2000). “A Comprehensive Liquid Simulation Study of Neat Formic Acid”. In: *The Journal of Physical Chemistry B* 104.34, pp. 8287–8294. DOI: 10.1021/jp000205u. eprint: <http://pubs.acs.org/doi/pdf/10.1021/jp000205u>. URL: <http://pubs.acs.org/doi/abs/10.1021/jp000205u>.
- Montoro, J., C. Gil, and J. L. F. Abascal (1993). “The Voronoi polyhedra as tools for structure determination in simple disordered systems”. In: *J. Phys. Chem.* 97.16. doi: 10.1021/j100118a044, pp. 4211–4215.
- Montoro, J. et al. (1994). “Ionic association in electrolyte solutions: A Voronoi polyhedra analysis”. In: *J. Chem. Phys.* 101.12, pp. 10892–10898.

- Mountain, Raymond D. (1999). "Voids and clusters in expanded water". In: *The Journal of Chemical Physics* 110.4, pp. 2109–2115. DOI: 10.1063/1.477853. URL: <http://link.aip.org/link/?JCP/110/2109/1>.
- Murthy, C. S., K. Singer, and I. R. McDonald (1981). In: *Mol. Phys.* 44, p. 135.
- Musso, Maurizio et al. (2002). "Isotropic Raman line shapes near gas–liquid critical points: The shift, width, and asymmetry of coupled and uncoupled states of fluid nitrogen". In: *J. Chem. Phys.* 116.18, pp. 8015–8027.
- (2004). "Critical Raman line behavior of fluid nitrogen". In: *Pure Appl. Chem.* 76, pp. 147–155.
- N., Medvedev N. (2000). *The Voronoi–Delaunay method in the structural investigation of non-crystalline systems*. SB RAS.
- Nakayama, H et al. (2000). "Raman spectral changes of neat CO₂ across the ridge of density fluctuation in supercritical region". In: *Chem. phys. Lett.* 320, p. 323.
- Narten, A. H. (1977). "Liquid ammonia: Molecular correlation functions from x-ray diffraction". In: *J. Chem. Phys.* 66.7, pp. 3117–3120.
- Nelson, D. D., G. T. Fraser, and W. Klemperer (1987). "Does ammonia Hydrogen Bond?" In: *Science* 238, p. 1670.
- Nelson, Jr D. D., G. T. Fraser, and W. Klemperer (1985). "Ammonia dimer: A surprising structure". In: *J. Chem. Phys.* 83.12, pp. 6201–6208.
- Neumann, Martin (1985). "The dielectric constant of water. Computer simulations with the MCY potential". In: *The Journal of Chemical Physics* 82.12, pp. 5663–5672. DOI: 10.1063/1.448553. URL: <http://link.aip.org/link/?JCP/82/5663/1>.
- Newman, M.E.J. and G.T. Barkema (1999). *Monte Carlo methods in statistical physics*. Clarendon Press. ISBN: 9780198517979. URL: <http://books.google.com/books?id=J5aLdDN4uFwC>.
- Nishikawa, Keiko and Ibuki Tanaka (1995). "Correlation lengths and density fluctuations in supercritical states of carbon dioxide". In: *Chemical Physics Letters* 244.1-2. 0009-2614 doi: DOI: 10.1016/0009-2614(95)00818-O, pp. 149–152.
- NIST (1962). *CRC Handbook of Chemistry and Physics*. 44th. Washington D.C.
- Noda, I. (1990). "Two dimensional infrared(2D-IR) spectroscopy: Theory and Applications". In: *Appl. Spectrosc.* 44, pp. 550–561.
- Odutola, J. A. et al. (1979). "Molecular beam electric deflection study of ammonia polymers". In: *J. Chem. Phys.* 70.11, pp. 4884–4886.
- Oger, L. et al. (1996). "Voronoi tessellation of packings of spheres: Topological correlation and statistics". In: *Phil. Mag. B* 74.2, pp. 177–197.
- Ogihara, Yuko et al. (2005). "Direct observation of cellulose dissolution in subcritical and supercritical water over a wide range of water densities". In: *Cellulose* 12 (6). 10.1007/s10570-005-9008-1, pp. 595–606. ISSN: 0969-0239. URL: <http://dx.doi.org/10.1007/s10570-005-9008-1>.

- Okabe, A. (2000). *Spatial tessellations: concepts and applications of Voronoi diagrams*. Wiley series in probability and statistics: Applied probability and statistics. Wiley. ISBN: 9780471986355. URL: <http://books.google.com/books?id=dT7YH3mjeeIC>.
- Olthof, E. H. T., A. van der Avoird, and P. E. S. Wormer (1994). "Structure, internal mobility, and spectrum of the ammonia dimer: Calculation of the vibration-rotation-tunneling states". In: *J. Chem. Phys.* 101.10, pp. 8430-8442.
- O'Reilly, D. E., E. M. Peterson, and C. E. Scheie (1973). "Self-diffusion in liquid ammonia and deuterioammonia". In: *J. Chem. Phys.* 58.10, pp. 4072-4075.
- Panagiotopoulos, Athanassios Z. (1987). "Direct determination of phase coexistence properties of fluids by Monte Carlo simulation in a new ensemble". In: *Molecular Physics* 61.4, pp. 813-826. URL: <http://www.informaworld.com/10.1080/00268978700101491>.
- Pentoney, R. E. (1966). "Liquid Ammonia-Solvent Combinations in Wood Plasticization. Properties of Treated Wood". In: *I&EC Product Research and Development* 5.2, pp. 105-110. DOI: 10.1021/i360018a003. eprint: <http://pubs.acs.org/doi/pdf/10.1021/i360018a003>. URL: <http://pubs.acs.org/doi/abs/10.1021/i360018a003>.
- Perić-Hassler, Lovorka et al. (2010). "Conformational properties of glucose-based disaccharides investigated using molecular dynamics simulations with local elevation umbrella sampling". In: *Carbohydrate Research* 345.12, pp. 1781-1801. ISSN: 0008-6215. DOI: 10.1016/j.carres.2010.05.026. URL: <http://www.sciencedirect.com/science/article/pii/S0008621510002260>.
- Phillips, James C. et al. (2005). "Scalable molecular dynamics with NAMD". In: *Journal of Computational Chemistry* 26.16, pp. 1781-1802. ISSN: 1096-987X. DOI: 10.1002/jcc.20289. URL: <http://dx.doi.org/10.1002/jcc.20289>.
- Pinkert, André et al. (2009). "Ionic Liquids and Their Interaction with Cellulose". In: *Chemical Reviews* 109.12. PMID: 19757807, pp. 6712-6728. DOI: 10.1021/cr9001947. eprint: <http://pubs.acs.org/doi/pdf/10.1021/cr9001947>. URL: <http://pubs.acs.org/doi/abs/10.1021/cr9001947>.
- Pöhler, Holger and Erdogan Kiran (1997a). "Volumetric Properties of Carbon Dioxide + Acetone at High Pressures". In: *Journal of Chemical & Engineering Data* 42.2, pp. 379-383. DOI: 10.1021/je9602881. eprint: <http://pubs.acs.org/doi/pdf/10.1021/je9602881>. URL: <http://pubs.acs.org/doi/abs/10.1021/je9602881>.
- (1997b). "Volumetric Properties of Carbon Dioxide + Ethanol at High Pressures". In: *Journal of Chemical & Engineering Data* 42.2, pp. 384-388. DOI: 10.1021/je9602982. eprint: <http://pubs.acs.org/doi/pdf/10.1021/je9602982>. URL: <http://pubs.acs.org/doi/abs/10.1021/je9602982>.

- Potoff, Jeffrey J. and J. Ilja Siepmann (2001). "Vapor-liquid equilibria of mixtures containing alkanes, carbon dioxide, and nitrogen". In: *AIChE Journal* 47.7, pp. 1676–1682. ISSN: 1547-5905. DOI: 10.1002/aic.690470719. URL: <http://dx.doi.org/10.1002/aic.690470719>.
- Preparata, F.P. and M.I. Shamos (1985). *Computational geometry: an introduction*. Texts and monographs in computer science. Springer-Verlag. ISBN: 9780387961316. URL: <http://books.google.com/books?id=gFtvRdUY09UC>.
- Pusztai, L. and et al. (1988). "Vacancies in molten salts: a characteristic feature of the structure". In: *J. Phys. C: Solid State Phys.* 21.19, p. 3687.
- Rajamäki, Timo et al. (2004). "High excitations in coupled-cluster series: vibrational energy levels of ammonia". In: *Molecular Physics* 102.21-22, pp. 2297–2310. DOI: 10.1080/00268970412331292759. eprint: <http://www.tandfonline.com/doi/pdf/10.1080/00268970412331292759>. URL: <http://www.tandfonline.com/doi/abs/10.1080/00268970412331292759>.
- Ramachandran, G.N., C. Ramakrishnan, and V. Sasisekharan (1963). "Stereochemistry of polypeptide chain configurations". In: *Journal of Molecular Biology* 7.1, pp. 95–99. ISSN: 0022-2836. DOI: 10.1016/S0022-2836(63)80023-6. URL: <http://www.sciencedirect.com/science/article/pii/S0022283663800236>.
- Rapaport, D. C. (1983). In: *Mol. Phys.* 48, p. 23.
- Rapaport, D.C. (2004). *The art of molecular dynamics simulation*. Cambridge University Press. ISBN: 9780521825689. URL: <http://books.google.com/books?id=iqDJ2hjQBMEC>.
- Reighard, Tricia S., Stephen T. Lee, and Susan V. Olesik (1996). "Determination of methanol/CO₂ and acetonitrile/CO₂ vapor-liquid phase equilibria using a variable-volume view cell". In: *Fluid Phase Equilibria* 123.1-2, pp. 215–230. ISSN: 0378-3812. DOI: DOI: 10.1016/S0378-3812(96)90029-1. URL: <http://www.sciencedirect.com/science/article/pii/S0378381296900291>.
- Rey-Castro, Carlos and Lourdes F. Vega (2006). "Transport Properties of the Ionic Liquid 1-Ethyl-3-Methylimidazolium Chloride from Equilibrium Molecular Dynamics Simulation. The Effect of Temperature". In: *The Journal of Physical Chemistry B* 110.29, pp. 14426–14435. DOI: 10.1021/jp062885s. eprint: <http://pubs.acs.org/doi/pdf/10.1021/jp062885s>. URL: <http://pubs.acs.org/doi/abs/10.1021/jp062885s>.
- Ricci, M. A. et al. (1995). "Microscopic structure of low temperature liquid ammonia: A neutron diffraction experiment". In: *The Journal of Chemical Physics* 102.19, pp. 7650–7655. DOI: 10.1063/1.469016. URL: <http://link.aip.org/link/?JCP/102/7650/1>.
- Richard, P. et al. (1998). In: *Physica A* 259, p. 205.
- Rodriguez, Javier, Munir S. Skaf, and Daniel Laria (2003). "Solvation of excess electrons in supercritical ammonia". In: *J. Chem. Phys.* 119.12, pp. 6044–6052.

- Rosenau, Thomas et al. (2001). "The chemistry of side reactions and byproduct formation in the system NMMO/cellulose (Lyocell process)". In: *Progress in Polymer Science* 26.9, pp. 1763–1837. ISSN: 0079-6700. DOI: DOI:10.1016/S0079-6700(01)00023-5. URL: <http://www.sciencedirect.com/science/article/pii/S0079670001000235>.
- Rovere, M, D W Heermann, and K Binder (1990). "The gas-liquid transition of the two-dimensional Lennard-Jones fluid". In: *Journal of Physics: Condensed Matter* 2.33, pp. 7009–7032. URL: <http://stacks.iop.org/0953-8984/2/7009>.
- Ruff, Imre et al. (1986). "Grand canonical Monte Carlo simulation of liquid argon". In: *J. Chem. Phys.* 85.4, pp. 2169–2177.
- Ruocco, G., M. Sampoli, and R. Vallauri (1992). "Analysis of the network topology in liquid water and hydrogen sulphide by computer simulation". In: *The Journal of Chemical Physics* 96.8, pp. 6167–6176. DOI: 10.1063/1.462889. URL: <http://link.aip.org/link/?JCP/96/6167/1>.
- Ruocco, G. et al. (1993). "Molecular dynamics results for stretched water". In: *J. Chem. Phys.* 99.10, pp. 8095–8104.
- Saitow, Ken-ichi, Daisuke Kajiya, and Keiko Nishikawa (2005). "Time Evolution of Density Fluctuation in Supercritical Region. I. Non-hydrogen-bonded Fluids Studied by Dynamic Light Scattering". In: *The Journal of Physical Chemistry A* 109.1, pp. 83–91. DOI: 10.1021/jp046555o. eprint: <http://pubs.acs.org/doi/pdf/10.1021/jp046555o>. URL: <http://pubs.acs.org/doi/abs/10.1021/jp046555o>.
- Saitow, Ken-ichi et al. (2001). "Terahertz absorption spectra of supercritical CHF₃ to investigate local structure through rotational and hindered rotational motions". In: *Chem. Phys. Lett.* 341.1-2. 0009-2614 doi: DOI: 10.1016/S0009-2614(01)00467-5, pp. 86–92.
- Saitow, Ken-ichi et al. (2003). "Local density enhancement in neat supercritical fluid due to attractive intermolecular interactions". In: *Chem. Phys. Lett.* 368.1-2. 0009-2614 doi: DOI: 10.1016/S0009-2614(02)01851-1, pp. 209–214.
- Sambasivarao, Somisetti V. and Orlando Acevedo (2009). "Development of OPLS-AA Force Field Parameters for 68 Unique Ionic Liquids". In: *Journal of Chemical Theory and Computation* 5.4, pp. 1038–1050. DOI: 10.1021/ct900009a. eprint: <http://pubs.acs.org/doi/pdf/10.1021/ct900009a>. URL: <http://pubs.acs.org/doi/abs/10.1021/ct900009a>.
- Sasaki, Mitsuru et al. (2000). "Dissolution and Hydrolysis of Cellulose in Subcritical and Supercritical Water". In: *Industrial & Engineering Chemistry Research* 39.8, pp. 2883–2890. DOI: 10.1021/ie990690j. eprint: <http://pubs.acs.org/doi/pdf/10.1021/ie990690j>. URL: <http://pubs.acs.org/doi/abs/10.1021/ie990690j>.

- Sastry, S., S. Torquato T. M. Truskett P. G. Debenedetti, and F. H. Stillinger (1998). In: *Mol. Phys.* 95, p. 289.
- Schafer, Tim et al. (2008). “ND-stretching vibrational energy relaxation of NH₂D in liquid-to-supercritical ammonia studied by femtosecond midinfrared spectroscopy”. In: *J. Chem. Phys.* 128.6, pp. 064502–8.
- Schenker, Iwan et al. (2009). “Quantification of the heterogeneity of particle packings”. In: *Phys. Rev. E* 80.2. Copyright (C) 2010 The American Physical Society Please report any problems to prola@aps.org PRE, p. 021302.
- Scherer, Philip C. (1931). “SOLUBILITY OF CELLULOSE IN AMMONIA SALT SOLUTIONS”. In: *Journal of the American Chemical Society* 53.11, pp. 4009–4013. DOI: 10.1021/ja01362a012. eprint: <http://pubs.acs.org/doi/pdf/10.1021/ja01362a012>. URL: <http://pubs.acs.org/doi/abs/10.1021/ja01362a012>.
- Schuler, Lukas D., Xavier Daura, and Wilfred F. van Gunsteren (2001). “An improved GROMOS96 force field for aliphatic hydrocarbons in the condensed phase”. In: *Journal of Computational Chemistry* 22.11, pp. 1205–1218. ISSN: 1096-987X. DOI: 10.1002/jcc.1078. URL: <http://dx.doi.org/10.1002/jcc.1078>.
- Schwartz, M. and C. H. Wang (1973). “Raman study of Fermi resonance, hydrogen bonding, and molecular reorientation in liquid ammonia”. In: 59.10, pp. 5258–5267. ISSN: 00219606. DOI: DOI: 10.1063/1.1679868. URL: <http://dx.doi.org/10.1063/1.1679868>.
- Sega, Marcello et al. (2004). “Free volume properties of a linear soft polymer: A computer simulation study”. In: *J. Chem. Phys.* 121.5, pp. 2422–2427.
- Seifried, Bernhard and Feral Temelli (2010). “Density of Carbon Dioxide Expanded Ethanol at (313.2, 328.2, and 343.2) K”. In: *Journal of Chemical & Engineering Data* 55.7, pp. 2410–2415. DOI: 10.1021/je900830s. eprint: <http://pubs.acs.org/doi/pdf/10.1021/je900830s>. URL: <http://pubs.acs.org/doi/abs/10.1021/je900830s>.
- Sette, F. et al. (2000). “Determination of the Short-Wavelength Propagation Threshold in the Collective Excitations of Liquid Ammonia”. In: *Phys. Rev. Lett.* 84 (18), pp. 4136–4139. DOI: 10.1103/PhysRevLett.84.4136. URL: <http://link.aps.org/doi/10.1103/PhysRevLett.84.4136>.
- Shih, Jing-Ping, Sheh-Yi Sheu, and Chung-Yuan Mou (1994). “A Voronoi polyhedra analysis of structures of liquid water”. In: *J. Chem. Phys.* 100.3, pp. 2202–2212.
- Sih, Roderick and Neil R. Foster (2008). “Viscosity measurements on saturated gas expanded liquid systems—Acetone and carbon dioxide”. In: *The Journal of Supercritical Fluids* 47.2. 0896-8446 doi: DOI: 10.1016/j.supflu.2008.07.004, pp. 233–239.
- Simon, Steven H., Vladimir Dobrosavljevic, and Richard M. Stratt (1991). “The mobility of electrons in simple insulating fluids as a percolation problem”. In: *J. Chem. Phys.* 94.11, pp. 7360–7375.

- Smith, W. and T. R. Forester (1996). "DL_POLY_2.0: A general-purpose parallel molecular dynamics simulation package". In: *Journal of Molecular Graphics* 14.3, pp. 136–141. ISSN: 0263-7855. DOI: DOI: 10.1016/S0263-7855(96)00043-4. URL: <http://www.sciencedirect.com/science/article/B6VNC-3VV619Y-3/2/e80d1e3054af4333e3a108aa8f593163>.
- Soares, Thereza A. et al. (2005). "An improved nucleic acid parameter set for the GRO-MOS force field". In: *Journal of Computational Chemistry* 26.7, pp. 725–737. ISSN: 1096-987X. DOI: 10.1002/jcc.20193. URL: <http://dx.doi.org/10.1002/jcc.20193>.
- Soyer, A. et al. (2000). "Voronoi Tessellation Reveals the Condensed Matter Character of Folded Proteins". In: *Phys. Rev. Lett.* 85.16. Copyright (C) 2011 The American Physical Society Please report any problems to prola@aps.org PRL, p. 3532.
- Span, Roland and Wolfgang Wagner (1996). "A New Equation of State for Carbon Dioxide Covering the Fluid Region from the Triple Point Temperature to 1100 K at Pressures up to 800 MPa". In: 25.6, pp. 1509–1596. ISSN: 00472689. DOI: DOI: 10.1063/1.555991. URL: <http://dx.doi.org/doi/10.1063/1.555991>.
- Spirko, V. (1983). "Vibrational anharmonicity and the inversion potential function of NH₃". In: *Journal of Molecular Spectroscopy* 101.1, pp. 30–47. ISSN: 0022-2852. DOI: 10.1016/0022-2852(83)90004-8. URL: <http://www.sciencedirect.com/science/article/pii/0022285283900048>.
- Spirko, V and W.P Kraemer (1989). "Anharmonic potential function and effective geometries for the NH₃ molecule". In: *Journal of Molecular Spectroscopy* 133.2, pp. 331–344. ISSN: 0022-2852. DOI: 10.1016/0022-2852(89)90196-3. URL: <http://www.sciencedirect.com/science/article/pii/0022285289901963>.
- Staff, Sun, Y.P. Sun, and E. Corporation (2002). *Supercritical Fluid Technology in Materials Science and Engineering: Synthesis, Properties and Applications*. Marcel Dekker. ISBN: 9780824744717. URL: <http://books.google.com/books?id=LbfmiOLibV4C>.
- Stanley, H. Eugene (1987). *Introduction to Phase Transitions and Critical Phenomena*. Oxford University Press.
- Starr, Francis W. et al. (2002). "What Do We Learn from the Local Geometry of Glass-Forming Liquids?" In: *Phys. Rev. Lett.* 89.12. Copyright (C) 2010 The American Physical Society Please report any problems to prola@aps.org PRL, p. 125501.
- Stubbs, John M., Jeffrey J. Potoff, and J. Ilja Siepmann (2004). "Transferable Potentials for Phase Equilibria. 6. United-Atom Description for Ethers, Glycols, Ketones, and Aldehydes". In: *The Journal of Physical Chemistry B* 108.45, pp. 17596–17605. DOI: 10.1021/jp049459w. eprint: <http://pubs.acs.org/doi/pdf/10.1021/jp049459w>. URL: <http://pubs.acs.org/doi/abs/10.1021/jp049459w>.
- Tassaing, T. et al. (2010). "Supercritical ammonia: A molecular dynamics simulation and vibrational spectroscopic investigation The structure of liquid carbon dioxide

- and carbon disulfide Analysis of the transverse and the longitudinal pseudodiffusion of CO₂ in sub- and supercritical states: A molecular-dynamics analysis". In: *The Journal of Chemical Physics* 133.21, pp. 214505–8.
- Thompson, Helen et al. (Mar. 2003). "Structural Studies of Ammonia and Metallic Lithium? Ammonia Solutions". In: *Journal of the American Chemical Society* 125.9, pp. 2572–2581. ISSN: 0002-7863. URL: <http://dx.doi.org/10.1021/ja021227s>.
- Ting, Simon S. T. et al. (1993). "Solubility of naproxen in supercritical carbon dioxide with and without cosolvents". In: *Industrial & Engineering Chemistry Research* 32.7, pp. 1471–1481. DOI: 10.1021/ie00019a022. eprint: <http://pubs.acs.org/doi/pdf/10.1021/ie00019a022>. URL: <http://pubs.acs.org/doi/abs/10.1021/ie00019a022>.
- Tokita, Nakako et al. (2004). "Voronoi space division of a polymer: Topological effects, free volume, and surface end segregation". In: *J. Chem. Phys.* 120.1, pp. 496–505.
- Tongraar, Anan, Teerakiat Kerdcharoen, and Supot Hannongbua (2006). "Simulations of Liquid Ammonia Based on the Combined Quantum Mechanical/Molecular Mechanical (QM/MM) Approach". In: *The Journal of Physical Chemistry A* 110.14, pp. 4924–4929. DOI: 10.1021/jp057342h. eprint: <http://pubs.acs.org/doi/pdf/10.1021/jp057342h>. URL: <http://pubs.acs.org/doi/abs/10.1021/jp057342h>.
- Toxvaerd, Soren (1990). "Molecular dynamics calculation of the equation of state of alkanes". In: *The Journal of Chemical Physics* 93.6, pp. 4290–4295.
- Tsai, Jerry and Mark Gerstein (2002). "Calculations of protein volumes: sensitivity analysis and parameter database". In: *Bioinformatics* 18.7, pp. 985–995.
- Tsuzuki, S. et al. (1996). In: *J. Phys. Chem.* 100, p. 4400.
- Tucker, Susan C. (Feb. 1999). "Solvent Density Inhomogeneities in Supercritical Fluids". In: *Chemical Reviews* 99.2, pp. 391–418. ISSN: 0009-2665. URL: <http://dx.doi.org/10.1021/cr9700437>.
- Tucker, Susan C. and Michael W. Maddox (Apr. 1998). "The Effect of Solvent Density Inhomogeneities on Solute Dynamics in Supercritical Fluids: A Theoretical Perspective". In: *The Journal of Physical Chemistry B* 102.14, pp. 2437–2453. ISSN: 1520-6106. URL: <http://dx.doi.org/10.1021/jp972382+>.
- Tuckerman, M. (2009). *Statistical mechanics: theory and molecular simulation*. Oxford Graduate Texts. Oxford University Press. ISBN: 9780198525264. URL: <http://books.google.com/books?id=Lo3Jqc0pgrcC>.
- Ullmann, F. (2003). *Ullmann's encyclopedia of industrial chemistry*. Ullmann's Encyclopedia of Industrial Chemistry v. 3. Wiley-VCH. ISBN: 9783527303854. URL: <http://books.google.com/books?id=QolUAAAAMAAJ>.

- Ungerer, Philippe et al. (2000). "Optimization of the anisotropic united atoms intermolecular potential for n-alkanes". In: *The Journal of Chemical Physics* 112.12, pp. 5499–5510.
- Vanommeslaeghe, K. et al. (2010). "CHARMM general force field: A force field for drug-like molecules compatible with the CHARMM all-atom additive biological force fields". In: *Journal of Computational Chemistry* 31.4, pp. 671–690. ISSN: 1096-987X. DOI: 10.1002/jcc.21367. URL: <http://dx.doi.org/10.1002/jcc.21367>.
- Varadan, P. and M. J. Solomon (2003). "Direct visualization of flow-induced microstructure in dense colloidal gels by confocal laser scanning microscopy". In: *J. Rheol.* 47.
- Varga, Neal E Franks; Julianna K (1980). Pat. 4196282.
- Verlet, Loup (July 1967). "Computer "Experiments" on Classical Fluids. I. Thermodynamical Properties of Lennard-Jones Molecules". In: *Phys. Rev.* 159.1, p. 98. DOI: 10.1103/PhysRev.159.98.
- Voloshin, V. P., S. Beaufils, and N. N. Medvedev (2002). "Void space analysis of the structure of liquids". In: *Journal of Molecular Liquids* 96-97. Physical Chemistry of Liquids, pp. 101–112. ISSN: 0167-7322. DOI: DOI: 10.1016/S0167-7322(01)00330-0. URL: <http://www.sciencedirect.com/science/article/B6TGR-459J6C5-8/2/4b4a01aea297f7324a04a8344e8c13ca>.
- Voloshin, Vladimir P. et al. (1995). "Investigation of free volume percolation under the liquid–glass phase transition". In: *The Journal of Chemical Physics* 102.12, pp. 4981–4986. DOI: 10.1063/1.469547. URL: <http://link.aip.org/link/?JCP/102/4981/1>.
- Voronoi, G. F. (1908). In: *Z. Angew. Math.* 134, p. 198.
- Vyalov, I., A. Idrissi, and M. Kiselev (2010a). "Cellobiose solvation free energy in scCO₂ with cosolvent". In: *Germany: Trilateral Seminar (Russia, Germany, France) : Solvation in Complex Liquids by Theory and Experiment, 23-25 June*.
- (2010b). "Clustering and structure of sub- and supercritical fluids." In: *Journées Nord-Ouest Européennes des Jeunes Chercheurs, Villeneuve d'Ascq, 18-19 Mars*.
- (2011). "Modelling solvation cellobiose in supercritical CO₂ and its mixtures with ethanol and acetone." In: *29th EMLG/JMLG Annual Meeting: New outlook on molecular liquids from short scale to long scale dynamics*.
- Vyalov, I. et al. (2010). "Investigation of the Local Structure in Sub and Supercritical Ammonia Using the Nearest Neighbor Approach: A Molecular Dynamics Analysis". In: *J. Phys. Chem. B* 114.46. doi: 10.1021/jp108701t, pp. 15003–15010.
- Vyalov, I. et al. (2011a). "Modelling solvation of nanocrystal polymorph of cellulose in supercritical CO₂ and its mixtures with ethanol and acetone." In: *"Supercritical fluids (SCF): fundamentals, technologies, innovations", 4–7 July, Listvyanka, lake Baykal*.

- Vyalov, I. et al. (2011b). "Reorientation relaxation in supercritical ammonia". In: *Journal of Molecular Liquids* 159.1. Intermolecular Interactions and Liquid Structure, Selected Papers on Molecular Liquids presented at the EMLG/JMLG 2009 Annual Meeting 6 - 10 September 2009, pp. 31–37. ISSN: 0167-7322. DOI: 10.1016/j.molliq.2010.09.012. URL: <http://www.sciencedirect.com/science/article/pii/S016773221000303X>.
- Wada, M. et al. (2001). "Improved Structural Data of Cellulose III Prepared in Supercritical Ammonia". In: *Macromolecules* 34.5. doi: 10.1021/ma001406z 0024-9297 doi: 10.1021/ma001406z, pp. 1237–1243.
- Wada, Masahisa et al. (2011). "Neutron crystallographic and molecular dynamics studies of the structure of ammonia-cellulose I: rearrangement of hydrogen bonding during the treatment of cellulose with ammonia". In: *Cellulose* 18 (2). 10.1007/s10570-010-9488-5, pp. 191–206. ISSN: 0969-0239. URL: <http://dx.doi.org/10.1007/s10570-010-9488-5>.
- Wesch, A., N. Dahmen, and K. H. Ebert (1996). "Measuring the static dielectric constants of pure carbon dioxide and carbon dioxide mixed with ethanol and toluene at elevated pressures". In: *Berichte der Bunsengesellschaft für physikalische Chemie* 100.8, pp. 1368–1371. ISSN: 0005-9021. DOI: 10.1002/bbpc.19961000816. URL: <http://dx.doi.org/10.1002/bbpc.19961000816>.
- Weygaert, R. van der and Astron. V. Icke (1989). In: *Astrophys.* 213, p. 1.
- Wolde, Pieter Rein ten and Daan Frenkel (1997). "Enhancement of Protein Crystal Nucleation by Critical Density Fluctuations". In: *Science* 277.5334, pp. 1975–1978. DOI: 10.1126/science.277.5334.1975. eprint: <http://www.sciencemag.org/content/277/5334/1975.full.pdf>. URL: <http://www.sciencemag.org/content/277/5334/1975.abstract>.
- Xu, Wenhao, Jichu Yang, and Yinyu Hu (2009). "Microscopic Structure and Interaction Analysis for Supercritical Carbon Dioxide-Ethanol Mixtures: A Monte Carlo Simulation Study". In: *The Journal of Physical Chemistry B* 113.14. doi: 10.1021/jp810193b 1520-6106 doi: 10.1021/jp810193b, pp. 4781–4789.
- Yang, R. Y., R. P. Zou, and A. B. Yu (2002). "Voronoi tessellation of the packing of fine uniform spheres". In: *Phys. Rev. E* 65.4. Copyright (C) 2010 The American Physical Society Please report any problems to prola@aps.org PRE, p. 041302.
- Yeh, Yu-ling and Chung-Yuan Mou (1999). "Orientational Relaxation Dynamics of Liquid Water Studied by Molecular Dynamics Simulation". In: *The Journal of Physical Chemistry B* 103.18, pp. 3699–3705. DOI: 10.1021/jp984584r. eprint: <http://pubs.acs.org/doi/pdf/10.1021/jp984584r>. URL: <http://pubs.acs.org/doi/abs/10.1021/jp984584r>.
- Yeo, Sang-Do et al. (2000). "Critical Properties of Carbon Dioxide + Methanol, + Ethanol, + 1-Propanol, and + 1-Butanol". In: *Journal of Chemical & Engineering Data* 45.5, pp. 932–935. DOI: 10.1021/je000104p. eprint: <http://pubs.acs.org/doi/pdf>

- f/10.1021/je000104p. URL: <http://pubs.acs.org/doi/abs/10.1021/je000104p>.
- Yoshii, Noriyuki and Susumu Okazaki (1998). "Molecular dynamics study of structure of clusters in supercritical Lennard-Jones fluid". In: *Fluid Phase Equilibria* 144.1-2, pp. 225–232. ISSN: 0378-3812. DOI: DOI: 10.1016/S0378-3812(97)00261-6. URL: <http://www.sciencedirect.com/science/article/B6TG2-3V5CNT7-T/2/09f7c7951357d9fd226b1263d54abc7d>.
- Zaninetti, L. (1992). In: *Phys. Letters A* 165.
- Zhang, Z. and Z. Duang (2005). In: *J. Chem. Phys.* 122, p. 214507.
- Zhang, Zhigang and Zhenhao Duan (2005). "An optimized molecular potential for carbon dioxide". In: *The Journal of Chemical Physics* 122.21, pp. 214507–15.
- ZHOU, Jinping and Lina ZHANG (2000). "Solubility of Cellulose in NaOH/Urea Aqueous Solution". In: *Polymer Journal* 32.10, pp. 866–870.
- Zugenmaier, P. (2007). *Crystalline cellulose and derivatives: characterization and structures*. Springer Series in Wood Science. Springer. ISBN: 9783540739333. URL: <http://books.google.com/books?id=5k06oU40BKsC>.